UNIVERSITY OF SOUTHAMPTON
Faculty of Social and Human Sciences
School of Mathematics

Cell Scale Modelling and Numerical Simulation of Transmembrane Potential in Neurons and Glia

by
Stuart George

A thesis submitted in partial fulfillment for the
degree of Doctor of Philosophy

June 2015

UNIVERSITY OF SOUTHAMPTON

ABSTRACT

FACULTY OF SOCIAL AND HUMAN SCIENCES
SCHOOL OF MATHEMATICS

Doctor of Philosophy

by Stuart George

We apply a generic description of the electrochemical behaviour of nerve cells to three specific types of cell, and take a systematic approach to the simplification of the model to determine which anatomical details of each cell have a significant influence on the electrochemical behaviour that occurs within it. These systematically simplified models are compared to established models with differing assumptions regarding cell anatomy, allowing for the suitability of these assumptions to be tested.

The first model we present in this thesis is of the squid giant axon. Our generic model, which accounts for three-dimensional current flow and extracellular resistance not considered in the canonical model of the axon, demonstrates that for large axons *in vivo* the canonical model does not correctly predict the relationship between axon radius and action potential propagation speed, a result we discuss in terms of the evolutionary costs associated with producing, maintaining and operating a very large axon.

The second model we present is of a myelinated axon, where asymptotic analysis of the generic model results in a simplified model accounting for the significant anatomical properties of the cell. Our simplified model makes predictions in line with experimental data. Comparison of this model with existing models demonstrates that some have over simplified the system by neglecting significant physiological details and some have under simplified it by including detailed descriptions of negligible details.

Finally, we present a model of the electrical behaviour of the Bergmann glial cell informed by its structure, and show that this accurately predicts the behaviour of the cell under experimental conditions. We couple this model of the electrical behaviour to a description of the behaviour of ion fluxes and concentrations within the microdomains, providing insight into the cell's ability to control ion concentrations in the extracellular space.

Contents

List of Figures

List of Tables

List of Publications

1. S. George, J. M. Foster and G. Richardson. Modelling in vivo action potential propagation along a giant axon. *J Math Biol* 2014 doi: 10.1007/s00285-013-0751-x.

2. S. George, K. L. Dobson, S. Coombes, G. Richardson and T. C. Bellamy. Computationally efficient modelling of cerebellar Bergmann glia. *In preparation* 2014.

Declaration of Authorship

I, Stuart George, declare that this thesis entitled **Cell Scale Modelling and Numerical Simulation of Transmembrane Potential in Neurons and Glia** and the work presented in it are both my own, and have been generated by me as a result of my own research. I confirm that

- this work was done wholly or mainly while in candidature for a research degree at this University;
- if any part of this thesis has previously been submitted for a degree or any other qualification at this University or any other institution, this has been clearly stated;
- where I have consulted the published work of others, this is always clearly attributed;
- where I have quoted from the works of others, the source is always given. With the exception of such quotations this thesis is entirely my own work;
- I have acknowledged all main sources of help;
- where the thesis is based on work done by myself jointly with others, I have made clear exactly what was done by others and what I have contributed myself;
- parts of this work have been published

Signed: Date:

Chapter 1

Introduction

1.1 The nervous system

The nervous system of an organism is comprised of the cells in its body which are specialised to carry electrical signals. These signals are used to pass information between different regions of the body, allowing for control of movements and actions, collection and processing of sensory inputs, and higher level processes — such as thought — occurring in the brain.

The cells of the nervous system can be broadly divided into two classes, neurons and glia, according to their primary function. Neurons are specialised to receive and integrate signals in outgrowths known as dendrons, and then transmit them over relatively large distances through long, thin, approximately cylindrical outgrowths called axons. Glia, on the other hand, play more of a regulatory role to maintain and support neurons, without actively transmitting signals.

1.1.1 The cell membrane

Crucial to the roles of both classes is the behaviour of the membrane of the cell, which separates its contents (the intracellular space) from the external environment (the extracellular space). This membrane is formed from a phospholipid bilayer, polar molecules

arranged in two layers, such that their hydrophilic 'heads' face outward into the intracellular and extracellular solutions (mainly water) and their hydrophobic 'tails' are between the two layers (see figure 1.1).

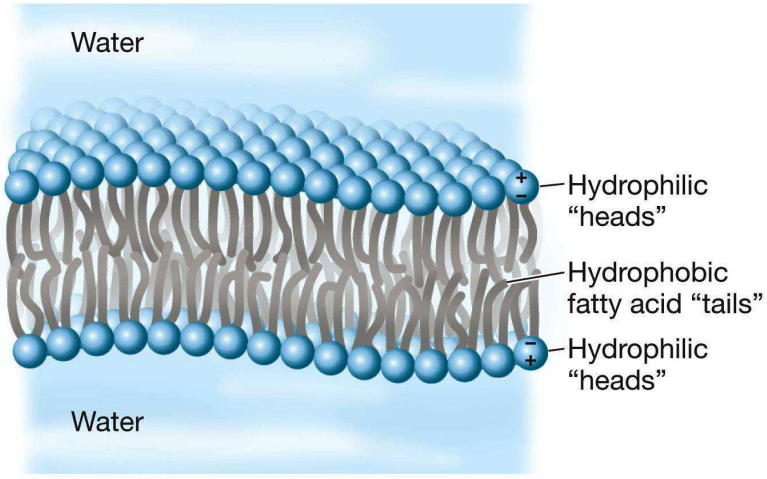

FIGURE 1.1: The phospholipid bilayer, showing the arrangement of the individual molecules. Reproduced from [94]

This bilayer has a very small electrical conductance ($10^{-4}\,\mathrm{S}\cdot\mathrm{m}^{-2}$ [61]) and provides an almost perfect barrier to the flow of ions. In neurons and glia, the electrochemical separation of the intracellular and extracellular spaces is used to create a potential jump across the membrane — known as the transmembrane potential — which is used for the transmission of information. In glia these signals can be subtle, and are modulated by a huge variety of chemical and structural factors (discussion of which we defer to chapter 4) but in neurons the principal method of signalling is a large increase in transmembrane potential, known as an action potential — in fact neurons and glia are distinguished by their ability to produce action potentials.

1.1.2 The action potential

Action potentials in neurons are primarily driven by flows of potassium and sodium ions. At rest, the cell has relatively high intracellular concentrations of potassium and relatively low intracellular concentrations of sodium, maintained by the action of Na^+/K^+-ATPase, an enzyme embedded in the cell membrane which exchanges intracellular sodium ions for extracellular potassium ions. The concentration gradients created

by this enzyme provide the energy needed for the long range transmission of signals, and also produce its steady-state transmembrane potential (this is predicted by the Goldman equation, which determines the transmembrane potential by balancing the effects of potential gradients with those arising from concentration gradients, and is typically around -70 mV [81], although it will vary between organisms and between neuron types [29]). The transmembrane potential is manipulated by specialised proteins called ion channels, which alter the conductances of the cell membrane to different ion species to harness the concentration and potential gradients.

1.1.3 Ion channels

The high resistance of the phospholipid bilayer means certain adaptations are necessary to allow ions to pass through it and change the transmembrane potential. Ion channels (see figure 1.2) are a wide class of protein-formed pores in the membrane that selectively allow certain ion species to flow from one side of the membrane to the other — as dictated by potential and concentration gradients — effectively increasing the conductance of the membrane. This effect can be undone by changes in the conformation of the protein (in response to the binding of a chemical to the protein or changes in transmembrane potential, for example, [38]), which perturb the finely tuned structure of the ion channel, effectively 'closing' it and returning the membrane to its original, lower conductance.

Ion channels can be separated into classes based on the ion species that can flow through them, and thus there are potassium channels, which only allow the flow of potassium ions, sodium channels, which only allow the flow of sodium ions, channels specific to a range of other ions and channels specific to (all) positively or negatively charged ions. Similarly, ion channels can be classified according to the stimuli they open and close in response to, which may be physical (transmembrane potential variations, stresses on the membrane) or chemical (the presence or absence of certain substances) [17]. The channels involved in action potential propagation are 'voltage-gated' — the protein which forms the channel changes its conformation in response to changes in the transmembrane potential — and so our subsequent work tends to be concerned solely with this family of channels. Ion channels which open and close in response to some stimulus are also known

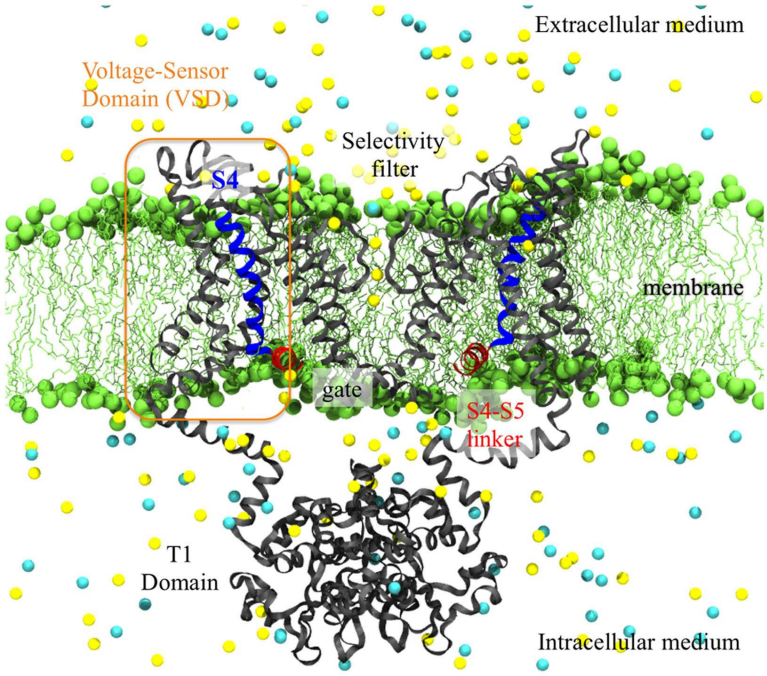

FIGURE 1.2: Protein structure of an ion channel (black) embedded in the cell membrane (green). Figure as originally published in Delemotte L *et al.* (2012) Molecular dynamics simulations of voltage-gated cation channels: insights on voltage-sensor domain function and modulation Front. Pharmacol. 3. doi: 10.3389/fphar.2012.00097

as 'active' channels, distinguishing them from 'passive' channels which don't open and close, and instead provide a constant increase to the conductance of the cell membrane.

1.1.4 Producing an action potential

The behaviour of voltage-gated ion channels was the subject of the seminal work of Hodgkin and Huxley, in a series of papers published in 1952, although their existence could only be inferred at the time [40, 41, 42, 43, 44, 45]. The work described in these papers was centred around empirical measurements of the conductance of the membrane of the squid giant neuron to different ions at different membrane potentials. While their subsequent model of membrane behaviour was not based on microscopic electrophysiological data from ion channels (the existence of which could only be conclusively demonstrated after technological advances in the 1970s [49, 66, 67]), it nevertheless showed how action potentials are produced by the interactions of different conductances through the cell membrane.

When the cell membrane is depolarised (the transmembrane potential raised) above a threshold by some local injection of current, a cycle of responses occur which lead to a propagating signal (a simulation of this cycle is shown in figure 1.3). The time constant (that is, the characteristic time scale over which the channel responds to transmembrane potential changes) for the opening of sodium channels ($\sim 10^{-4}$ s) is much smaller than that of the potassium ($\sim 5 \times 10^{-3}$ s) [27, 44], which means that the initial current flow in response to the depolarisation is almost entirely due to the movement of sodium ions. Sodium channels open in response to the depolarisation and the concentration and potential gradients cause positively charged sodium ions to flow into the cell from the extracellular medium, further depolarising it and beginning a positive feedback loop which opens further sodium channels. This sodium current is responsible for the sharp upward spike seen in figure 1.3. As the transmembrane potential increases, the potassium channels also begin to open, and the potassium concentration gradient causes positively charged potassium ions to flow out of the cell. On a similar timescale the sodium channels inactivate, preventing further flow of positive ions into the cell, and so the transmembrane potential returns to its resting value (after a slight 'overshoot', known as a hyperpolarisation).

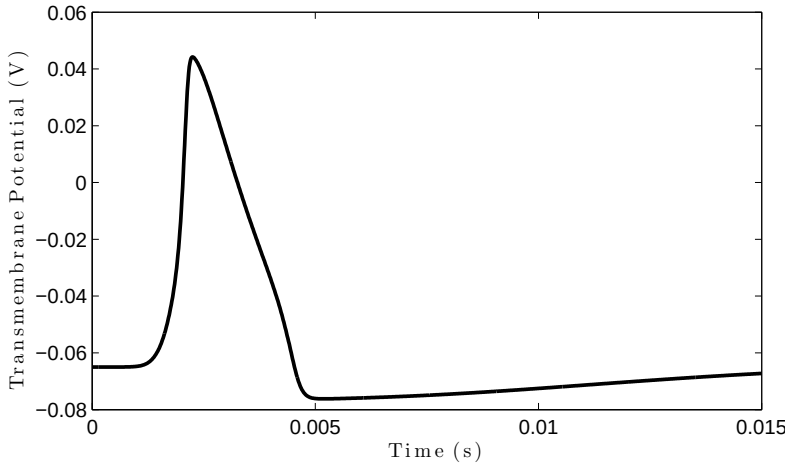

FIGURE 1.3: Transmembrane potential during an action potential. The initial, rapid depolarisation is caused by the flow of sodium ions, driven into the cell by the concentration and potential gradients and the slower repolarisation is caused by the flow of potassium ions, driven out by the concentration gradient.

As the local membrane depolarisation in response to the influx of sodium ions reaches its peak (∼40 mV), longitudinal current flow in the neuron raises the membrane potential in neighbouring regions above the threshold required to begin the action potential cycle.

Thus, as each region of membrane reaches its peak potential and excites the regions adjacent to it, the action potential propagates along the neuron in the form of a travelling wave.

1.1.5 Currents through the cell membrane

The exact form of the equations used to describe the current through the ion channels, j^*, is dependent on the kind of membrane being modelled. For squid neurons the seminal model is, as mentioned above, that of Hodgkin and Huxley. However, the form and basic structure of the Hodgkin-Huxley model can be easily adapted to represent the behaviour of almost any voltage-gated ion channel, and therefore is relevant to neuron models in general.

In general terms, the Hodgkin-Huxley model is constructed by assuming the cell membrane has independent pathways by which charge can flow through the membrane (e.g. sodium and potassium channels). Each pathway has some maximal conductance (corresponding to every channel of that type being open), and the actual conductance available is this maximal conductance multiplied by the proportion of open channels. The proportion of open channels is governed by time-dependent, non-linear differential equations. Each channel type has an associated opening rate and closing rate (which are dependent on the transmembrane potential), from which the rate of change of the open proportion can be established. It should be noted again, however, that the model is derived phenomenologically — written down and tuned in order that the results match with experimental data — rather than being systematically derived from the underlying physiology of the cell membrane, as the existence of ion channels was not demonstrated until around twenty years after the work was published [66].

The Hodgkin-Huxley model of the membrane current density, j^*, in the squid giant axon is given by

$$j^* = g_{\mathrm{K}} n^4 \left(\Phi^* - \Phi_{\mathrm{K}}\right) + g_{\mathrm{Na}} m^3 h \left(\Phi^* - \Phi_{\mathrm{Na}}\right) + g_{\mathrm{L}} \left(\Phi^* - \Phi_{\mathrm{l}}\right), \tag{1.1}$$

where there are three pathways, one specific to potassium ions, one to sodium ions and a leak current carried by no specific ion. The transmembrane potential is denoted by Φ^* (with a superscript asterisk signifying a dimensional variable), and the maximal membrane conductances per unit area for the potassium, sodium and leak currents are given by g_{K}, g_{Na} and g_{L} respectively. The reversal potentials Φ_{K}, Φ_{Na} and Φ_{l} represent the transmembrane potential at which the concentration gradient and potential gradient balance, and thus the point at which the direction of the current will switch from into the cell to out of it, or *vice versa*. The gating variables, n, m and h, determine the proportion of the potassium and sodium conductances available – essentially the proportion of open channels, but note that n, m and h are not *linearly* proportional to the number of open channels — and are determined from the transmembrane potential by the following differential equations

$$\frac{\partial n}{\partial t^*} = \frac{n_\infty\left(\Phi^*\right) - n}{\tau_n^*\left(\Phi^*\right)}, \tag{1.2}$$

$$\frac{\partial m}{\partial t^*} = \frac{m_\infty\left(\Phi^*\right) - m}{\tau_m^*\left(\Phi^*\right)}, \tag{1.3}$$

$$\frac{\partial h}{\partial t^*} = \frac{h_\infty\left(\Phi^*\right) - h}{\tau_h^*\left(\Phi^*\right)}, \tag{1.4}$$

where

$$\tau_i^* = \frac{1}{\alpha_i^*\left(\Phi^*\right) + \beta_i^*\left(\Phi^*\right)}, \tag{1.5}$$

$$i_\infty = \alpha_i^*\left(\Phi^*\right)\tau_i^*\left(\Phi^*\right), \tag{1.6}$$

$$i = n, m, h \tag{1.7}$$

and

$$\alpha_n^* = \frac{10^4\left(\Phi^* + 0.055\right)}{1 - \exp\left(-100\left(\Phi^* + 0.055\right)\right)}, \qquad \beta_n^* = 125\exp\left(-12.5\left(\Phi^* + 0.065\right)\right), \tag{1.8}$$

$$\alpha_m^* = \frac{10^5\left(\Phi^* + 0.04\right)}{1 - \exp\left(-100\left(\Phi^* + 0.04\right)\right)}, \qquad \beta_m^* = 4000\exp\left(-55.6\left(\Phi^* + 0.065\right)\right), \tag{1.9}$$

$$\alpha_h^* = 70\exp\left(-50\left(\Phi^* + 0.065\right)\right), \qquad \beta_h^* = \frac{1000}{1 + \exp\left(-100\left(\Phi^* + 0.035\right)\right)}, \tag{1.10}$$

In essence each gating variable, i, tends to its steady state value, i_∞, at a rate determined

by the time constant τ_i^*, which is itself determined by the empirically derived functions α_i and β_i. Note that the form of the expressions above is slightly different from the form written in [44], as we have chosen to express all variables in terms of volts and seconds, rather than millivolts and milliseconds (which explains the large constants appearing in the rates above).

Alternatively, we can rewrite equations (1.2) to (1.4) as follows

$$\frac{\partial n}{\partial t^*} = \alpha_n^*(\Phi^*)(1-n) - \beta_n^*(\Phi^*)\, n, \tag{1.11}$$

$$\frac{\partial m}{\partial t^*} = \alpha_m^*(\Phi^*)(1-m) - \beta_m^*(\Phi^*)\, m, \tag{1.12}$$

$$\frac{\partial h}{\partial t^*} = \alpha_h^*(\Phi^*)(1-h) - \beta_h^*(\Phi^*)\, h, \tag{1.13}$$

in which form it is clearer that α_i^* is the activation rate of gating variable i — the rate at which it tends to 1, the state where all the channels are open — and β_i^* is the inactivation rate — at which it tends to 0, where all the channels are closed.

Note that while n, m, and h can vary spatially (that is, vary with position along in a neuron), the equations that govern their behaviour depend only on time.

Figures 1.4 to 1.6 show the form of these activation and inactivation rates, as functions of transmembrane potential. It is useful to notice firstly that for n and m the activation rates increase with transmembrane potential and the inactivation rates decrease, while for h the form of the rates is reversed. This is due to the qualitatively different behaviour of the sodium channel (the behaviour of which is modelled by m and h) to the potassium — where the potassium channel simply opens or closes at increased or decreased transmembrane potentials respectively, the sodium channel closes at decreased transmembrane potential, opens as the transmembrane potential increases and then closes again in response to continued increases. Thus m represents the 'opening' of the sodium channel in response to increased transmembrane potential and h the 'closing', and therefore h behaves in the opposite way to m. Secondly, we notice that the rates for m are both an order of magnitude larger than those for n and h, which means τ_m^* is significantly smaller than τ_n^* and τ_h^* (see figure 1.7), reflecting (as mentioned above) the

fact that sodium channels respond to changes in transmembrane potential much faster than potassium channels.

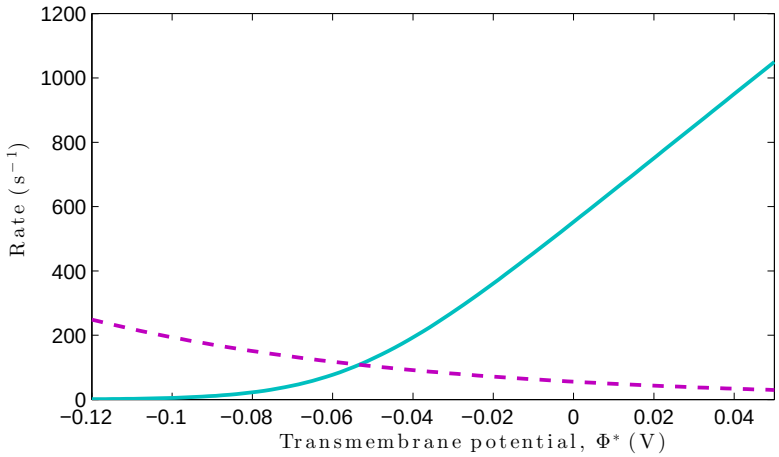

FIGURE 1.4: Activation ($\alpha_n^*(\Phi^*)$ (——)) and inactivation ($\beta_n^*(\Phi^*)$ (- - -)) rates for the potassium channel gating variable n.

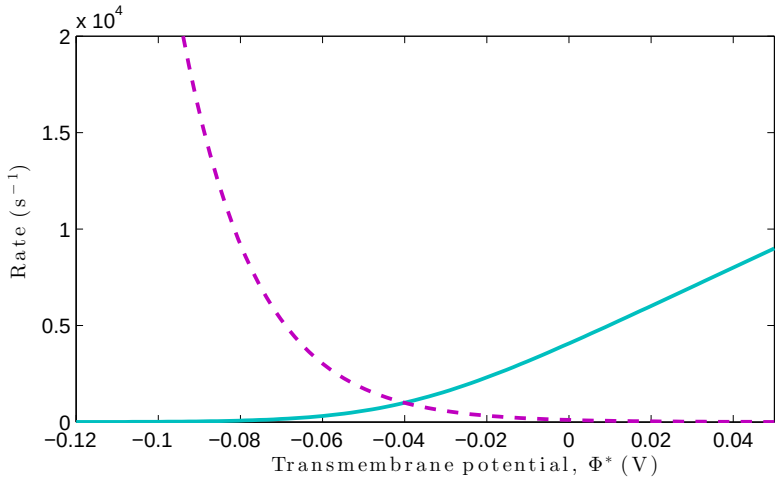

FIGURE 1.5: Activation ($\alpha_m^*(\Phi^*)$ (——)) and inactivation ($\beta_m^*(\Phi^*)$ (- - -)) rates for the sodium channel gating variable m.

Figure 1.8 shows the total current density through the membrane during an action potential (positive currents here are currents *out* of the cell) and figure 1.9 shows the breakdown into the three components (potassium, sodium and leak). Finally, figure 1.10 shows the behaviour of the three gating variables during the action potential.

1.1.5.1 The effects of stochasticity

The behaviour of individual ion channels is stochastic and under certain conditions this can have significant effects on membrane behaviour — for example causing signals to

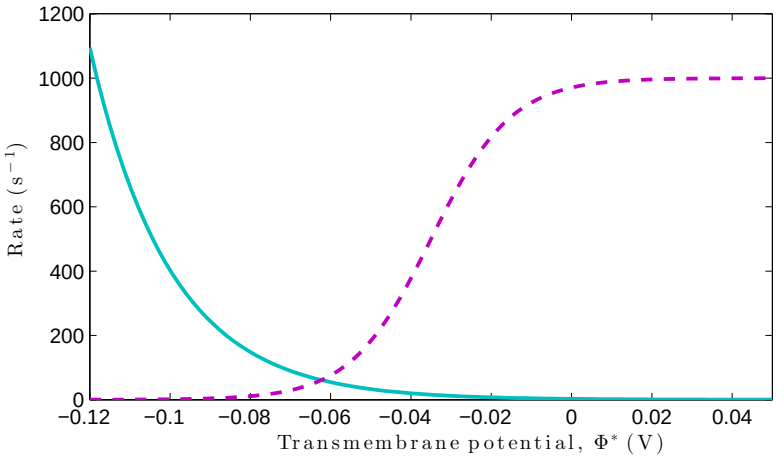

FIGURE 1.6: Activation ($\alpha_h^*(\Phi^*)$ (——)) and inactivation ($\beta_h^*(\Phi^*)$ (- - -)) rates for the sodium channel gating variable h.

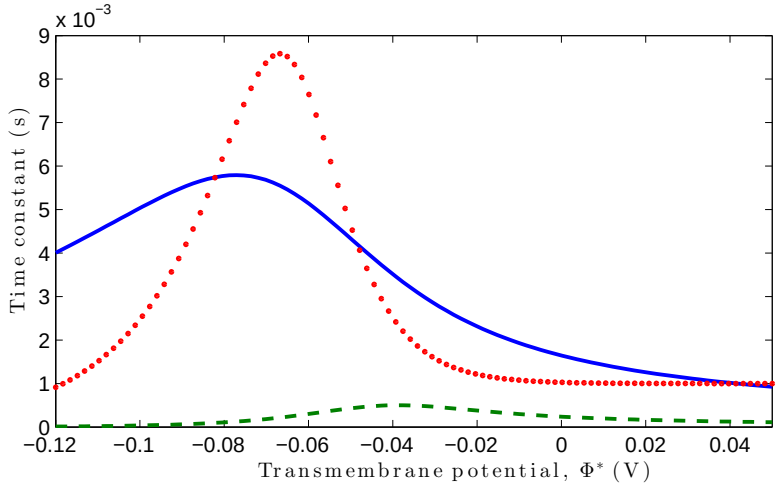

FIGURE 1.7: Time constants of the three gating variables τ_n (——), τ_m (- - -) and τ_h (·····) as a function of transmembrane potential.

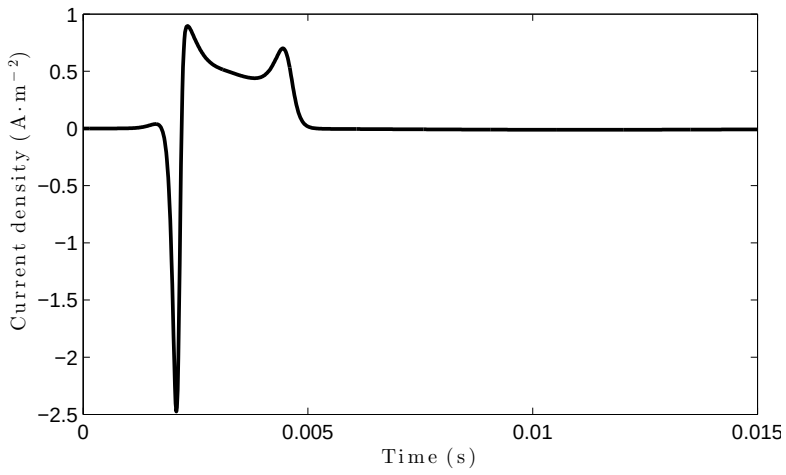

FIGURE 1.8: Current density through the cell membrane during an action potential (positive currents are directed out of the cell)

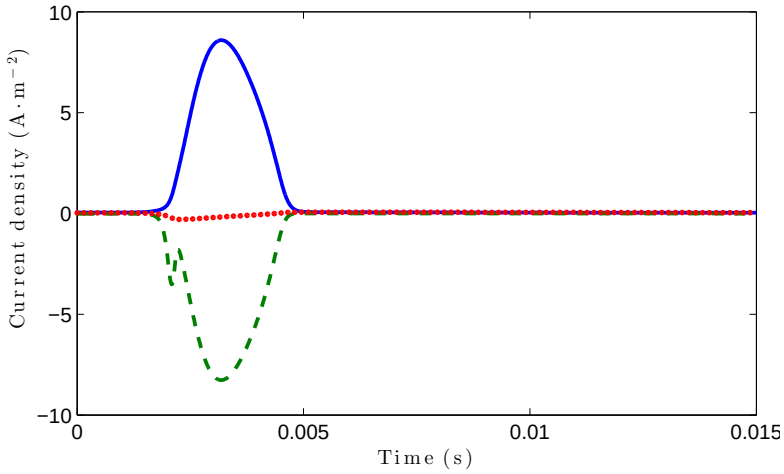

FIGURE 1.9: Current density through the cell membrane during an action potential broken down by component. Current densities shown through potassium channels (——), sodium channels (– – –) and leak channels (·····).

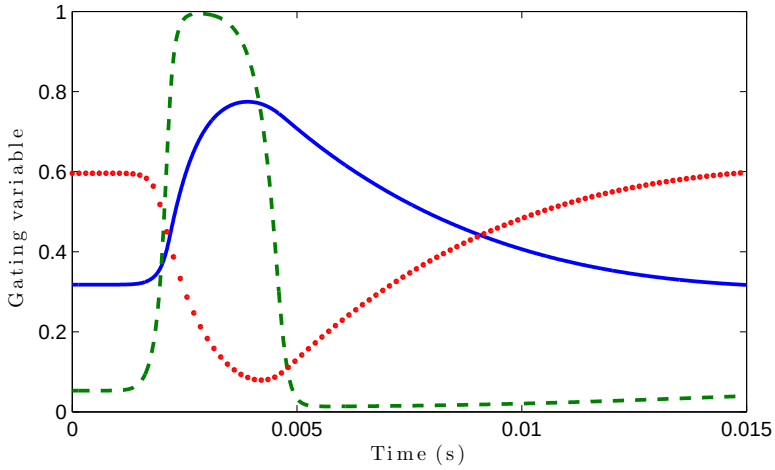

FIGURE 1.10: Values of the gating variables n (——), m (– – –) and h (·····) during an action potential. Note the significantly faster opening of the sodium channel (green).

'jump' towards clusters of open channels and thus propagate at non-uniform speeds [22]. However, in many neurons — and specifically in the types studied in this work — the number of channels is large enough that a homogenised macroscopic model — accounting for average ion channel activity — is appropriate [102].

A more complete discussion of ion channel behaviour and the modelling challenges they present can be found in [38] and the references therein, but in this work we will use the models proposed by Hodgkin and Huxley, as this provides a wide body of theory and experimental data to draw on.

1.2 A generic description of the current in a nerve cell

Here we describe a generic model of the current flow in the vicinity of a cell membrane. This model was first written down by Neu and Krassowska in [68], in the context of cardiac myocytes, which are also electrochemically excitable cells. It has subsequently been used by others to study both cardiac myocytes ([89]) and neurons [53, 88]. Furthermore, it can be systematically derived from a detailed asymptotic analysis of the Nernst-Planck equations of electrochemistry [88].

With the relatively small currents encountered during action potentials, the electrolyte behaviour in the interior and exterior regions of the cell (denoted by Ω^* and Ω^{c*} respectively) is well approximated by Ohm's law and current conservation (superscript asterixes (*) denote dimensional variables)

$$\boldsymbol{J}^* = -\sigma_{\text{in}} \nabla^* \phi^* \quad \text{and} \quad \nabla^* \cdot \boldsymbol{J}^* = 0 \quad \text{in } \Omega^*, \tag{1.14}$$

$$\boldsymbol{J}^* = -\sigma_{\text{out}} \nabla^* \phi^* \quad \text{and} \quad \nabla^* \cdot \boldsymbol{J}^* = 0 \quad \text{in } \Omega^{c*}, \tag{1.15}$$

where $\boldsymbol{J}^*$ and ϕ^* denote current density and electric potential respectively, and $\sigma_{\text{in,out}}$ represents the conductivity of the intracellular and extracellular electrolytes.

1.2.1 The influence of the cell membrane

The behaviour of the membrane is modelled with reference to the ion channels in the membrane and the behaviour of the extremely narrow (on the order of one nanometre wide) charged Debye layers lying on either side of it. It is possible to demonstrate that the charge densities lying in the Debye layers on either side of the membrane are equal and opposite ([88]) such that the membrane and Debye layers behave as a capacitor. This balance of charge requires that any current which flows from the bulk electrolyte (either intracellular or extracellular) into its corresponding Debye layer must be balanced by an equal current flowing from the *opposite* Debye layer into *its* corresponding electrolyte (see figure 1.12). As a result, the macroscopic current density, $\boldsymbol{J}^*$, flowing across the

membrane and Debye layers must be continuous:

$$\boldsymbol{J}^* \cdot \boldsymbol{n}|_{\partial\Omega^*} = \boldsymbol{J}^* \cdot \boldsymbol{n}|_{\partial\Omega^{c*}}\,, \tag{1.16}$$

where $\boldsymbol{n}$ the unit vector normal to the membrane.

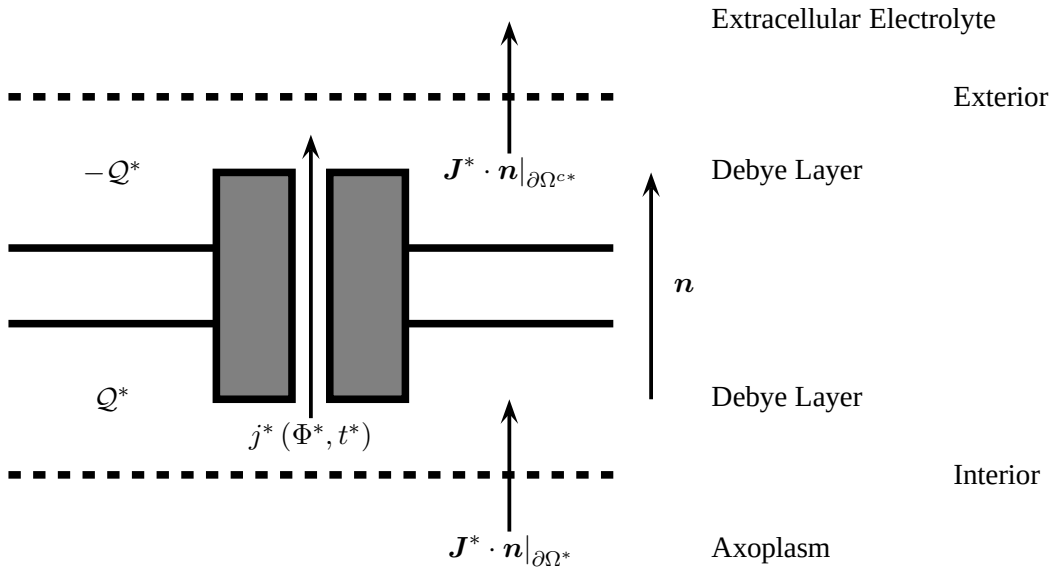

FIGURE 1.11: Current flows near to the cell membrane. The current flow from one Debye layer to the other through the ion channels is denoted $j^*(\Phi^*, t^*)$. Current flow *into* the interior Debye layer *from* the bulk axoplasm ($\boldsymbol{J}^* \cdot \boldsymbol{n}|_{\partial\Omega^*}$) must be matched by an equivalent current flow ($\boldsymbol{J}^* \cdot \boldsymbol{n}|_{\partial\Omega^{c*}}$) *from* the exterior Debye layer *into* the bulk extracellular electrolyte, so that the charges in each Debye layer ($\pm\mathcal{Q}^*$) remain balanced. We can thus consider $\boldsymbol{J}^* \cdot \boldsymbol{n}$ as a current which flows across both the membrane and Debye layers.

We define the transmembrane potential as the potential drop across the membrane *and* Debye layers, as follows

$$[\phi^*]^{\partial\Omega^*}_{\partial\Omega^{c*}} = \Phi^*. \tag{1.17}$$

For sufficiently small transmembrane potentials, such as those encountered in an action potential, the membrane and Debye layers behave as a linear capacitor ([88]) whilst the ion channels straddling it can be modelled as a nonlinear resistor with current-voltage dependency given by $j^*(\Phi^*, t^*)$ in parallel with this capacitor (we have chosen to represent $j^*(\Phi^*, t^*)$ in the form of the Hodgkin-Huxley model of ion channel current, as detailed in section 1.1.5). The equivalent circuit is shown in figure 1.12 and the corresponding transmembrane current density $\boldsymbol{J}^* \cdot \boldsymbol{n}|_{\partial\Omega^*}$, including the behaviour of

the Debye layers, satisfies

$$\boldsymbol{J}^* \cdot \boldsymbol{n}|_{\partial\Omega^*} = C\frac{\partial \Phi^*}{\partial t^*} + j^*\left(\Phi^*, t^*\right). \tag{1.18}$$

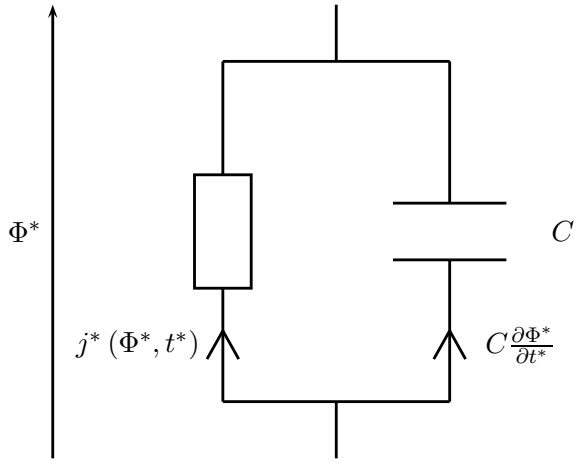

FIGURE 1.12: Equivalent circuit diagram for currents through the cell membrane

1.2.2 Model closure

To close this system, we require a far-field condition on ϕ^* as distance from the cell membrane tends to infinity. The precise statement of this condition is dependent on the geometry of the cell under consideration, but in general it will take the form

$$\phi^* \to 0 \qquad \text{as} \qquad |\boldsymbol{x}^*| \to \infty \tag{1.19}$$

Equations (1.14) to (1.19) now comprise the following cell-scale model for the electrolyte potential and the transmembrane potential, Φ^* (defined as the difference between the

intra- and extra-cellular potentials):

$$\boldsymbol{J}^* = -\sigma_{\text{in}} \nabla^* \phi^* \qquad \text{in } \Omega^* \tag{1.20}$$

$$\boldsymbol{J}^* = -\sigma_{\text{out}} \nabla^* \phi^* \qquad \text{in } \Omega^{c*} \tag{1.21}$$

$$\nabla^* \cdot \boldsymbol{J}^* = 0 \qquad \text{in } \Omega^*, \tag{1.22}$$

$$\nabla^* \cdot \boldsymbol{J}^* = 0 \qquad \text{in } \Omega^{c*}, \tag{1.23}$$

$$\boldsymbol{J}^* \cdot \boldsymbol{n}|_{\partial\Omega^*} = \boldsymbol{J}^* \cdot \boldsymbol{n}|_{\partial\Omega^{c*}}\,, \tag{1.24}$$

$$[\phi^*]^{\partial\Omega^*}_{\partial\Omega^{c*}} = \Phi^*, \tag{1.25}$$

$$\boldsymbol{J}^* \cdot \boldsymbol{n}|_{\partial\Omega^*} = C\frac{\partial\Phi^*}{\partial t^*} + j^*\left(\Phi^*, t^*\right). \tag{1.26}$$

$$\phi^* \to 0 \qquad |\boldsymbol{x}^*| \to \infty \tag{1.27}$$

This model forms the basis of our study of three very different types of cell, where the principal differences in behaviour are caused by marked variations in the geometry of the cell.

1.3 Overview of this thesis

In the following chapters we apply this model to three cells that have developed specific physical properties in order to better perform their function. In all cases we aim to assess the impacts of physiological features on the models of cell behaviour, to determine where details must be included in the modelling process and where simplifications can be made. The systematic nature of this approach allows us to judge the validity of approximations made in existing models, as well as justify the simplifications we make mathematically.

In chapter 2 we examine a particularly large neuron found in the squid, and find that the assumption that current flows one-dimensionally along the axis of the neuron leads to quantitatively and qualitatively different predictions of action potential propagation from the generic model, which accounts for current flows in three dimensions. The implications of this are discussed in the context of the evolutionary cost of a vary large neuron.

In chapter 3 we consider a class of neurons found in vertebrates that increase their signalling speeds by forming organised structures with glial cells. Asymptotic analysis of the generic model in this case results in a model of these neurons which accounts for all the significant geometrical features of the system, which we compare to models found in the literature. We find some existing models over simplify the problem, by ignoring physiological details which have a significant influence on the propagation of action potentials, while others under simplify it, by including detailed descriptions of features which do not.

Finally, in chapter 4 we study the behaviour of the Bergmann glial cell, a cell found in the cerebellum which has a role in supporting the behaviour of neurons surrounding it. We write down a model of the electrical properties of the cell informed by its structure and demonstrate that this accurately predicts the behaviour of the cell in experimental conditions. To better understand the function of the cell we then write down a model of the ion concentrations within it, which we derive from the Poisson-Nernst-Planck equations that underlie the generic model described above [88].

Chapter 2

Action potential propagation in very large axons

2.1 Introduction

In this chapter we present analysis of the generic model in equations (1.20) to (1.27) in the context of a very large cell. In this context, the model can be reduced to a singular integro-differential equation describing the transmembrane potential of the cell, and we develop a numerical method for the solution of this equation. Our description of the transmembrane potential takes into account current flows in three dimensions, and we compare it to the established simplified model, the cable equation, where the current flow is assumed to be one dimensional. We find that below a critical radius (which depends upon intracellular and extracellular conductivities, and the size of ion channel currents through the membrane) the current flow in the cell is predominantly axial, and thus well approximated by the one dimensional cable equation. Above this critical radius, however, we find the cable equation does not predict the correct relationship between the size of the neuron and the speed at which action potentials propagate within it. We note that, *in vivo*, the properties of a particular cell — the squid giant neuron — place its radius close to this critical value, and discuss the implications of our results in terms of the evolutionary costs associated with producing and maintaining very large neurons. The work presented in this chapter is published in [26].

2.1.1 The squid giant axon

The squid giant neuron is an unusually large neuron (up to around 1mm in diameter) found in the mantle of some species of squid, although very large neurons are also found in other types of invertebrate (for example in sea slugs of the genus *aplysia* [46], and some species of lobster [8]). These giant neurons mediate the squid's 'escape response', which allows it to rapidly evade potential predatory threats [80, 75]. Larger neurons are known to transmit action potentials faster, and since the speed of the escape response is critical to the survival of the squid this accounts for the large size of the giant neuron. Increasing the size of the cell comes with an increased cost to the squid, in terms of the energy needed for its growth, maintenance and operation, and thus we expect it to have reached some kind of 'optimal' size balancing these factors.

A neuron can be thought of as a central cell body — containing its nucleus and many of the proteins and structures necessary for its growth and maintenance — connected to long, branching, radial processes. These processes are divided into those that carry signals towards the cell body (dendrons) and those that carry signals away (axons). The dendrons are generally short, branch regularly and contain few active ion channels, whereas axons are longer, branch much less (and only towards the distal end) and contain high densities of active ion channels. Since the action potential in the squid giant neuron can occur only where there are active ion channels, we ignore the rest of the cell for the purposes of this work, and consider only the unbranching, uniform section of the axon.

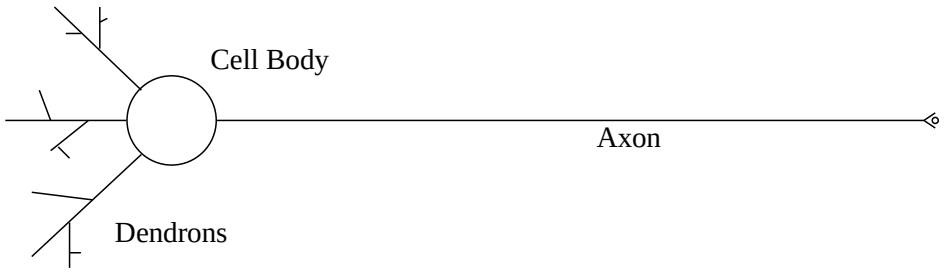

FIGURE 2.1: Sketch of neuron. Signals originating in the dendrons are transmitted to the cell body, and then transmitted away along the axon

2.1.2 The cable equation description of an axon

In addition to their description of membrane currents detailed in section 1.1.5, Hodgkin and Huxley (and many others since) used the cable equation to describe the longitudinal propagation of action potentials along axons [44]. The cable equation is a nonlinear diffusion equation, originally used to study signal transmission in transatlantic telegraph cables [105] but quickly adapted for use in neurobiology. Key to the use of this model are the implicit assumptions that current flow within the axon is predominantly axial and that the potentials outside the axon are uniformly small (this is equivalent to requiring that the resistance of the axon to be significantly larger than that of the extracellular space). This approach yields good agreement with empirical studies — Hodgkin and Huxley tested their model by taking parameters from a particular axon, measuring the speed of signal transmission within this axon, and then comparing the result with a travelling wave solution to their model. The empirical speed was found to be 21.2 ms^{-1}, which compares favourably to the 18.8 ms^{-1} predicted by their model [44]. The source of this error has motivated a number of subsequent works. In particular, improvements have been made to ion channel conductance models that take advantage of the wealth of information about ion channel structure now available, improved empirical data on single-channel behaviour, and knowledge of the features of excitable membranes, such as thresholds and refractory periods [78, 107]. These have been found to significantly reduce the disagreement between theory and experiment [6, 11].

The generic description of the current in the axon (equations (1.20) to (1.27)) can be reduced to the cable equation, but only in the limit of very thin axons and equal intra- and extracellular conductivities, which we discuss in sections 2.2 and 2.2.1. This condition is satisfied for a wide range of axons, however some — and in particular the squid giant axons used by Hodgkin and Huxley — inhabit a grey area where it is not obvious that this criterion is met.

An important feature of the Hodgkin-Huxley experiment [44], and indeed most other experiments on squid axons since ([1],[85]) is that it is conducted *in vitro* with an excised axon suspended in a bath of seawater, an electrolyte with relatively high conductivity.

The external conditions in a live squid are rather different as, *in vivo*, the axon is surrounded by a collagenous sheath, as well as other closely packed cells (see for example, figure 2A in [15]), all acting to decrease the conductivity of the extracellular space relative to the intracellular space [9]. This, as we shall demonstrate, has important consequences for the validity of the cable equation approximation *in vivo*, and means that it breaks down at significantly smaller radii than in the highly conductive external medium of seawater used by Hodgkin and Huxley. A corollary of the breakdown of the cable equation approximation is that action potential propagation velocities do not scale with the square root of axon radius, but instead saturate to some constant value (for large radii). Based on our estimate of extracellular conductivity we suggest that physiological axon radius is close to optimal (certainly further gains in action potential propagation speed become increasingly expensive). The difference between potentials measured in the squid axon *in vivo* and *in vitro* was noted by Moore and Cole soon after Hodgkin and Huxley's work was published [62]. Although they did not measure the speeds at which signals propagated, they did find differences of the time course of the action potential. However they were unable to perform these measurements with the squid's mantle intact, and by slicing it open to access the giant axon will have effectively increased the extracellular conductivity. The reduction in speed of action potentials travelling in closely packed tissues has also been noted in conduction velocities in muscle fibres measured *in vivo* [10]. We found no reference in the literature to an experiment explicitly comparing speeds *in vivo* to those measured *in vitro*, but we believe such an experiment may be possible using a voltage-sensitive dye, such as those described in [115].

A useful observation on signalling speed can be made by examining travelling wave solutions to the cable equation (as noted by [39]). We begin with the cable equation (as used by Hodgkin and Huxley, and derived from the underlying electrochemical equations in section 2.2.1)

$$C\frac{\partial \Phi^*}{\partial t^*} = \frac{\sigma R}{2}\frac{\partial^2 \Phi^*}{\partial x^{*2}} - j^*\left(\Phi^*\left(x^*, t^*\right), \boldsymbol{w}\left(x^*, t^*\right)\right), \tag{2.1}$$

where Φ^* is the transmembrane potential (defined as the difference between the intra-

and extra-cellular potentials), j^* represents the current density through the ion channels, x^* is distance along the axon, t^* is time, C is the capacitance of the membrane per unit area, σ is the conductivity of the axoplasm, R is the axon radius and $\boldsymbol{w}(x^*, t^*)$ is a vector of gating variables describing the conductivity of the axon membrane to specific ion species (a $*$ denotes a dimensional variable). Specifically, the Hodgkin-Huxley form of the membrane current j^* has the form

$$j^*(\Phi^*, \boldsymbol{w}) = \sum_{i=1}^{N} g_i^* w_i (\Phi^* - \Phi_{ei}), \tag{2.2}$$

$$\frac{\partial w_i}{\partial t} = \alpha_i^*(\Phi^*)(1 - w_i) - \beta_i^*(\Phi^*) w_i, \tag{2.3}$$

where Φ_{ei} is the reversal potential for each ion species, g_i^* is the maximal membrane conductance per unit area of the i^{th} ion species, w_i is the proportion of this conductance accessible through open ion channels and α_i^* and β_i^* are functions (which are given in [44]) that describe opening and closing rates for each species of ion channel.

Making the travelling wave ansatz $\Phi^* = f^*(\xi^*)$ and $w_i = \omega_i(\xi^*)$, where $\xi^* = \frac{x^*}{v} - t^*$ gives

$$-C\frac{df^*}{d\xi^*} = \frac{\sigma R}{2v^2}\frac{d^2 f^*}{d\xi^{*2}} - \sum_i g_i^* \omega_i(\xi^*)(f^*(\xi^*) - \Phi_{ei}), \tag{2.4}$$

$$\frac{dw_i}{d\xi^*} = -(\alpha_i^*(f^*(\xi^*))(1 - w_i(\xi^*)) - \beta_i^*(f^*(\xi^*)) w_i(\xi^*)), \tag{2.5}$$

and imposing the boundary conditions $f^* \to -70\text{mV}$ as $\xi^* \to \pm\infty$, so that the membrane is at resting potential far from the propagating wave, yields a nonlinear eigenvalue problem, with eigenvalue $\frac{\sigma R}{2v^2}$. This gives us the following result for the wave speed, v (assuming membrane capacitance to be fixed)

$$v \propto \sigma^{\frac{1}{2}} R^{\frac{1}{2}}, \tag{2.6}$$

such that the propagation velocity of the signal in the axon scales with the square root of the axon radius. We expect our model to reproduce this behaviour for sufficiently small radii (since the cable equation is valid in the asymptotic limit as axon radius goes to zero), and larger extracellular to intracellular conductance ratios, but for larger radii

and smaller ratios we expect to observe differing predictions from the two models. Later in this study we will revisit this notion of travelling wave speeds and make a comparison between predictions from our model and that of Hodgkin and Huxley. By doing this we can both assess the range of parameters over which their approximation is justified and gain an understanding of the behaviour of very large axons, in configurations for which the cable equation is unsuitable.

2.2 Model Formulation

We approximate the axon as a uniform cylinder, allowing us to consider the special case of the generic model (equations (1.20) to (1.27)) where the intracellular space is defined as follows

$$\Omega^* = \{(r^*, \theta, x^*) \,|0 \leq r^* < R, 0 \leq \theta \leq 2\pi, -\infty < x^* < \infty\} \tag{2.7}$$

where (r^*, θ, x^*) are cylindrical coordinates. This case represents an infinitely long axon with a uniformly circular cross-section of radius R, and is described by our model as follows:

$$\boldsymbol{J}^* = -\sigma_{\text{in}} \nabla^* \phi^* \qquad \text{in } r^* < R \tag{2.8}$$

$$\boldsymbol{J}^* = -\sigma_{\text{out}} \nabla^* \phi^* \qquad \text{in } r^* > R \tag{2.9}$$

$$\nabla^* \cdot \boldsymbol{J}^* = 0 \qquad \text{in } r^* < R, \tag{2.10}$$

$$\nabla^* \cdot \boldsymbol{J}^* = 0 \qquad \text{in } r^* > R, \tag{2.11}$$

$$\boldsymbol{J}^* \cdot \boldsymbol{n}^*|_{r=R^-} = \boldsymbol{J}^* \cdot \boldsymbol{n}^*|_{r=R^+}\,, \tag{2.12}$$

$$[\phi^*]_{r^*=R^+}^{r^*=R^-} = \Phi^*, \tag{2.13}$$

$$\boldsymbol{J}^* \cdot \boldsymbol{n}^*|_{r^*=R^-} = C\frac{\partial \Phi^*}{\partial t^*} + j^*\left(\Phi^*, t^*\right). \tag{2.14}$$

$$\phi^* \to 0 \qquad r^* \to \infty \tag{2.15}$$

The above system can be simplified as follows, by substituting equations (2.8) and (2.9) into equations (2.10) to (2.14), and noting that, in this geometry, $\boldsymbol{n} = \boldsymbol{e}_r$

$$\nabla^{*2}\phi^* = 0 \qquad \text{in } r^* < R \text{ and } r^* > R, \tag{2.16}$$

$$\sigma_{\text{in}} \frac{\partial \phi^*}{\partial r^*}\bigg|_{r^*=R^-} = \sigma_{\text{out}} \frac{\partial \phi^*}{\partial r^*}\bigg|_{r^*=R^+}, \tag{2.17}$$

$$[\phi^*]_{r^*=R^+}^{r^*=R^-} = \Phi^*, \tag{2.18}$$

$$C\frac{\partial \Phi^*}{\partial t^*} = -\sigma_{\text{in}} \frac{\partial \phi^*}{\partial r^*}\bigg|_{r^*=R^-} - j^*\left(\Phi^*, t^*\right), \tag{2.19}$$

$$\phi^* \to 0 \qquad \text{as } r^* \to \infty \tag{2.20}$$

We nondimensionalise via the scalings

$$\begin{aligned} &\boldsymbol{x}^* = L\boldsymbol{x}, \quad t^* = \tau t, \quad \Phi^* = \Phi_0\Phi + \Phi_{\text{rest}}, \quad \phi^* = \Phi_0\phi + \Phi_{\text{rest}}, \\ &g_i^* = g_0 g, \quad j^* = g_0\Phi_0 j, \qquad \alpha^* = \frac{1}{\tau}\alpha, \qquad \beta^* = \frac{1}{\tau}\beta. \end{aligned} \tag{2.21}$$

Here τ represents the typical timescale for an action potential and g_0 a typical membrane conductance per unit area. Φ_{rest} is the membrane resting potential (around -70mV), and Φ_0 a typical transmembrane potential (so that Φ represents deviations from resting potential). After these scalings, equations (2.16) to (2.20) can be written in the form

$$\nabla^2\phi = 0 \qquad \text{in } r < \varepsilon \text{ and } r > \varepsilon, \tag{2.22}$$

$$\frac{\partial \phi}{\partial n}\bigg|_{r=\varepsilon^-} = \bar{\sigma}\frac{\partial \phi}{\partial n}\bigg|_{r=\varepsilon^+}, \tag{2.23}$$

$$[\phi]_{r=\varepsilon^+}^{r=\varepsilon^-} = \Phi, \tag{2.24}$$

$$\mathcal{C}\frac{\partial \Phi}{\partial t} = -\frac{\partial \phi}{\partial n}\bigg|_{r=\varepsilon^-} - j\left(\Phi, t\right), \tag{2.25}$$

$$\phi \to 0 \qquad r \to \infty \tag{2.26}$$

where

$$j\left(\Phi, t\right) = \sum_{i=1}^{N} g_i w_i \left(\Phi - \bar{\Phi}_{ei}\right), \tag{2.27}$$

$$\frac{\partial w_i}{\partial t} = \alpha_i\left(\Phi\right)\left(1 - w_i\right) - \beta_i\left(\Phi\right) w_i, \tag{2.28}$$

and $\bar{\Phi}_{ei}$ is given by

$$\bar{\Phi}_{ei} = \frac{\Phi_{ei} + \Phi_{\text{rest}}}{\Phi_0}, \tag{2.29}$$

which is the dimensionless equilibrium potential for the i^{th} ion species, measured from the membrane resting potential rather than from zero.

The dimensionless parameters ε, $\mathcal{C}$ and $\bar{\sigma}$ are defined by

$$\varepsilon = \frac{R}{L} \qquad \mathcal{C} = \frac{CL}{\tau\sigma_{\text{in}}} \qquad \bar{\sigma} = \frac{\sigma_{\text{out}}}{\sigma_{\text{in}}}, \tag{2.30}$$

where ε is the dimensionless axon radius, and $\mathcal{C}$ and $\bar{\sigma}$ represent the ratio of charge stored in the Debye layers to charge moved longitudinally through the axon during a typical action potential, and the ratio of extracellular to intracellular conductivities respectively.

We choose Φ_0 to be the thermal voltage (roughly 2.5×10^{-2} V), which is comparable to a typical transmembrane potential (resting transmembrane potential is around -7$\times 10^{-2}$ V) and the typical membrane conductance g_0 to be the maximal conductance through the voltage-gated sodium channels (1200 S·m^{-2} [55]). Values for the parameters C and σ_{in} can be found in the literature ($C \approx 1 \times 10^{-2}$ F·m^{-2} [44] and $\sigma_{\text{in}} \approx 1$ S·m^{-1} [99] (= 2.825 S·m^{-1} in [44])), while the effect of several values of σ_{out} is discussed in section 2.4.

We determine the length scale L by balancing the axoplasm conductivity per unit length with membrane conductance per unit area

$$L = \frac{\sigma_{\text{in}}}{g_0}, \tag{2.31}$$

such that the dimensionless axon radius becomes

$$\epsilon = \frac{Rg_0}{\sigma_{\text{in}}} \tag{2.32}$$

Where this parameter is very small the resistance of the interior of the axon is large compared to that of the extracellular space, so that extracellular potentials are small and the intracellular potential is well approximated by the local transmembrane potential, Φ (see section 2.2.1 and [88]). Using the parameter values chosen above, $L = O(2.5\text{mm})$,

yielding $\epsilon \approx 0.2$ for larger squid axons ($\epsilon = 0.10$ for the exact parameters in [44]) and it is not obvious (as discussed above) whether this is small enough for the cable equation to be a suitable approximation to the general model.

2.2.1 Deriving the cable equation approximation

For a thin axon (defined as an axon where the dimensionless radius $\varepsilon \ll 1$) we can simplify our model using a power series expansion in ε. We introduce inner and exterior regions, distances $O(\varepsilon)$ and $O\left(\varepsilon^{\frac{1}{2}}\right)$ from the axon, respectively, although, as we will demonstrate, the cable equation can be derived from the equations in the inner region alone. A detailed discussion of this problem, as well as the full treatment of the solution for the outer region, is given in [88]. In this region we rescale coordinates as follows:

$$x = \varepsilon^{\frac{1}{2}}\xi \qquad r = \varepsilon\rho, \tag{2.33}$$

Substituting these expressions into equations (2.22) to (2.25) leads to the following system:

$$\frac{1}{\varepsilon\rho}\frac{\partial}{\partial\rho}\left(\rho\frac{\partial\phi}{\partial\rho}\right) + \frac{\partial^2\phi}{\partial\xi^2} = 0 \tag{2.34}$$

$$[\phi]_{\rho=1^+}^{\rho=1^-} = \Phi, \tag{2.35}$$

$$\left.\frac{\partial\phi}{\partial\rho}\right|_{\rho=1^-} = \bar{\sigma}\left.\frac{\partial\phi}{\partial\rho}\right|_{\rho=1^+}, \tag{2.36}$$

$$\mathcal{C}\frac{\partial\Phi}{\partial t} = -\frac{1}{\varepsilon}\left.\frac{\partial\phi}{\partial\rho}\right|_{\rho=1^-} - j(\Phi, t). \tag{2.37}$$

We look for a solution of the following form (where we have included $O(\varepsilon\log(\varepsilon))$ terms due to the far-field logarithmic singularity encountered when solving Laplace's equation in cylindrical coordinates, and a superscript (in) denotes a variable in the inner

expansion).

$$\Phi = \Phi_0 + \varepsilon \log(\varepsilon)\, \Phi_1 + \varepsilon \Phi_2 + \cdots, \tag{2.38}$$

$$\phi = \begin{cases} \Phi_0 + \varepsilon \log(\varepsilon) \left(\phi_1^{(\mathrm{in})} + \Phi_1\right) + \varepsilon \left(\phi_2^{(\mathrm{in})} + \Phi_2\right) + \cdots & \text{for } 0 \le \rho < 1 \\ \varepsilon \log(\varepsilon)\, \phi_1^{(\mathrm{in})} + \varepsilon \phi_2^{(\mathrm{in})} + \cdots & \text{for } \rho > 1 \end{cases}. \tag{2.39}$$

The assumption being made here, that ϕ is small in $\rho > 1$ ($\phi = O(\varepsilon \log \varepsilon)$) is key to the understanding of why this simplification breaks down where it does. As noted in section 2.4 this is not true once the axon radius becomes sufficiently large that the intracellular resistance is comparable to the effective extracellular resistance. Furthermore this critical radius diminishes as the extracellular conductivity decreases (since decreases in extracellular conductivity increase extracellular resistance).

Substitution of the expansions in equations (2.38) and (2.39) into equations (2.34) to (2.37) gives (at $O(1)$)

$$\frac{1}{\rho}\frac{\partial}{\partial \rho}\left(\rho \frac{\partial \phi_2^{(\mathrm{in})}}{\partial \rho}\right) = -\Phi_{0,\xi\xi} \qquad \rho < 1, \tag{2.40}$$

$$\frac{1}{\rho}\frac{\partial}{\partial \rho}\left(\rho \frac{\partial \phi_2^{(\mathrm{in})}}{\partial \rho}\right) = 0 \qquad \rho > 1, \tag{2.41}$$

$$\left[\phi_2^{(\mathrm{in})}\right]_{\rho=1^+}^{\rho=1^-} = 0, \tag{2.42}$$

$$\left.\frac{\partial \phi_2^{(\mathrm{in})}}{\partial \rho}\right|_{\rho=1^-} = \bar{\sigma} \left.\frac{\partial \phi_2^{(\mathrm{in})}}{\partial \rho}\right|_{\rho=1^+}, \tag{2.43}$$

which has the solution

$$\phi_2^{(\mathrm{in})} = \begin{cases} -\frac{1}{4}\Phi_{0,\xi\xi}\left(\rho^2 - 1\right) + \gamma(\xi, t) & \text{for } \rho < 1 \\ -\frac{1}{2\bar{\sigma}}\Phi_{0,\xi\xi} \log(\rho) + \gamma(\xi, t) & \text{for } \rho > 1 \end{cases}. \tag{2.44}$$

Finally, substitution of equation (2.44) into equation (2.37) yields the cable equation

$$\mathcal{C}\frac{\partial \Phi_0}{\partial t} = \frac{1}{2}\frac{\partial^2 \Phi_0}{\partial \xi^2} - j(\Phi, t). \tag{2.45}$$

2.3 Solution of the problem for large ϵ

In the following sections we formulate a numerical procedure for solving equations (2.22) to (2.25) without approximating it by the cable equation or exploiting the smallness of ϵ. The approach is valid for a general axon geometry, and so we begin by briefly describing the general solution, before specialising to the cylindrical case.

Initially we approach the problem by introducing a Green's function, $G(\boldsymbol{x};\boldsymbol{x_0})$, defined as the solution to

$$\nabla^2 G = 0, \tag{2.46}$$

$$\left.\frac{\partial G}{\partial n}\right|_{\partial\Omega} = \bar{\sigma}\left.\frac{\partial G}{\partial n}\right|_{\partial\Omega^c}, \tag{2.47}$$

$$[G]^{\partial\Omega}_{\partial\Omega^c} = \delta(\boldsymbol{x}-\boldsymbol{x_0}), \tag{2.48}$$

with a suitable far-field condition (in terms of the Green's function, $G \to 0$ as distance from the axon membrane becomes large), where $\boldsymbol{x_0}$ denotes a point on the axon membrane, and $\delta(\cdot)$ the Dirac delta function.

The solution to equations (2.22) to (2.24) can then be written in terms of a surface integral over the axon surface $\partial\Omega$

$$\phi(\boldsymbol{x},t) = \oint_{\partial\Omega_{\boldsymbol{x}_0}} G(\boldsymbol{x},\boldsymbol{x}_0)\,\Phi(\boldsymbol{x}_0,t)\; d\Omega_{\boldsymbol{x}_0}, \tag{2.49}$$

such that equation (2.25) can be rewritten as the following (singular) integro-differential equation for the transmembrane potential in the axons, Φ

$$\mathcal{C}\frac{\partial}{\partial t}\Phi(\boldsymbol{x},t) = -\frac{\partial}{\partial n}\left(\oint_{\partial\Omega_{\boldsymbol{x}_0}} G(\boldsymbol{x},\boldsymbol{x}_0)\,\Phi(\boldsymbol{x}_0,t)\; d\Omega_{\boldsymbol{x}_0}\right)\Bigg|_{\partial\Omega} - j(\Phi,t), \tag{2.50}$$

in which $j(\Phi,t)$ is given by equations (2.27) and (2.28).

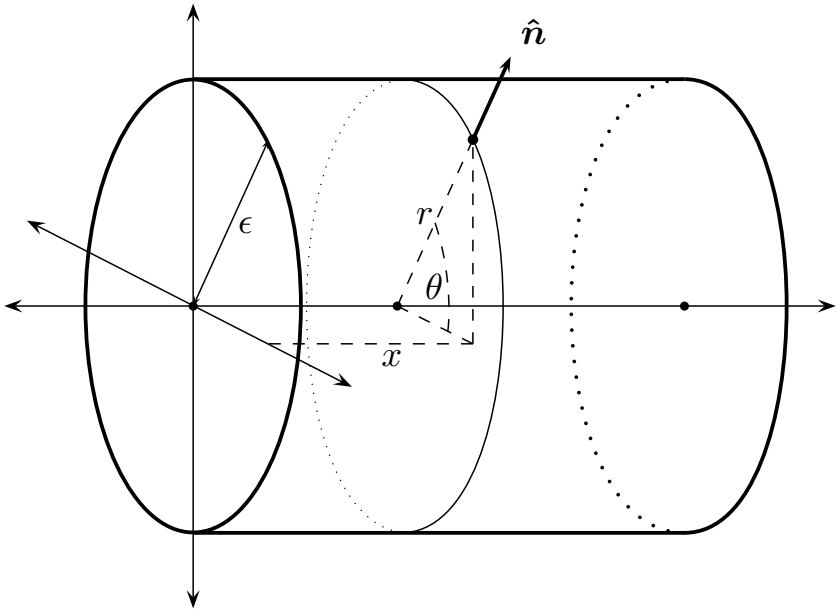

FIGURE 2.2: Schematic of the cylindrical geometry. The unit normal vector $\hat{\boldsymbol{n}}$ is directed *out* of the cylinder

2.3.1 A uniform cylindrical axon

We now consider the specific case of a uniform cylindrical axon of dimensionless radius ϵ, as seen in figure 2.2, with axisymmetric membrane potential Φ. We rewrite equation (2.49) in cylindrical polar coordinates $(x, y, z) = (x, r\cos(\theta), r\sin(\theta))$ as follows:

$$\phi(x, r, \theta, t) = \int_{-\infty}^{\infty} \int_{0}^{2\pi} G(x, r, \theta; x_0, \theta_0)\, \epsilon\, d\theta_0 \Phi(x_0, t)\, dx_0. \tag{2.51}$$

With the assumption that Φ is axisymmetric we can integrate over θ, i.e.

$$\mathcal{G}(x - x_0, r) = \int_{0}^{2\pi} G(x, r, \theta; x_0, \theta_0)\, d\theta_0, \tag{2.52}$$

so that $\mathcal{G}$ is the Green's function for a 'ring' of charge around the axon membrane, located at x_0. We observe that the axial dependence of G occurs solely as a function of $x - x_0$ and that integration of equations (2.46) to (2.48) over θ (on noting that

$\delta(\boldsymbol{x}-\boldsymbol{x_0}) = \frac{1}{\epsilon}\delta(x-x_0)\,\delta(\theta-\theta_0))$ yields the following problem for $\mathcal{G}(X,r)$:

$$\frac{\partial^2 \mathcal{G}}{\partial X^2} + \frac{1}{r}\frac{\partial}{\partial r}\left(r\frac{\partial \mathcal{G}}{\partial r}\right) = 0 \text{ in } r<\epsilon \text{ and } r>\epsilon, \tag{2.53}$$

$$\left.\frac{\partial \mathcal{G}}{\partial r}\right|_{r=\epsilon^-} = \bar{\sigma}\left.\frac{\partial \mathcal{G}}{\partial r}\right|_{r=\epsilon^+}, \tag{2.54}$$

$$\left[\mathcal{G}\right]_{r=\epsilon^+}^{r=\epsilon^-} = \frac{1}{\epsilon}\delta(X), \tag{2.55}$$

$$\mathcal{G} \to 0 \quad \text{as} \quad r \to \infty. \tag{2.56}$$

Equation (2.50) can be rewritten in terms of this axisymmetric Green's function, $\mathcal{G}$, in the form

$$\mathcal{C}\frac{\partial \Phi}{\partial t} = -\frac{\partial}{\partial r}\left(\int_{-\infty}^{\infty} \mathcal{G}(x-x_0,r)\,\Phi(x_0,t)\,\epsilon\,dx_0\right)\Bigg|_{r=\epsilon^-} - j(\Phi,t), \tag{2.57}$$

Ideally, we would like to be able to replicate the travelling wave approach in section 2.1.2 to find the relationship between signal speed and axon radius in this model. Making the change of variables $\xi = t - \frac{x}{v}$ results in the nonlinear integro-differential eigenvalue problem

$$\mathcal{C}\frac{d}{d\xi}\Phi(\xi) = -\frac{\partial}{\partial r}\left(\int_{-\infty}^{\infty} \mathcal{G}(v(\xi-\xi_0),r)\,\Phi(\xi_0)\,\epsilon v\,d\xi_0\right)\Bigg|_{r=\epsilon^-} - \sum_{i=1}^{N} g_i w_i(\xi)\left(\Phi(\xi)-\Phi_{ei}\right), \tag{2.58}$$

$$\frac{dw_i}{d\xi} = -\left(\alpha_i(\Phi(\xi))\left(1-w_i(\xi)\right) - \beta_i(\Phi(\xi))\,w_i(\xi)\right), \tag{2.59}$$

$$\Phi(\xi) \to 0 \quad \text{as } \xi \to \pm\infty. \tag{2.60}$$

where the eigenvalue v again depends upon ϵ and $\bar{\sigma}$. In section 2.1.2 we were able to explicitly determine how wave speed scales with ϵ, but the nature of the integral operator in this problem makes direct solution of this nonlinear eigenvalue problem non-trivial. Instead, we solve the time-dependent problem numerically, allow the solution to converge to the travelling wave solution and then measure the speed of the subsequent wave. This allows us to numerically determine the eigenvalue's dependence on the value of ϵ and $\bar{\sigma}$.

2.3.2 Finding the Green's function

Before we can progress with the numerical solution of the problem, we need first to find the appropriate Green's function. Here we shall assume that Φ is periodic with some large period 2λ — so that in the limit $\lambda \to \infty$ we retrieve the exact result. We adapt the Green's function problem in equations (2.53) to (2.56) to reflect the periodic nature of the problem

$$\frac{\partial^2 \mathcal{G}}{\partial X^2} + \frac{1}{r}\frac{\partial}{\partial r}\left(r\frac{\partial \mathcal{G}}{\partial r}\right) = 0 \quad \text{in } r < \epsilon \text{ and } r > \epsilon, \tag{2.61}$$

$$\left.\frac{\partial \mathcal{G}}{\partial r}\right|_{r=\epsilon^-} = \bar{\sigma}\left.\frac{\partial \mathcal{G}}{\partial r}\right|_{r=\epsilon^+}, \tag{2.62}$$

$$[\mathcal{G}]_{r^+}^{r^-}\epsilon = \frac{1}{\epsilon}\sum_{n=-\infty}^{\infty}\delta\left(X + 2n\lambda\right), \tag{2.63}$$

$$\mathcal{G} \to 0 \quad \text{as} \quad r \to \infty. \tag{2.64}$$

We look for a solution to equations (2.61) to (2.64) for the Green's function $\mathcal{G}(X, r)$ in terms of its Fourier series

$$\mathcal{G}\left(X, r\right) = \frac{g_0}{2} + \sum_{n=1}^{\infty} g_n \cos\left(\frac{n\pi X}{\lambda}\right). \tag{2.65}$$

Substitution of equation (2.65) into equation (2.61) yields

$$\begin{aligned}\frac{\partial^2 \mathcal{G}}{\partial X^2} + \frac{1}{r}\frac{\partial}{\partial r}\left(r\frac{\partial \mathcal{G}}{\partial r}\right) = &\sum_{n=1}^{\infty} g_n'' \cos\left(\frac{n\pi X}{\lambda}\right) + \frac{1}{r}\sum_{n=1}^{\infty} g_n' \cos\left(\frac{n\pi X}{\lambda}\right) \\ &- \frac{\pi^2}{\lambda^2}\sum_{n=1}^{\infty} n^2 g_n \cos\left(\frac{n\pi X}{\lambda}\right) + \frac{g_0''}{2} + \frac{1}{2r}g_0' = 0 \quad \text{in } r < \epsilon \text{ and } r > \epsilon,\end{aligned} \tag{2.66}$$

which leads to the following ODEs for the functions $g_n\left(r\right)$

$$g_0'' + \frac{1}{r}g_0' = 0, \tag{2.67}$$

$$g_n'' + \frac{g_n'}{r} - \left(\frac{n\pi}{\lambda}\right)^2 g_n = 0 \quad \text{for} \quad n \geq 1. \tag{2.68}$$

Solution of equation (2.67) yields

$$g_0 = \begin{cases} c_{1,0} + c_{2,0} \ln(r) & \text{for } r < \epsilon \\ d_{1,0} + d_{2,0} \ln(r) & \text{for } r > \epsilon \end{cases} \tag{2.69}$$

In order to avoid a singular solution at $r = 0$ and as $r \to \infty$, we require $c_{2,0} = d_{2,0} = 0$. Solution of equation (2.68) gives

$$g_n = \begin{cases} c_{1,n}\mathcal{I}_0\left(\frac{n\pi r}{\lambda}\right) + c_{2,n}\mathcal{K}_0\left(\frac{n\pi r}{\lambda}\right) & \text{for } r < \epsilon \\ d_{1,n}\mathcal{I}_0\left(\frac{n\pi r}{\lambda}\right) + d_{2,n}\mathcal{K}_0\left(\frac{n\pi r}{\lambda}\right) & \text{for } r > \epsilon \end{cases}. \tag{2.70}$$

where $\mathcal{I}_\alpha(\cdot)$ and $\mathcal{K}_\alpha(\cdot)$ denote modified Bessel functions of the first and second kind respectively. Again we require $c_{2,n} = d_{1,n} = 0$, to avoid singularities in this solution, leaving

$$g_n = \begin{cases} c_{1,n}\mathcal{I}_0\left(\frac{n\pi r}{\lambda}\right) & \text{for } r < \epsilon \\ d_{1,n}\mathcal{K}_0\left(\frac{n\pi r}{\lambda}\right) & \text{for } r > \epsilon \end{cases}. \tag{2.71}$$

The jump condition on $\mathcal{G}$ (equation (2.63)) is used to fix $c_{1,n}$ in terms of $d_{1,n}$ for all n as follows:

$$\delta(x - x_0) = \frac{1}{\lambda} + \sum_{n=1}^{\infty} \frac{1}{\lambda} \cos\left(\frac{n\pi(x - x_0)}{\lambda}\right), \tag{2.72}$$

$$[g_0]_{r=\epsilon^+}^{r=\epsilon^-} = c_{1,0} - d_{1,0} = \frac{1}{\lambda}, \tag{2.73}$$

$$[g_n]_{r=\epsilon^+}^{r=\epsilon^-} = \left(c_{1,n}\mathcal{I}_0\left(\frac{n\pi\epsilon}{\lambda}\right) - d_{1,n}\mathcal{K}_0\left(\frac{n\pi\epsilon}{\lambda}\right)\right) = \frac{1}{\lambda}, \tag{2.74}$$

$$\Rightarrow \begin{cases} c_{1,0} = \dfrac{1 + d_{1,0}\lambda}{\lambda} \\ c_{1,n} = \dfrac{d_{1,n}\lambda\mathcal{K}_0\left(\frac{n\pi\epsilon}{\lambda}\right) + 1}{\lambda\mathcal{I}_0\left(\frac{n\pi\epsilon}{\lambda}\right)} \end{cases}. \tag{2.75}$$

The condition on $\mathcal{G}$ as $r \to \infty$ (equation (2.64)) fixes $d_{1,0} = 0$. Finally, $d_{1,n}$ can be determined using the jump condition on $\frac{\partial \mathcal{G}}{\partial r}$ (equation (2.63))

$$\frac{dg_n}{dr} = \begin{cases} n\pi \dfrac{\left(d_{1,n}\lambda \mathcal{K}_0\left(\frac{n\pi\epsilon}{\lambda}\right)+1\right)\mathcal{I}_1\left(\frac{n\pi r}{\lambda}\right)}{\lambda^2 \mathcal{I}_0\left(\frac{n\pi\epsilon}{\lambda}\right)} & \text{for } r<\epsilon, \\ -n\pi \dfrac{d_{1,n}\mathcal{K}_1\left(\frac{n\pi r}{\lambda}\right)}{\lambda} & \text{for } r>\epsilon \end{cases}, \tag{2.76}$$

$$\begin{aligned} \left.\frac{dg_n}{dr}\right|_{r=\epsilon^-} &- \bar{\sigma} \left.\frac{dg_n}{dr}\right|_{r=\epsilon^+} = 0, \\ &= \frac{n\pi\left(d_{1,n}\lambda\left(\bar{\sigma}\mathcal{I}_0\left(\frac{n\pi\epsilon}{\lambda}\right)\mathcal{K}_1\left(\frac{n\pi\epsilon}{\lambda}\right)+\mathcal{I}_1\left(\frac{n\pi\epsilon}{\lambda}\right)\mathcal{K}_0\left(\frac{n\pi\epsilon}{\lambda}\right)\right)+\mathcal{I}_1\left(\frac{n\pi\epsilon}{\lambda}\right)\right)}{\lambda^2\mathcal{I}_0\left(\frac{n\pi\epsilon}{\lambda}\right)}, \end{aligned} \tag{2.77}$$

$$\Rightarrow d_{1,n} = -\frac{\mathcal{I}_1\left(\frac{n\pi\epsilon}{\lambda}\right)}{\lambda\left(\bar{\sigma}\mathcal{I}_0\left(\frac{n\pi\epsilon}{\lambda}\right)\mathcal{K}_1\left(\frac{n\pi\epsilon}{\lambda}\right)+\mathcal{I}_1\left(\frac{n\pi\epsilon}{\lambda}\right)\mathcal{K}_0\left(\frac{n\pi\epsilon}{\lambda}\right)\right)}. \tag{2.78}$$

We now have the following explicit expression for $\mathcal{G}$:

$$\mathcal{G}(X,r) = \begin{cases} \dfrac{1}{\lambda} + \displaystyle\sum_{n=1}^{\infty} \frac{\bar{\sigma}\mathcal{K}_1\left(\frac{n\pi\epsilon}{\lambda}\right)}{\lambda\left(\bar{\sigma}\mathcal{I}_0\left(\frac{n\pi\epsilon}{\lambda}\right)\mathcal{K}_1\left(\frac{n\pi\epsilon}{\lambda}\right)+\mathcal{I}_1\left(\frac{n\pi\epsilon}{\lambda}\right)\mathcal{K}_0\left(\frac{n\pi\epsilon}{\lambda}\right)\right)}\mathcal{I}_0\left(\frac{n\pi r}{\lambda}\right)\cos\left(\frac{n\pi X}{\lambda}\right) & \\ & \text{for } r<\epsilon \\ -\displaystyle\sum_{n=1}^{\infty} \frac{\mathcal{I}_1\left(\frac{n\pi\epsilon}{\lambda}\right)}{\lambda\left(\bar{\sigma}\mathcal{I}_0\left(\frac{n\pi\epsilon}{\lambda}\right)\mathcal{K}_1\left(\frac{n\pi\epsilon}{\lambda}\right)+\mathcal{I}_1\left(\frac{n\pi\epsilon}{\lambda}\right)\mathcal{K}_0\left(\frac{n\pi\epsilon}{\lambda}\right)\right)}\mathcal{K}_0\left(\frac{n\pi r}{\lambda}\right)\cos\left(\frac{n\pi X}{\lambda}\right) & \\ & \text{for } r>\epsilon \end{cases} \tag{2.79}$$

and can thus calculate its derivative:

$$\frac{\partial\mathcal{G}}{\partial r}(X,r) = \begin{cases} \displaystyle\sum_{n=1}^{\infty} \frac{n\pi\bar{\sigma}\mathcal{K}_1\left(\frac{n\pi\epsilon}{\lambda}\right)}{\lambda^2\left(\bar{\sigma}\mathcal{I}_0\left(\frac{n\pi\epsilon}{\lambda}\right)\mathcal{K}_1\left(\frac{n\pi\epsilon}{\lambda}\right)+\mathcal{I}_1\left(\frac{n\pi\epsilon}{\lambda}\right)\mathcal{K}_0\left(\frac{n\pi\epsilon}{\lambda}\right)\right)}\mathcal{I}_1\left(\frac{n\pi r}{\lambda}\right)\cos\left(\frac{n\pi X}{\lambda}\right) & \\ & \text{for } r<\epsilon \\ \displaystyle\sum_{n=1}^{\infty} \frac{n\pi\mathcal{I}_1\left(\frac{n\pi\epsilon}{\lambda}\right)}{\lambda^2\left(\bar{\sigma}\mathcal{I}_0\left(\frac{n\pi\epsilon}{\lambda}\right)\mathcal{K}_1\left(\frac{n\pi\epsilon}{\lambda}\right)+\mathcal{I}_1\left(\frac{n\pi\epsilon}{\lambda}\right)\mathcal{K}_0\left(\frac{n\pi\epsilon}{\lambda}\right)\right)}\mathcal{K}_1\left(\frac{n\pi r}{\lambda}\right)\cos\left(\frac{n\pi X}{\lambda}\right) & \\ & \text{for } r>\epsilon \end{cases} \tag{2.80}$$

The limit $r \to \epsilon$ is trivial, and can be taken simply by evaluating at $r = \epsilon$.

We note that the singular integral term in equation (2.57) is a Fourier convolution of $\frac{\partial\mathcal{G}}{\partial r}|_{r=\epsilon^-}$ and Φ. This suggests that equation (2.57) may be tractable to a spectral method

and leads us to also consider the Fourier series of Φ and j which we write in the form

$$\Phi(x,t) = P_0(t) + \sum_{n=1}^{\infty} P_n(t) \cos\left(\frac{n\pi x}{\lambda}\right), \tag{2.81}$$

$$j(\Phi,t) = j_0(t) + \sum_{n=1}^{\infty} j_n(t) \cos\left(\frac{n\pi x}{\lambda}\right). \tag{2.82}$$

On noting that the n^{th} term in the Fourier cosine series of the convolution $(f \star g)(x)$ is $\frac{1}{2} f_n g_n$ (where f_n and g_n are the n^{th} terms in the Fourier cosine series of the functions $f(x)$ and $g(x)$, respectively) we see that equation (2.57) can be transformed to

$$\frac{dP_n}{dt} = -\frac{\lambda}{2\mathcal{C}} \left.\frac{dg_n}{dr}\right|_{r=\epsilon^-} P_n(t) - j_n(t). \tag{2.83}$$

Given a functional dependence for (Φ, t) this formulation of the problem allows us to use a Runge-Kutta method to solve for $P_n(t)$ and thus for $\Phi(x,t)$ and has the notable advantage (over solving equation (2.57) directly) that the singularity in $\mathcal{G}$ can be dealt with easily. In the frequency domain, this singularity occurs in the limit $n \to \infty$, as the Bessel functions in equation (2.79) also tend to infinity. We note that due to equation (2.83), large and positive g_n simply implies that $P_n \to 0$ very quickly, or equivalently that very high frequency components of our solution decay very quickly.

2.3.3 Numerical solution of equation (2.83) via a spectral method.

Given an initial condition $\Phi(x,0)$, we calculate initial conditions for the gating variables w_i by the assumption that the axon is at rest, and thus $w_i(x,0)$ is the steady state solution to equation (2.28), and we use these values to determine the membrane current $j(\Phi(x,0),0)$ through equation (2.27). Once Φ and j are known, we make use of the fast Fourier transform (FFT) to determine the coefficients P_n and j_n in equation (2.83). We can also use the values of Φ and w_i (in the time domain) to find the derivatives in equation (2.28). This allows us to write the time derivatives of P_n and w_i in the form

$$\frac{dP_n}{dt} = f_1(t, x, P_n, j_n) \tag{2.84}$$

$$\frac{dw_i}{dt} = f_{2,i}(t, x, \Phi, w_i) \tag{2.85}$$

which is amenable to solution using a standard, fourth order, Runge-Kutta method. The only complication here is that we have to use an inverse FFT at each iteration, turning the updated values P_n into an updated Φ, calculating new gating variable values and then new membrane channel values in the time domain, and finally using the FFT to convert back into the frequency domain. A sensible choice of λ depends on the choices we make for other parameters in our model (namely ϵ and σ_{in}, and the length of time for which we run the simulation) but we note that the results presented here are robust for $\lambda > 750$.

2.3.4 An analytic solution to a simplified problem

In this section, we consider a simplified case of equations (2.22) to (2.25) for a uniform cylindrical axon, by replacing the Hodgkin Huxley ion channel dynamics with a linear membrane resistance. Although this problem is less interesting from a physiological perspective, it is simple enough to permit an analytical solution and can therefore be used to verify the results of our numerical simulations. This simplified model can be stated as follows

$$\nabla^2 \phi = 0 \text{ in } r < \epsilon \text{ and } r > \epsilon, \tag{2.86}$$

$$\left.\frac{\partial \phi}{\partial r}\right|_{r=\epsilon^-} = \bar{\sigma} \left.\frac{\partial \phi}{\partial r}\right|_{r=\epsilon^+}, \tag{2.87}$$

$$[\phi]_{r=\epsilon^+}^{r=\epsilon^-} = \Phi(x,t), \tag{2.88}$$

$$\mathcal{C}\frac{\partial \Phi}{\partial t} = -\left.\frac{\partial \phi}{\partial r}\right|_{r=\epsilon^-} - g_{\text{leak}}\Phi(x,t), \tag{2.89}$$

and

$$\Phi(x,0) = \cos(kx). \tag{2.90}$$

This has the solution

$$\phi(x,r,t) = \begin{cases} \dfrac{\bar{\sigma}\mathcal{K}_1(k\epsilon)}{\bar{\sigma}\mathcal{I}_0(k\epsilon)\mathcal{K}_1(k\epsilon)+\mathcal{I}_1(k\epsilon)\mathcal{K}_0(k\epsilon)}\cos(kx)\mathcal{I}_0(kr)\times \\ \exp\left(-\left(\dfrac{k\bar{\sigma}\mathcal{I}_1(k\epsilon)\mathcal{K}_1(k\epsilon)}{C\left(\bar{\sigma}\mathcal{I}_0(k\epsilon)\mathcal{K}_1(k\epsilon)+\mathcal{I}_1(k\epsilon)\mathcal{K}_0(k\epsilon)\right)}+\dfrac{g_{\text{leak}}}{C}\right)t\right) & \text{for } r<\epsilon \\ -\dfrac{\bar{\sigma}\mathcal{I}_1(k\epsilon)}{\bar{\sigma}\mathcal{I}_0(k\epsilon)\mathcal{K}_1(k\epsilon)+\mathcal{I}_1(k\epsilon)\mathcal{K}_0(k\epsilon)}\cos(kx)\mathcal{K}_0(kr)\times \\ \exp\left(-\left(\dfrac{k\bar{\sigma}\mathcal{I}_1(k\epsilon)\mathcal{K}_1(k\epsilon)}{C\left(\bar{\sigma}\mathcal{I}_0(k\epsilon)\mathcal{K}_1(k\epsilon)+\mathcal{I}_1(k\epsilon)\mathcal{K}_0(k\epsilon)\right)}+\dfrac{g_{\text{leak}}}{C}\right)t\right) & \text{for } r>\epsilon \end{cases}, \tag{2.91}$$

which yields the following expression for the transmembrane potential

$$\Phi(x,t) = \cos(kx)\exp\left(-\left(\frac{k\bar{\sigma}\mathcal{I}_1(k\epsilon)\mathcal{K}_1(k\epsilon)}{C\left(\bar{\sigma}\mathcal{I}_0(k\epsilon)\mathcal{K}_1(k\epsilon)+\mathcal{I}_1(k\epsilon)\mathcal{K}_0(k\epsilon)\right)}+\frac{g_{\text{leak}}}{C}\right)t\right), \tag{2.92}$$

where $\mathcal{I}_\alpha(x)$ and $\mathcal{K}_\alpha(x)$ are again modified Bessel functions of the first and second kind respectively.

We verify the accuracy of our numerical scheme by using it to solve equations (2.86) to (2.89), and note that the method is robust with respect to changes in resolution and period, λ. Figure 2.3 shows this comparison graphically, and figure 2.4 shows how the errors can be reduced to the scale of machine accuracy by taking sufficiently many time steps.

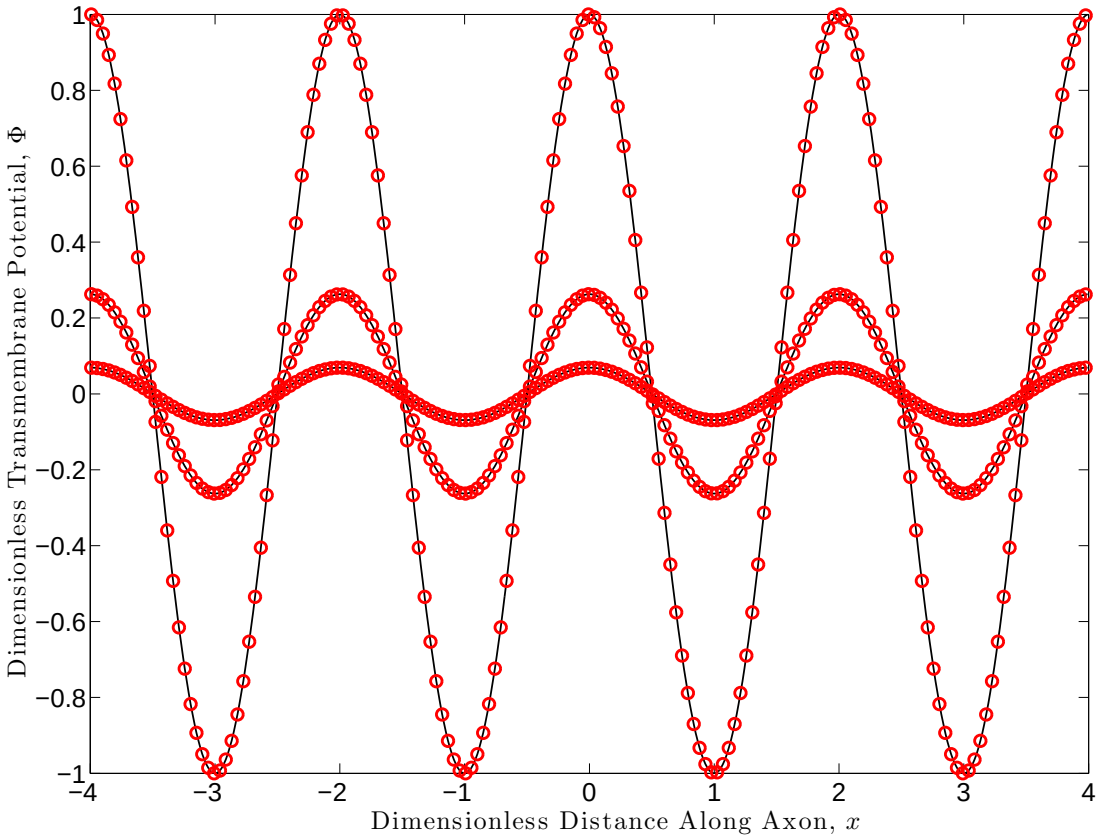

FIGURE 2.3: Numerical (solid curve) and analytic (circles) solutions to equations (2.86)–(2.89), at times $t = 0, 0.025, 0.05$, using 512 space points and 5000 time steps

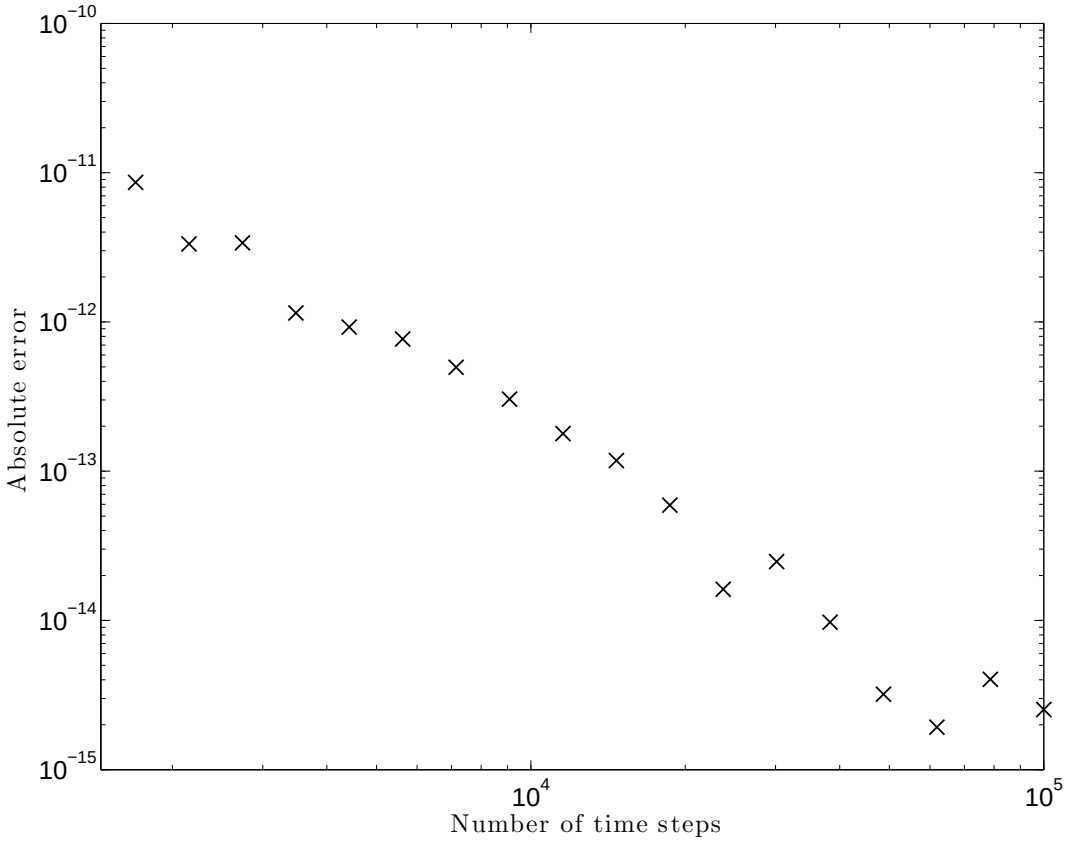

FIGURE 2.4: Mean absolute error in simulation at $t = 0.25$ as a function of number of time steps, using 512 space steps.

2.4 Results

We use our algorithm to calculate solutions to our model for a range of dimensionless axon radii ϵ, and for a range of conductivities. The results of these simulations are compared to solutions of the equivalent cable equation in order to gauge its validity both *in vitro* and *in vivo*.

In all cases, we have chosen to truncate the infinite series in equations (2.81) and (2.82) after 16384 ($= 2^{14}$) terms. This value was chosen by repeatedly running the simulation with increasing numbers of terms until the results were seen to converge. The periodicity value, λ, was chosen in the same way, increasing it over repeated simulations. As stated previously, a value of $\lambda = 750$ was found to be large enough that convergence was seen.

2.4.1 The case *in vitro* ($\bar{\sigma} = 1$)

We begin by looking at the case where intracellular and extracellular conductivities are equal which we believe to be the case in the *in vitro* experiments conducted in [44]. We note the divergence of our results from those predicted by the cable equation as ϵ increases, as expected. However, as shown in figure 2.5, this divergence does not become significant until the dimensionless axon radius is considerably larger than that typically occurring in a squid. A comparison between our solutions and those of the cable equation is also informative, and we note that the cable equation slightly overestimates the width of the wave profile (see figure 2.6). Figure 2.7 shows cross-sections of the intracellular and extracellular potentials generated during an action potential. The magnitude of the extracellular potentials generated in the smaller axon ($\epsilon = 0.1$, top) are less than a third those of the intracellular potentials, resulting in the close agreement between the cable equation predictions and the results of our simulations. The size of the extracellular potentials increases slightly as ϵ increases, but not enough (over the physiological range of radii) to mean that the cable equation approach ceases to give an accurate estimate of action potential velocity.

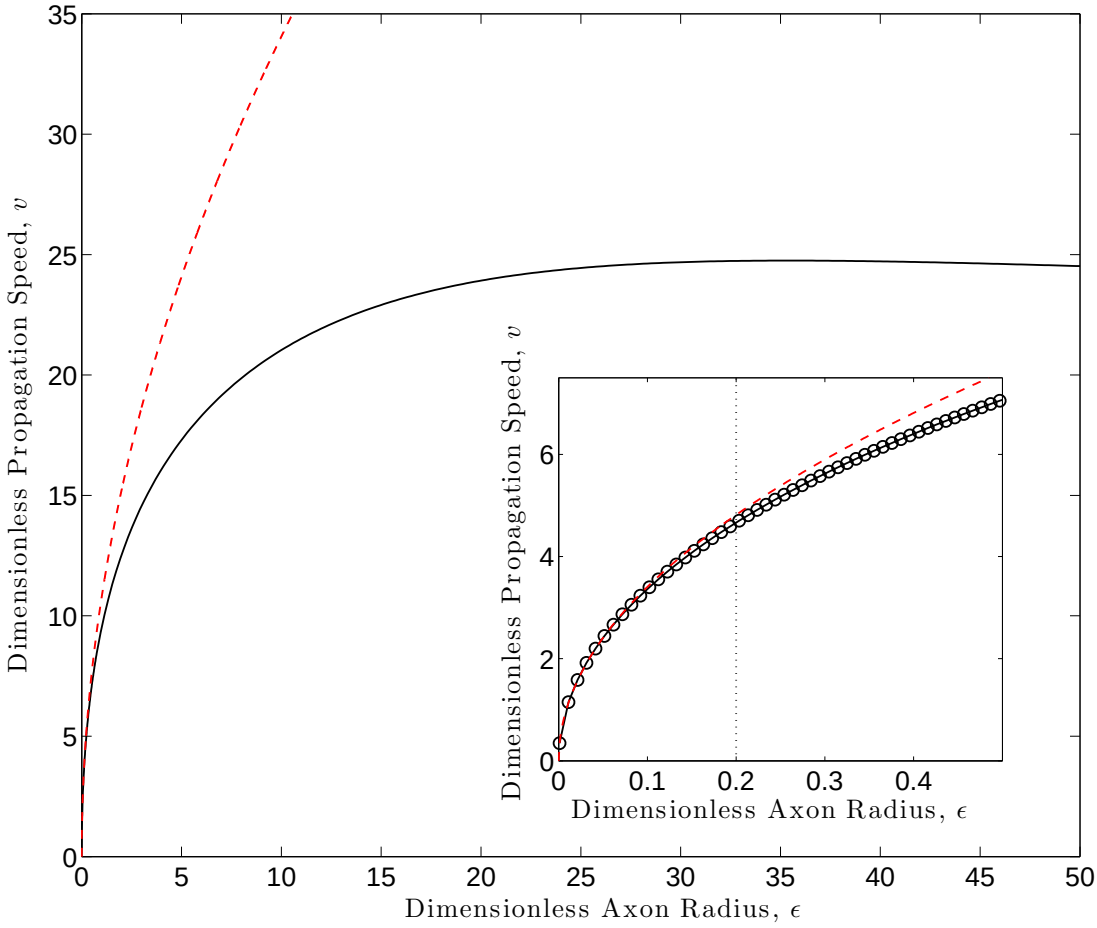

FIGURE 2.5: Variation of dimensionless propagation speed, v, with dimensionless axon radius, ϵ, with $\bar{\sigma} = 1$, as calculated by our simulation (solid, black curve) and predicted by the cable equation (dashed, red curve). Dotted line on inset is at $\epsilon = 0.2$, the approximate upper bound on ϵ, corresponding to the largest squid axons. Over a physiological range of ϵ, the discrepancy between the two models is not significant. Simulations were run with $\lambda = 750$, for $t = 0$ to 30 with a time step of 0.001 and 8192 space steps

2.4.2 The case *in vivo* ($\bar{\sigma} = 0.1$)

An estimate for the extracellular conductivity of a nerve bundle of $\sigma_{\text{out}} = 0.385$ S·m^{-1} is given in [2], which is roughly one tenth of the intracellular conductivity used by Hodgkin and Huxley (and therefore yields $\bar{\sigma} = 0.1$ in our model). We must note that the determination of these parameters is non-trivial, and significant variation exists in measurements of both intracellular and extracellular conductivities. We feel, however, that this only strengthens the argument for considering scenarios where $\bar{\sigma} \neq 1$.

For the case, where $\bar{\sigma} = 0.1$,we find that the divergence from the solutions of the cable

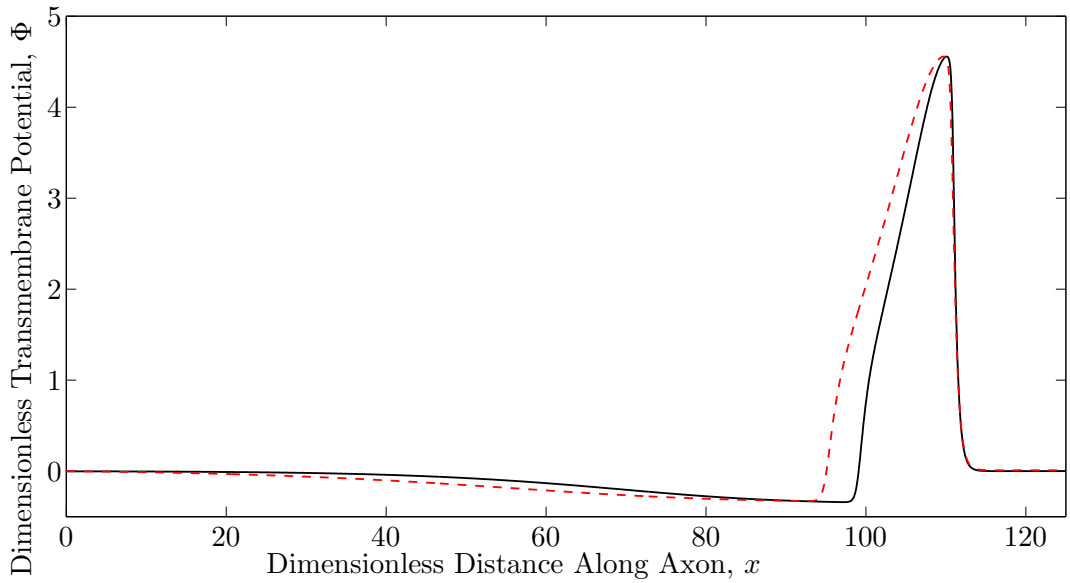

FIGURE 2.6: A typical travelling wave profile from our simulation (solid, black curve) and the cable equation (dashed, red curve) for the *in vitro* case, $\epsilon = 0.2$, $\bar{\sigma} = 1$

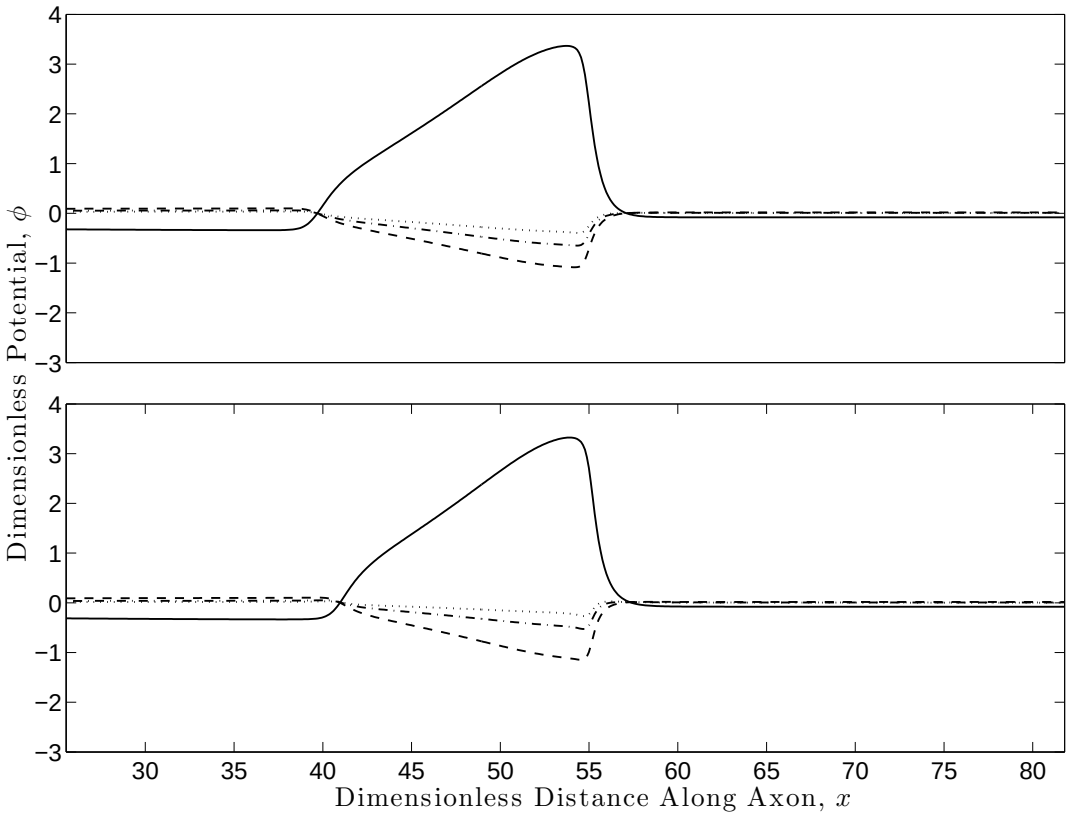

FIGURE 2.7: Cross-section of intracellular (solid curve) and extracellular potentials during an action potential, in axons of dimensionless radius $\epsilon = 0.1$ (upper panel) and $\epsilon = 0.3$ (lower panel), for $\bar{\sigma} = 1$. Intracellular cross-section is taken at $r = \epsilon - 10^{-6}$, with extracellular cross-sections at $r = \epsilon + 10^{-6}$ (dashed curve), $r = 1.05\epsilon$ (dashed and dotted curve) and $r = 1.1\epsilon$ (dotted curve)

equation (in terms of propagation speed, in figure 2.8, and travelling wave profile, in figure 2.9) is much more pronounced, and becomes apparent for a physiologically viable range of axon radii, suggesting that the cable equation is an inaccurate model for the behaviour of axons *in vivo*. The cross-sections in figure 2.10 explain this inaccuracy — the increased extracellular resistance allows for significant potential changes in the extracellular electrolyte, which cause the transmembrane potential changes during an action potential to be generated by an increase in the intracellular potential and a decrease in the extracellular potential, as opposed to the *in vitro* case where the action potential is generated almost entirely by an increase in the intracellular potential.

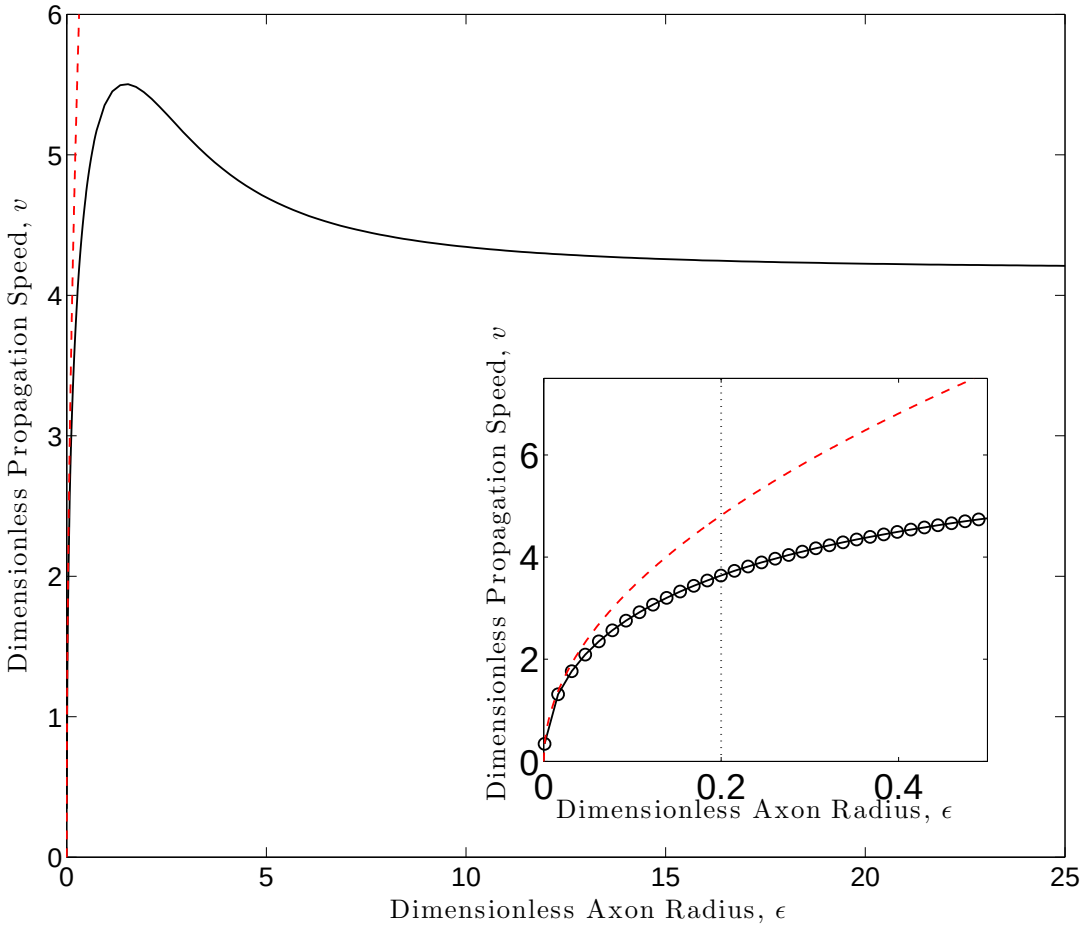

FIGURE 2.8: Variation of dimensionless propagation speed, v, with dimensionless axon radius, ϵ, with $\bar{\sigma} = 0.1$, as calculated by our simulation (solid, black curve) and predicted by the cable equation (dashed, red curve). Dotted line on inset is at $\epsilon = 0.2$, the approximate upper bound on ϵ, corresponding to the largest squid axons. The discrepancy between the two models over a physiological range of ϵ is clear. Simulation parameters are identical to the case $\bar{\sigma} = 1$

Figure 2.11 shows contour plots of the potentials generated close to the axon membrane

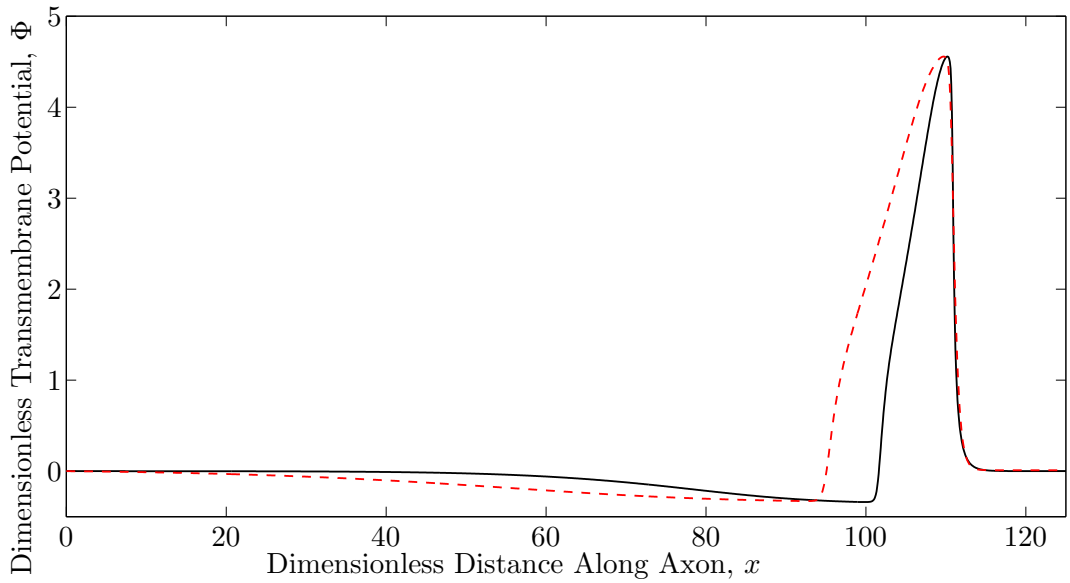

FIGURE 2.9: A typical travelling wave profile from our simulation (solid, black curve) and the cable equation (dashed, red curve) for the *in vivo* case, $\epsilon = 0.2$, $\bar{\sigma} = 0.1$

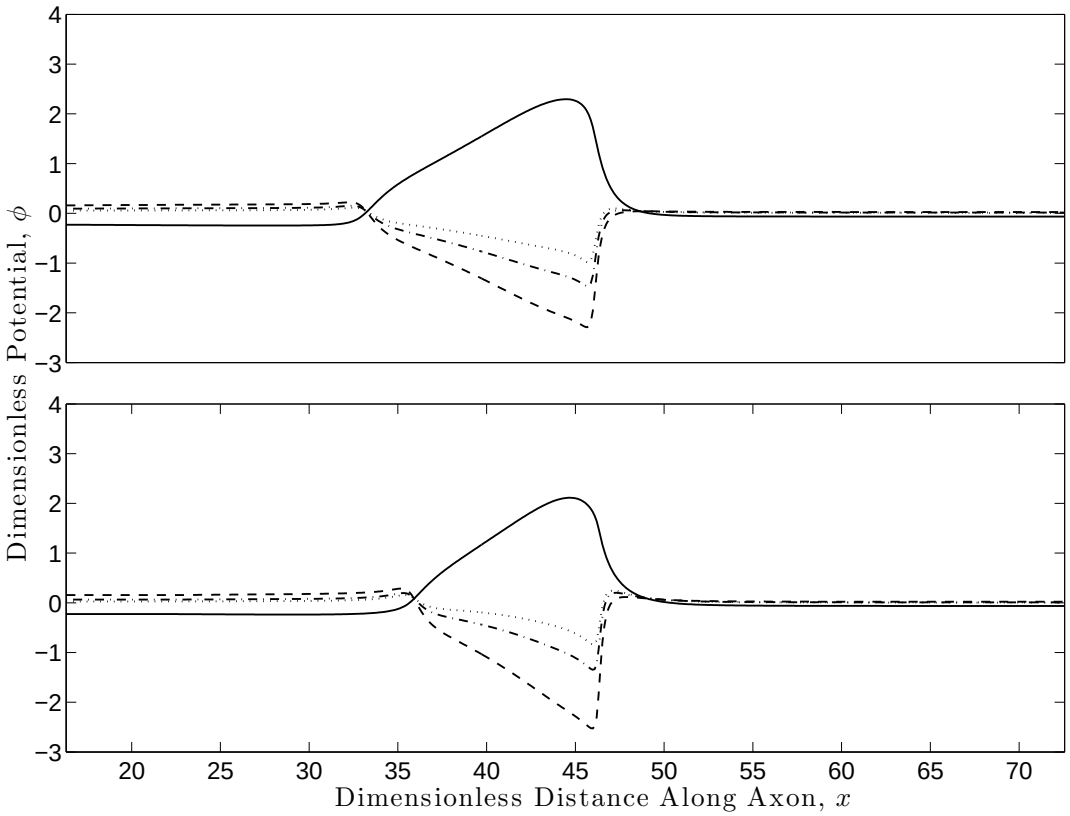

FIGURE 2.10: Cross-section of intracellular (solid curve) and extracellular potentials during an action potential, in axons of dimensionless radius $\epsilon = 0.1$ (upper panel) and $\epsilon = 0.3$ (lower panel), for $\bar{\sigma} = 0.1$. Intracellular cross-section is taken at $r = \epsilon - 10^{-6}$, with extracellular cross-sections at $r = \epsilon + 10^{-6}$ (dashed curve), $r = 1.05\epsilon$ (dashed and dotted curve) and $r = 1.1\epsilon$ (dotted curve).

during the propagation of an action potential. As mentioned above, the extracellular potentials are seen to be much larger in the case $\bar{\sigma} = 0.1$ (left-hand column), and as such the cable equation is a much worse approximation to this case.

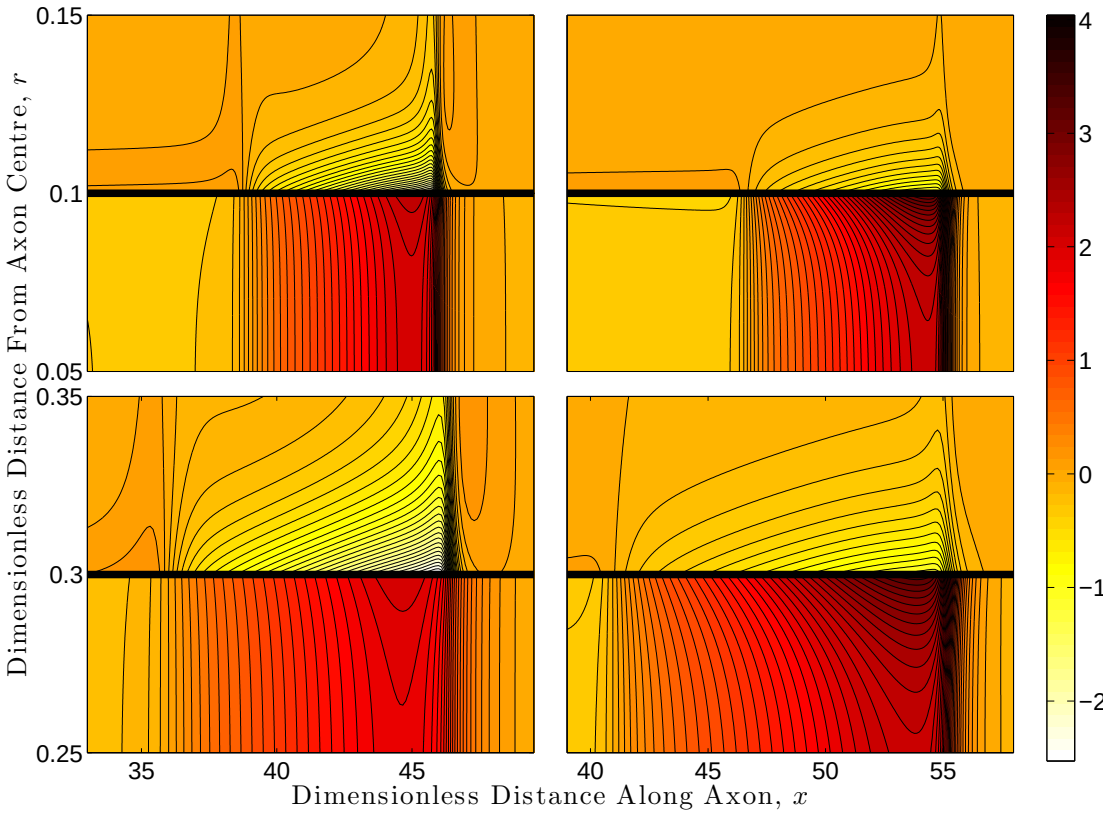

FIGURE 2.11: Contour plots of intracellular and extracellular potentials generated by the propagation of an action potential, for dimensionless radii $\epsilon = 0.1$ (upper panels) and $\epsilon = 0.3$ (lower panels) and $\bar{\sigma} = 0.1$ (left panels) and $\bar{\sigma} = 1$ (right panels). The thick solid line through the centre of each panel shows the location of the axon membrane

2.5 Discussion

At least one of a squid's escape responses is initiated by an action potential propagating along its giant axon, which triggers the contraction of the circular muscle groups around its siphon and gives rise to a powerful propulsive jet of water [80, 75]. Fast action potential propagation (along the giant axon) is thus associated with rapid escape and is therefore expected to be a characteristic that is under strong selection pressure.

Study of the cable equation model of action potential propagation predicts that signal conduction speed is maximised by maximising the axoplasmic conductivity of the axon

or the axon radius. The fact that the cable equation predicts that propagation speed will scale like $R^{\frac{1}{2}}$ without limit means that it does not predict an 'optimal' axon size, simply that bigger is better. Instead, arguments concerning the increased metabolic cost of growing and maintaining a larger axon are used to explain why the squid giant axon is not larger than it is. Producing and maintaining a larger cell requires more raw materials such as the phospholipids comprising the membrane and proteins forming the ion channels, as well as more energy to operate as, for example, larger numbers of ions must be moved to depolarise the larger surface are of the membrane and to maintain resting potential. These higher costs mean that there is an evolutionary pressure working against very large cells, and thus the actual size of the axon is determined by optimising the trade-off between higher escape speed and the attendant metabolic price.

Our approach suggests that there is a law of diminishing returns (in terms of increased propagation velocity for increases in axon radius) which means — in the physiological case for a large axon ($\bar{\sigma} = 0.1$, $R \approx 0.5$mm) — that increases in propagation velocity scale significantly more slowly with increases in axon radius, R, than the $R^{\frac{1}{2}}$ dependence predicted by the cable equation. In addition there is a maximal radius, for a given conductivity ratio $\bar{\sigma}$, at which the propagation velocity obtains a maximum value and above which further increases in axon size result in a *decrease* in propagation speed. We note however that even in the physiological case $\bar{\sigma} = 0.1$ the optimal radius is significantly larger than any physiologically feasible giant axon. This suggests that metabolic cost is still a limiting factor in determining the size of the axon — in fact we see that the metabolic cost of increased propagation velocity is significantly larger than that suggested by the cable equation.

Chapter 3

Action potential propagation in myelinated neurons

3.1 Introduction

Speed, as discussed in chapter 2, is a key consideration for neural signalling, particularly for neurons which carry signals related to movement and reflexes. We have seen that larger neurons conduct signals faster, but this comes at an increased metabolic cost, as well as taking up more physical space. Neurons in most vertebrates have an adaptation called myelination which increases the speed of signal propagation by a different method. Long segments of the axon are insulated by a substance called myelin, created by glial cells close to the neuron and it is this insulation, and the organisation of the rest of the cell around it, that increases the speed at which the action potential propagates. Although myelination is principally associated with vertebrates, it is present in several other taxa, where it is thought to have evolved independently, suggesting that the principles by which it functions are universally beneficial [36].

In this chapter, we present analysis of the generic model in equations (1.20) to (1.27) in the context of the myelinated axon, exploiting its geometrical features to simplify the resulting model of axonal behaviour. This provides general, qualitative insights into the behaviour of the transmembrane potential in myelinated axons, which have applications

in simplifying existing computational models. It is also demonstrated that two existing models are special cases of our more general model, which allows us to assess the validity of these existing models over a range of physiological parameters.

3.1.1 Organisation of the myelinated axon

Myelin is produced by glia called Schwann cells, which are found in close proximity to mammalian neurons. Schwann cells have a specialised membrane formed from a fatty, dielectric material called myelin. Outgrowths from Schwann cells wrap around axons many times, forming an insulating sheath which increases the resistance of the axon membrane and decreases its capacitance (see figure 3.1). The outgrowths of neighbouring Schwann cells do not touch, so that the myelin sheath is not continuous along the entire axon — small gaps called nodes of Ranvier are left at regular intervals.

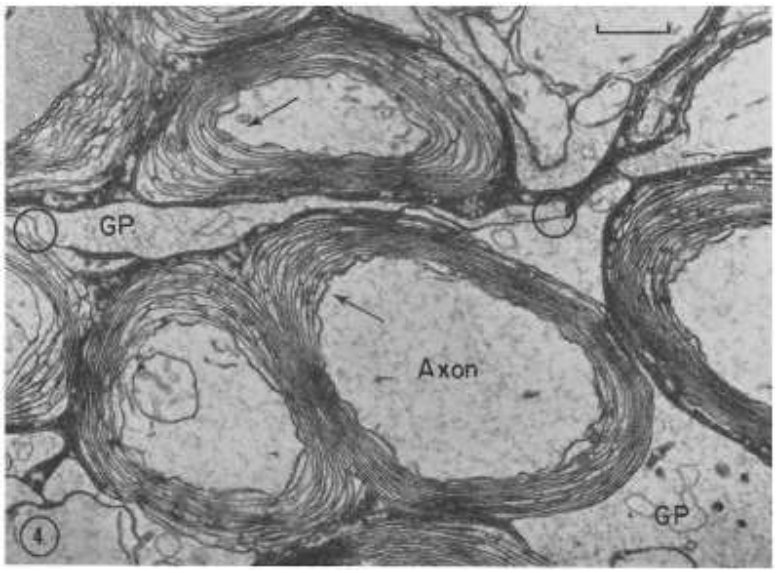

FIGURE 3.1: An axon (labelled) and myelin sheath (arrow). Reproduced from [37]

The ion channels at and around the node of Ranvier show clear spatial organisation. Sodium channels are concentrated at the centre of the node of Ranvier [16, 20], where there is little or no myelination and the axon membrane is exposed directly to the extracellular space, whereas potassium channels are concentrated in what is known as the paranodal region, close to the node of Ranvier but within the myelin sheath [79, 84]. Figure 3.2 shows a single node of Ranvier under the effects of fluorescent dyes which bind to sodium channels (green) and potassium channels (red).

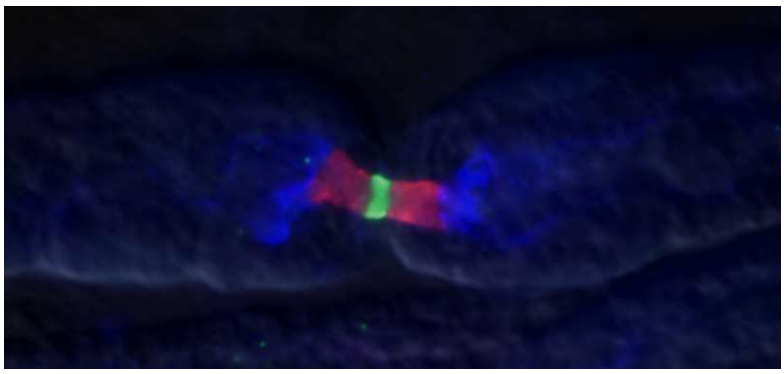

FIGURE 3.2: A node of Ranvier. Different proteins in the cell membrane have been stained with different dyes. The green dye binds to the protein that forms the sodium channel, which is strongly concentrated at the centre of the node. The red dye binds to the protein caspr, which is associated with the connection between the myelin sheath and the axon. The blue dye binds to the protein which forms the potassium channel. Figure provided by Peter Schrager, PhD, from an email (peter_shrager@urmc.rochester.edu) in August 2015

This concentration of ion channels causes action potentials to 'jump' from node to node, a phenomena known as saltatory conduction, which can be orders of magnitude faster than uniform propagation in an unmyelinated neuron of equivalent size.

A characteristic feature of the paranodal region adjacent to the node is that thickness of the myelin sheath 'tapers off' here, with each roll of myelin overlapping the previous and thus the capacitance of the membrane, which is related to the thickness of the cell membrane and myelin sheath and is fairly constant in the other regions, can vary spatially in the paranode.

3.1.2 Modelling the cell

3.1.2.1 The geometry of the myelinated axon

Figure 3.3 shows the geometry of a simplified myelinated axon (not to scale). The axon is assumed to be uniformly cylindrical and formed of identical, repeating subunits consisting of a node and its neighbouring paranodal and internodal regions. The assumption that the properties of each region don't vary along the length of the axon is useful for the sake of clarity, although the analysis of the model does not rely on it.

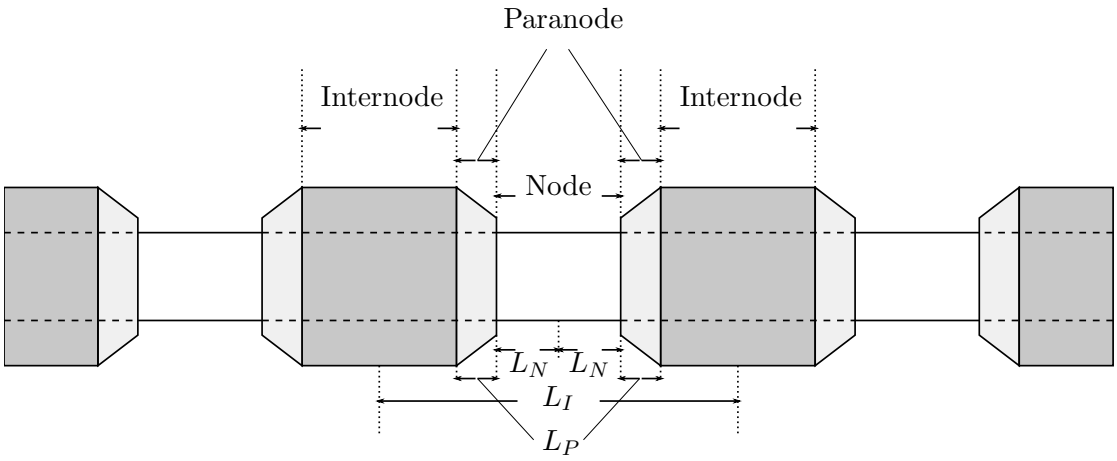

FIGURE 3.3: Simplified geometry of the myelinated axon (not to scale). The white regions are the nodes of Ranvier, where the cell membrane is exposed to the extracellular space, the sodium channel density is high and the membrane capacitance per unit area is highest. The light-grey regions are the paranodes, where the axon is partially myelinated, the potassium channel density is high and the membrane capacitance per unit area is lower. The dark-grey regions are the internodes, where the axon is fully myelinated, there are very few ion channels and the membrane capacitance is lowest.

Also shown in figure 3.3 are the labels we've used for the sizes of the different regions of the axon. Roughly, $L_N \approx 1 \times 10^{-6}\,\mathrm{m}$, $L_P \approx 1 \times 10^{-6}\,\mathrm{m}$, $L_I \approx 100 - 1000 \times 10^{-6}\,\mathrm{m}$, and it is the large discrepancies in scale between the nodal and internodal widths that accounts for the increased speed of action potential propagation.

3.1.2.2 A description of the electrical behaviour

Equations (1.20) to (1.27) from chapter 1 can be used to model the electrochemical behaviour in the myelinated axon. We first define the intracellular region

$$\Omega^* = \{r^* < R, 0 \leq \theta < 2\pi, -\infty < x^* < \infty\} \tag{3.1}$$

where r^*, θ and x^* are the radius, azimuth and longitudinal coordinates of a cylindrical coordinate system with its longitudinal axis lying along the centre of the axon. We have to adapt equation 1.27 to allow for the different properties of the myelinated and unmyelinated regions of the membrane, but otherwise the equations can be used unchanged.

The current flow through the nodal membrane (white regions in figure 3.3) is determined by the capacitance per unit area of the nodal membrane (C_N) and the current flows

through the ion channels (current density $j_N^*(\Phi^*, t^*)$)

$$\boldsymbol{J}^* \cdot \boldsymbol{e}_r|_{r^*=R^-} = C_N \frac{\partial \Phi^*}{\partial t^*} + j_N^*(\Phi^*, t^*) \qquad kL_I - L_N < x^* < kL_I + L_N, \tag{3.2}$$

where we define the longitudinal coordinate, x^*, such that the origin is at the centre of some reference node and the other nodes of the axon are then centred at $x^* = kL_I$, for $k \in \mathbb{Z}$.

Similarly, the current flows through the paranodal region (light-grey regions in figure 3.3) are determined by the capacitance per unit area of the membrane in this region ($C_P(x^*)$), and the current flows through the ion channels (current density $j_P^*(\Phi^*, t^*)$)

$$\boldsymbol{J}^* \cdot \boldsymbol{e}_r|_{r^*=R^-} = C_P(x^*) \frac{\partial \Phi^*}{\partial t^*} + j_P^*(\Phi^*, x^*, t^*) \tag{3.3}$$
$$kL_I - L_N - L_P < x^* < kL_I - L_N \text{ and } kL_I + L_N < x^* < kL_I + L_N + L_P,$$

Note that the paranodal capacitance per unit area and current density vary spatially — the thickness of the myelin sheath varies as it tapers into the node of Ranvier, affecting the capacitance, and the density of ion channels varies (see figure 3.2). Finally, the current flows through the internodal membranes (dark-grey regions in figure 3.3) are determined by the capacitance per unit area (C_I) and the current flows through the ion channels (current density $j_I^*(\Phi^*, t^*)$)

$$\boldsymbol{J}^* \cdot \boldsymbol{e}_r|_{r^*=R^-} = C_I \frac{\partial \Phi^*}{\partial t^*} + j_I^*(\Phi^*, t^*) \tag{3.4}$$
$$\left(k - \frac{1}{2}\right) L_I < x^* < kL_I - L_N - L_P \text{ and } kL_I + L_N + L_P < x^* < \left(k + \frac{1}{2} L_I\right),$$

This boundary condition of course holds throughout the entire internodal region on either side of the node, but we have chosen to define it this way to break the axon into a series of repeated, identical units, each of width L_I, spanning from the centre of one internodal region to the centre of the next. The solution to the model on one such subunit is then valid for every subunit, with a boundary condition at $x^* = \left(k - \frac{1}{2}\right) L_I$ and $x^* = \left(k + \frac{1}{2}\right) L_I$ to ensure continuity of current and potential.

The distribution of the ion channels in the axon plays a major role in determining

j_N^*, j_P^* and j_I^*. As seen in figure 3.2, the ion channels at the node of Ranvier are all sodium specific, and so we expect j_N^* to be comprised of a sodium and a general leak component, but not of a potassium component. The channels in the paranodal region are all potassium specific, and the distribution varies, with the highest densities being found closest to the node of Ranvier. We thus model j_P^* as being comprised of a potassium component and a general leak component, with size depending on distance from the node. We expect some currents to flow through the internodal membrane as the insulating effect of the myelin is not perfect, but the number of ion channels is low, and thus we expect the current density j_I^* to be small and comprised of only a leak component.

3.2 General, dimensional problem

The problem in dimensional form is thus

$$\boldsymbol{J}^* = -\sigma_{\text{in}} \nabla^* \phi^* \qquad r^* < R, \tag{3.5}$$

$$\boldsymbol{J}^* = -\sigma_{\text{out}} \nabla^* \phi^* \qquad r^* > R, \tag{3.6}$$

$$\nabla^* \cdot \boldsymbol{J}^* = 0 \qquad r^* < R \text{ and } r^* > R, \tag{3.7}$$

$$[\phi^*]_{r^*=R^+}^{r^*=R^-} = \Phi^*(x^*, t^*), \tag{3.8}$$

$$\boldsymbol{J} \cdot \boldsymbol{e}_r|_{r^*=R^+} = \boldsymbol{J} \cdot \boldsymbol{e}_r|_{r^*=R^-} \tag{3.9}$$

$$\boldsymbol{J}^* \cdot \boldsymbol{e}_r|_{r^*=R^-} = C_N \frac{\partial \Phi^*}{\partial t^*} + j_N^*(\Phi^*, t^*) \qquad kL_I - L_N < x^* < kL_I + L_N, \tag{3.10}$$

$$\boldsymbol{J}^* \cdot \boldsymbol{e}_r|_{r^*=R^-} = C_P(x^*) \frac{\partial \Phi^*}{\partial t^*} + j_P^*(\Phi^*, x^*, t^*) \quad kL_I - L_N - L_P < x^* < kL_I - L_N \quad kL_I + L_N < x^* < kL_I + L_N + L_P, \tag{3.11}$$

$$\boldsymbol{J}^* \cdot \boldsymbol{e}_r|_{r^*=R^-} = C_I \frac{\partial \Phi^*}{\partial t^*} + j_I^*(\Phi^*, t^*) \qquad \left(k - \frac{1}{2}\right) L_I < x^* < kL_I - L_N - L_P \quad kL_I + L_N + L_P < x^* < \left(k + \frac{1}{2} L_I\right), \tag{3.12}$$

$$\phi^* \to 0 \qquad r^* \to \infty \tag{3.13}$$

Here a * denotes a dimensional variable; $\boldsymbol{J}^*$ is current density; R is the axon radius; σ_{in} and σ_{out} are the conductivities of the axoplasm (inside the axon) and the extracellular electrolyte; ϕ^* is the electric potential; Φ^* is the transmembrane potential; L_I is the distance separating one node from the next; L_N is half the width of one node; L_P is the width of the paranodal region; C_N, $C_P(x^*)$ and C_I are the capacitances per unit area of the nodal, paranodal and internodal membranes, respectively (C_P varies with x^* because the thickness of the myelin sheath varies throughout the paranode) and $j_N^*(\Phi^*, t^*)$, $j_P^*(\Phi^*, x^*, t^*)$ and $j_I^*(\Phi^*, t^*)$ are the membrane current densities of the nodal, paranodal and internodal membranes, respectively (again, j_P^* varies with x^* because the ion channel density varies throughout the paranode).

The current densities are modelled by adapting the Hodgkin-Huxley approach given in [44] and equation (1.1) except the sodium, potassium and leak currents are explicitly separated to flow through different regions of the axon membrane, as follows

$$j_N^* = g_{\text{Na}} m^3 h \left(\Phi^* - \Phi_{\text{Na}}\right) + g_{\text{L}} \left(\Phi^* - \Phi_{\text{l}}\right), \tag{3.14}$$

$$j_P^* = g_{\text{K}}\left(x^*\right) n^4 \left(\Phi^* - \Phi_{\text{K}}\right) + g_{\text{L}} \left(\Phi^* - \Phi_{\text{l}}\right), \tag{3.15}$$

$$j_I^* = g_{\text{L}} \left(\Phi^* - \Phi_{\text{l}}\right) \tag{3.16}$$

with the gating variables h, m and n are defined as in equations (1.8) to (1.10). With the currents in this form it is also possible to model different leak current densities through different regions of the membrane by using a different value of g_{L} in each of the above equations.

We note that the ion channels in vertebrate neurons are not identical to those in the squid, but the qualitative gating behaviour is very similar (a fast acting sodium channel and a slower potassium channel), and that the Hodgkin-Huxley form has been adapted for modelling myelinated axons in other works [24, 63]

3.2.1 Non-dimensionalisation

We non-dimensionalise as follows

$$\Phi^* = \tilde{\Phi}\Phi, \qquad \phi^* = \tilde{\Phi}\phi, \qquad \boldsymbol{J}^* = \frac{\sigma_{\text{in}}\tilde{\Phi}}{L_I}\boldsymbol{J}, \tag{3.17}$$

$$j_N^* = g_{\text{Na}}\tilde{\Phi}j_N, \qquad j_P^* = \bar{g}_{\text{K}}\tilde{\Phi}j_P, \qquad j_I^* = g_{\text{L}}\tilde{\Phi}j_I \tag{3.18}$$

$$x^* = L_I x, \qquad r^* = L_N r, \qquad t^* = \tau t, \tag{3.19}$$

where $\tilde{\Phi}$ is a characteristic membrane potential (somewhere on the order of 10 millivolts), τ is a characteristic time scale and we choose the characteristic longitudinal length scale to be the internodal separation, L_I. The characteristic radial length scale is chosen to be L_N because the axon radius is small compared to the internodal separation L_I but is around the same order of magnitude as L_N. The choice of radial length scale therefore ensures that the position of the axon membrane is of order unity.

We choose the characteristic membrane current densities from the Hodgkin-Huxley forms in equations (3.14) to (3.16). Thus g_{Na} is the maximal conductance per unit area of the nodal membrane to sodium ions, $\bar{g}_{\text{K}}$ the average maximal conductance per unit area of the paranodal membrane to potassium ions and g_{L} the general leak conductance of the internodes. The values of these parameters are given in table 3.1.

Application of these scalings to equations (3.5) to (3.13) leads to the dimensionless version of the model

$$\boldsymbol{J} = -\frac{1}{\varepsilon}\frac{\partial\phi}{\partial r}\boldsymbol{e}_r - \frac{\partial\phi}{\partial x}\boldsymbol{e}_x \qquad r < \lambda_R, \tag{3.20}$$

$$\boldsymbol{J} = -\bar{\sigma}\frac{1}{\varepsilon}\frac{\partial\phi}{\partial r}\boldsymbol{e}_r - \bar{\sigma}\frac{\partial\phi}{\partial x}\boldsymbol{e}_x \qquad r > \lambda_R, \tag{3.21}$$

$$\frac{1}{\varepsilon r}\frac{\partial}{\partial r}\left(rJ_r\right) + \frac{\partial}{\partial x}J_x = 0 \qquad r < \lambda_R \text{ and } r > \lambda_R, \tag{3.22}$$

$$\left[\phi\right]_{r=\lambda_R^+}^{r=\lambda_R^-} = \Phi\left(x,t\right), \tag{3.23}$$

$$\boldsymbol{J}\cdot\boldsymbol{e}_r\big|_{r=\lambda_R^-} = \mathcal{C}\frac{\partial\Phi}{\partial t} + \tilde{j}_N j_N\left(\Phi,t\right) \qquad k-\varepsilon < x < k+\varepsilon, \tag{3.24}$$

$$\boldsymbol{J}\cdot\boldsymbol{e}_r\big|_{r=\lambda_R^-} = \mathcal{C}\tilde{C}_P\left(x\right)\frac{\partial\Phi}{\partial t} + \tilde{j}_P\left(x\right)j_P\left(\Phi,t\right) \quad k-\varepsilon-\varepsilon\lambda_P < x < k-\varepsilon \quad k+\varepsilon < x < k+\varepsilon+\varepsilon\lambda_P, \tag{3.25}$$

$$\boldsymbol{J}\cdot\boldsymbol{e}_r\big|_{r=\lambda_R^-} = \varepsilon\left(\tilde{C}_I\mathcal{C}\frac{\partial\Phi}{\partial t} + \tilde{j}_I j_I\left(\Phi,t\right)\right) \qquad \left(k-\frac{1}{2}\right) < x < k-\varepsilon-\varepsilon\lambda_P \quad k+\varepsilon+\varepsilon\lambda_P < x < \left(k+\frac{1}{2}\right), \tag{3.26}$$

$$\boldsymbol{J}\cdot\boldsymbol{e}_r\big|_{r=\lambda_R^+} = \boldsymbol{J}\cdot\boldsymbol{e}_r\big|_{r=\lambda_R^-}, \tag{3.27}$$

$$\phi \to 0 \qquad r \to \infty \tag{3.28}$$

where we have defined the following dimensionless parameters:

$$\varepsilon = \frac{L_N}{L_I}, \qquad \lambda_R = \frac{R}{L_N}, \qquad \lambda_P = \frac{L_P}{L_N}, \qquad \bar{\sigma} = \frac{\sigma_{\text{out}}}{\sigma_{\text{in}}} \tag{3.29}$$

$$\mathcal{C} = \frac{C_N L_I}{\sigma_{\text{in}}\tau}, \qquad \tilde{C}_I = \frac{C_I L_I}{C_N L_N}, \qquad \tilde{j}_N = \frac{g_{\text{Na}}L_I}{\sigma_{\text{in}}}, \quad \tilde{j}_I = \frac{g_{\text{L}}L_I^2}{\sigma_{\text{in}}L_N}, \tag{3.30}$$

and the following dimensionless functions

$$\tilde{C}_P\left(x\right) = \frac{C_P\left(x\right)}{C_N}, \qquad \tilde{j}_P\left(x\right) = \frac{g_{\text{K}}\left(x\right)L_I}{\sigma_{\text{in}}} = \frac{g_{\text{K}}\left(x\right)}{g_{\text{Na}}}\tilde{j}_N, \tag{3.31}$$

3.2.1.1 Estimates of parameter values

The values of these parameters are given below, using estimates of the properties of the myelinated axon given in table 3.1.

$$\varepsilon = 3.3 \times 10^{-4} - 3.3 \times 10^{-2}, \qquad \lambda_R = 0.6 - 3.8, \tag{3.32}$$

$$\lambda_P = 6.2, \qquad \bar{\sigma} = 0.2 \tag{3.33}$$

$$\mathcal{C} = 0.014 - 0.14, \qquad \tilde{C}_I = 0.31 - 3.1, \tag{3.34}$$

$$\tilde{j}_N = 0.34 - 3.4, \qquad \tilde{j}_I = 1.3 \times 10^{-3} - 1.3 \times 10^{-1}, \tag{3.35}$$

The values of the dimensionless functions describing the capacitance per unit area and current density in the paranodal regions will be of the following orders of magnitude

$$\tilde{C}_P(x) = 10^{-3} - 1, \qquad \tilde{j}_P(x) = 0.1 - 1 \tag{3.36}$$

Most notably, $\varepsilon \ll 1$, a fact we shall make use of when analysing the behaviour of the axon.

TABLE 3.1: Parameters describing the myelinated axon

Parameter	Description	Value	Unit	Reference
R	Axon radius	$0.4 - 5 \times 10^{-6}$	m	[63, 93]
L_N	Node width	$0.35 - 1.6 \times 10^{-6}$	m	[63, 92]
L_P	Paranode width	4×10^{-6}	m	[73]
L_I	Internodal spacing	$0.2 - 2 \times 10^{-3}$	m	[5]
C_N	Nodal membrane capacitance per unit area	5×10^{-2}	$\mathrm{F} \cdot \mathrm{m}^{-2}$	[7, 98]
C_P	Paranodal membrane capacitance per unit area	$10^{-5} - 10^{-2}$	$\mathrm{F} \cdot \mathrm{m}^{-2}$	
C_I	Internodal membrane capacitance per unit area	5×10^{-5}	$\mathrm{F} \cdot \mathrm{m}^{-2}$	[7]
g_{Na}	Sodium conductance per unit area	1200	$\mathrm{S} \cdot \mathrm{m}^{-2}$	[63]
g_{K}	Potassium conductance per unit area	360	$\mathrm{S} \cdot \mathrm{m}^{-2}$	[63]
g_{L}	General leak conductance	3 (Node) 0.015 (Internode)	$\mathrm{S} \cdot \mathrm{m}^{-2}$	[14, 63]
σ_{in}	Axoplasmic conductivity	0.7	$\mathrm{S} \cdot \mathrm{m}^{-1}$	[96]
σ_{out}	Extracellular conductivity	3	$\mathrm{S} \cdot \mathrm{m}^{-1}$	[24]
τ	Sodium channel opening time constant	10^{-4}	s	[27]

3.3 Asymptotic analysis of problem

The small parameter ε in equations (3.20) to (3.28) means the problem is amenable to asymptotic analysis. This allows us to separate the problem into one on the length scale of the internodal separation and one on the short ($O(\varepsilon)$) length scale of the node width. We can then derive a simplified model of the axon's behaviour from the solutions to the problems on these two length scales.

3.3.1 The outer problem

In the outer region, which is defined such that $x = O(1)$, we expand in powers of ε as follows:

$$\phi = \phi_0^{(\mathrm{O})}(x,r,t) + \varepsilon\phi_1^{(\mathrm{O})}(x,r,t) + \varepsilon^2\phi_2^{(\mathrm{O})}(x,r,t) + \cdots, \tag{3.37}$$

$$\boldsymbol{J} = \boldsymbol{J}_0^{(\mathrm{O})}(x,r,t) + \varepsilon\boldsymbol{J}_1^{(\mathrm{O})}(x,r,t) + \varepsilon^2\boldsymbol{J}_2^{(\mathrm{O})}(x,r,t) + \cdots, \tag{3.38}$$

$$\Phi = \Phi_0^{(\mathrm{O})}(x,r,t) + \varepsilon\Phi_1^{(\mathrm{O})}(x,r,t) + \varepsilon^2\Phi_2^{(\mathrm{O})}(x,r,t) + \cdots \tag{3.39}$$

where the superscript $^{(\mathrm{O})}$ denotes a quantity in the outer.

3.3.1.1 The leading order outer problem

By substituting the expansions above into equations (3.20) to (3.28) at leading order, we obtain the following problem for $\phi_0^{(\mathrm{O})}$

$$\frac{\partial\phi_0^{(\mathrm{O})}}{\partial r} = 0 \qquad r < \lambda_R, \tag{3.40}$$

$$\frac{\partial\phi_0^{(\mathrm{O})}}{\partial r} = 0 \qquad r > \lambda_R, \tag{3.41}$$

$$\left[\phi_0^{(\mathrm{O})}\right]_{r=\lambda_R^+}^{r=\lambda_R^-} = \Phi_0^{(\mathrm{O})}(x,t), \tag{3.42}$$

$$\phi_0^{(\mathrm{O})} \to 0 \qquad r \to \infty \tag{3.43}$$

which has solution

$$\phi_0^{(\mathrm{O})} = \begin{cases} \Phi_0^{(\mathrm{O})}(x,t) & r < \lambda_R \\ 0 & r > \lambda_R \end{cases} \tag{3.44}$$

The key insight is that the leading order potential is a function of distance along the axon and time only (and thus is independent of distance from the axon centre). However, the solution for the leading order potential is not fully determined (its dependence on x and t is unknown) and in order to find this dependence we need to proceed to higher orders and look for a solvability condition, this is described in section 3.3.3.1.

3.3.1.2 The first order outer problem

We also need to determine the leading order current density, $\boldsymbol{J}_0^{(\mathrm{O})}$, which is found by proceeding to next order in equations (3.20) to (3.28), whence we obtain the following problem

$$\frac{1}{r}\frac{\partial}{\partial r}\left(r\boldsymbol{J}_0^{(\mathrm{O})}\cdot\boldsymbol{e}_r\right) = 0 \qquad r<\lambda_R \text{ and } r>\lambda_R, \tag{3.45}$$

$$\boldsymbol{J}_0^{(\mathrm{O})} = -\frac{\partial\phi_1^{(\mathrm{O})}}{\partial r}\boldsymbol{e}_r - \frac{\partial\Phi_0^{(\mathrm{O})}}{\partial x}\boldsymbol{e}_x \quad r<\lambda_R, \tag{3.46}$$

$$\boldsymbol{J}_0^{(\mathrm{O})} = -\bar{\sigma}\frac{\partial\phi_1^{(\mathrm{O})}}{\partial r}\boldsymbol{e}_r \qquad r>\lambda_R, \tag{3.47}$$

$$\left[\phi_1^{(\mathrm{O})}\right]_{r=\lambda_R^+}^{r=\lambda_R^-} = \Phi_1^{(\mathrm{O})}(x,t), \tag{3.48}$$

$$\boldsymbol{J}_0^{(\mathrm{O})}\cdot\boldsymbol{e}_r\Big|_{r=\lambda_R^-} = 0, \tag{3.49}$$

$$\phi_1^{(\mathrm{O})} \to 0 \qquad r\to\infty \tag{3.50}$$

where we have substituted in the solution for $\phi_0^{(\mathrm{O})}$ from (3.44). We determine the first order potential from the problem obtained by substituting (3.46) and (3.47) into equation (3.45)

$$\frac{1}{r}\frac{\partial}{\partial r}\left(r\frac{\partial\phi_1^{(\mathrm{O})}}{\partial r}\right) = 0 \qquad r<\lambda_R \text{ and } r>\lambda_R \tag{3.51}$$

The boundary condition in (3.49) can be rewritten as

$$\left.\frac{\partial \phi_1^{(\mathrm{O})}}{\partial r}\right|_{r=\lambda_R^-} = 0 \tag{3.52}$$

which, along with the jump condition in (3.48) determines $\phi_1^{(\mathrm{O})}$ as follows

$$\phi_1^{(\mathrm{O})} = \begin{cases} \Phi_1(x,t) & r < \lambda_R \\ 0 & r > \lambda_R \end{cases}. \tag{3.53}$$

Thus the first order potential in the internodal region is also a function of distance along the axon and time only. Substituting this into equations (3.46) and (3.47) yields

$$\boldsymbol{J}_0^{(\mathrm{O})} = \begin{cases} -\dfrac{\partial \Phi_0^{(\mathrm{O})}}{\partial x}\boldsymbol{e}_x & r < \lambda_R \\ 0 & r > \lambda_R \end{cases}. \tag{3.54}$$

or that the leading order current flows entirely within the axon, and doesn't vary with distance from the axon centre (i.e. $\boldsymbol{J}_0^{(\mathrm{O})} = J_0^{(\mathrm{O})}(x,t)$).

In order to connect the longitudinal current flow in two neighbouring internodal regions, it is necessary to consider the problem at the node between them.

3.3.2 The inner problem about a nodal region

In order to investigate the solution in the nodal region we rescale equations (3.20) to (3.28) to focus on the node, by writing $x = k + \varepsilon\xi$, such that ξ is on the scale of the

node width. This yields the following system

$$\boldsymbol{J} = -\frac{1}{\varepsilon}\frac{\partial \phi}{\partial r}\boldsymbol{e}_r - \frac{1}{\varepsilon}\frac{\partial \phi}{\partial \xi}\boldsymbol{e}_x \qquad r < \lambda_R, \quad (3.55)$$

$$\boldsymbol{J} = -\frac{1}{\varepsilon}\bar{\sigma}\frac{\partial \phi}{\partial r}\boldsymbol{e}_r - \frac{1}{\varepsilon}\bar{\sigma}\frac{\partial \phi}{\partial \xi}\boldsymbol{e}_x \qquad r > \lambda_R, \quad (3.56)$$

$$\frac{1}{\varepsilon}\frac{1}{r}\frac{\partial}{\partial r}\left(rJ_r\right) + \frac{1}{\varepsilon}\frac{\partial}{\partial \xi}\left(J_x\right) = 0 \qquad r < \lambda_R \text{ and } r > \lambda_R, \quad (3.57)$$

$$\left[\phi\right]_{r=\lambda_R^+}^{r=\lambda_R^-} = \Phi\left(\xi, t\right), \quad (3.58)$$

$$\boldsymbol{J}\cdot\boldsymbol{e}_r\big|_{r=\lambda_R^-} = \mathcal{C}\frac{\partial \Phi}{\partial t} + \tilde{j}_N j_N\left(\Phi, t\right) \qquad -1 < \xi < 1, \quad (3.59)$$

$$\boldsymbol{J}\cdot\boldsymbol{e}_r\big|_{r=\lambda_R^-} = \mathcal{C}\tilde{C}_P\left(\xi\right)\frac{\partial \Phi}{\partial t} + \tilde{j}_P\left(\xi\right) j_P\left(\Phi, t\right) \qquad -1-\lambda_P < x < -1$$

$$1 < x < 1+\lambda_P, \quad (3.60)$$

$$\boldsymbol{J}\cdot\boldsymbol{e}_r\big|_{r=\lambda_R^-} = \varepsilon\left(\tilde{C}_I\mathcal{C}\frac{\partial \Phi}{\partial t} + \tilde{j}_I j_I\left(\Phi, t\right)\right) \qquad -\infty < x < -1-\lambda_P$$

$$1+\lambda_P < x < \infty, \quad (3.61)$$

$$\boldsymbol{J}\cdot\boldsymbol{e}_r\big|_{r=\lambda_R^+} = \boldsymbol{J}\cdot\boldsymbol{e}_r\big|_{r=\lambda_R^-} \quad (3.62)$$

$$\phi \to 0 \qquad r \to \infty, \quad (3.63)$$

In this inner region, centred on the node, we expand in powers of ε, as follows

$$\phi = \phi_0^{(\mathrm{i})}\left(\xi, r, t\right) + \varepsilon\phi_1^{(\mathrm{i})}\left(\xi, r, t\right) + \varepsilon^2\phi_2^{(\mathrm{i})}\left(\xi, r, t\right) + \cdots, \quad (3.64)$$

$$\boldsymbol{J} = \boldsymbol{J}_0^{(\mathrm{i})}\left(\xi, r, t\right) + \varepsilon\boldsymbol{J}_1^{(\mathrm{i})}\left(\xi, r, t\right) + \varepsilon^2\boldsymbol{J}_2^{(\mathrm{i})}\left(\xi, r, t\right) + \cdots, \quad (3.65)$$

$$\Phi = \Phi_0^{(\mathrm{i})}\left(\xi, r, t\right) + \varepsilon\Phi_1^{(\mathrm{i})}\left(\xi, r, t\right) + \varepsilon^2\Phi_2^{(\mathrm{i})}\left(\xi, r, t\right) + \cdots, \quad (3.66)$$

$$j = j_0^{(\mathrm{i})}\left(\xi, r, t\right) + \varepsilon j_1^{(\mathrm{i})}\left(\xi, r, t\right) + \varepsilon^2 j_2^{(\mathrm{i})}\left(\xi, r, t\right) + \cdots, \quad (3.67)$$

3.3.2.1 The leading order inner problem

To leading order the problem in the inner, obtained by substituting the above expansions into equations (3.55) to (3.63) is

$$\frac{\partial \phi_0^{(\mathrm{i})}}{\partial r} = 0, \qquad r < \lambda_R \text{ and } r > \lambda_R, \tag{3.68}$$

$$\frac{\partial \phi_0^{(\mathrm{i})}}{\partial \xi} = 0, \qquad r < \lambda_R \text{ and } r > \lambda_R, \tag{3.69}$$

$$\left[\phi_0^{(\mathrm{i})}\right]_{r=\lambda_R^+}^{r=\lambda_R^-} = \Phi_0^{(\mathrm{i})}, \tag{3.70}$$

$$\phi_0^{(\mathrm{i})} \to 0 \qquad r \to \infty, \tag{3.71}$$

This has solution

$$\phi_0^{(\mathrm{i})} = \begin{cases} \Phi_0^{(\mathrm{i})}(t) & r < \lambda_R \\ 0 & r > \lambda_R \end{cases}. \tag{3.72}$$

That is the leading order transmembrane potential does not vary with position across the width of the entire node and paranodal region, which is a key result for the subsequent analysis in section 3.3.3.

3.3.2.2 The first order inner problem

The problem for the leading order current $\boldsymbol{J}_0^{(\mathrm{i})}$ is obtained by proceeding to first order in the expansions in equations (3.55) to (3.63)

$$\boldsymbol{J}_0^{(\mathrm{i})} = -\frac{\partial \phi_1^{(\mathrm{i})}}{\partial r}\boldsymbol{e}_r - \frac{\partial \phi_1^{(\mathrm{i})}}{\partial \xi}\boldsymbol{e}_x \qquad r < \lambda_R, \tag{3.73}$$

$$\boldsymbol{J}_0^{(\mathrm{i})} = -\bar{\sigma}\frac{\partial \phi_1^{(\mathrm{i})}}{\partial r}\boldsymbol{e}_r - \bar{\sigma}\frac{\partial \phi_1^{(\mathrm{i})}}{\partial \xi}\boldsymbol{e}_x \qquad r > \lambda_R, \tag{3.74}$$

$$\frac{1}{r}\frac{\partial}{\partial r}\left(r\boldsymbol{J}_0^{(\mathrm{i})}\cdot\boldsymbol{e}_r\right) + \frac{\partial}{\partial \xi}\left(\boldsymbol{J}_0^{(\mathrm{i})}\cdot\boldsymbol{e}_x\right) = 0 \qquad r < \lambda_R \text{ and } r > \lambda_R, \tag{3.75}$$

$$\left[\phi_1^{(\mathrm{i})}\right]_{r=\lambda_R^+}^{r=\lambda_R^-} = \Phi_1^{(\mathrm{i})}, \tag{3.76}$$

$$\boldsymbol{J}_0^{(\mathrm{i})}\cdot\boldsymbol{e}_r\Big|_{r=\lambda_R^-} = \mathcal{C}\frac{\partial \Phi_0^{(\mathrm{i})}}{\partial t} + \tilde{j}_N j_N, \qquad -1 < \xi < 1, \tag{3.77}$$

$$\boldsymbol{J}_0^{(\mathrm{i})}\cdot\boldsymbol{e}_r\Big|_{r=\lambda_R^-} = \mathcal{C}\tilde{C}_P(x)\frac{\partial \Phi_0^{(\mathrm{i})}}{\partial t} + \tilde{j}_P(x)\, j_P \qquad -1-\lambda_P < \xi < -1$$

$$1 < \xi < 1+\lambda_P, \tag{3.78}$$

$$\boldsymbol{J}_0^{(\mathrm{i})}\cdot\boldsymbol{e}_r\Big|_{r=\lambda_R^-} = 0 \qquad -\infty < \xi < -1-\lambda_P$$

$$1+\lambda_P < \xi < \infty, \tag{3.79}$$

$$\boldsymbol{J}_0^{(\mathrm{i})}\cdot\boldsymbol{e}_r\Big|_{r=\lambda_R^-} = \boldsymbol{J}_0^{(\mathrm{i})}\cdot\boldsymbol{e}_r\Big|_{r=\lambda_R^+} \tag{3.80}$$

$$\phi_1^{(\mathrm{i})} \to 0 \qquad r \to \infty, \tag{3.81}$$

3.3.2.3 Matching conditions

We now need to match the leading order solution in the inner to the leading order solution in the outer, which we do using Van Dyke's matching principle. This leads to the following conditions

$$\lim_{\xi\to-\infty}\phi_0^{(\mathrm{i})}(\xi,t) = \lim_{x\to k^-}\phi_0^{(\mathrm{O})}(x,t) \tag{3.82}$$

$$\lim_{\xi\to\infty}\boldsymbol{J}_0^{(\mathrm{i})}(\xi,r,t)\cdot\boldsymbol{e}_x = \lim_{x\to k^+}\boldsymbol{J}_0^{(\mathrm{O})}(x,t)\cdot\boldsymbol{e}_x, \tag{3.83}$$

$$\lim_{\xi\to\infty}\phi_0^{(\mathrm{i})}(\xi,t) = \lim_{x\to k+}\phi_0^{(\mathrm{O})}(x,t), \tag{3.84}$$

$$\lim_{\xi\to-\infty}\boldsymbol{J}_0^{(\mathrm{i})}(\xi,r,t)\cdot\boldsymbol{e}_x = \lim_{x\to k^-}\boldsymbol{J}_0^{(\mathrm{O})}(x,t)\cdot\boldsymbol{e}_x, \tag{3.85}$$

These conditions can be simplified using our solutions for the leading order transmembrane potentials and currents in the internodal region (equations (3.44) and (3.54)) and for the leading order transmembrane potential in the nodal region (equation (3.72)) to obtain

$$\Phi_0^{(\mathrm{i})}(t) = \Phi_0^{(\mathrm{O})}\left(k^+, t\right) \tag{3.86}$$

$$\Phi_0^{(\mathrm{i})}(t) = \Phi_0^{(\mathrm{O})}\left(k^-, t\right), \tag{3.87}$$

$$\lim_{\xi\to\infty} \boldsymbol{J}_0^{(\mathrm{i})}(\xi, r, t)\cdot\boldsymbol{e}_x = J_0^{(\mathrm{O})}\left(k^+, t\right), \tag{3.88}$$

$$\lim_{\xi\to-\infty} \boldsymbol{J}_0^{(\mathrm{i})}(\xi, r, t)\cdot\boldsymbol{e}_x = J_0^{(\mathrm{O})}\left(k^-, t\right), \tag{3.89}$$

3.3.3 Determining the leading order transmembrane potential at the nodes of Ranvier

We relate the leading order currents in the nodal region to the leading order currents in the internodal region by integrating equation (3.75) over the cylindrical volume D shown in figure 3.4, bounded by the surfaces S_1 ($\xi = -L$), S_2 ($\xi = L$) and a surface located at the axon membrane ($r = \lambda_R$). Explicitly, we obtain

$$\int_{\xi=-L}^{\xi=L}\int_{r=0}^{r=\lambda_R}\left(\frac{1}{r}\frac{\partial}{\partial r}\left(r\boldsymbol{J}_0^{(\mathrm{i})}\cdot\boldsymbol{e}_r\right)+\frac{\partial}{\partial\xi}\left(\boldsymbol{J}_0^{(\mathrm{i})}\cdot\boldsymbol{e}_x\right)\right)2\pi r\,dr\,d\xi = \oiint_{\partial D}\boldsymbol{J}_0^{(\mathrm{i})}\cdot\boldsymbol{n}\,dS, \tag{3.90}$$

where the integrand on the left-hand side is the divergence of $\boldsymbol{J}_0^{(\mathrm{i})}$, and implies that the leading order current density is conserved in the volume D. As equation (3.75) determines that the volume integral is zero

$$\oiint_{\partial D}\boldsymbol{J}_0^{(\mathrm{i})}(\xi, r, t)\cdot\boldsymbol{n}\,dS = 0, \tag{3.91}$$

The surface at the axon membrane can now be subdivided to allow for the presence of the nodal, paranodal and internodal membranes (S_3, $S_{4a,b}$ and $S_{5a,b}$ in figure 3.4).

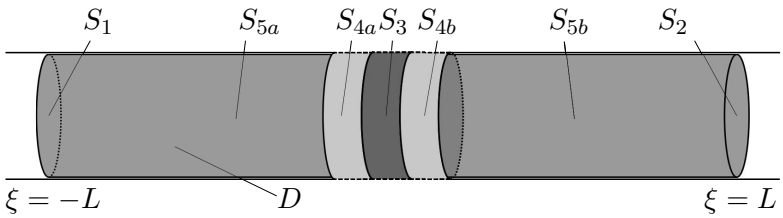

FIGURE 3.4: Volume and surfaces for the application of the divergence theorem in equation (3.90). S_3 is the nodal membrane, $S_{4a,b}$ are the paranodal membranes and $S_{5a,b}$ are the myelinated membranes in the internodes. S_1 and S_2 are cross-sections through the axon normal to the x axis at $\xi = \pm L$.

Dividing the surface integral into its constituent parts yields

$$\begin{aligned}\iint_{S_1} \left(\boldsymbol{J}_0^{(\mathrm{i})}(\xi,r,t)\cdot(-\boldsymbol{e}_x)\right)\Big|_{\xi=-L}\,dS + \iint_{S_2}\left(\boldsymbol{J}_0^{(\mathrm{i})}(\xi,r,t)\cdot\boldsymbol{e}_x\right)\Big|_{\xi=L}\,dS \\ + \left(\iint_{S_3} + \iint_{S_{4a}\cup S_{4b}} + \iint_{S_{5a}\cup S_{5b}}\right)\left(\boldsymbol{J}_0^{(\mathrm{i})}(\xi,r,t)\cdot\boldsymbol{e}_r\right)\Big|_{r=\lambda_R^-}\,dS = 0,\end{aligned} \tag{3.92}$$

We now expand the volume D by taking the limit $L \to \infty$. This allows us to determine the longitudinal current through the surfaces S_1 and S_2 in the inner by matching it to the current in the outer, in the internodal region far from the node. The surface integrals over S_1 and S_2 can thus be rewritten by applying the matching conditions in equations (3.88) and (3.89)

$$\lim_{L\to\infty}\iint_{S_1}\left(\boldsymbol{J}_0^{(\mathrm{i})}(\xi,r,t)\cdot(-\boldsymbol{e}_x)\right)\Big|_{\xi=-L}\,dS = \iint_{S_1} J_0^{(\mathrm{O})}\left(k^+,t\right)\,dS \tag{3.93}$$

$$\lim_{L\to\infty}\iint_{S_2}\left(\boldsymbol{J}_0^{(\mathrm{i})}(\xi,r,t)\cdot\boldsymbol{e}_x\right)\Big|_{\xi=L}\,dS = \iint_{S_2} J_0^{(\mathrm{O})}\left(k^-,t\right)\,dS \tag{3.94}$$

We can substitute the leading order longitudinal current inside the axon in the internodal regions from equation (3.54), where we determined

$$J_0^{(\mathrm{O})}(x,t) = -\frac{\partial}{\partial x}\left(\Phi_0^{(\mathrm{O})}(x,t)\right) \tag{3.95}$$

The leading order current through the nodal membrane (S_3) is given by equation (3.77), the current through the paranodal membranes ($S_{4a,b}$) by equation (3.78) and the current through the internodal membranes ($S_{5a,b}$) by equation (3.79), allowing us to rewrite

equation (3.92) as follows

$$\begin{aligned}\iint_{S_1} \frac{\partial}{\partial x}\left(\Phi_0^{(\mathrm{O})}(x,t)\right)\Big|_{x=k^-} dS - \iint_{S_2} \frac{\partial}{\partial x}\left(\Phi_0^{(\mathrm{O})}(x,t)\right)\Big|_{x=k^+} dS \\ + \iint_{S_3} \mathcal{C}\frac{\partial}{\partial t}\left(\Phi_0^{(\mathrm{i})}(t)\right) + \tilde{\jmath}_N j_N\left(\Phi_0^{(\mathrm{i})}(t), t\right) dS \\ + \iint_{S_{4a}\cup S_{4b}} \mathcal{C}\tilde{C}_P(\xi)\frac{\partial}{\partial t}\left(\Phi_0^{(\mathrm{i})}(t)\right) + \tilde{\jmath}_P(\xi)\, j_P\left(\Phi_0^{(\mathrm{i})}(t), t\right) dS + \iint_{S_{5a}\cup S_{5b}} 0\, dS = 0,\end{aligned} \tag{3.96}$$

We now write the integrals with the explicit definitions of the surfaces S_1 to S_4 (and note that S_4 is really comprised of two surfaces, to the left and right of the node), to obtain

$$\begin{aligned}&\int_0^{\lambda_R} \frac{\partial}{\partial x}\left(\Phi_0^{(\mathrm{O})}(x,t)\right)\Big|_{x=k^-} 2\pi r\, dr \\ &- \int_0^{\lambda_R} \frac{\partial}{\partial x}\left(\Phi_0^{(\mathrm{O})}(x,t)\right)\Big|_{x=k^+} 2\pi r\, dr \\ &+ \int_{-1}^{1}\left(\mathcal{C}\frac{\partial}{\partial t}\left(\Phi_0^{(\mathrm{i})}(t)\right) + \tilde{\jmath}_N j_N\left(\Phi_0^{(\mathrm{i})}(t), t\right)\right) 2\pi\lambda_R\, d\xi \\ &+ \int_{-1-\lambda_P}^{-1}\left(\mathcal{C}\tilde{C}_P(\xi)\frac{\partial}{\partial t}\left(\Phi_0^{(\mathrm{i})}(t)\right) + \tilde{\jmath}_P(\xi)\, j_P\left(\Phi_0^{(\mathrm{i})}(t), t\right)\right) 2\pi\lambda_R\, d\xi \\ &+ \int_{1}^{1+\lambda_P}\left(\mathcal{C}\tilde{C}_P(\xi)\frac{\partial}{\partial t}\left(\Phi_0^{(\mathrm{i})}(t)\right) + \tilde{\jmath}_P(\xi)\, j_P\left(\Phi_0^{(\mathrm{i})}(t), t\right)\right) 2\pi\lambda_R\, d\xi = 0,\end{aligned} \tag{3.97}$$

Each of the first three integrands is constant over the domain of integration, so the integration here is trivial. The integral over the paranodal membranes has to account for the variable capacitance and current density, but since the potential is not variable over the paranodal region we simply introduce the notation

$$\bar{C}_P = \frac{\int_1^{1+\lambda_P} \tilde{C}_P(\xi)\, d\xi}{\lambda_P}, \qquad \bar{\jmath}_P = \frac{\int_1^{1+\lambda_P} \tilde{\jmath}_P(\xi)\, d\xi}{\lambda_P}, \tag{3.98}$$

(assuming the properties of the paranodal membranes are symmetrical about the node), such that $\bar{C}_P$ and $\bar{\jmath}_P$ are the averages of $\tilde{C}_P$ and $\tilde{\jmath}_P$ over the paranodal region. The remaining integration is trivial as all other terms in the integrand are constant over the region of integration, and thus we obtain the following condition on the jump in the

derivative of the leading order potential $\Phi_0^{(\mathrm{O})}(x,t)$ across the node

$$\begin{aligned}\pi\lambda_R^2\left(\frac{\partial}{\partial x}\left(\Phi_0^{(\mathrm{O})}(x,t)\right)\Big|_{x=k^-}-\frac{\partial}{\partial x}\left(\Phi_0^{(\mathrm{O})}(x,t)\right)\Big|_{x=k^+}\right)\\ +4\pi\lambda_R\left(\mathcal{C}\frac{\partial}{\partial t}\left(\Phi_0^{(\mathrm{i})}(t)\right)+\tilde{\jmath}_N j_N\left(\Phi_0^{(\mathrm{i})}(t),t\right)\right)\\ +4\pi\lambda_R\lambda_P\left(\mathcal{C}\bar{C}_P\frac{\partial}{\partial t}\left(\Phi_0^{(\mathrm{i})}(t)\right)+\bar{\jmath}_P j_P\left(\Phi_0^{(\mathrm{i})}(t),t\right)\right)=0,\end{aligned}\tag{3.99}$$

which can be rearranged to give the following relationship between the transmembrane potentials in the inner and the outer

$$\begin{aligned}\left(1+\lambda_P\bar{C}_P\right)\mathcal{C}\frac{\partial}{\partial t}\left(\Phi_0^{(\mathrm{i})}(t)\right)=\frac{\lambda_R}{4}\left(\frac{\partial}{\partial x}\left(\Phi_0^{(\mathrm{O})}(x,t)\right)\Big|_{x=k^+}-\frac{\partial}{\partial x}\left(\Phi_0^{(\mathrm{O})}(x,t)\right)\Big|_{x=k^-}\right)\\ -\tilde{\jmath}_N j_N\left(\Phi_0^{(\mathrm{i})}(t),t\right)-\lambda_P\bar{\jmath}_P j_P\left(\Phi_0^{(\mathrm{i})}(t),t\right),\end{aligned}\tag{3.100}$$

Substituting for $\Phi_0^{(\mathrm{i})}(t)$ from equation (3.86) gives

$$\begin{aligned}\left(1+\lambda_P\bar{C}_P\right)\mathcal{C}\left.\frac{\partial}{\partial t}\left(\Phi_0^{(\mathrm{O})}(x,t)\right)\right|_{x=k}=\frac{\lambda_R}{4}\left(\left.\frac{\partial}{\partial x}\left(\Phi_0^{(\mathrm{O})}(x,t)\right)\right|_{x=k^+}-\left.\frac{\partial}{\partial x}\left(\Phi_0^{(\mathrm{O})}(x,t)\right)\right|_{x=k^-}\right)\\ -\tilde{\jmath}_N j_N\left(\Phi_0^{(\mathrm{O})}(k,t),t\right)\\ -\lambda_P\bar{\jmath}_P j_P\left(\Phi_0^{(\mathrm{O})}(k,t),t\right),\end{aligned}\tag{3.101}$$

This equation essentially describes conservation of current in the inner region, accounting for the capacitive currents onto the nodal and paranodal membranes and current loss through the ion channels in these regions.

3.3.3.1 The outer, and a solvability condition on $\phi_0^{(\mathrm{O})}(x,t)$

In order to determine an equation for the leading order outer potential $\phi_0^{(\mathrm{O})}(x,t)$, we must proceed to second order in the expansion of equations (3.20) to (3.28), where we

find

$$\frac{1}{r}\frac{\partial}{\partial r}\left(r\boldsymbol{J}_1^{(\mathrm{O})}\cdot\boldsymbol{e}_r\right)+\frac{\partial}{\partial x}\left(\boldsymbol{J}_0^{(\mathrm{O})}\cdot\boldsymbol{e}_x\right)=0 \qquad r<\lambda_R, \quad (3.102)$$

$$\boldsymbol{J}_1^{(\mathrm{O})}=-\frac{\partial\phi_2^{(\mathrm{O})}}{\partial r}\boldsymbol{e}_r-\frac{\partial\phi_1^{(\mathrm{O})}}{\partial x}\boldsymbol{e}_x \qquad r<\lambda_R, \quad (3.103)$$

$$\left[\phi_2^{(\mathrm{O})}\right]_{r=\lambda_R^+}^{r=\lambda_R^-}=\Phi_2^{(\mathrm{O})}(x,t), \quad (3.104)$$

$$\left.\frac{\partial}{\partial r}\left(\phi_2^{(\mathrm{O})}\right)\right|_{r=\lambda_R^-}=-\left(\tilde{C}_I\mathcal{C}\frac{\partial}{\partial t}\left(\Phi_0^{(\mathrm{O})}(x,t)\right)+\tilde{\jmath}_I j_I\left(\Phi_0^{(\mathrm{O})}(x,t),t\right)\right), \quad (3.105)$$

$$\phi_2^{(\mathrm{O})}\to 0 \qquad r\to\infty \quad (3.106)$$

Substituting the solution for $\boldsymbol{J}_0^{(\mathrm{O})}$ from equation (3.54) (i.e. $\boldsymbol{J}_0^{(\mathrm{O})}=-\frac{\partial}{\partial x}\left(\Phi_0^{(\mathrm{O})}(x,t)\right)\boldsymbol{e}_x$ for $r<\lambda_R$) into equation (3.102) and integrating once with respect to r yields

$$\frac{\partial\phi_2^{(\mathrm{O})}}{\partial r}=-\frac{r}{2}\frac{\partial^2}{\partial x^2}\left(\Phi_0^{(\mathrm{O})}(x,t)\right)+\frac{c_1(x,t)}{r} \quad (3.107)$$

The boundary condition at $r=\lambda_R$ (equation (3.105)) determines the function $c_1(x,t)$ as

$$c_1(x,t)=\frac{\lambda_R^2}{2}\frac{\partial^2}{\partial x^2}\left(\Phi_0^{(\mathrm{O})}(x,t)\right)-\lambda_R\left(\tilde{C}_I\mathcal{C}\frac{\partial}{\partial t}\left(\Phi_0^{(\mathrm{O})}(x,t)\right)+\tilde{\jmath}_I j_I\left(\Phi_0^{(\mathrm{O})}(x,t),t\right)\right). \quad (3.108)$$

Integrating equation (3.107) with respect to r yields the following expression for $\phi_2^{(\mathrm{O})}$:

$$\phi_2^{(\mathrm{O})}=c_1(x,t)\ln(r)-\frac{r^2}{4}\frac{\partial^2}{\partial x^2}\left(\Phi_0^{(\mathrm{O})}(x,t)\right)+c_2, \quad (3.109)$$

In order to avoid the unphysical logarithmic singularity in the potential at $r=0$, we require that $c_1(x,t)\equiv 0$, that is

$$\tilde{C}_I\mathcal{C}\frac{\partial}{\partial t}\left(\Phi_0^{(\mathrm{O})}(x,t)\right)=\frac{\lambda_R}{2}\frac{\partial^2}{\partial x^2}\left(\Phi_0^{(\mathrm{O})}(x,t)\right)-\tilde{\jmath}_I j_I\left(\Phi_0^{(\mathrm{O})}(x,t),t\right). \quad (3.110)$$

This tells us that the leading order transmembrane potential in the internodal regions obeys the above diffusion equation in which the sink term $-\tilde{\jmath}_I j_I\left(\Phi_0^{(\mathrm{O})}(x,t),t\right)$ represents current flowing out through the myelinated membrane.

3.3.4 A model of the leading order transmembrane potential

We now have sufficient equations to determine the leading order transmembrane potential $\Phi_0(x,t)$. To summarise, equations (3.101) and (3.110) give the following system for $\Phi_0^{(\mathrm{O})}(x,t)$ which, on dropping the sub- and superscripts, takes the form

$$\begin{aligned}\left(1+\lambda_P\bar{C}_P\right)\mathcal{C}\left.\frac{\partial\Phi}{\partial t}\right|_{x=k} &= \frac{\lambda_R}{4}\left(\left.\frac{\partial\Phi}{\partial x}\right|_{x=k^+} - \left.\frac{\partial\Phi}{\partial x}\right|_{x=k^-}\right) \\ &\quad - \tilde{\jmath}_N j_N\left(\Phi(k,t),t\right) - \lambda_P\bar{\jmath}_P j_P\left(\Phi(k,t),t\right),\end{aligned} \tag{3.111}$$

$$\tilde{C}_I\mathcal{C}\frac{\partial\Phi}{\partial t} = \frac{\lambda_R}{2}\frac{\partial^2\Phi}{\partial x^2} - \tilde{\jmath}_I j_I(\Phi,t) \tag{3.112}$$

So we have the diffusion equation in each of the myelinated regions, with jump conditions at the nodes that couple the solution in each myelinated region to its neighbours.

3.3.5 The case with small membrane currents

Let us consider the case where the transmembrane capacitive currents are small, being of size $O\left(\delta^2\right)$ in the dimensionless model, where $\delta \ll 1$. This is equivalent to the distinguished limit in which the parameters $\mathcal{C}$, $\tilde{\jmath}_N$, $\bar{\jmath}_P$ and $\tilde{\jmath}_I$ are all $O\left(\delta^2\right)$, which motivates us to rewrite them in the form

$$\mathcal{C} = \delta^2\hat{\mathcal{C}}, \qquad \tilde{\jmath}_N = \delta^2\hat{\jmath}_N, \qquad \bar{\jmath}_P = \delta^2\hat{\jmath}_P, \qquad \tilde{\jmath}_I = \delta^2\hat{\jmath}_I \tag{3.113}$$

Equations (3.111) and (3.112) are then rewritten as follows

$$\begin{aligned}\left(1+\lambda_P\bar{C}_P\right)\delta^2\hat{\mathcal{C}}\left.\frac{\partial\Phi}{\partial t}\right|_{x=k} &= \frac{\lambda_R}{4}\left(\left.\frac{\partial\Phi}{\partial x}\right|_{x=k^+} - \left.\frac{\partial\Phi}{\partial x}\right|_{x=k^-}\right) \\ &\quad - \delta^2\left(\hat{\jmath}_N j_N\left(\Phi(k,t),t\right) + \lambda_P\hat{\jmath}_P j_P\left(\Phi(k,t),t\right)\right),\end{aligned} \tag{3.114}$$

$$\delta^2\tilde{C}_I\hat{\mathcal{C}}\frac{\partial\Phi}{\partial t} = \frac{\lambda_R}{2}\frac{\partial^2\Phi}{\partial x^2} - \delta^2\hat{\jmath}_I j_I(\Phi,t) \tag{3.115}$$

In this limit, we expect the transmembrane potential Φ to vary slowly along the axon, as the transmembrane currents which influence Φ are small. We make the ansatz $\Phi = \Phi(\eta,t)$, where $\eta = \delta x$ is a length scale much longer than the internodal separation, the size of which is determined by the size of the capacitive and transmembrane currents

(which are $O\left(\delta^2\right)$). It follows that Φ is only changed significantly by the capacitive and transmembrane currents in many nodal and internodal regions.

Substituting this ansatz into equations (3.114) and (3.115) and making the change of variables $\eta = \delta x$ yields the following system, which holds on the long length scale

$$\left(1+\lambda_P \bar{C}_P\right) \delta^2 \hat{\mathcal{C}} \left.\frac{\partial}{\partial t}\left(\Phi\left(\eta,t\right)\right)\right|_{\eta=\delta k} = \frac{\delta \lambda_R}{4}\left(\left.\frac{\partial}{\partial \eta}\left(\Phi\left(\eta,t\right)\right)\right|_{\eta=\delta k^+} - \left.\frac{\partial}{\partial \eta}\left(\Phi\left(\eta,t\right)\right)\right|_{\eta=\delta k^-}\right) - \delta^2\left(\hat{\jmath}_N j_N\left(\Phi\left(\delta k,t\right),t\right) + \lambda_p \hat{\jmath}_P j_P\left(\Phi\left(\delta k,t\right),t\right)\right) \tag{3.116}$$

$$\delta^2 \frac{\partial^2}{\partial \eta^2}\left(\Phi\left(\eta,t\right)\right) = \delta^2 \frac{2}{\lambda_R}\left(\tilde{C}_I \hat{\mathcal{C}} \frac{\partial}{\partial t}\left(\Phi\left(\eta,t\right)\right) + \hat{\jmath}_I j_I\left(\Phi\left(\eta,t\right),t\right)\right), \tag{3.117}$$

In order to simplify these equations, we integrate equation (3.117) across the single internodal region $\delta k < \eta < \delta\left(k+1\right)$

$$\int_{\delta k}^{\delta(k+1)} \frac{\partial^2}{\partial \eta^2}\left(\Phi\left(\eta,t\right)\right)\, d\eta = \frac{2}{\lambda_R}\int_{\delta k}^{\delta(k+1)} \tilde{C}_I \hat{\mathcal{C}} \frac{\partial}{\partial t}\left(\Phi\left(\eta,t\right)\right) + \hat{\jmath}_I j_I\left(\Phi\left(\eta,t\right),t\right)\, d\eta, \tag{3.118}$$

The integrand on the right-hand side is approximately constant over the domain of integration, since our ansatz for Φ implies that it does not change significantly over the scale of the internodal separation; thus we obtain

$$\left.\frac{\partial \Phi}{\partial \eta}\right|_{\eta=\delta k^+} = \left.\frac{\partial \Phi}{\partial \eta}\right|_{\eta=\delta(k+1)^-} - \delta \frac{2}{\lambda_R}\left(\tilde{C}_I \hat{\mathcal{C}} \left.\frac{\partial}{\partial t}\left(\Phi\left(\eta,t\right)\right)\right|_{\eta=\delta k} + \hat{\jmath}_I j_I\left(\Phi\left(\delta k,t\right),t\right)\right) \tag{3.119}$$

Similarly, by integrating over the internodal region $\delta\left(k-1\right) < \eta < \delta k$, we obtain

$$\left.\frac{\partial \Phi}{\partial \eta}\right|_{\eta=\delta k^-} = \left.\frac{\partial \Phi}{\partial \eta}\right|_{\eta=\delta(k-1)^+} + \delta \frac{2}{\lambda_R}\left(\tilde{C}_I \hat{\mathcal{C}} \left.\frac{\partial}{\partial t}\left(\Phi\left(\eta,t\right)\right)\right|_{\eta=\delta k} + \hat{\jmath}_I j_I\left(\Phi\left(\delta k,t\right),t\right)\right) \tag{3.120}$$

These two expressions can now be substituted into equation (3.116) to obtain a single equation for $\Phi(\eta,t)$, the transmembrane potential on the long length scale

$$\begin{aligned}\left(1+\lambda_P\bar{C}_P\right)\hat{\mathcal{C}}\left.\frac{\partial}{\partial t}\left(\Phi\left(\eta,t\right)\right)\right|_{\eta=\delta k} = \quad & \frac{\lambda_R}{4\delta}\left(\left.\frac{\partial}{\partial\eta}\left(\Phi\left(\eta,t\right)\right)\right|_{\eta=\delta(k+1)^-} - \left.\frac{\partial}{\partial\eta}\left(\Phi\left(\eta,t\right)\right)\right|_{\eta=\delta(k-1)^+}\right) \\ & - \left(\tilde{C}_I\hat{\mathcal{C}}\left.\frac{\partial}{\partial t}\left(\Phi\left(\eta,t\right)\right)\right|_{\eta=\delta k} + \hat{\jmath}_I j_I\left(\Phi\left(\delta k,t\right),t\right)\right) \\ & - \left(\hat{\jmath}_N j_N\left(\Phi\left(\delta k,t\right),t\right) + \lambda_P\hat{\jmath}_P j_P\left(\Phi\left(\delta k,t\right),t\right)\right)\end{aligned} \tag{3.121}$$

In the limit $\delta\to 0$, we can use the definition of the second derivative to rewrite

$$\frac{\left(\left.\frac{\partial}{\partial\eta}\left(\Phi\left(\eta,t\right)\right)\right|_{\eta=\delta(k+1)^-} - \left.\frac{\partial}{\partial\eta}\left(\Phi\left(\eta,t\right)\right)\right|_{\eta=\delta(k-1)^+}\right)}{2\delta} = \left.\frac{\partial^2}{\partial\eta^2}\left(\Phi\left(\eta,t\right)\right)\right|_{\eta=\delta k} \tag{3.122}$$

Rearranging the above to collect the time derivatives leaves

$$\begin{aligned}\left(1+\lambda_P\bar{C}_P+\tilde{C}_I\right)\hat{\mathcal{C}}\left.\frac{\partial}{\partial t}\left(\Phi\left(\eta,t\right)\right)\right|_{\eta=\delta k} = \frac{\lambda_R}{2}\left.\frac{\partial^2}{\partial\eta^2}\left(\Phi\left(\eta,t\right)\right)\right|_{\eta=\delta k} & - \hat{\jmath}_N j_N\left(\Phi\left(\delta k,t\right),t\right) \\ & - \lambda_P\hat{\jmath}_P j_P\left(\Phi\left(\delta k,t\right),t\right) - \hat{\jmath}_I j_I\left(\Phi\left(\delta k,t\right),t\right)\end{aligned} \tag{3.123}$$

The point $\eta=\delta k$ is arbitrary, so we write the following equation for the transmembrane potential on the long length scale

$$\left(1+\lambda_P\bar{C}_P+\tilde{C}_I\right)\hat{\mathcal{C}}\frac{\partial\Phi}{\partial t} = \frac{\lambda_R}{2}\frac{\partial^2\Phi}{\partial\eta^2} - \hat{\jmath}_N j_N\left(\Phi,t\right) - \lambda_P\hat{\jmath}_P j_P\left(\Phi,t\right) - \hat{\jmath}_I j_I\left(\Phi,t\right) \tag{3.124}$$

which shows that for small enough membrane currents, the behaviour of the myelinated axon is determined by the cable equation, just as the behaviour of the unmyelinated axon is. However, the equation holds on the long length-scale, η, which accounts for the increase in signalling speed seen in myelinated neurons. We note that this form of the cable equation is the same as that derived by Basser [7], which was obtained by homegenisation of a model comprised of two cable equations describing the nodal and internodal behaviours, although our formulation includes the influence of a paranodal region.

Referring to our estimates of parameter sizes in section 3.2.1.1, we see that for short internodal distances ($L_I \approx 10^{-4}$, which is the lower end of the range given in table 3.1), $\mathcal{C} \approx 10^{-2}$ and $\tilde{\jmath}_I \approx 10^{-3}$, so the assumption that these parameters are $O\left(\delta^2\right)$ where $\delta \ll 1$ is reasonable. However, $\tilde{\jmath}_N \approx 0.3$ and $\tilde{\jmath}_P \approx 0.1$ are significantly larger, requiring $\delta \approx 0.5$. We note that the values of $\tilde{\jmath}_N$ and $\tilde{\jmath}_P$ are obtained from g_{Na} and g_{K}, the maximal conductance per unit area of the cell membrane to sodium and potassium ions respectively, which is appropriate during the transmission of an action potential when large proportions of these ion channels are open. For small membrane depolarisations, where the full action potential cycle is not initiated and many ion channels remain closed, the actual conductances per unit area may be much less than g_{Na} and g_{K} and thus the characteristic transmembrane currents will be much smaller than $\tilde{\jmath}_N$ and $\tilde{\jmath}_P$. This model, then, is certainly a good approximation to the passive behaviour of axons with closely spaced nodes (i.e. when the transmembrane potential is sufficiently close to resting potential that no action potentials are initiated), but we expect it to break down as the internodal separation increases, and when a large proportion of the ion channels in the cell membrane are open, as would be the case during an action potential. However, in section 3.5.1 we compare numerical solutions of the full system (in equations (3.111) and (3.112)) to the simplified form where the transmembrane currents are small (in equation (3.124)) and note that under much of the range of parameters in table 3.1 the two show good agreement even during action potential propagation.

3.4 Special cases

The form of our model permits simplification or modification to account for several special cases.

3.4.1 The case with no paranodal regions

We note that in the simple case $\lambda_P = 0$, equations (3.111) and (3.112) can be simplified to

$$\mathcal{C}\left.\frac{\partial \Phi}{\partial t}\right|_{x=k} = \frac{\lambda_R}{4}\left(\left.\frac{\partial \Phi}{\partial x}\right|_{x=k^+} - \left.\frac{\partial \Phi}{\partial x}\right|_{x=k^-}\right) - \tilde{j}_N j_N\left(\Phi\left(k,t\right),t\right), \tag{3.125}$$

$$\tilde{C}_I \mathcal{C}\frac{\partial \Phi}{\partial t} = \frac{\lambda_R}{2}\frac{\partial^2 \Phi}{\partial x^2} - \tilde{j}_I j_I\left(\Phi,t\right) \tag{3.126}$$

which is the same model we would have derived had we initially just considered the nodal and internodal membrane and ignored the paranode altogether. We note that the model without paranodes is identical to the one with, under the effective node size and ion channel currents given below

$$C_N L_N^{\text{eff}} = C_N L_N + \int_{L_N}^{L_N+L_P} C_P\left(x^*\right)\, dx^*, \tag{3.127}$$

$$L_N^{\text{eff}} j_N^{*\,\text{eff}}\left(\Phi^*,t^*\right) = L_N j_N^*\left(\Phi^*,t^*\right) + \int_{L_N}^{L_N+L_P} j_P^*\left(\Phi^*,x^*,t^*\right)\, dx^* \tag{3.128}$$

whence it is easy to see that the effective node size and current density are chosen by ensuring that the total capacitance of and current through the effective nodal region is equal to the combined capacitance of and current through the actual nodal and paranodal regions. Thus the introduction of the paranodal region has no qualitative effect of the behaviour of the model, but instead simply modifies the properties of the node.

3.4.2 The case with idealised internodal membrane

In the case of perfectly insulating myelin with no capacitance (i.e. $j_I^* = 0$ and $C_I = 0$), the equation governing the transmembrane potential in the internodal region $m-1 < x < m$ simplifies to

$$\frac{\lambda_R}{2}\frac{\partial^2 \Phi}{\partial x^2} = 0, \tag{3.129}$$

thus, by integrating over the internodal region we find

$$\frac{\partial \Phi}{\partial x} = \Phi(k,t) - \Phi(k-1,t) \tag{3.130}$$

or that the potential is linear in the internodal region and therefore the gradient is constant, determined by the potential at the nodes at either end. In this case we can write $\Phi_k = \Phi(k,t)$ and the full problem can be simplified to

$$\mathcal{C}\frac{\partial \Phi_k}{\partial t} = \frac{\lambda_R}{4}\left(\Phi_{k+1} - 2\Phi_k + \Phi_{k-1}\right) - \tilde{j}_N j_N\left(\Phi_k, t\right), \tag{3.131}$$

where the spatial derivatives in the problem have been eliminated to leave us with a single difference equation describing $\{\Phi_i(t)\}$ the transmembrane potentials at the nodes.

This is the same form as the model written down by McNeal [57], which has subsequently been used by others [87, 111, 114]. The more systematic nature of our approach allows us to show exactly the simplifying assumptions that must hold in order for this model to be appropriate, as well as providing a more general model to use when it is not.

In section 3.5.2 we compare this simplified form of the model to the full model in equations (3.111) and (3.112), and find that, for the parameter ranges in table 3.1, the capacitance of the myelinated membrane in the internodal regions has a significant impact on the behaviour of the axon. Key to understanding this point is the dimensionless parameter $\tilde{C}_I$, which is the ratio of the total capacitance of the membrane in an internodal region to that in the nodal region. Although the capacitance per unit area of the internodal membrane, C_I, is small compared to that of the nodal membrane, C_N, the area of the internodal region is larger than that of the node by almost the same proportion (the internodal capacitance per unit area is around one thousand times smaller than that at the node and the internodal separation is around one thousand times larger than the width of a node) and thus the total capacitances are of the same order of magnitude ($\tilde{C}_I \approx 1$). For small values of $\tilde{C}_I$ ($\tilde{C}_I \ll 1$), equation (3.129) is a valid approximation to equation (3.112), but clearly this is not the case for $\tilde{C}_1 = O(1)$.

3.4.3 Demyelination

Certain neurological diseases (particularly multiple sclerosis, but many other conditions have a similar effect) are characterised by the myelin sheath degrading and peeling back from the node of Ranvier [56]. Two types of demyelination are shown in figure 3.5. In the first the myelin sheath appears to stay roughly in tact, but its structure is disrupted such that it no longer forms a neat, concentric spiral around the axon. In the second the myelin is stripped away from the axon entirely by cells of the immune system. In section 3.5.3 we explore the effects of these two kinds of demyelination.

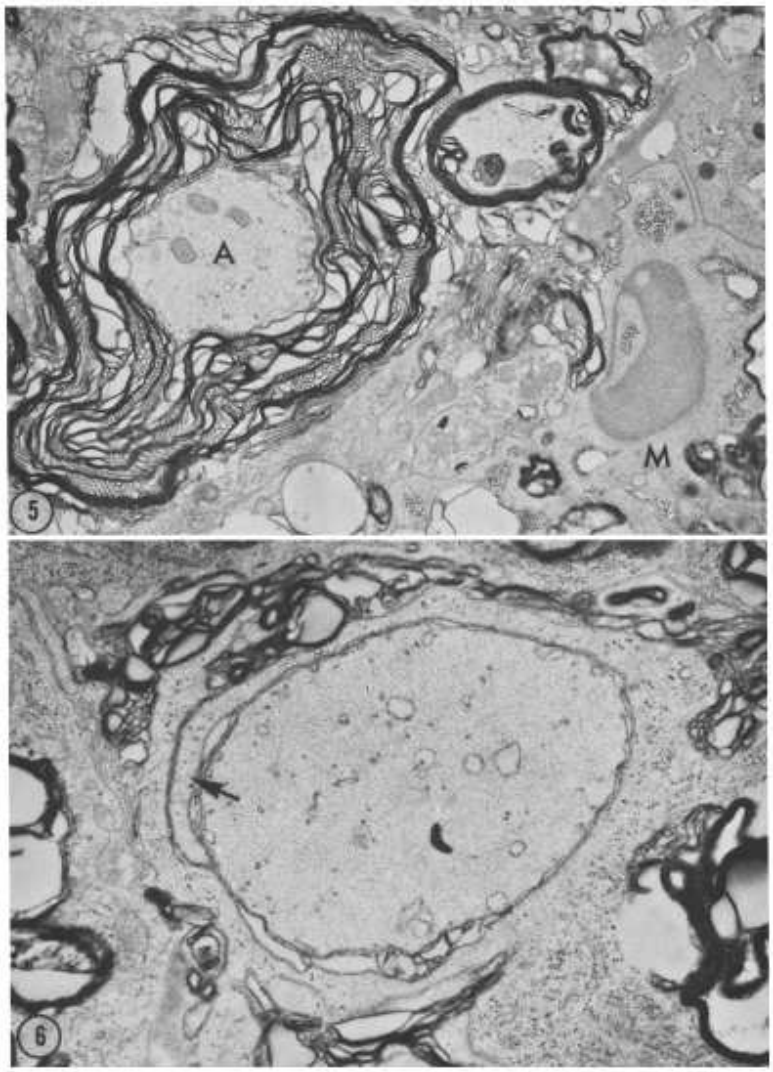

FIGURE 3.5: Two forms of demyelinated axons. In the upper panel the myelin sheath is peeling off the axon (A) in layers, in the lower it has been stripped by the immune system. ©Wisniewski and Bloom, 1975. Originally published in J. Exp. Med. doi:10.1084/jem.141.2.346.

In order to model demyelination, we assume that changes in the capacitance and leak conductance per unit area of the internodal membranes can be accounted for simply by changing the sizes of the parameters C_I and g_{L} in the internodal regions. As long as these parameters remain small compared to the capacitance and conductance per unit area of the nodal membrane this will not affect the analysis of the problem.

When the myelin is destroyed or degraded near the node of Ranvier, however, the underlying cell membrane will be exposed, which has a significantly higher capacitance per unit area. In order to account for this we modify the surface integrals in equation (3.90) to include a new, demyelinated region. We let the myelin peel back from the nodes by a distance L_D from the edges of the node of Ranvier, and let the newly exposed membrane have a capacitance per unit area of C_D and a current density j_D^*. There are two possible cases here, where the extent of the demyelination is less than or greater than the size of the paranodal region ($L_D < L_P$ and $L_D > L_P$), which we have to treat differently in order to correctly determine the capacitance of the node, paranode and demyelinated region.

If $L_D < L_P$, part of the paranodal region is demyelinated, and will have a capacitance per unit area of C_D because the underlying cell membrane at the paranode has been exposed, but the remainder will retain its original capacitance of $\tilde{C}_P(\xi)$. The conductance per unit area of the paranodal region is unchanged throughout, as the ion channels are still present. The surface integrals in equation (3.90) are redefined in this case as follows

$$\begin{aligned}
&\int_0^{\lambda_R} \frac{\partial}{\partial x}\left(\Phi_0^{(\mathrm{O})}(x,t)\right)\Big|_{x=k^-} 2\pi r\,dr \\
&-\int_0^{\lambda_R} \frac{\partial}{\partial x}\left(\Phi_0^{(\mathrm{O})}(x,t)\right)\Big|_{x=k^+} 2\pi r\,dr \\
&+\int_{-1}^{1}\left(\mathcal{C}\frac{\partial}{\partial t}\left(\Phi_0^{(\mathrm{i})}(t)\right)+\tilde{j}_N j_N\left(\Phi_0^{(\mathrm{i})}(t),t\right)\right)2\pi\lambda_R\,d\xi \\
&+2\int_1^{1+\lambda_D}\left(\mathcal{C}\tilde{C}_D\frac{\partial}{\partial t}\left(\Phi_0^{(\mathrm{i})}(t)\right)+\tilde{j}_P(\xi)\,j_P\left(\Phi_0^{(\mathrm{i})}(t),t\right)\right)2\pi\lambda_R\,d\xi \\
&+2\int_{1+\lambda_D}^{1+\lambda_P}\left(\mathcal{C}\tilde{C}_P(\xi)\frac{\partial}{\partial t}\left(\Phi_0^{(\mathrm{i})}(t)\right)+\tilde{j}_P(\xi)\,j_P\left(\Phi_0^{(\mathrm{i})}(t),t\right)\right)2\pi\lambda_R\,d\xi=0, \qquad (3.132)
\end{aligned}$$

where we have defined the following dimensionless parameters

$$\lambda_D = \frac{L_D}{L_N}, \qquad \tilde{C}_D = \frac{C_D}{C_N}, \qquad \tilde{\jmath}_D = \frac{g_D L_I}{\sigma} \tag{3.133}$$

where g_D is the conductance per unit area of the demyelinated membrane. We also define

$$\bar{C}_{P,D} = \frac{\int_{1+\lambda_D}^{1+\lambda_P} \tilde{C}_P(\xi)\, d\xi}{\lambda_P - \lambda_D} \tag{3.134}$$

such that $\bar{C}_{P,D}$ is the average capacitance per unit area of the remaining paranodal membrane. This modifies equations (3.111) and (3.112) to

$$\begin{aligned}\left(1 + (\lambda_P - \lambda_D)\bar{C}_{P,D} + \lambda_D \tilde{C}_D\right)\mathcal{C}\left.\frac{\partial \Phi}{\partial t}\right|_{x=k} = \frac{\lambda_R}{4}\left(\left.\frac{\partial \Phi}{\partial x}\right|_{x=k^+} - \left.\frac{\partial \Phi}{\partial x}\right|_{x=k^-}\right) \\ -\tilde{\jmath}_N j_N(\Phi(k,t),t) - \lambda_P \bar{\jmath}_P j_P(\Phi(k,t),t)\end{aligned} \tag{3.135}$$

If $L_D > L_P$, the entire paranodal region and the demyelinated region will now have a capacitance per unit area of C_D because the underlying cell membrane has been exposed. The conductance per unit area of the paranodal region is again unchanged. In this case, the surface integrals in equation (3.90) are redefined similarly to equation (3.132), except the demyelinated region now extends past the paranodal region, and equations (3.111) and (3.112) are modified to become

$$\begin{aligned}\left(1 + \lambda_D \tilde{C}_D\right)\mathcal{C}\left.\frac{\partial \Phi}{\partial t}\right|_{x=k} = \frac{\lambda_R}{4}\left(\left.\frac{\partial \Phi}{\partial x}\right|_{x=k^+} - \left.\frac{\partial \Phi}{\partial x}\right|_{x=k^-}\right) \\ -\tilde{\jmath}_N j_N(\Phi(k,t),t) - \lambda_P \bar{\jmath}_P j_P(\Phi(k,t),t) \\ -(\lambda_D - \lambda_P)\tilde{\jmath}_D j_D(\Phi(k,t),t)\end{aligned} \tag{3.136}$$

In both cases, the form of the equation in the internodal regions is unchanged, but the parameters are modified to account for the altered properties of the internodal membrane, as follows

$$\tilde{C}_{I,D}\mathcal{C}\frac{\partial \Phi}{\partial t} = \frac{\lambda_R}{2}\frac{\partial^2 \Phi}{\partial x^2} - \tilde{\jmath}_{I,D} j_I(\Phi, t) \tag{3.137}$$

where we define the following dimensionless parameters

$$\tilde{C}_{I,D} = \frac{C_{I,D} L_I}{C_N L_N}, \qquad \tilde{j}_{I,D} = \frac{g_{\mathrm{I,D}} L_I^2}{\sigma L_N} \tag{3.138}$$

where $C_{I,D}$ and $g_{\mathrm{I,D}}$ are the capacitance per unit area and conductance per unit area of the internodal membrane with degraded myelin.

Similarly to equations (3.127) and (3.128), we can derive the following effective node sizes and currents when the demyelination is smaller than the paranodal region ($L_D < L_P$)

$$C_N L_N^{\mathrm{eff}} = C_N L_N + C_D L_D + \int_{L_D}^{L_P} C_P\left(x^*\right)\, dx^*, \tag{3.139}$$

$$L_N^{\mathrm{eff}} j_N^{*\,\mathrm{eff}}\left(\Phi^*, t\right) = L_N j_N^*\left(\Phi, t\right) + \int_{L_N}^{L_N+L_P} j_P^*\left(\Phi^*, x^*, t^*\right)\, dx^* \tag{3.140}$$

and in the case where the demyelination extends beyond the paranodal region ($L_D > L_P$)

$$C_N L_N^{\mathrm{eff}} = C_N L_N + C_D L_D, \tag{3.141}$$

$$L_N^{\mathrm{eff}} j_N^{*\,\mathrm{eff}}\left(\Phi^*, t\right) = L_N j_N^*\left(\Phi, t\right) + \int_{L_N}^{L_N+L_P} j_P^*\left(\Phi^*, x^*, t^*\right)\, dx^* + \left(L_P - L_D\right) j_D^*\left(\Phi^*, t^*\right) \tag{3.142}$$

The current through the demyelinated region is likely to be a small, non-specific leak current, and therefore will act against the sodium channel currents which initiate action potentials. Thus we see that in both cases the demyelination has increased the time constant of the nodal membrane (by increasing its capacitance) without contributing any useful current. If the capacitance of the demyelinated region is large (that is, of the same order of magnitude as the unmyelinated membrane at the node of Ranvier), then the demyelination can increase the time constant of the nodal behaviour by a significant amount, severely slowing down the transmission of the action potential or, in some cases, preventing it altogether (as shown in figures 3.16 and 3.17 — full explanation of these figures is deferred to section 3.5.3, after the full details of the numerical method used for the simulation have been presented).

3.5 Numerical simulations of the model

We now perform numerical simulations of the model in order to explore the influences of different parameters on the behaviour of the axon. To begin, we compare the full model in equations (3.111) and (3.112) with the modified cable equation derived under the assumption that the membrane capacitances and transmembrane currents are small (equation (3.124)) using a range of physiologically relevant parameters found in the literature (table 3.1).

We then compare the full model to the much simpler difference equation model used by McNeal and others, to judge the validity of neglecting the capacitance and conductance of the internodal membrane [57, 87, 111, 114].

Finally, we make a brief exploration of the effects of demyelination, using the form of the model given in equations (3.135) and (3.136).

In all cases, the ion channel currents through the membrane will take the Hodgkin-Huxley form in equations (3.14) to (3.16), but with a different leak conductance per unit area in the internodal region than in the nodal and paranodal regions. Thus the exact forms of the current will be

$$j_N^* = g_{\mathrm{Na}} m^3 h \left(\Phi^* - \Phi_{\mathrm{Na}}\right) + g_{\mathrm{L,N}} \left(\Phi^* - \Phi_{\mathrm{l}}\right), \tag{3.143}$$

$$j_P^* = g_{\mathrm{K}} n^4 \left(\Phi^* - \Phi_{\mathrm{K}}\right) + g_{\mathrm{L,N}} \left(\Phi^* - \Phi_{\mathrm{l}}\right), \tag{3.144}$$

$$j_I^* = g_{\mathrm{L,I}} \left(\Phi^* - \Phi_{\mathrm{l}}\right) \tag{3.145}$$

with $g_{L,N} = 3\,\mathrm{S}\cdot\mathrm{m}^{-2}$ and $g_{\mathrm{L,I}} = 0.015\,\mathrm{S}\cdot\mathrm{m}^{-2}$ chosen according to the values found in the literature (see table 3.1). We have also chosen $g_{\mathrm{K}} = 90\,\mathrm{S}\cdot\mathrm{m}^{-2}$, which is not the value given in table 3.1, because we found during simulations that the potassium currents generated were too large, and were preventing the initiation or transmission of an action potential (potassium currents act to drive the transmembrane potential back towards resting potential). We note that this calibration is probably necessary because the potassium conductances quoted in the literature are derived by adapting the model Hodgkin and Huxley used for the squid axon, not from detailed electrophysiology of

the paranodal region, and are assumed to be be present over the same area as the sodium conductances. In our model the potassium conductances are present over a larger area, and thus should be correspondingly smaller in order for the total potassium and sodium currents to remain in proportion. We also note that previous modelling work has suggested that the exact descriptions of the membrane dynamics is less important than using approximately correct time constants and total conductances [63].

The values we use for $g_{\mathrm{K}}(x^*)$ and $C_P(x^*)$ are now chosen to be constant because we can, as described above in equations (3.98a and b), replace these values with their averages across the paranodal region without affecting the behaviour of the model.

For each of the simulations below, we must increase the transmembrane potential above threshold to initiate an action potential, which we have done by injecting a transient stimulus current to the left-most node in the simulation. We have chosen the Gaussian form given below for this current, although any current that sufficiently increases the transmembrane potential will have the same effect

$$I^*_{\mathrm{stim}}(t^*) = \bar{I} e^{-\left(\frac{t^*-0.0015}{0.0005}\right)^2} \tag{3.146}$$

3.5.1 Comparisons between the full model and the simplified case with small capacitances and transmembrane currents

Figures 3.7 and 3.8 compare the transmission of an action potential in the full model with jump condition (equations (3.111) and (3.112)) and in the modified cable equation model (equation (3.124)). The shapes of the propagating action potentials, shown in figure 3.8, are similar but not identical, and the speeds of transmission ($2.229\,\mathrm{m}\cdot\mathrm{s}^{-1}$ in the full case and $1.996\,\mathrm{m}\cdot\mathrm{s}^{-1}$ in the simplified) differ by around ten percent. The exact parameters used for this simulation are taken from table 3.1, where a single value is given, or chosen from roughly the middle of the range, if a range is given. The parameters we have chosen from a range are given in table 3.2. With these parameter values, the parameter δ described in section 3.3.5, which defines the long length-scale for equation (3.124), is around 0.85, and clearly the modified cable equation approximation is not valid for all physiological cases.

We note that the exact numerical values of the speeds reported here are closely related to the specific parameter set we have chosen but the qualitative relationship between the two models is maintained across the range of parameters (at least, those which do not determine the size of δ). To tie the behaviour of the model to experimental data, we note that if we use the exact parameter set given in [63] (which is in turn derived from the experimental work in [33]) then the speed predicted by the full model with jump condition (equations (3.111) and (3.112)) is $9.209\,\mathrm{m{\cdot}s^{-1}}$, which compares favourably with the value of $9.5\,\mathrm{m\cdot s^{-1}}$ cited in [34] and [63], and fits within the range of experimentally measured speeds found in [33]. It is also notable that with these parameters the cable equation model (equation (3.124)) predicts a speed of $7.684\,\mathrm{m{\cdot}s^{-1}}$, a significant difference of seventeen percent from the full model's prediction.

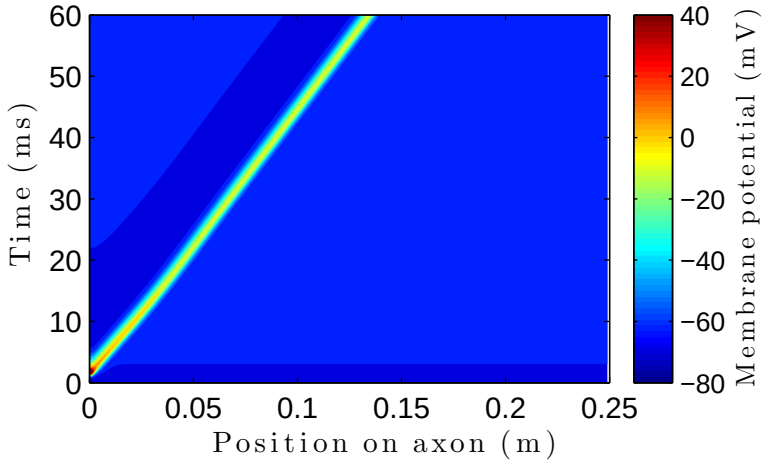

FIGURE 3.6: Action potential transmission in the full model (equations (3.111) and (3.112)), with parameters from tables 3.1 and 3.2, as described in the text. The transmembrane potential is raised on the left by injecting a stimulus current, and an action potential is initiated and propagates to the right.

TABLE 3.2: Parameters to produce figures 3.6 to 3.8, 3.12 and 3.13

Parameter	Value	Unit
R	1×10^{-6}	m
L_N	1×10^{-6}	m
L_I	1×10^{-3}	m
C_P	5×10^{-5}	$\mathrm{F \cdot m^{-2}}$

Figures 3.10 to 3.11 compare equivalent simulations with a smaller internodal separation ($L_I = 10^{-4}\,\mathrm{m}$, see tables 3.1 and 3.3 for remaining parameters). The shapes of the propagating action potentials, shown in figure 3.11, are now essentially identical, and

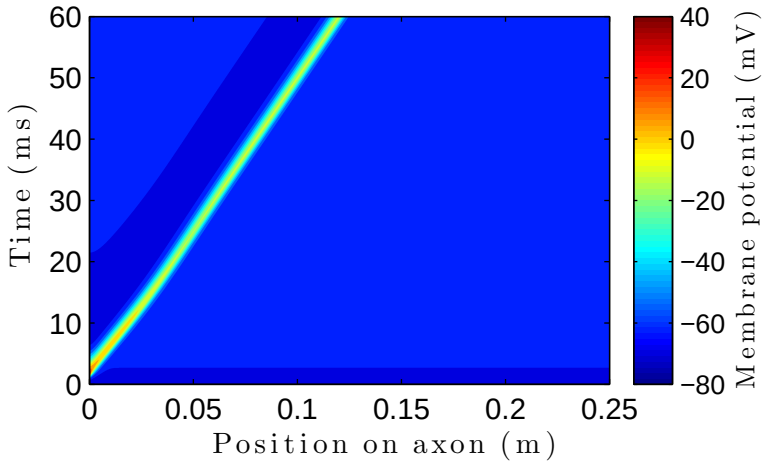

FIGURE 3.7: Action potential transmission in the modified cable equation model (equation (3.124)), with parameters from tables 3.1 and 3.2, as described in the text. The transmembrane potential is raised on the left by injecting a stimulus current, and an action potential is initiated and propagates to the right.

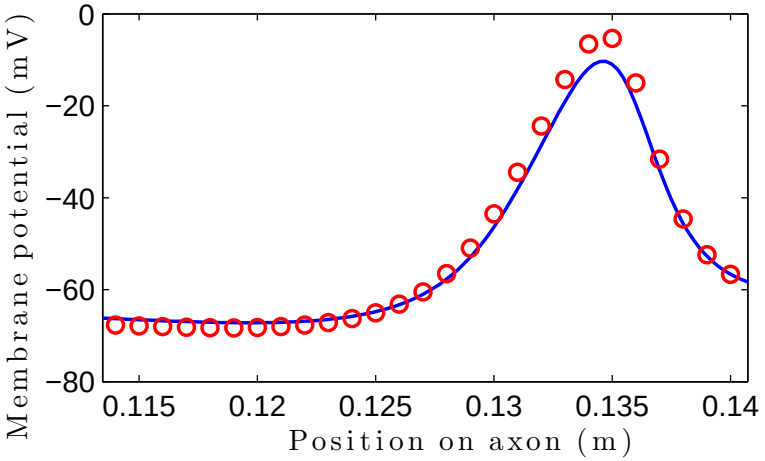

FIGURE 3.8: The transmembrane potential in the axon during action potential propagation with parameters from tables 3.1 and 3.2, as described in the text. The transmembrane potential predicted at the nodes by the full model (red circles) is compared to that predicted throughout the axon by the modified cable equation (blue curve). The difference between the two models is noticeable for this set of parameters but, as noted in the text, does not result in significantly different predictions of transmission speeds.

the speeds of transmission ($1.204\,\mathrm{m\cdot s^{-1}}$ in the full case and $1.178\,\mathrm{m\cdot s^{-1}}$ in the simplified) differ only by around one percent. With the parameter values chosen, $\delta \approx 0.27$ and it appears that the modified cable equation is a valid approximation to make.

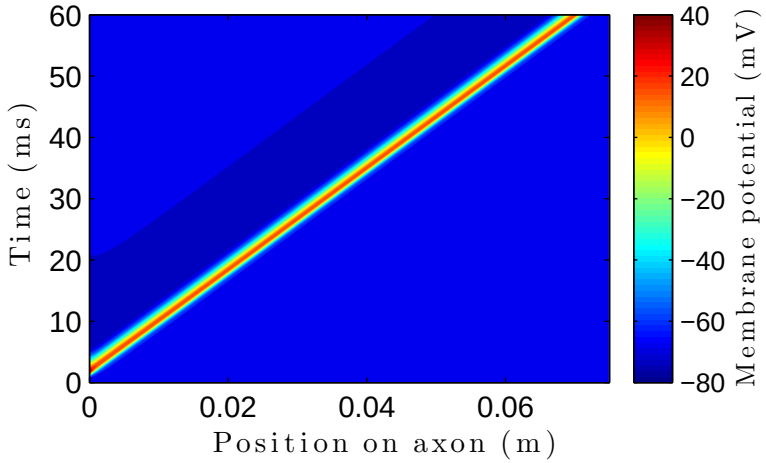

FIGURE 3.9: Action potential transmission in the full model (equations (3.111) and (3.112)), with parameters from tables 3.1 and 3.3, as described in the text. The transmembrane potential is raised on the left by injecting a stimulus current, and an action potential is initiated and propagates to the right.

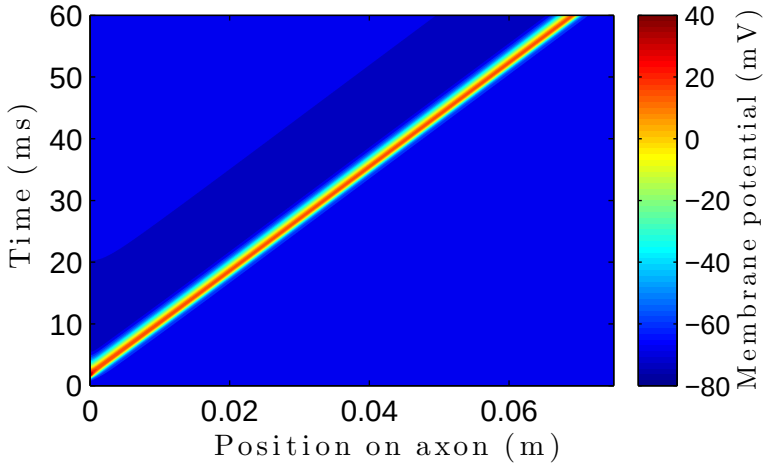

FIGURE 3.10: Action potential transmission in the modified cable equation model (equation (3.124)), with parameters from tables 3.1 and 3.3, as described in the text. The transmembrane potential is raised on the left by injecting a stimulus current, and an action potential is initiated and propagates to the right.

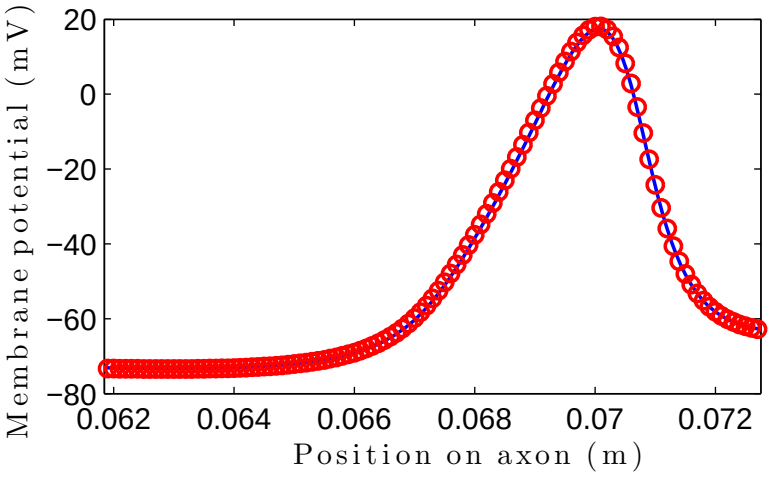

FIGURE 3.11: The transmembrane potential in the axon during action potential propagation with parameters from tables 3.1 and 3.3, as described in the text. The transmembrane potential predicted at the nodes by the full model (red circles) is compared to that predicted throughout the axon by the modified cable equation (blue curve). The difference between the two models is negligible for this set of parameters.

TABLE 3.3: Parameters to produce figures 3.10 and 3.11

Parameter	Value	Unit
R	1×10^{-6}	m
L_N	1×10^{-6}	m
L_I	1×10^{-4}	m
C_P	5×10^{-5}	$\mathrm{F \cdot m^{-2}}$

3.5.2 The effects of capacitance and transmembrane currents in the internodal regions

Figures 3.12 and 3.13 show the transmission of an action potential in the difference equation model (equation (3.131)) derived under the idealisation of the internodal membrane where its capacitance and leak conductance per unit area are negligible. The parameters used are those taken from the middle of the ranges in table 3.1 (given in tables 3.1 and 3.2). This is the same physical case as that in figures 3.6 and 3.7), and comparison of the transmembrane potential in the axon during the simulation shows that idealising the internodal membrane has a significant effect on the size and shape of the action potential. The speed of transmission of the action potential in the model with idealised internodal membrane is $4.053\,\mathrm{m \cdot s^{-1}}$, compared to $2.229\,\mathrm{m \cdot s^{-1}}$ from the full model in figure 3.6, which is a very significant difference.

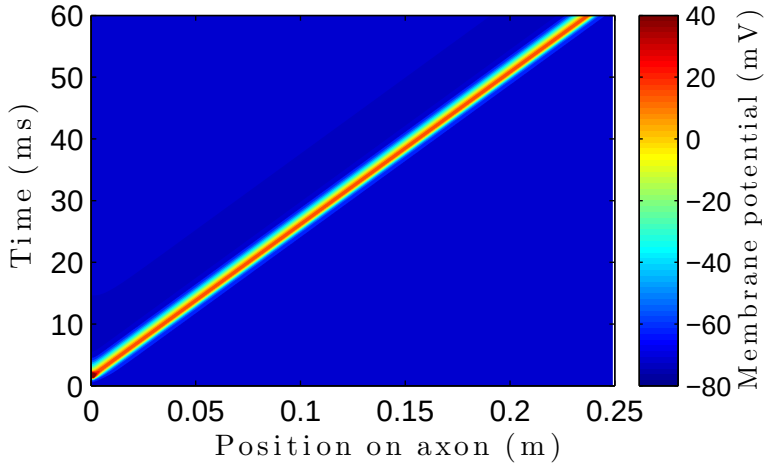

FIGURE 3.12: Action potential transmission in the difference equation model (equation (3.131)), with parameters from tables 3.1 and 3.2, as described in the text. The transmembrane potential is raised on the left by injecting a stimulus current, and an action potential is initiated and propagates to the right.

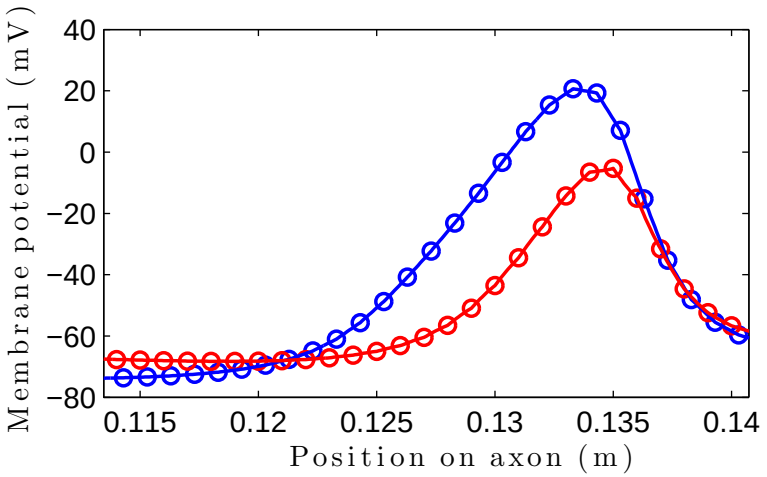

FIGURE 3.13: The transmembrane potential in the axon during action potential propagation with parameters from tables 3.1 and 3.2, as described in the text. The transmembrane potential predicted at the nodes by the full model (red circles) is compared to that predicted throughout the axon by the modified cable equation (blue curve). The difference between the two models is pronounced for this set of parameters.

Figures 3.14 and 3.15 again show the transmission of an action potential in the model with idealised internodal membrane (equation (3.131)), but with a small internodal separation (tables 3.1 and 3.3). This is the same physical case as that in figures 3.9 and 3.10), and in this case comparison of the transmembrane potential in the axon during the simulation shows much better agreement between the two models. However, the speed of transmission of the action potential in the model with idealised internodal membrane is $1.293\,\mathrm{m}\cdot\mathrm{s}^{-1}$, compared to $1.204\,\mathrm{m}\cdot\mathrm{s}^{-1}$ from the full model in figure 3.6, which is still

a difference of around seven percent. As mentioned in section 3.4.2, we note that the idealised internodal membrane simplification relies on $\tilde{C}_I \ll 1$ and $\tilde{j}_I \ll 1$ and although in this case the parameters we have chosen give values of $\tilde{C}_I \approx 0.1$ and $\tilde{j}_I \approx 0.01$, it would appear that these are not small enough for a good approximation. In order to find transmission speeds that agree to one percent, it is necessary to reduce $\tilde{C}_I$ and $\tilde{j}_I$ by a factor of ten (i.e. $\tilde{C}_I \approx 0.01$, $\tilde{j}_I \approx 0.001$), which requires either the capacitance per unit area and leak conductance per unit area of the internodal membrane or the internodal separation to be significantly less than values quoted in the literature.

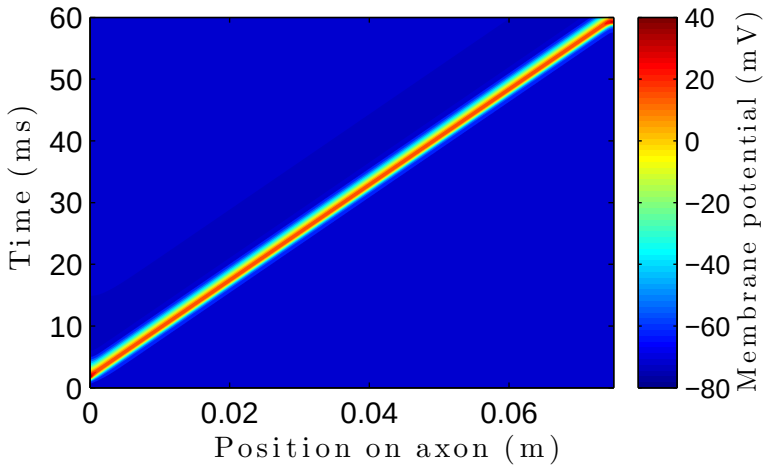

FIGURE 3.14: Action potential transmission in the difference equation model (equation (3.131)), with parameters from tables 3.1 and 3.2, as described in the text. The transmembrane potential is raised on the left by injecting a stimulus current, and an action potential is initiated and propagates to the right.

3.5.3 The effects of demyelination

Figures 3.16 and 3.17 show the effects of demyelination on signal transmission. We solve equations (3.136) and (3.137) and change the amount of demyelination (the value of L_D) at the point $x^* = 0.1\,\mathrm{m}$. In this way we simulate a signal propagating from a healthy axon, with no damage to the myelin sheath ($L_D = 0$), into a region of demyelination where the myelin sheath has retreated from the nodes of Ranvier, either by a distance of $5\,\mu\mathrm{m}$ (figure 3.16, $L_D = 5\times10^{-6}\,\mathrm{m}$) or $10\,\mu\mathrm{m}$ (figure 3.17, $L_D = 10\times10^{-6}\,\mathrm{m}$). We choose the capacitance per unit area of the demyelinated membrane to be $C_D = 5\times10^{-3}\mathrm{F}\cdot\mathrm{m}^{-2}$, such that it is significantly larger that of the internodal membrane but less than that

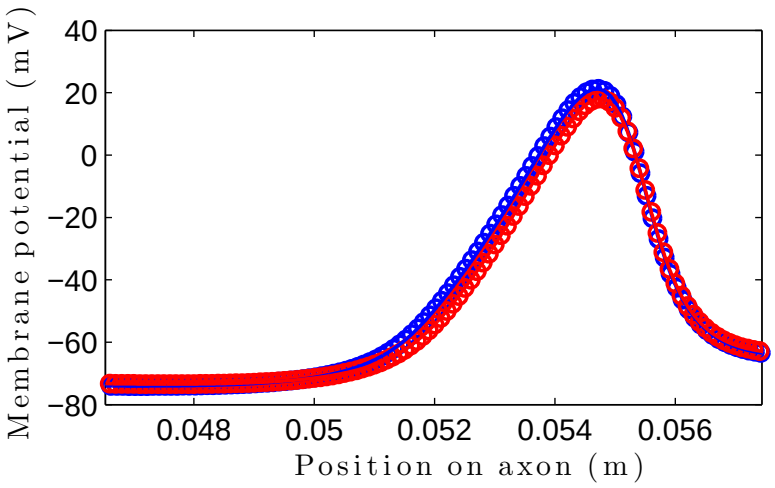

FIGURE 3.15: The transmembrane potential in the axon during action potential propagation with parameters from tables 3.1 and 3.2, as described in the text. The transmembrane potential predicted at the nodes by the full model (red circles) is compared to that predicted throughout the axon by the modified cable equation (blue curve). The difference between the two models is much smaller for this set of parameters than for that with larger internodal separation, but still noticeable.

of the nodal membrane — we do not expect the capacitance per unit area of the demyelinated membrane to be as large as that of the nodal membrane, as the influence of the myelin sheath is unlikely to be totally removed from these areas, even if much of the myelin is destroyed. For the purposes of this comparison, we have not changed the capacitance per unit area or the leak conductance per unit area of the internodal membrane.

The axon in the region $x^* < 0.1\,\mathrm{m}$ is identical to that in figure 3.6, and the signal propagates at the same speed of $2.229\,\mathrm{m}\cdot\mathrm{s}^{-1}$. In figure 3.16, with a smaller demyelinated region, the action potential is maintained, but the speed of propagation is slowed to $1.370\,\mathrm{m}\cdot\mathrm{s}^{-1}$, whereas in figure 3.17, with larger demyelinated regions, the signal is blocked completely.

Figures 3.18 and 3.19 show the effects of different types of demyelination on the propagation speeds of action potentials. In figure 3.18 we increase the size of the demyelinated region at the node, to simulate the myelin sheath peeling back and uncovering a progressively larger area of cell membrane to contribute to the capacitance of the node. This causes the action potential to propagate more slowly before, eventually, blocking its propagation altogether. The extent of the demyelination can be quite large (around

ten times the width of the node of Ranvier, or around twice the width of the paranodal region) before the signal is blocked. In figure 3.19 we increase the capacitance per unit area of the internodal membrane, to simulate the effects of degradation of the entire myelin sheath. This again causes the action potential to propagate more slowly and eventually fail, but we note that we can only increase the capacitance per unit area of the internodal range by a factor of two before the action potential is blocked.

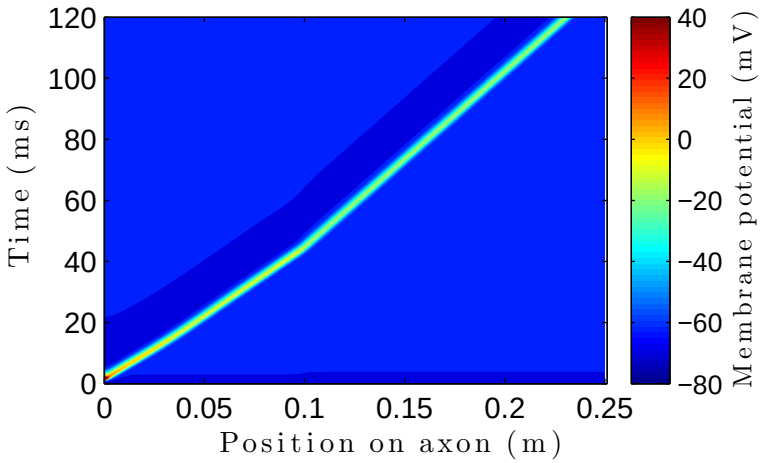

FIGURE 3.16: An action potential propagating from a healthy axon, with no demyelination ($x^* < 0.1\,\text{m}$) into an area where the myelin sheath has retreated from the nodes by $5\,\mu\text{m}$ ($x^* > 0.1\,\text{m}$). The action potential is maintained in the demyelinated region, but propagates more slowly. Parameters are given in tables 3.1 and 3.4.

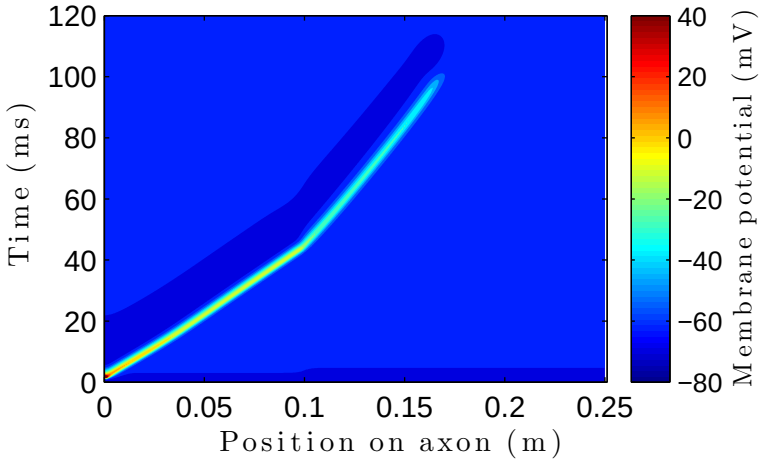

FIGURE 3.17: An action potential propagating from a healthy axon, with no demyelination ($x^* < 0.1\,\text{m}$) into an area where the myelin sheath has retreated from the nodes by $10\,\mu\text{m}$ ($x^* > 0.1\,\text{m}$). The action potential does not propagate into the demyelinated region. Parameters are given in tables 3.1 and 3.4.

TABLE 3.4: Parameters to produce figures 3.16 and 3.17

Parameter	Value	Unit
R	1×10^{-6}	m
L_N	1×10^{-6}	m
L_I	1×10^{-3}	m
L_D ($x^* < 0.1$, figures 3.16 and 3.17)	0	m
L_D ($x^* > 0.1$, figures 3.16)	5×10^{-6}	m
L_D ($x^* > 0.1$, figures 3.17)	10×10^{-6}	m
C_P	5×10^{-5}	$\mathrm{F \cdot m^{-2}}$
C_D	5×10^{-3}	$\mathrm{F \cdot m^{-2}}$
$C_{I,D}$	5×10^{-5}	$\mathrm{F \cdot m^{-2}}$
$g_{\mathrm{I,D}}$	0.0089	$\mathrm{S \cdot m^{-2}}$

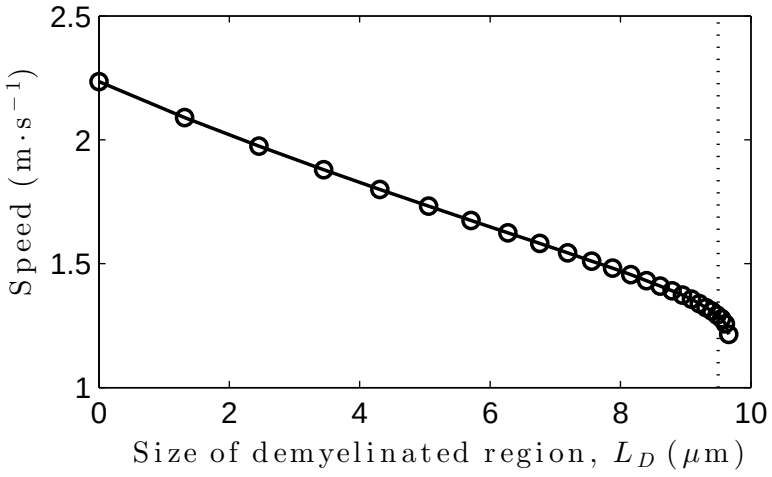

FIGURE 3.18: Propagation speeds of action potentials against size of demyelinated region. The speed decreases linearly with the amount of demyelination, up to the dashed vertical line ($L_D \approx 9.5\,\mu$m for this set of parameters — the same trend holds for other parameter choices but the value of L_D will vary) and beyond this value, the speed of propagation drops rapidly to zero. We note, however, that beyond this value (to the right of the dashed line) the action potentials propagate for a long time, but do fail eventually. Parameters are taken from tables 3.1 and 3.5.

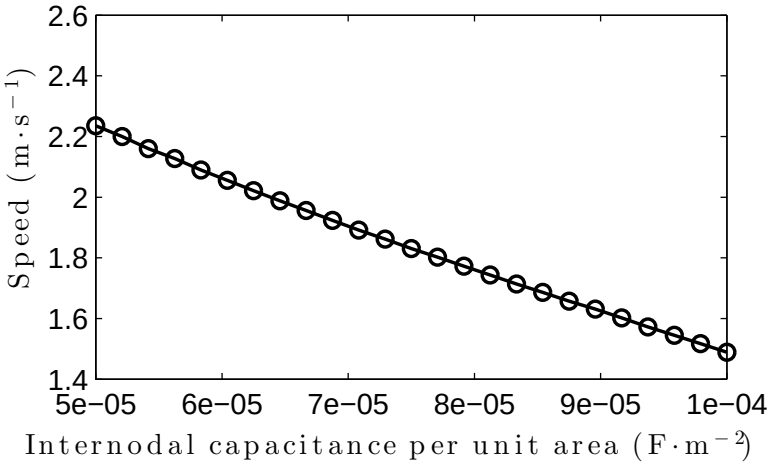

FIGURE 3.19: Propagation speed decreases as internodal capacitance per unit area increases. Parameters are taken from tables 3.1 and 3.5 but with no demyelination at the nodes (i.e. $L_D = 0$). For internodal capacitance per unit area larger than $10^{-4}\,\mathrm{F}\cdot\mathrm{m}^{-2}$, propagation fails for this parameter set.

TABLE 3.5: Parameters to produce figure 3.18

Parameter	Value	Unit
R	1×10^{-6}	m
L_N	1×10^{-6}	m
L_I	1×10^{-3}	m
L_D	$0 - 10 \times 10^{-6}$	m
C_P	5×10^{-5}	$\mathrm{F}\cdot\mathrm{m}^{-2}$
C_D	5×10^{-3}	$\mathrm{F}\cdot\mathrm{m}^{-2}$
$C_{I,D}$	5×10^{-5}	$\mathrm{F}\cdot\mathrm{m}^{-2}$
$g_{\mathrm{I,D}}$	0.0089	$\mathrm{S}\cdot\mathrm{m}^{-2}$

3.6 Discussion

We have systematically derived a model of the myelinated axon from a generic description of its electrochemical behaviour and a simplified description of its geometry, producing a model which predicts action potential propagation speeds in line with those found in experimental data. This modelling work shows that models of the myelinated axon can be significantly simplified by noting that the leading-order transmembrane potential does not vary spatially on the scale of a node of Ranvier and the paranodal regions. This allows spatial variations in properties such as ion channel density and capacitance to be modelled simply by replacing them with an appropriate (constant) average value found by integrating over the region and dividing by its surface area. We propose that this explains why previous modelling work (Moore *et al.*, for example [63]) has found that precise descriptions of the ion channel dynamics in the nodal region have less impact on the behaviour of models than choices of time constants and total conductances — variations in ion channel behaviour or density on the scale of a node only contribute to the behaviour of the axon if they change the average behaviour of the ion channels.

More significantly, this demonstrates that no qualitatively different behaviour can be produced in a model with paranodal regions than one without. Equations (3.127) and (3.128) show how to construct an axon with only nodal regions which is equivalent to one with paranodal regions included. This principle holds not just for the case of nodal and paranodal regions, but more generally for any model of the node of Ranvier, with any number of different regions and even for the demyelinated axon. Provided the size of the regions is small compared to the internodal separation it will be possible to build an equivalent model containing only nodal and internodal regions. We suggest that this could partly simplify complex models of the myelinated axon, such as that presented in [73], which represents three separate regions at the node of Ranvier.

As an axon with strongly segregated nodal and paranodal regions is, apparently, equivalent to one without, it is natural to ask why such clear segregation exists in the first place. It has been suggested that the density of sodium channels at the node of Ranvier

is close to the theoretical maximum [90], and thus there is no space in which to insert potassium channels to repolarise the cell during the action potential cycle. Increasing the size of the node is ineffective, as this also increases the capacitance of the membrane and thus increases the size of the current required to depolarise it, resulting in no net gain. However, equations (3.127) and (3.128) show that the paranode can increase the effective current through the node without significantly increasing the effective capacitance (i.e. if C_P is small, then $C_N L_N^{\text{eff}} \approx C_N L_N$ but $L_N^{\text{eff}} j_N^{*\,\text{eff}} = L_N j_N^* + L_P j_P^*$). This allows the potassium channels in the paranode to repolarise the membrane without the capacitance of the paranode significantly increasing the time constant of the membrane's response to the sodium current. Thus we suggest that the paranodes are simply a response to the physical limits on current density at the node of Ranvier, which explains their existence despite their apparent lack of influence on the axon's behaviour.

We also note that the presence of the myelin sheath at the paranodes is likely to interfere with the action of the ion channels in this region — current must flow through the ion channels and then either through the myelin sheath or through a very narrow space between the axon and the myelin sheath. This added resistance may make the ion channels in the paranodal region less effective, yielding a smaller current density through the same number of ion channels. If this is the case, it is appropriate that the potassium channels should be in the paranodal region and the sodium channels in the node — the sodium channels depolarise the membrane, which needs to happen quickly to maintain propagation speeds, whereas the potassium channels repolarise the membrane over a longer time scale and as such are not required to produce such large current densities.

Demyelination, by contrast, has almost the exact opposite effect to that of the paranodes. Instead of increasing the current through the node without increasing the capacitance, demyelinated regions increase the capacitance without contributing any useful current (if j_D^* is small, or at least acts against action potential initiation, then $C_N L_N^{\text{eff}} = C_N L_N + C_D L_D$ but $L_N^{\text{eff}} j_N^{*\,\text{eff}} \approx L_N j_N^*$). This is what slows the response of the demyelinated axon (and prevents action potential propagation altogether in some cases).

We also note the size discrepancy between the nodes of Ranvier and the internodes can amplify the effect of demyelination. Increasing the node size by a factor of two

or three slows propagation slightly but is unlikely to actually block signals. However, demyelinating on the order of just one percent of the internodal region (which can be around a millimetre long) can increase the size of the node by a factor of ten — because the internode is so much bigger, relatively small effects on the internodal scale can be very large on the scale of the node of Ranvier. This means that only relatively small proportions of the myelin sheath have to be damaged before the effects are felt on signal propagation.

The effects of increasing the capacitance per unit area of the internodal membrane (figure 3.19) suggest that the action potential is not very robust to degradation of the myelin sheath, with only small increases in the capacitance per unit area causing the action potential to fail. Studies in the literature have found, however, that action potentials can propagate to a certain extent in entirely demyelinated axons, albeit at much reduced speeds [23]. If the demyelination takes the form seen in the top panel of figure 3.5, then we suggest that the capacitance per unit area of the internodal membrane must still be significantly lowered by the presence of the myelin sheath, even if its structure has been somewhat disrupted. Other studies have found, in some cases, that active ion channels are in fact present in the internodal membrane in small numbers, and this may be enough to overcome the increased capacitance caused by demyelination [13].

Chapter 4

Modelling the electrochemical behaviour of the Bergmann glial cell

4.1 Introduction

The Bergmann glial cell, named for Karl Bergmann (1814–1865), is found in the cerebellum. It plays many roles in the correct functioning of this region of the brain, many of which are not fully understood [110].

The cerebellum is the region of the brain associated with motor control and coordination [28, 104]. Its principal features are two types of neurons — Purkinje cells, neurons with many branches in their dendrons (see figure 4.1), and parallel fibres, straighter neurons that cross the Purkinje cells at right-angles. These two types of cell are intricately interconnected by thousands of junctions called synapses (see section 4.1.2), each of which is enclosed by part of a Bergmann glial cell [52, 65].

One role that Bergmann glial cells certainly play is in the normal development of the cerebellum, where they form a kind of scaffolding to direct the growth of neurons [82, 113]. We will not consider this role further however, focussing instead on the electrical roles of mature glia.

FIGURE 4.1: A Purkinje cell stained with fluorescent dye, showing the branching structure. Each branch will form many synapses (there can be hundreds of thousands of synapses on one Purkinje cell [52]), and each synapse will be enclosed by a Bergmann glial cell. © Priller *et al.* , 2001. Originally published in J. Cell. Biol. doi: 10.1083/jcb.200105103

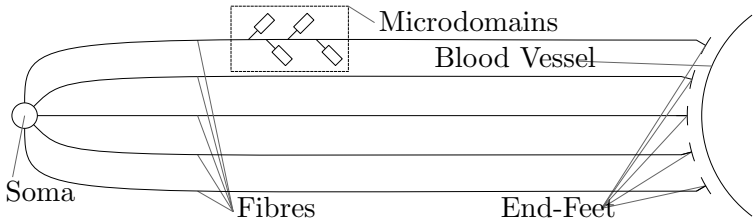

FIGURE 4.2: Simplified geometry of a Bergmann glial cell. The soma is a roughly spherical or ellipsoidal (major axis $O(10)$ μm [77]) body, which contains the nucleus of the cell, and many of the structures necessary for its growth. The fibres extend around 100 to 300 μm from the soma where they widen to a broad, flat area called the end-foot. Intricate structures called microdomains branch from the fibre (as shown in figure 4.3) all along its length, and enclose synapses in large, flat regions (paddles). Ion channels are found in the surfaces of the fibres and the microdomains.

Mature Bergmann glial cells play an ongoing homeostatic role, where they maintain the optimal cerebellar conditions for neural signalling by removing by-products of action potential generation [4]. In addition to this, they are also thought to play a role in modulating communication between neurons, increasing or decreasing the strength of the connections between the Purkinje cells and the parallel fibres according to particular chemical or electrical cues [76].

In this chapter we construct a simple mathematical model of the Bergmann glial cell,

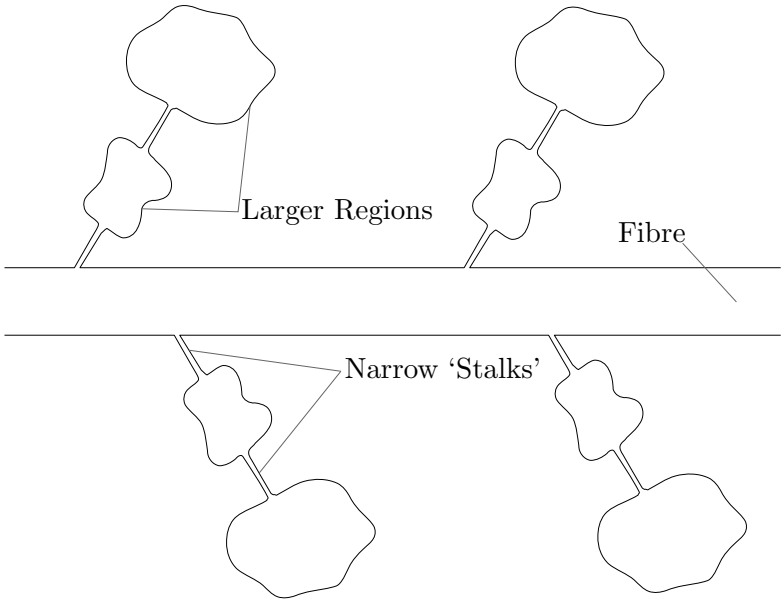

FIGURE 4.3: Detail of microdomains. The large, flat areas which enclose the synapses are connected to the fibre by narrow stalks. The conductivity of the intracellular electrolyte is roughly constant (the concentrations of ions in it do not change significantly), so the resistance of the stalks will be much greater than the wider paddles due to the difference in cross-sectional areas. To distinguish between the two paddles and stalks in each microdomain, we use 'proximal' for those closest to the fibre, and 'distal' for those furthest away. The actual geometry of the microdomain is shown in figure 4.4

FIGURE 4.4: Reconstruction of a microdomain from electron microscopy data [30]. The geometry of the microdomain is extremely convoluted, so certain simplifying assumptions are necessary. Reproduced, with permission, from [30].

which describes its electrical and chemical responses to neuronal activity in the cerebellum. This modelling work was performed in conjunction with experimental work by Tomas Bellamy and Katherine Dobson at the University of Nottingham. Initially, this experimental work was used to inform the development of the model, as described in section 4.2.2.1, where the response of early iterations of the model were qualitatively tested against data collected from real cells, which provided insight into the degree to which the cell's complex structure could be simplified. Quantitative properties of this structure where then extracted from the experimental data, as detailed in section 4.2.4, and used as parameters in the model. Later, the model was used to inform the further experimental work described in section 4.3.1, where data was collected specifically to determine certain properties of the cell, in order to provide estimates for other parameters in the model.

The modelling begins with a simple equivalent circuit model of part of the Bergmann glial cell, and the current flows predicted by this circuit are compared to experimental recordings of current flows in five separate cells. The first iteration of the model is not able to match the qualitative behaviour of the cell seen in experiments, so the model is improved by taking into account more of the cell's structural details. The improved model now compares well with the experimental behaviour, and can be used to extract estimates of the physical parameters of the cell which are not readily accessible by any other means (the results of this process are summarised in section 4.2.4.5, with the full details being given in the preceeding sections).

We then couple this simple equivalent circuit model to a partial differential equation model which captures more of the cell's anatomical details, allowing us to predict the behaviour of the cell under different conditions from those imposed in the first experiments. Further experiments were then designed in Nottingham to reflect these new conditions, with the new model now able to extract more details of the cell from these experiments.

The resulting model now accurately predicts the electric response of the cell, given some information about its structure and physiological properties. We couple this model to the model of ion movements inside the cell (detailed in section 4.4), which allows us to

make quantitative predictions about the fluxes of ions within the cell, and also more qualitative predictions about the cell's function in general.

4.1.1 Structure of the Bergmann glial cell

The Bergmann glial cell is comprised of the soma and five or six long processes (fibres) extending from the soma (the body of the cell) to an 'end-foot', where the fibre widens to a larger area which lies on, or close to, the wall of a blood vessel. The connections between the Purkinje cells and the parallel fibres are found along the lengths of these fibres, where small outgrowths (microdomains) branch from the fibre and expand into large, flat surfaces which surround the synapse. A sketch of the key features of the cell is shown in figure 4.2, with a close up of the microdomains in figure 4.3.

The most obvious aspects of the Bergmann glial cell's morphology (the microdomains and end-foot) seem to be specifically adapted to the functions the cell performs. We will now examine these functions more closely, to try to explain some of these adaptations.

4.1.2 The role of synapses

A synapse is a connection between two neurons, usually where the axon of one connects to a dendron of the other. As shown in figure 4.5, the classical view of the synapse is of two neuronal processes in very close proximity (the gap between them, the synaptic cleft, is around 20nm wide [116]). The end of the pre-synaptic axon contains small vesicles filled with neurotransmitters — chemicals which carry neuronal signals — and the post-synaptic dendron contains ion channels which are activated by these neurotransmitters. Incoming pre-synaptic action potentials cause the vesicles to release their neurotransmitters into the synaptic cleft where they diffuse across to the post-synaptic membrane. The ion channels in this membrane are 'ligand-gated' — they are activated by the presence of a particular chemical — and activate in response to the presence of the neurotransmitter, allowing the passage of sodium ions into the post-synaptic cell and causing the signal to be propagated through the dendron.

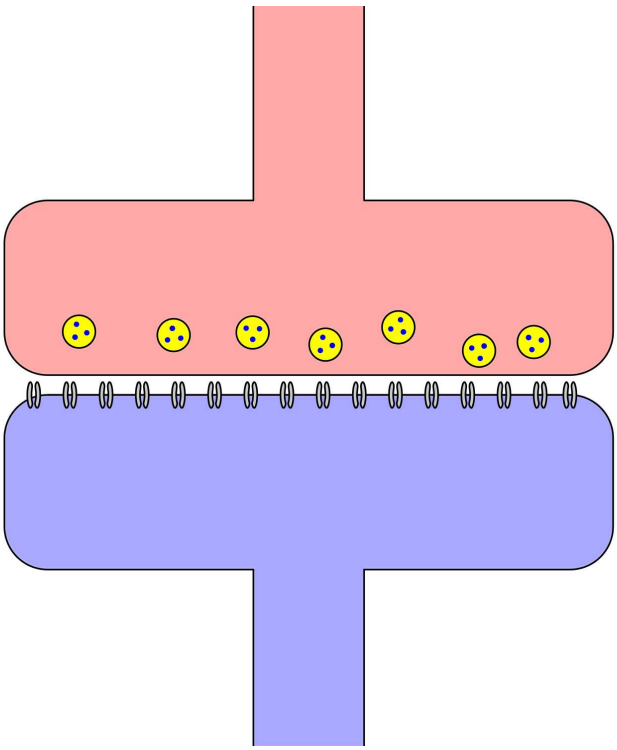

FIGURE 4.5: The classical view of the synapse: incoming signals from the pre-synaptic axon (red) cause vesicles (yellow) containing neurotransmitters to fuse with the cell membrane and release into the synaptic cleft. These neurotransmitters are taken up by ligand-gated ion channels in the dendron (blue), which depolarises and propagates the signal further.

The 'tripartite synapse' is model of synaptic behaviour stemming from the discovery that some synapses are also closely surrounded (again the separation is around 20nm) by a third, glial cell, as seen in figure 4.6 [4, 32]. This cell is not involved in the actual transmission of the signal, but plays some vital roles in the behaviour of the synapse. Firstly, neurotransmitters diffusing out of the synaptic cleft may initiate unwanted signals at nearby synapses, so the glial cell encloses the synapse and takes up the neurotransmitter, allowing it to be usefully recycled and preventing signalling cross-talk. Secondly, the movement of neurotransmitter across the synaptic cleft is driven by diffusion — a relatively slow process, which is why the synaptic cleft needs to be so narrow. A large concentration gradient will increase the speed of the process, so removing the neurotransmitter from the synaptic cleft quickly maintains this concentration gradient for the next signal. The neurotransmitter released at Purkinje/parallel fibre synapses is glutamate, and glutamate transporters are found in high densities in the membranes of Bergmann glia [12, 47, 91]. The uptake of the glutamate into the Bergmann glia relies

on the sodium concentration gradient between the extracellular space and the interior of the microdomain, and thus accumulation of sodium ions in the microdomain will reduce the size of the concentration gradient available to the glutamate transporter, in turn reducing its efficacy [101].

Finally, the glial cell appears to play some role in modulating the synapse, controlling the strength of the connection between the neurons through a collection of chemical signals [4, 32, 76].

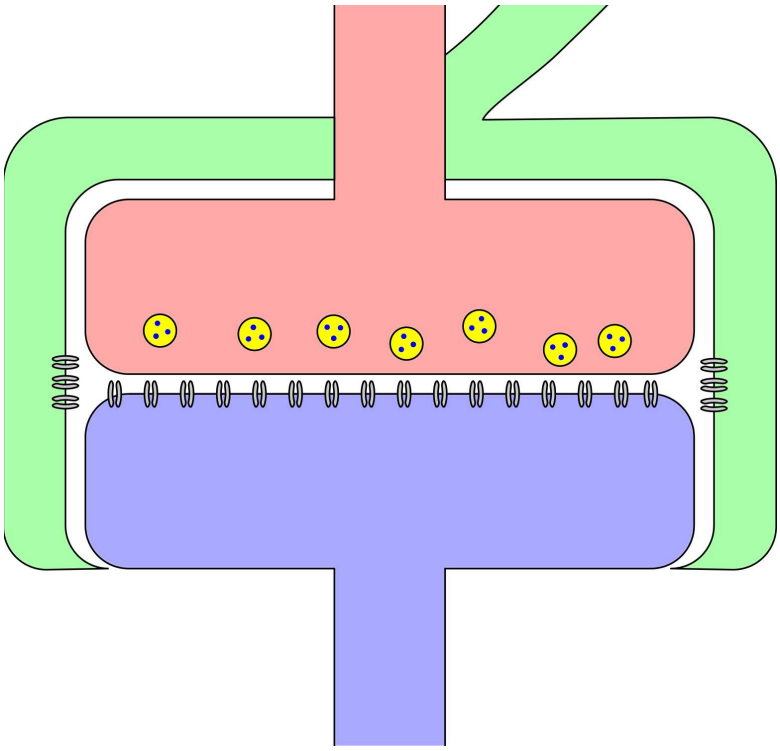

FIGURE 4.6: The tripartite synapse: the signal is passed from the axon to the dendron exactly as before, but the entire synapse is now ensheathed by glial cell. Receptors in the glial membrane mean activity at the synapse can affect glial behaviour.

The microdomains of Bergmann glial cells form the enclosing regions of tripartite synapses (see figure 4.7, reproduced from [30]). The extremely narrow stalk which connects the microdomain to the fibre suggests that the microdomains are effectively electrically isolated, which in theory allows for very fine-grained control of synaptic modulation (i.e. each Bergmann glial cell can independently vary the strengths of hundreds of synapses) [30].

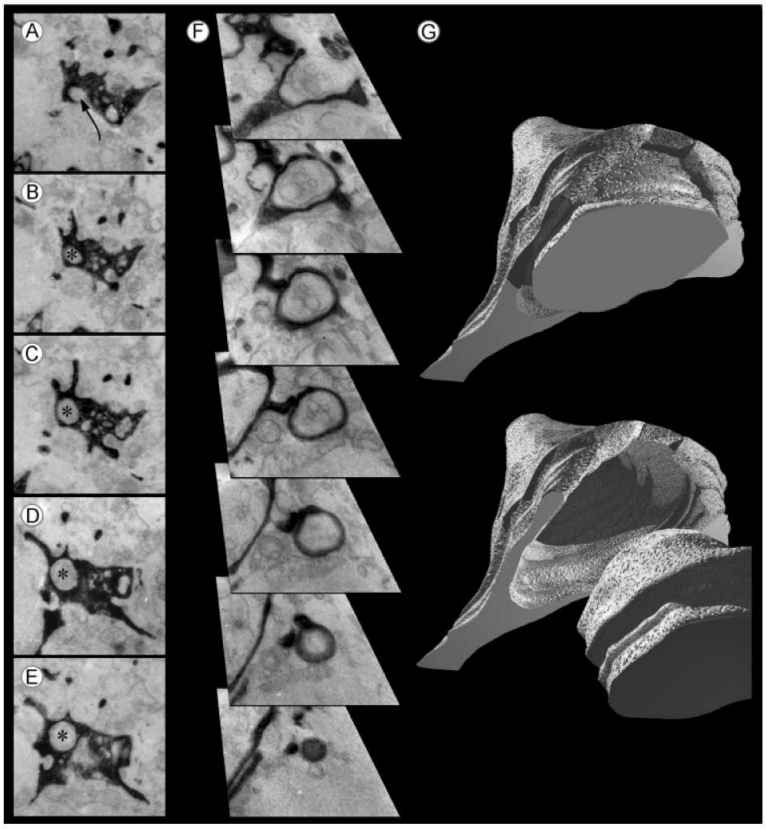

FIGURE 4.7: TEM images of the Bergmann glial cell at a tripartite synapse. The left-hand columns show sections through the cerebellar tissue at different depths. The conical structure in the right-hand column is the Bergmann glia, reconstructed in three dimensions from these sections, and the domed structure beneath it is the synapse it is enclosing. Reproduced, with permission, from [30].

4.1.3 Spatial buffering

The specific class of glial cells that Bergmann glia belong are called 'astrocytes' — because of their vaguely star-shaped appearance — and one of the known ways astrocytes support neuronal function is to maintain extracellular potassium concentrations. The passage of an action potential in an axon causes potassium ions to pass out of the neuron and into the extracellular space. In a large neuron — such as a squid giant axon — firing isolated bursts of action potentials, the flux of ions is small enough that the concentrations do not change significantly. However, tissues in the brain can be much more active — neurons in the cerebellum can fire at around 40 Hz almost continually, and in bursts at up to 200 Hz — and as such potassium ions can accumulate in the extracellular spaces [60, 21]. Accumulated potassium ions decrease the concentration gradient across the neuron membrane, raising the potassium reversal potential and making the neuron

more excitable. Obviously this is undesirable in a case where strict control of neural activity is required, so it is believed that astrocytes act to return the extracellular potassium concentration to its normal level by redistributing ions through a process known as 'spatial buffering' [48, 74].

Astrocytes express 'inward-rectifying' potassium channels (Kir channels), which have a high conductance to ions flowing from the extracellular to the intracellular space, and a much lower conductance in the opposite direction [69, 83]. These channels allow the astrocyte to move potassium from the extracellular space despite the high potential gradient opposing this movement. The flux of potassium ions into the astrocyte causes a local depolarisation, creating a potential gradient which redistributes the ions throughout the cell, thus moving them away from the region of high neural activity (there is also a concentration gradient created, which can modulate the behaviour of ion channels in the cell membrane). Over a much longer timescale than that of neural activity ($O(1)$ s, [18]) potassium ions leak back out of the astrocyte into the extracellular space, causing a smaller, slower increase in potassium concentration (hence 'buffering'), over a larger area (hence 'spatial' buffering).

Astrocytes make this behaviour more efficient by connecting with their neighbours in structures known as 'gap junctions'. Gap junctions form between astrocytes in close proximity, where proteins similar to ion channels span the cell membranes of *both* astrocytes, allowing ions to pass from one to the other without flowing through the extracellular space. A large collection of astrocytes (or certain other types of cell, for example, cardiac myocytes [95]) connected in this way is known as a 'syncytium', and there is a growing body of evidence that this structure contributes to the effectiveness of spatial buffering [58, 108], for example, the large spatial extent of the syncytium may mean that potassium ions can be buffered over larger distances than would be possible in a single cell — glial cells in a syncytium have been found to be electrically-coupled at separations of around 300 μm, although it is not known for certain that spatial buffering can be effective on this scale [50, 109].

4.1.4 Potassium siphoning

The Bergmann glial cell is thought to perform a behaviour very similar to spatial buffering, known as potassium siphoning. Potassium siphoning has been most extensively studied in Müller cells — glia found in the retina — but Bergmann glia are thought to play a similar role. The cell takes up potassium at regions of high concentration, as described above, but the subsequent intracellular fluxes of potassium are contained within a single cell. Bergmann glia do form a syncytium, but it does not appear to be as vital for spatial buffering [103]. Instead, the blood vessel at the glial end-foot provides a sink for the potassium ions, which are deposited into the circulatory system and easily disposed of [71]. It has been proposed that this interaction between the astrocyte and circulatory system allows for the creation of localised changes in blood flow at the site of more intense neuronal activity, although there is some disagreement on the significance of this effect [3, 59].

4.1.5 Overview of our modelling work

In this chapter we construct a simple model of the Bergmann glial cell, informed where possible by experimental data. This allows us to produce a simple picture of the physical structure of the cell, and only include more details where the data shows their effects are significant. The simplified model we produce accurately predicts the electrical response of the cell at the cell scale. In order to explore the behaviour of the cell near to the synapse, and to assess its ability to transport potassium ions, we also write down a simple model of the behaviour of ions in the microdomains, including the effects of potential and concentration gradients, allowing us to track the changes in ion fluxes and concentrations that occur in response to simulated synaptic activity. This allows us to quantify, for example, the rate at which sodium ions can flow from the microdomains into the fibre, and hence judge the cell's effectiveness at maintaining a favourable sodium concentration for the action of the glutamate transporter mentioned in section 4.1.2.

4.2 Modelling the electrical response of a microdomain

Current models of the Bergmann glial cell focus primarily on the potassium siphoning behaviour of the fibre, and do not take the geometry of the rest of the cell (i.e. the microdomains) into account. Anatomical data suggests that around 90% of the Bergmann glia cell's surface area is made up by the membranes of the microdomains, and that this membrane contains Kir channels, so it is plausible to suggest that there is some kind of potassium siphoning effect occurring [30].

Generalised models of astrocyte potassium buffering focus strongly on the precise representation of the ion channel dynamics involved in ion movements. In certain cases (see, for example [112]), this extends to ignoring entirely the geometry of the astrocyte, and instead considering a model consisting of a synapse, astrocyte and blood vessel, with no spatial variations within these regions. This approach may be useful to understanding the behaviour of large ensembles of astrocytes, but it cannot really elucidate the behaviour of a single cell, and tells us more about the behaviour of the ion channels than how the cell's structure influences its role.

In addition, the models of ion channels used require large numbers of parameters (55 are used in [112]). Many of these parameters are not known with any great certainty and others have to be estimated with no supporting biological data, and the sensitivity of the resulting model to these parameter choices means that this approach is not useful for providing general insights into the cell's function.

Models accounting for spatial variations within astrocytes also exist, some which are approached analytically (for example [18]) and others computationally (for example [100]). However, these also use very simplified geometries — cylindrical or approximately cylindrical cells — which cannot easily account for behaviours in the Bergmann glial cell microdomains.

The microdomains of the Bergmann glial cell seem to be particularly badly designed for the purpose of potassium siphoning. Any potassium ions entering the microdomains have to pass through the very narrow stalk (with very high resistance) to get to the

fibre and then the end-foot. It may be the case that all of the siphoning behaviour of the cell occurs within the fibre, with the microdomains performing entirely independent roles, but with the large surface area of the microdomains, a relatively small effect per microdomain could be amplified into a large effect over the entire cell. It also may be that under low-levels of neural activity, the siphoning effect of the microdomains is small but in periods of intense activity the cumulative effect of the large numbers of microdomains becomes significant. Our model suggests, in fact, that a reasonably large proportion (up to around twenty percent, depending on the exact properties of the cell) of the potassium ions introduced at a microdomain can flow out of the cell through the end-foot membrane, which suggests that the microdomains can contribute significantly to the siphoning behaviour of the cell (a quantification of the proportion of ion channels flowing out through the end-foot membrane as a function of its conductance per unit area is shown in figure 4.33, though a full explanation of the figure is deferred until the explicit details of the model have been presented).

We write down a partial differential equation model of the behaviour of the cell based on its morphology, certain aspects of which can be exploited to simplify the model. Simulations of the cell can then be used to predict both its electrical response and the movements of potassium and sodium ions within it.

There are two parts to the model: a description of the behaviour of a microdomain — including the effects of the ion channels in its membrane — and a description of the behaviour of the fibre.

4.2.1 Microdomain morphology

There has been little modelling work performed on the behaviour of microdomains. In Grosche *et al.* [30], a model was used to show that depolarisations in a single microdomain have a very small effect on the membrane potential found in the fibre, suggesting that the microdomains are electrically isolated from one another. This model used an extremely detailed representation of the morphology of a single microdomain, consisting of around 50 different sub-compartments, and was solved in the NEURON

simulation environment to gauge the effects of microdomain depolarisations on the fibre. However, the complexity of the model means it's not easily scaleable to a whole cell level, and an analysis of the behaviour of the model suggests that it can be simplified considerably without losing the key qualitative behaviours.

Simplifying the model allows us to work on the scale of the whole cell, where we can determine how the effects of single microdomains combine when they are depolarised in large numbers. If we retain only the important physical features of the microdomain we can create a more tractable model, which provides better insight into cell behaviour.

A more detailed look at microdomains shows (at least) two distinct large regions, which we refer to hereon as 'paddles', connected by narrow stalks (see figure 4.8). Assuming that the conductivity of the intracellular electrolyte is approximately constant (we demonstrate the validity of this assumption in section B), the resistance encountered between the fibre (A in figure 4.8) and the distal end of the microdomain (E) is essentially determined by the cross-sectional area of the microdomain. The majority of the potential drop across the microdomain therefore happens in the narrowest regions, the stalks (B and D). Although this ignores a lot of the details of the anatomy seen in figure 4.4, its efficacy is borne out by the modelling work in [30], where simulations show two large potential drops through the microdomain, corresponding to the two stalks, and no other significant sources of resistance (see section 4.6.2 for a direct comparison of our model to theirs).

The key property of the paddles in the microdomain (with regards to the model) is their very high surface area to volume ratio [30]. Their small volume and low resistance to the movement of charge within them mean that variations in concentration and potential equilibrate quickly, such that each paddle can be thought of as being equipotential. The large surface area means that membrane effects — ion channel and capacitive currents — tend to dominate the behaviour, and thus are the most significant factors our model must include.

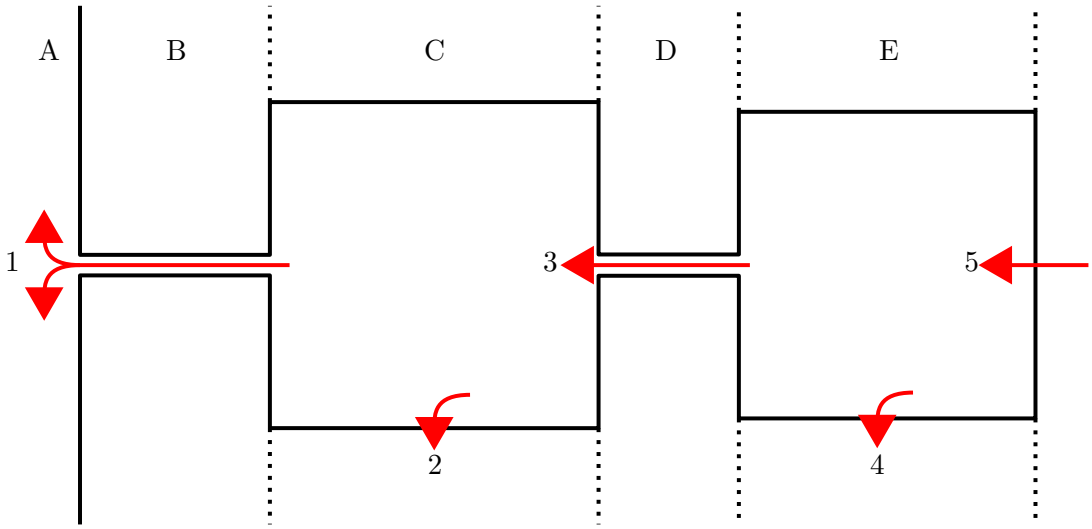

FIGURE 4.8: A simplified model of the microdomain, derived from the anatomical details in figure 4.4. The model consists of the fibre (A), a proximal high resistance, low capacitance stalk (B), a proximal low resistance, high capacitance paddle (C), a distal high resistance, low capacitance stalk and a distal low resistance high capacitance paddle. The current sources/sinks considered are: (1) flow between the fibre and the proximal paddle; (2) leak currents through the proximal paddle membrane; (3) flow between the proximal and distal paddles; (4) leak currents through the distal paddle membrane; (5) ion channel modulated currents in response to synaptic activity.

4.2.2 Equivalent circuit models for the glial cell

In order to determine the structure of the microdomain, we construct a simple equivalent circuit model based on its anatomical features. The large areas of cell membrane in the paddles have a significant capacitance (from the bilayer structure) and conductance (from the presence of ion channels) and so can be modelled as a circuit comprising a capacitor and resistor in parallel [88]. The narrow stalks of the microdomain can, as mentioned above, be thought of as resistances and the model of the microdomain can be built from just these two features — the membrane in the paddles and the resistances between them.

4.2.2.1 Description of the voltage clamp experiment

Once the behaviour of the equivalent circuit has been determined, we determine the parameters of the model by fitting to experimental data, obtained by imposing known transmembrane potentials on a cell. This data was obtained by our collaborators at the University of Nottingham, and an example of it is shown in figure 4.9, showing

the current through the microdomain membranes in response to a step change in the transmembrane potential. A description of the experimental procedure is given below, full details can be found in [25]. This data is obtained by inserting an electrode into the cell at the soma and one into the extracellular space, far from the cell, such that the potential drop across the whole cell can be recorded and current can be injected directly into the cell (this setup is sketched in figure 4.10). Injecting current into the soma through the recording electrode (labelled in figure 4.10) depolarises the cell membrane in the fibre and microdomains, causing current flows out of the cell, and so a feedback loop can be created to hold the potential drop across the cell at a fixed value by balancing the current out of the cell through the fibre and microdomain membranes with the current in through the electrode. The electrode current required to keep the potential drop steady (which is recorded) is thus equivalent to the current flowing through the cell membranes. In figure 4.9, the potential drop across the cell is initially held at $-80\,\mathrm{mV}$, which results in a small inward current through the fibre and microdomain membranes. At 50 ms the potential drop across the cell is quickly switched to $0\,\mathrm{mV}$ causing a brief, large outward current that decays exponentially to a constant value over a scale of 10–50 ms. After 250 ms the potential drop is returned to $-80\,\mathrm{mV}$, which causes a brief inward current before the cell returns to equilibrium. Our complete data set was obtained by applying ten such voltage step changes (from -60 to $+140\,\mathrm{mV}$) to each of five cells.

4.2.3 Equivalent circuit model based on a single paddle microdomain

We initially construct a simple model of the cell membrane in the microdomain as a resistor and capacitor in parallel, connected to the fibre of the Bergmann glial cell (which is assumed to be equipotential because of its relatively large width, and hence its low resistance) by a single, high-resistance stalk (i.e. a microdomain with only one paddle, rather than the two described previously). Using the known potential difference across the microdomains (imposed by the experiment), we can write down equations which describe the behaviour of this circuit and solve them to find the current through it.

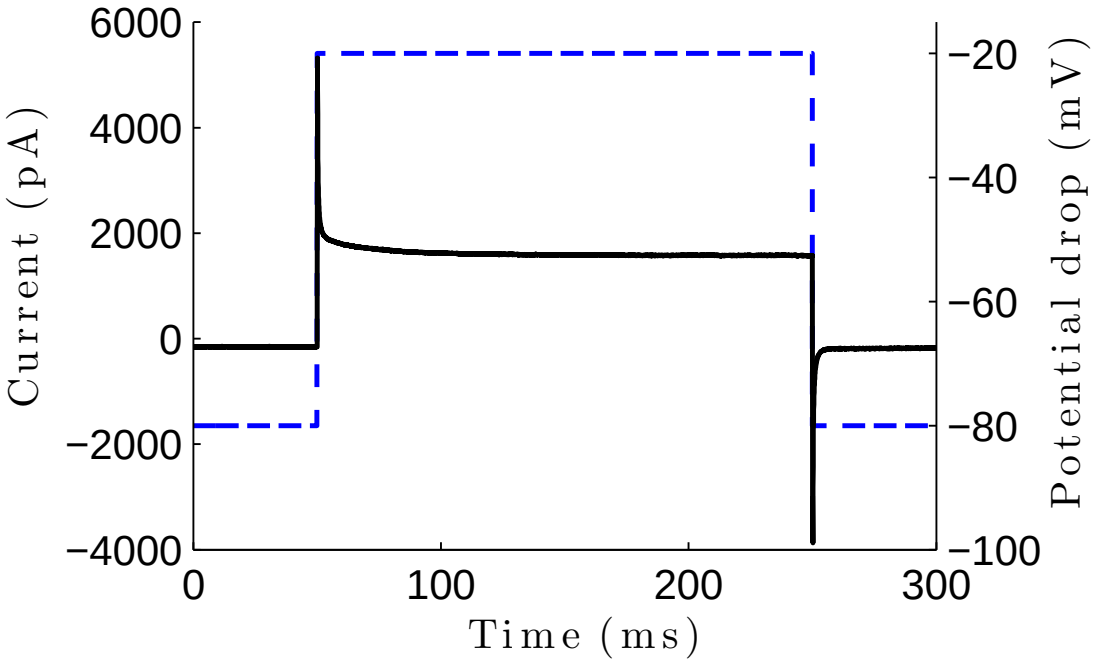

FIGURE 4.9: Example of experimental results showing current through the cell membrane (black curve, left-hand axis) and imposed potential drop across the cell (blue curve, right-hand axis). The key feature of this data is the behaviour after the large spike at 50 ms, which shows two rates of exponential decay. We determine the parameters of our equivalent circuit by fitting its response to this biexponential decay.

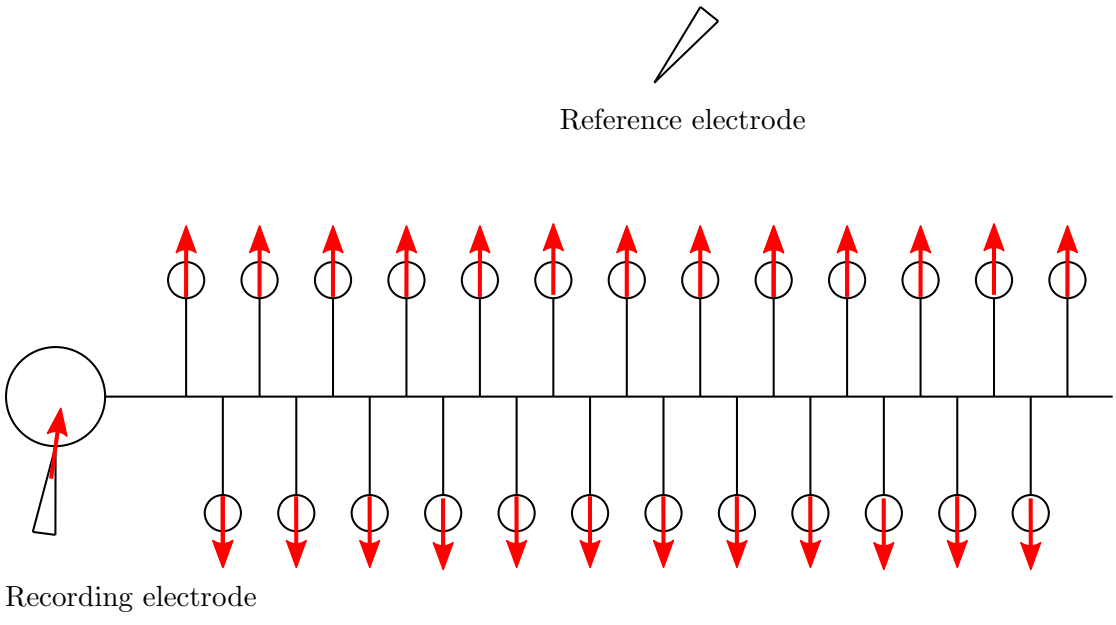

FIGURE 4.10: A sketch of the voltage clamp experimental set up. In order to maintain a fixed potential drop between the recording and reference electrodes, the current applied through the recording electrode must balance the current flow out of the cell through the microdomains. The record of the current input to the cell thus reflects the total current out of the cell through the microdomain membranes, and can be compared to the outputs of our simulations.

The radius of the fibre is around ten times that of the stalks in the microdomains (see table 4.2 for a complete list of parameters of the cell) and as such we do not expect it to have a significant resistance compared to the stalks, unless it contains constrictions or obstructions of some kind. We therefore begin by neglecting its resistance such that the entire fibre (including the soma) is equipotential. In this case the cell can be modelled as many of the circuits described above connected in parallel, and the current through each microdomain will be identical. The total current recorded at the soma (by the recording electrode) will therefore simply be equal to the current through one microdomain multiplied by the number of microdomains (we have to estimate the number of microdomains from values given in the literature — [54] and [86] both contain estimates of the number of microdomains per unit length).

Analysis of the data shows that it contains two exponential decay rates, one faster and one slower, whereas this simple model predicts only one. We can fit the model to either the fast or the slow rate by changing parameters, but obviously neither predicts the response of the cell very well. See figure 4.11 for the fit to the faster decay rate, and figure 4.12 for the slower.

Although this model doesn't compare well to the experimental data, the analysis is useful firstly because it demonstrates exactly why a single-paddle model of the microdomain is not enough to predict the full behaviour of the microdomain and secondly because it can be used to inform subsequent modelling work — it's clear we need to add a mechanism which will contribute a different decay rate. Further discussion with our experimental collaborators suggested that this second decay rate could be contributed by a second region of the microdomain, and thus we produced the second iteration of the model, detailed below.

4.2.4 Equivalent circuit model based on a two paddle microdomain

Examination of the electron micrographs of the microdomain in figure 4.4 suggests that there is a significant resistance within the microdomain itself, in addition to the resistance between the fibre and the microdomain. This motivates the equivalent circuit model of a two-paddle microdomain seen in figure 4.13 (and overlaid on the relevant

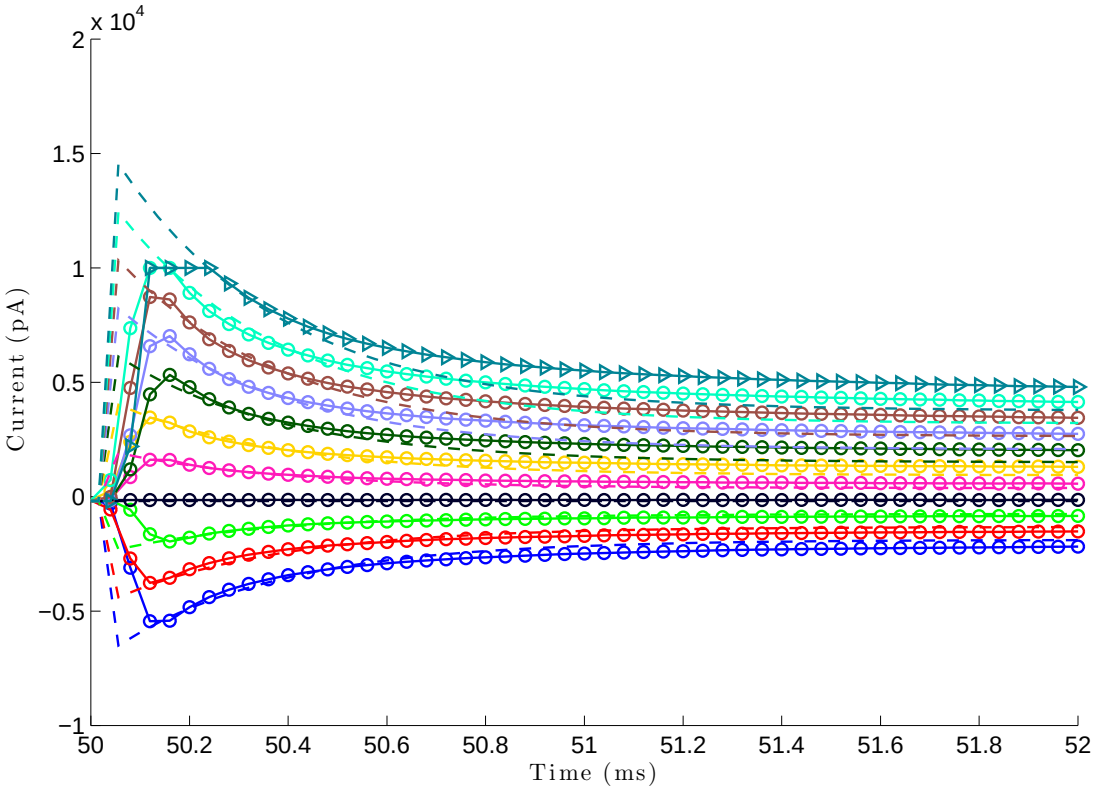

FIGURE 4.11: Single paddle equivalent circuit model fitted to fast decay rate of experimental data. Triangles show data used to fit parameters, circles show other data, dashed curves are predictions of the model. The initial agreement between the model and the data is good, but gets worse over time because the data does not decay at a constant rate.

morphology in figure 4.14). We can determine the parameters of the equivalent circuit (the surface areas of the two paddles, the paddle membrane's passive conductance per unit area and the resistance of the two stalks) by solving the equations describing its behaviour and fitting the predicted response to experimental data. Again, we assume that the fibre and soma are equipotential and thus that the current through each microdomain is identical. The total current recorded at the some is therefore equal to the current through one microdomain multiplied by the number of microdomains (which, again, we estimate from the same values in the literature used for the single paddle equivalent circuit).

Using some basic properties of the circuit illustrated in figure 4.13, we can derive an ODE governing the current through the cell in response to an applied voltage. We know voltages sum across elements in series, and currents sum through elements in parallel,

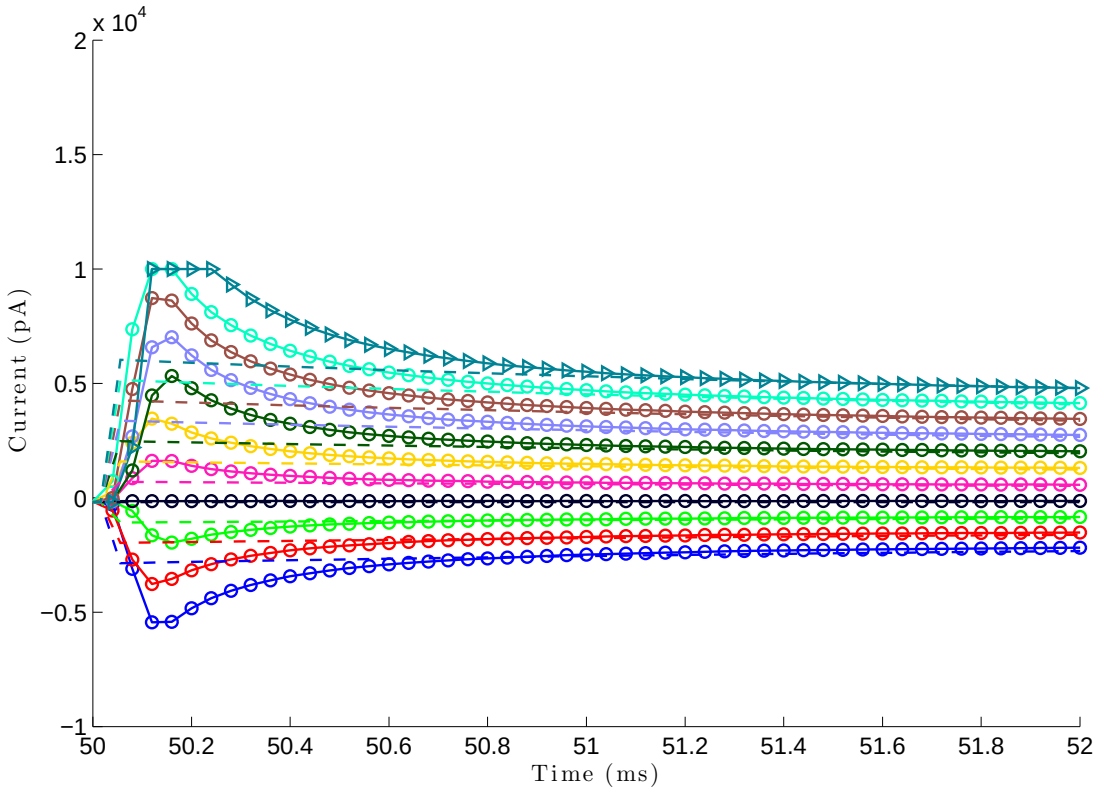

FIGURE 4.12: Single paddle equivalent circuit model fitted to slow decay rate of experimental data. Again, triangles show data used to fit parameters, circles show other data, dashed curves are predictions of the model. The model and data agree well on a longer time-scale, but the initial spikes in the data are not present in the model.

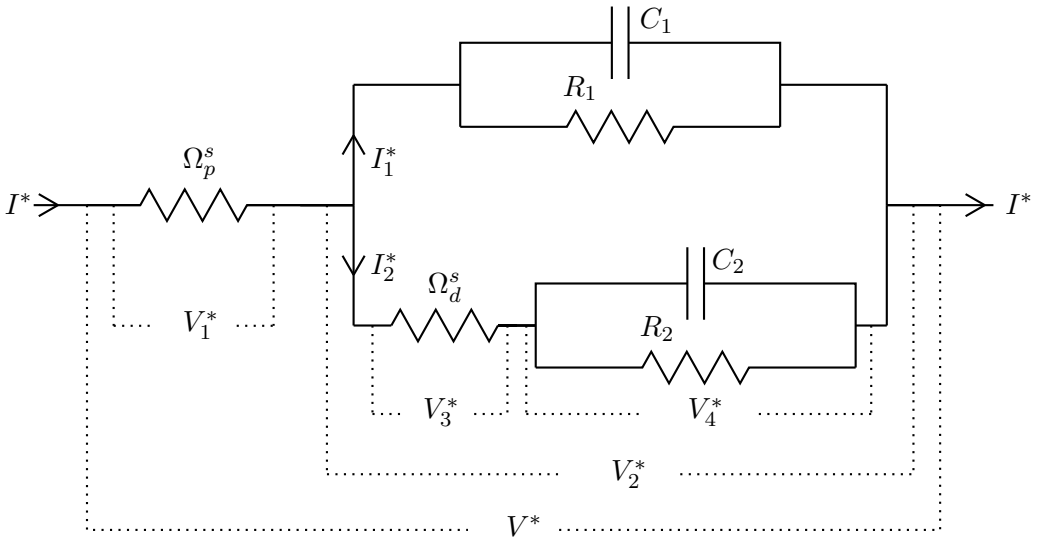

FIGURE 4.13: Equivalent circuit representing a microdomain with two distinct paddles.

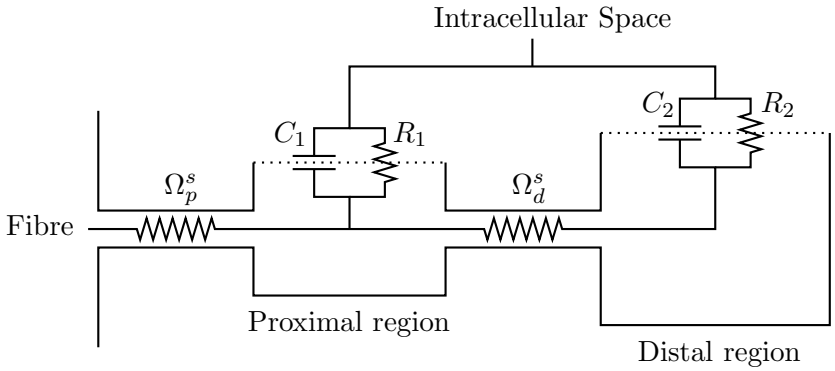

FIGURE 4.14: The equivalent circuit for the model of the microdomain presented in figure 4.8, overlaid on its morphology. Labelled are the resistances of the two stalks (Ω_p^s, Ω_d^s), the capacitances of the two paddles (C_1, C_2) and the resistances of the two paddles (R_1,R_1).

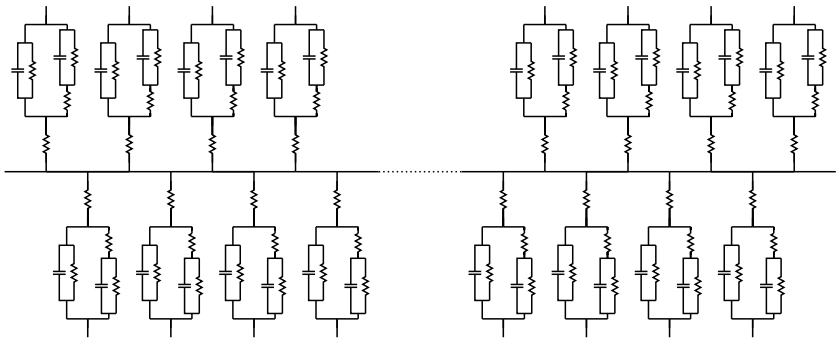

FIGURE 4.15: The equivalent circuit model of the whole cell. Assuming the resistance of the fibre is negligible, the cell behaves like many microdomains in parallel

thus:

$$V^* = V_1^* + V_2^* \tag{4.1}$$

$$V_2^* = V_3^* + V_4^* \tag{4.2}$$

$$I^* = I_1^* + I_2^* \tag{4.3}$$

where $V_{1,2,3,4}$ and $I_{1,2}$ are as labelled in figure 4.13. The current through the top half of the second component in figure 4.13, I_1^*, is determined using Ohm's law through the resistor and the law of capacitance

$$I_1^* = \frac{V_2^*}{R_1} + C_1 \dot{V}_2^* \tag{4.4}$$

where R_1 and C_1 are the resistance and capacitance of the proximal paddle membrane,

respectively. The current, I_2^*, through each part of the bottom half of the second component in figure 4.13 is given by the following expressions

$$I_2^* = \frac{V_4^*}{R_2} + C_2\dot{V}_4^*, \tag{4.5}$$

$$I_2^* = \frac{V_3^*}{\Omega_d^s} \tag{4.6}$$

where R_2 and C_2 are the resistance and capacitance of the distal paddle membrane, and Ω_d^s is the resistance of the distal stalk. From equations (4.2) and (4.6)

$$V_4^* = V_2^* - I_2^*\Omega_d^s \tag{4.7}$$

which can be substituted into equation (4.5)

$$I_2^* = C_2\dot{V}_2^* - C_2\dot{I}_2^*\Omega_d^s + \frac{1}{R_2}V_2^* - I_2^*\frac{\Omega_d^s}{R_2} \tag{4.8}$$

Equations (4.3) and (4.4) give us an alternative expression for I_2^*

$$I_2^* = I^* - C_1\dot{V}_2^* - \frac{1}{R_1}V_2^* \tag{4.9}$$

which can be combined with equation (4.8) to give the following result for the total current through the equivalent circuit for the two paddle microdomain (that is, the current from the fibre into the microdomain)

$$\begin{aligned}
I^* &= C_1\dot{V}_2^* + V_2^*\frac{1}{R_1} + C_2\dot{V}_2^* - C_2\dot{I}_2^*\Omega_d^s + V_2^*\frac{1}{R_2} - I_2^*\frac{\Omega_d^s}{R_2} \\
&= (C_1 + C_2)\,\dot{V}_2^* + \left(\frac{1}{R_1} + \frac{1}{R_2}\right)V_2^* - C_2R_1\dot{I}_2^* - \frac{\Omega_d^s}{R_2}I_2^* \\
&= (C_1 + C_2)\,\dot{V}_2^* + \left(\frac{1}{R_1} + \frac{1}{R_2}\right)V_2^* - C_2R_1\left(\dot{I}^* - C_1\ddot{V}_2^* - \frac{1}{R_1}\dot{V}_2^*\right) \\
&\quad - \frac{\Omega_d^s}{R_2}\left(I^* - C_1\dot{V}_2^* - \frac{1}{R_1}V_2^*\right) \\
&= C_1C_2\Omega_d^s\ddot{V}_2^* + \left(C_1\left(1 + \frac{\Omega_d^s}{R_2}\right) + C_2\left(1 + \frac{\Omega_d^s}{R_1}\right)\right)\dot{V}_2^* \\
&\quad + \left(\frac{1}{R_1} + \frac{1}{R_2} + \frac{\Omega_d^s}{R_1R_2}\right)V_2^* - C_2\Omega_d^s\dot{I}^* - \frac{\Omega_d^s}{R_2}I^*
\end{aligned} \tag{4.10}$$

We can now use equation (4.1) and Ohm's law through the first resistor to derive the following expression for V_2^*

$$V_2^* = V^* - I^*\Omega_p^s \tag{4.11}$$

where Ω_p^s is the resistance of the proximal stalk. This can be substituted in to our expression for I^* to obtain

$$\begin{aligned} I^* = {} & C_1C_2\Omega_d^s\ddot{V}^* + \left(C_1\left(1+\frac{\Omega_d^s}{R_2}\right) + C_2\left(1+\frac{\Omega_d^s}{R_1}\right)\right)\dot{V}^* \\ & + \left(\frac{1}{R_1}+\frac{1}{R_2}+\frac{\Omega_d^s}{R_1R_2}\right)V^* - C_1C_2\Omega_p^s\Omega_d^s\ddot{I}^* \\ & - \left(\Omega_p^s\left(C_1\left(1+\frac{\Omega_d^s}{R_2}\right) + C_2\left(1+\frac{\Omega_d^s}{R_1}\right)\right) + C_2\Omega_d^s\right)\dot{I}^* \\ & - \left(\Omega_p^s\left(\frac{1}{R_1}+\frac{1}{R_2}+\frac{\Omega_d^s}{R_1R_2}\right) + \frac{\Omega_d^s}{R_2}\right)I^* \end{aligned} \tag{4.12}$$

All of the coefficients in this equation are constants, determined by the parameters of the circuit and so we rewrite the equation in the more manageable form below

$$\ddot{I}^* + \alpha\dot{I}^* + \beta I^* = \gamma\ddot{V}^* + \zeta\dot{V}^* + \eta V^*, \tag{4.13}$$

where

$$\alpha = \frac{1}{C_2}\left(\frac{1}{\Omega_d^s}+\frac{1}{R_2}\right) + \frac{1}{C_1}\left(\frac{1}{\Omega_p^s}+\frac{1}{\Omega_d^s}+\frac{1}{R_1}\right) \tag{4.14}$$

$$\beta = \frac{1}{C_1C_2}\left(\frac{1}{R_1\Omega_d^s}+\frac{1}{\Omega_d^sR_2}+\frac{1}{R_1R_2}+\frac{1}{\Omega_p^sR_2}+\frac{1}{\Omega_p^s\Omega_d^s}\right) \tag{4.15}$$

$$\gamma = \frac{1}{\Omega_p^s} \tag{4.16}$$

$$\zeta = \frac{1}{\Omega_p^s}\left(\frac{1}{C_2}\left(\frac{1}{\Omega_d^s}+\frac{1}{R_2}\right) + \frac{1}{C_1}\left(\frac{1}{\Omega_d^s}+\frac{1}{R_1}\right)\right) \tag{4.17}$$

$$\eta = \frac{1}{C_1C_2\Omega_p^s}\left(\frac{1}{R_1\Omega_d^s}+\frac{1}{\Omega_d^sR_2}+\frac{1}{R_1R_2}\right) \tag{4.18}$$

We also know the form of V^*, which is the potential imposed by the experiment

$$V^* = \begin{cases} -V_H - V_R & t^* < t_0 \\ -V_H - V_R + V_S & t^* \geq t_0 \end{cases} \tag{4.19}$$

where V_H is the holding potential ($= -80\,\text{mV}$), V_R is the membrane resting potential

($\approx -75\,\mathrm{mV}$) and V_S is the step in the holding potential (which varies between -60 and $+140\,\mathrm{mV}$). We write the potential in this way because it's deviations from the resting potential which drive net current flows through the membrane, not deviations from zero. We can write this more compactly using the Heaviside step function (H) as follows

$$V^* = -V_H - V_R + V_S H\left(t^* - t_0\right) \tag{4.20}$$

from which we can easily calculate the necessary derivatives

$$\dot{V}^* = V_S \delta\left(t^* - t_0\right) \tag{4.21}$$

$$\ddot{V}^* = V_S \dot{\delta}\left(t^* - t_0\right) \tag{4.22}$$

4.2.4.1 Choosing initial conditions

In setting up the experiment, the cell is held at a potential of $-80\,\mathrm{mV}$ until its behaviour reaches a steady-state. At $t = 0$, therefore, we know

$$I^*\left(t^* = 0\right) = I^- = \frac{\eta}{\beta}\left(-V_H - V_R\right), \tag{4.23}$$

$$\dot{I}^*\left(t^* = 0\right) = 0 \tag{4.24}$$

(The experiment is run long enough after the jump in potential that another equilibrium is reached. As $t^* \to +\infty$, therefore, we also know

$$\lim_{t^* \to \infty} I^* = I^+ = \frac{\eta}{\beta}\left(-V_H - V_R + V_S\right) \tag{4.25}$$

which we cannot impose as an initial condition, but will return to later to determine the value of $\frac{\eta}{\beta}$.)

4.2.4.2 Non-dimensionalising the problem

We can now collect this into the following closed problem

$$\ddot{I}^* + \alpha \dot{I}^* + \beta I^* = \gamma V_S \dot{\delta}\left(t^* - t_0\right) + \zeta V_S \delta\left(t^* - t_0\right) + \eta\left(-V_H - V_R + V_S H\left(t^* - t_0\right)\right), \tag{4.26}$$

$$I^*(0) = I^-, \tag{4.27}$$

$$\dot{I}^*(0) = 0 \tag{4.28}$$

We nondimensionalise the system as follows

$$I^* = \frac{\eta\left(V_H + V_R\right)}{\beta} I, \qquad t^* = \frac{1}{\sqrt{\beta}} t, \tag{4.29}$$

which yields the following statement of the dimensionless problem

$$\ddot{I} + \kappa \dot{I} + I = \lambda \bar{V} \dot{\delta}\left(t - T\right) + \mu \bar{V} \delta\left(t - T\right) + \bar{V} H\left(t - t_0\right) - 1, \tag{4.30}$$

$$I(0) = -1, \tag{4.31}$$

$$\dot{I}(0) = 0 \tag{4.32}$$

where

$$\bar{V} = \frac{V_S}{V_H + V_R} \tag{4.33}$$

$$\kappa = \frac{\alpha}{\sqrt{\beta}}, \tag{4.34}$$

$$\lambda = \frac{\beta\gamma}{\eta}, \tag{4.35}$$

$$\mu = \frac{\sqrt{\beta}\zeta}{\eta} \tag{4.36}$$

4.2.4.3 Solution

It can be shown that the following expression solves equations (4.30) to (4.32)

$$I = -1 + \bar{V} H\left(t - T\right)\left(1 + k_1 e^{-m_1(t-T)} + k_2 e^{-m_2(t-T)}\right) \tag{4.37}$$

where

$$k_1 = \frac{1}{2}\left(\lambda - 1 + \frac{2\mu - \kappa(\lambda+1)}{\sqrt{\kappa^2 - 4}}\right), \tag{4.38}$$

$$k_2 = \frac{1}{2}\left(\lambda - 1 - \frac{2\mu - \kappa(\lambda+1)}{\sqrt{\kappa^2 - 4}}\right), \tag{4.39}$$

$$m_1 = \frac{1}{2}\left(\kappa - \sqrt{\kappa^2 - 4}\right), \tag{4.40}$$

$$m_2 = \frac{1}{2}\left(\kappa + \sqrt{\kappa^2 - 4}\right) \tag{4.41}$$

Thus we can clearly see the solution takes the form of a biexponential decay, which we can now fit to the two decay rates seen in the data.

4.2.4.4 Fitting to data

To fit this expression to the experimental data we use the method of least squares to minimise differences between the exponential decay seen in the data and the decay in the model. This analysis determines k_1^*, k_2^*, m_1^* and m_2^*, defined as the minimisers of

$$\sum_i \left(y_i^* - k_1^* e^{-m_1^* t^*} - k_2^* e^{-m_2^* t^*}\right)^2 \tag{4.42}$$

where $\{y_i^*\}$ are the (dimensional) data points and $\{t_i^*\}$ are the (dimensional) times at which the data points are taken.

As seen in figures 4.16 and 4.17, the behaviour of the cell is predicted well by the model, with the medium and long term currents being basically indistinguishable. The difference in the very short-term behaviour immediately after the voltage step is due to the limitations of the experimental apparatus, which cannot register the cell's response over this time-scale.

The values from the least-squares regression tell us the values of k_1, k_2, m_1 and m_2 to use in the dimensionless equation to obtain the best fit to the data. Once we know this, we can work backwards to find κ, λ, μ and τ, and thence α, β, γ, η and ζ, and finally the resistances and capacitances of the equivalent circuit, by simply inverting the definitions in equations (4.14) to (4.18), (4.34) to (4.36) and (4.38) to (4.41). The analytic solution

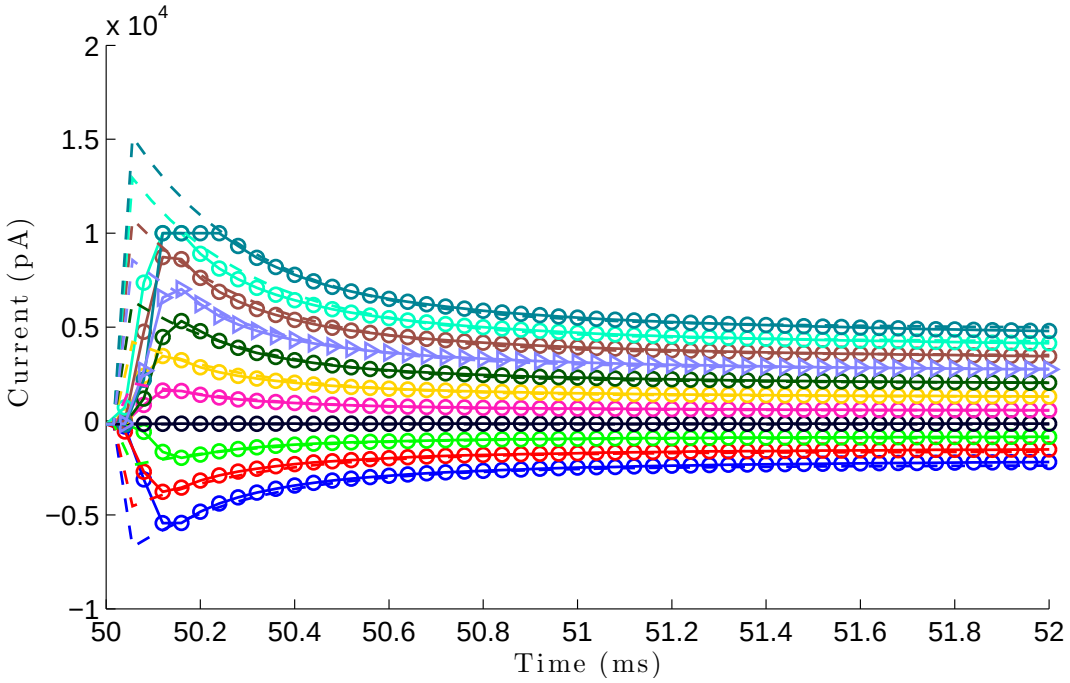

FIGURE 4.16: Comparison of the model to the experimental data from the first cell. Line with triangles is data used for fitting, lines with circles are the rest of the data, dashed lines are model predictions

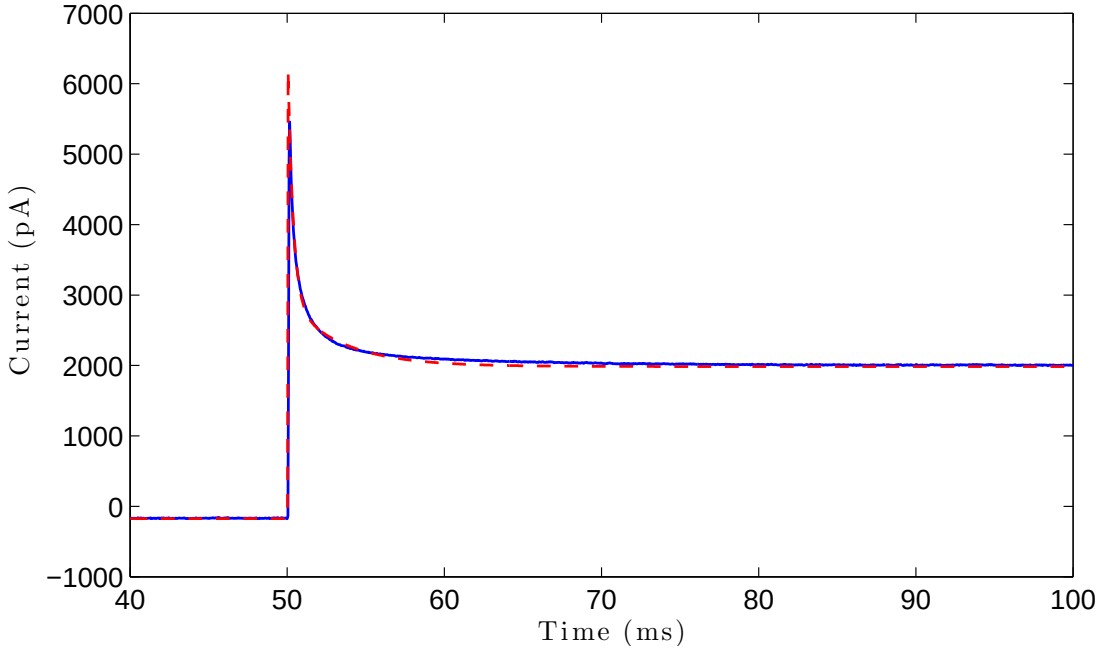

FIGURE 4.17: Comparison of the model (red, dashed) to a single experiment (blue, solid), over a longer time-scale

for the resistances and capacitances is too convoluted to be illuminating when written out in full, but it is trivial to find these values computationally.

In order to pin down all the parameters of the cell it is necessary to make some assumptions — we have six parameters to determine (Ω_p^s and Ω_d^s, C_1 and C_2 and R_1 and R_2) and only five bits of information from the data (k_1, k_2, m_1, m_2 and the long time scale steady state current, I^+), and the number of microdomains is unknown. The capacitance of the lipid bilayer is primarily determined by its thickness, which is fixed by the molecular structure, not any of the properties of the cell, so we can assume that the capacitance of all the membranes in the circuit is $0.01\,\mathrm{F}\cdot\mathrm{m}^2$, which is a value widely used in the literature [30, 44]. We also assume that the conductance per unit area of the microdomain membrane is constant (that is, all the ion channels in the microdomain are uniformly distributed — throughout both paddles). With these assumptions, the capacitance and resistance of the membranes in the two paddles become, respectively, proportional and inversely proportional to the surface area. Mathematically, we make the substitutions

$$C_1 = CA_p, \tag{4.43}$$

$$C_2 = CA_d, \tag{4.44}$$

$$R_1 = \frac{1}{g^m A_p}, \tag{4.45}$$

$$R_2 = \frac{1}{g^m A_d}, \tag{4.46}$$

where C is the capacitance of the membrane per unit area, g^m is the conductance per unit area of the membrane ($\mathrm{S}\cdot\mathrm{m}^{-2}$) and A_p and A_d are the surface areas of the two paddles. This reduces the number of undetermined parameters in the model by one.

We also have to account for the fact that the current measured experimentally is the sum of the currents through all of the microdomains. To do this, we note that the current through each microdomain is identical, such that the current recorded at the soma is equal to the current through one microdomain multiplied by the number of microdomins. We estimate the number of microdomains on the fibre to be around one hundred, based

on a fibre of length 100 μm and a density of one microdomain per micrometer ($10^6\,\mathrm{m}^{-1}$), from the information in [54] and [86].

4.2.4.5 Cell parameters determined by the model

We have experimental data from five different cells, each of which was subjected to ten different voltage steps. We can thus obtain ten sets of estimates from each cell by choosing a voltage step, using the data from that particular experiment to fit the parameters of the model and repeating this process for each of the voltage steps until we have used all the data.

A summary of the parameters found is given in table 4.1, with values taken from the literature given in table 4.2. The measurements of microdomain surface area given in [30] are around 300 $\mu\mathrm{m}^2$ ($O\left(10^{-10}\right)$ m^2) (although these results may underestimate the true area of the microdomain because of the lack of resolution of the electron micrographs over the highly convoluted three dimensional geometry of the microdomain), and the leak conductance per unit area is estimated to be somewhere between 0.83 and 83 $\mathrm{S}\cdot\mathrm{m}^{-2}$, and thus we feel satisfied that the results of the analysis are reasonably trustworthy. We also now have estimates for parameters that aren't given in the literature anywhere else — the resistance of the stalks — which agree reasonably well with the estimates we can make based on the geometry of the cell seen in the electron micrographs in [30].

The complete sets of parameters determined by this approach are given in tables A.1 to A.5 in appendix A.

There are variations in the parameters from fitting to different voltage steps, and with this in mind we have tried to quantify the scale of the uncertainty in our estimates. What we see is that for three of the five parameters (A_p, Ω_p^s and Ω_d^s) the standard deviations of our measurements are around 10% of the means, whereas for the other two (A_d, g^m) they are closer to 40–60%. This seems like a large variation, but given the nature of what is being measured it is useful simply to be able to estimate an order of magnitude.

TABLE 4.1: Summary of results from fitting equivalent circuit model to experimental data

Cell		A_p $(\times 10^{-12}\,\mathrm{m}^2)$	A_d $(\times 10^{-12}\,\mathrm{m}^2)$	Ω_p^s $(\times 10^9\,\Omega)$	Ω_d^s $(\times 10^9\,\Omega)$	g^m $(\mathrm{S}\cdot\mathrm{m}^{-2})$
1	Mean	45.5	697	0.92	1.99	1.710
	Std. Dev	4.33	270.1	0.077	0.211	1.0920
2	Mean	42.9	145	0.91	1.91	3.650
	Std. Dev	4.96	54.7	0.071	0.163	0.9886
3	Mean	42.9	145	0.91	1.91	3.650
	Std. Dev	3.65	69.3	0.028	0.234	0.9307
4	Mean	64.7	152	1.42	2.86	2.190
	Std. Dev	4.38	127.8	0.025	0.439	0.5672
5	Mean	49.0	221	1.19	1.86	2.970
	Std. Dev	4.25	88.1	0.036	0.104	0.8724

4.3 Modelling the fibre

4.3.1 Motivation and details of a second experiment

In the previous analysis, we have assumed that the longitudinal resistance of the fibre is negligible, and thus that the fibre is approximately equipotential. Although the resulting model of current flows in the microdomains fits well to the experimental data, exploratory data obtained by our collaborators suggested that potential gradients did exist in the fibre, and should be reflected in the model. A simple model of the behaviour of the fibre (detailed below) was coupled to the existing model of the microdomains to account for potential variations within the fibre. An experiment was then designed to rigorously determine the potential gradients present in the fibre (details of the experiment are given below, and full detail can be found in [25]) for comparison with the model. Again, good agreement was found between our predictions and the experimental data.

The data is obtained by stimulating input currents to the microdomains at varying distances from the soma and measuring the depolarisation of the soma membrane (a sketch of the experimental setup is shown in figure 4.18). In these experiments, electrodes

TABLE 4.2: Values and estimates for parameters derived from the literature

Quantity	**Symbol**	**Value**	**Ref**
Resting potential	$\tilde{\Phi}$	$(-80 \text{ to } -50) \times 10^{-3}$ V $-82 \pm 6 \times 10^{-3}$ V	[64] [19]
Intracellular electrolyte conductivity	σ	$0.83\,\mathrm{S}\cdot\mathrm{m}^{-1}$	[30]
Membrane capacitance per unit area	C	$0.01\ \mathrm{F}\cdot\mathrm{m}^{-2}$	[30]
Fibre radius	R	$1.5\ \times 10^{-6}$ m	[31]
Fibre length (rat)	L	$200\ \times 10^{-6}$ m	[31]
Microdomain density	N^*	$5 \times 10^5\,\mathrm{m}^{-1}$	[54]
Total synapses ensheathed		2142 – 6358	[86]
Equivalent density (assuming 1–5 fibres, 100–300 μm long)	N^*	1×10^6 – $6 \times 10^7\,\mathrm{m}^{-1}$	
Stalk radius		$0.15\ \times 10^{-6}$ m	[30],[31]
Stalk length		$7\ \times 10^{-6}$ m	[30]
Stalk Resistance (from $\frac{\text{Length}}{\text{Electrolyte Conductivity}\times\text{Cross-sectional Area}}$)	Ω_p^s, Ω_d^s	$10^8\,\Omega$	
Microdomain volume		$16\ \times 10^{-18}$ m^3	[30]
Microdomain surface area	A_p, A_d	$317\ \times 10^{-12}$ m^2	[30]
Total microdomain surface area		90% Cell Surface Area	[30]
Microdomain membrane conductance per unit area	g	$8\,\mathrm{S}\cdot\mathrm{m}^{-2}$ $(0.8 - 80)$	[30]
Extracellular bath solution KCl Extracellular bath solution NaCl Pipette solution KCl		3.5 mol·m^{-3} 130 mol·m^{-3} 140 mol·m^{-3}	[97] [97] [97]

are inserted into the soma of the cell and the extracellular space far from the cell, allowing the potential drop across the cell to be measured. More electrodes are then used to stimulate the parallel fibres in the tissue surrounding the cell, activating the synapses with Purkinje fibres and causing current to flow into the Bergmann glial cell at the microdomains surrounding these synapses. The parallel fibres lie perpendicular across the Bergmann glial cell fibre, and so it is assumed that the distance between the parallel fibre and the soma (measured parallel to the Bergmann glial cell fibre) is equal to the distance between the stimulated microdomain and the soma. In this way a relationship can be established between the distance between the soma and the stimulated microdomain and the size of the response at the soma.

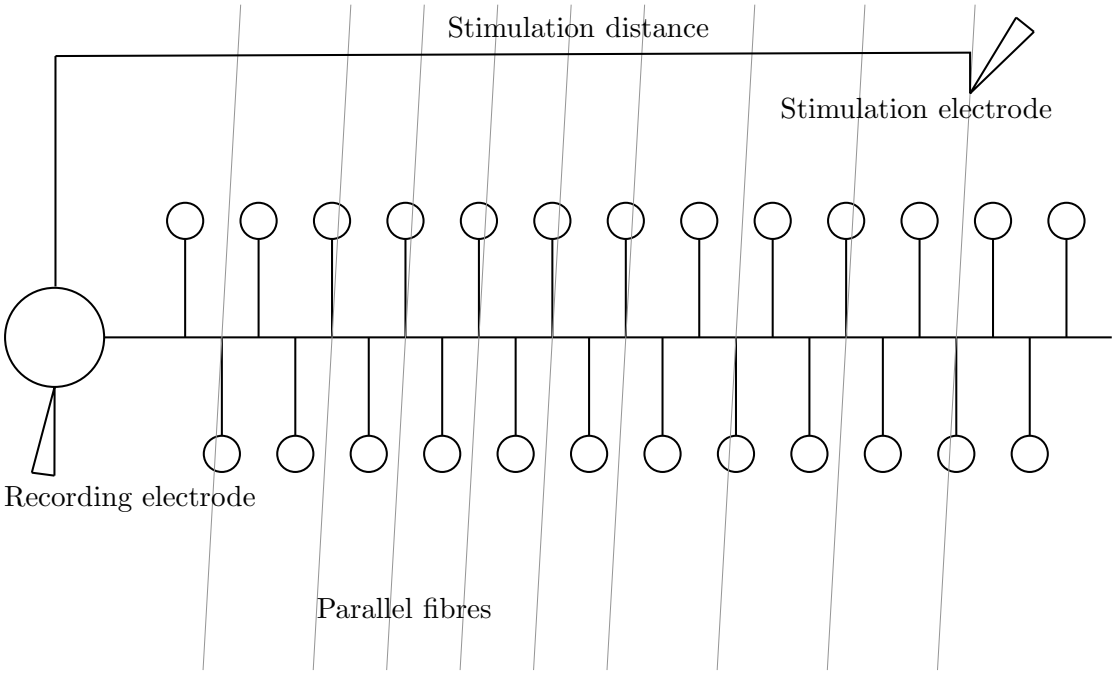

FIGURE 4.18: A sketch of the experimental set up to determine the length constant of the cell. Action potentials are induced in the parallel fibres by the stimulating electrode, activating the synapses and stimulating the membrane at the Bergmann glial cell microdomain, and the response in the Bergmann glial cell is recorded in the soma. The parallel fibres are approximately perpendicular to the Bergmann glial cell fibre, so that the distance between the two electrodes (measured parallel to the Bergmann glial cell fibre) is approximately equal to the distance between the soma and the stimulated microdomain.

If the resistance of the fibre were truly negligible, we would expect the response of the soma to be independent of the distance to the stimulated microdomain, but the data clearly shows that this is not the case. Fitting exponential models to the data in figure 4.19 suggests that the three cells have length constants on the order of $30\,\mu$m, which is significantly shorter than our estimates of the length of the fibre in table 4.2 and thus we expect to see variations in the transmembrane potential within the fibre.

This motivates a model of the behaviour of the Bergmann glial cell which accounts for the resistance of the fibre. While the underlying behaviour of the microdomains will be equivalent to that described in section 4.2.4, we restructure the model to focus on the response of the transmembrane potential to currents through the microdomain membrane (where the equivalent circuit analysis dealt with the reverse case of currents induced by known changes in transmembrane potential).

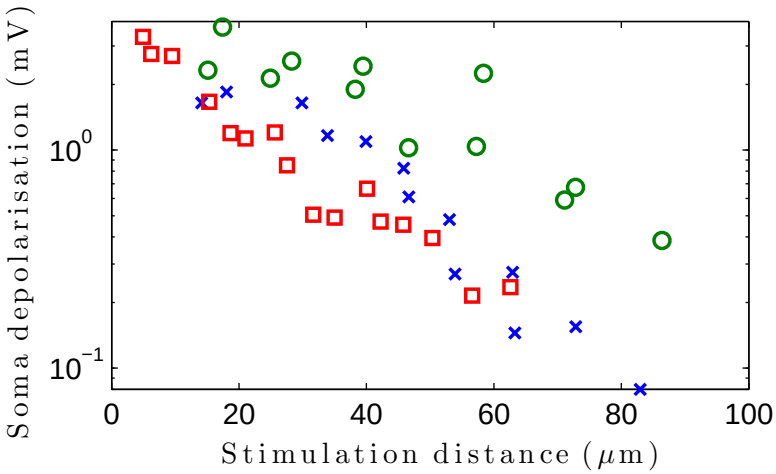

FIGURE 4.19: The maximum depolarisation observed in the soma decays as the distance to the stimulus current increases, obtained experimentally. Fitting an exponential model to the data predicts length constants of 30 μm (blue cell), 47 μm (green cell) and 17 μm (red cell)

4.3.2 Microdomains

If we denote the transmembrane potential in the fibre and proximal and distal paddles of the microdomain by Φ^*, ϕ^*, and ψ^* respectively, then the equivalent circuit tells us that the transmembrane potential in the proximal paddle behaves as follows

$$A_p C \frac{d\phi^*}{dt^*} = \frac{\Phi^* - \phi^*}{\Omega_p^s} + \frac{\psi^* - \phi^*}{\Omega_d^s} - A_p g_p^m \phi^*, \tag{4.47}$$

where all parameters are defined as in the equivalent circuit analysis in section 4.2.4. The terms in this equation represent (on the left-hand-side) the capacitive current flowing out of the proximal paddle membrane and (on the right-hand-side), the current through the proximal stalk from the fibre ($\Phi^* - \phi^*$ is the potential difference between the fibre and the proximal paddle) the current through the distal stalk from the distal paddle ($\phi^* - \psi^*$ is the potential drop between the proximal and distal paddles) and the leak current through passive ion channels in the proximal paddle membrane.

Similarly, for the distal paddle

$$A_d C \frac{d\psi^*}{dt^*} = -\frac{\psi^* - \phi^*}{\Omega_d^s} - A_d g_d^m \psi^* + I_c^*, \tag{4.48}$$

where I_c^* is the active ion channel current into the distal paddle, and all other parameters are again defined as in the equivalent circuit, except we have now allowed the passive leak conductances to vary across paddles (the equivalent circuit analysis was performed with $g_p^m = g_d^m = g^m$). The terms in this equation represent (on the left-hand-side) the capacitive current flowing out of the distal paddle membrane and (on the right-hand-side) the current through the distal stalk to the proximal paddle, the current through the passive ion channels and the current through the active ion channels.

Thus equations (4.48) and (4.48) are identical to the equivalent circuit presented in section 4.2.4, only they model the behaviour of the transmembrane potentials in the microdomain, rather than the membrane currents.

The fact that the transmembrane potential in the fibre is spatially varying (such that $\Phi^* = \Phi^*(x^*, t^*)$, where x^* denotes distance from the soma along the fibre) means that the transmembrane potentials in the microdomain must now also vary spatially. Thus we define ϕ_i^* and ψ_i^* to be the transmembrane potentials in the proximal and distal paddles of the i^{th} microdomain, located at a distance x_i from the soma, and obtain the following set of ODEs

$$A_p C \frac{d\phi_i^*}{dt^*} = \frac{\Phi^*(x_i, t^*) - \phi_i^*}{\Omega_p^s} + \frac{\psi_i^* - \phi_i^*}{\Omega_d^s} - A_p g_p^m \phi_i^* \qquad i = 1, \ldots, N \tag{4.49}$$

$$A_d C \frac{d\psi_i^*}{dt^*} = -\frac{\psi_i^* - \phi_i^*}{\Omega_d^s} - A_d g_d^m \psi_i^* + I_c^* \qquad i = 1, \ldots, N \tag{4.50}$$

which describe the behaviour of the transmembrane potential in each of the N microdomains.

4.3.2.1 Morphology and electrical properties of the fibre

The fibre of the Bergmann glial cell is sufficiently thin that we can apply the cable equation approximation detailed in part 2, which represents the longitudinal resistance of the fibre and the capacitance of and leak currents through its membrane. In this form, the currents from the microdomains form source terms to the cable equation, allowing us to investigate the behaviour of the complete cell.

We have chosen to model the microdomains as discrete current sources on the fibre membrane. The current I_i between the i^{th} microdomain and the fibre is given by Ohm's law (as in equation (4.49) above), and is proportional to the potential difference between the proximal paddle and the fibre, being given by

$$I_i = -\frac{\Phi^*(x_i) - \phi_i^*}{\Omega_p^s} \tag{4.51}$$

where ϕ_i denotes the transmembrane potential in the proximal paddle of the i^{th} microdomain.

We estimate from the data in figure 4.19 that the length constant of the fibre is of the order of ten micrometers, and thus is fairly large compared to the distance between microdomains (a distance of $10\,\mu$m on the fibre covers around five to five hundred microdomains (see table 4.2)). The large length constant suggests that the model could be simplified by instead treating the microdomains as a continuous distribution of current sources but, given the uncertainty in the estimates of the number of microdomains on the fibre, we have chosen to continue with the discrete current source model. We have, in fact, performed simulations of the model with this simplification and found that in the relevant parameter range the difference between the two approaches is negligible; discrepancies only occur for cells with very small numbers of microdomains.

In addition to the cable conductor model to describe the capacitance, resistance and leak conductances in the fibre we also introduce leak (i.e. constant, passive) conductances through membrane at the soma and end-foot.

The equation describing the behaviour of the fibre is thus

$$2\pi R_f C\frac{\partial \Phi^*}{\partial t^*} = \sigma\pi R_f^2\frac{\partial^2 \Phi^*}{\partial x^{*2}} - 2\pi R_f g_f \Phi^* - \sum_i \delta(x^* - x_i)\frac{\Phi^* - \phi_i^*}{\Omega_p^s}, \tag{4.52}$$

where R_f is the fibre radius, σ is the intracellular electrolyte conductivity, g_f is the leak conductance per unit area of the fibre membrane and x_i is the distance from the soma of the i^{th} microdomain. (This is the standard cable equation for a fibre with a distributed leak conductance, to which we have added current sources describing the current between the fibre and the microdomains.)

Boundary condition at the soma: We assume the membrane of the soma has constant, passive conductance per unit area g_s and surface area A_s. The total current flowing out through the soma membrane is given by

$$I_s^* = A_s g_s \, \Phi^*|_{x=0} \tag{4.53}$$

We currently do not account for the capacitive effects of the soma membrane, which we expect to be small relative to those of the microdomains.

Kirchoff's law dictates that the longitudinal current in the fibre at the soma must equal the current out of the cell through the soma membrane, thus

$$-\, I^*|_{x=0} = I_s^* \tag{4.54}$$

and since the current density in the fibre is given by the longitudinal gradient of the transmembrane potential, as follows:

$$I^*|_{x=0} = -\pi R_f^2 \sigma \left. \frac{\partial \Phi^*}{\partial x^*} \right|_{x^*=0}, \tag{4.55}$$

the boundary condition on Φ^* at the end of the fibre attached to the soma is

$$\left. \frac{\partial \Phi^*}{\partial x^*} \right|_{x^*=0} = \frac{A_s g_s}{\pi R_f^2 \sigma} \, \Phi^*|_{x^*=0}\,, \tag{4.56}$$

Boundary condition at the end-foot: We assume the end-foot has constant, passive conductance per unit area g_e and surface area A_e. The current through the end-foot is thus given by

$$I_e^* = A_e g_e \, \Phi^*|_{x=L} \tag{4.57}$$

where L is the length of the fibre. Again, we have ignored the capacitance of the end-foot membrane, which we expect to be relatively small.

Kirchoff's law again dictates that the longitudinal current in the fibre at the end-foot must equal the current out of the cell through the end-foot membrane, and thus the

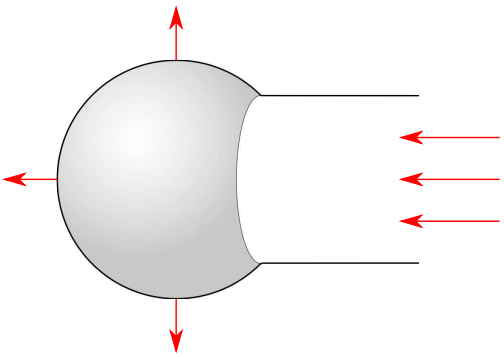

FIGURE 4.20: Sketch of soma, with current flows in red

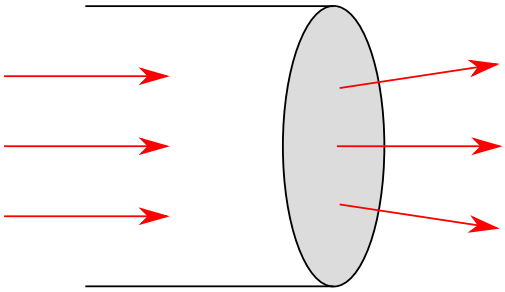

FIGURE 4.21: Sketch of end-foot, with current flows in red

boundary condition at the end-foot is

$$\left.\frac{\partial \Phi^*}{\partial x^*}\right|_{x^*=L} = -\frac{A_e g_e}{\pi R_f^2 \sigma}\, \Phi^*|_{x^*=L} \tag{4.58}$$

4.3.2.2 Full model of the electrical behaviour of the cell

Equation (4.52), describing the behaviour of the fibre, is coupled to equations (4.49) and (4.50), describing the behaviour of the microdomains, to produce a complete model of the electrical behaviour of the Bergmann glial cell.

Appropriate boundary conditions are imposed by considering the behaviour at the soma (4.56) and the end-foot (4.58), and the problem is closed by imposing an initial condition on the potential in the fibre and the two parts of the microdomain. The full model is

thus

$$2\pi R_f C\frac{\partial\Phi^*}{\partial t^*} = \sigma\pi R_f^2\frac{\partial^2\Phi^*}{\partial x^{*2}} - 2\pi R_f g_f\Phi^* - \sum_i \delta\left(x^* - x_i\right)\frac{\Phi^* - \phi_i^*}{\Omega_p^s}, \tag{4.59}$$

$$CA_p\frac{\partial\phi_i^*}{\partial t^*} = \frac{\Phi^*\left(x_i\right) - \phi_i^*}{\Omega_p^s} + \frac{\psi_i^* - \phi_i^*}{\Omega_d^s} - A_p g_p^m\phi_i^*, \tag{4.60}$$

$$CA_d\frac{\partial\psi_i^*}{\partial t^*} = -\frac{\psi_i^* - \phi_i^*}{\Omega_d^s} - A_d g_d^m\psi_i^* + I_{c,i}^* \tag{4.61}$$

$$\frac{\partial\Phi^*}{\partial x^*}\left(0,t^*\right) = \frac{A_s g_s}{\pi R_f^2\sigma}\Phi^*\left(0,t^*\right), \tag{4.62}$$

$$\frac{\partial\Phi^*}{\partial x^*}\left(L,t^*\right) = -\frac{A_e g_e}{\pi R_f^2\sigma}\Phi^*\left(L,t^*\right), \tag{4.63}$$

$$\Phi^*\left(x^*,0\right) = f_1^*\left(x^*\right), \tag{4.64}$$

$$\phi_i^*\left(x^*,0\right) = f_2^*\left(x_i\right), \tag{4.65}$$

$$\psi_i^*\left(x^*,0\right) = f_3^*\left(x_i\right), \tag{4.66}$$

The parameters of this model are determined from estimates from the literature (see table 4.2) or, where possible, from fitting the equivalent circuit model in section 4.2.4 to experimental data (these parameters are summarised in table 4.1). The radius of the fibre is determined by fitting the length constant of the model to the data shown in figure 4.19.

From the comparison of the experimental data and the response of the model to experimental conditions shown in figures 4.23 to 4.25, we can see that the model makes good predictions of the electrical behaviour of the Bergmann glial cell. We now derive a model of the ion transport in the microdomains, to allow us to investigate the cell's ability to redistribute ions.

4.4 Ion concentrations

To obtain more insight into the function of the Bergmann glia, we need a model capable of describing ion transport through these cells. This will allow us to quantify both the cell's effectiveness in siphoning potassium ions away from active synapses and the significance of sodium ion accumulation on the transport of glutamate into the cell. The

flow of current within the microdomain may also be affected by the ion concentrations, so it is useful to explore the electrochemistry of the cell in a little more detail, to determine the size and significance of all these effects.

In appendix B we examine the effects that currents in the microdomains have on the intracellular ion concentrations and produce the model of ion concentrations given in equations (4.67) to (4.70) which describes the behaviour of sodium and potassium ions in the microdomains. This model is derived from the Poisson-Nernst-Planck equations, a basic continuum model of ion concentrations in an electric field, accounting for the fluxes of ions induced by the concentration and potential gradients in the microdomains, and the effects of the ion concentrations on the electric field and the conductivity of the electrolyte (see, for example, [72]). These changes in conductivity mean that the resistance of the stalks, Ω_p^s and Ω_d^s, should in fact become functions of the potassium concentrations in the paddles the stalk connects (i.e. $\Omega_p^s = \Omega_{p,i}^s\left(K_f, K_{p,i}^*\right)$ and $\Omega_d^s = \Omega_{d,i}^s\left(K_{p,i}^*, K_{d,i}^*\right)$ where K_f is the concentration in the fibre, and $K_{p,i}^*$ and $K_{d,i}^*$ are the potassium concentrations in the proximal and distal paddles of the i^{th} microdomain. However, simulations suggest that the variations in concentrations under realistic conditions are small enough that the resistances of the stalks do not vary significantly, and so the behaviour of the transmembrane potentials can be decoupled from the behaviour of the ion concentrations. Thus equations (4.59) to (4.66) are sufficient to describe the transmembrane potential with or without changes in ion concentrations and the ion concentrations then passively follow the electric fields.

The situation we consider in appendix B is of three reservoirs of ions, representing the fibre, proximal paddle and distal paddle, connected by the proximal and distal stalks, and is summarised in figure 4.22. The dominant species of ions in these reservoirs (those found at highest concentrations) are potassium and chloride, with a much smaller concentration of sodium ions. The electrolyte in the majority of the fibre and microdomains (excluding the very narrow Debye layers close to the membrane) is charge neutral, meaning that the concentration of positive ions is balanced (almost) exactly by the concentration of negative ions. Practically, this means that the concentrations of potassium and chloride ions are equal everywhere except in the Debye layers, and so we only have

to track the behaviour of one ion to determine the concentrations of both. The fibre is large enough that the concentration within it is not changed by the relatively small fluxes from the microdomains, so we denote by K_f and N_f the constant concentrations of potassium and sodium ions in the fibre, respectively. The relatively small volumes of the proximal and distal paddles mean that the concentrations within them will not vary spatially, although they can change over time in response to changes in transmembrane potential or to input fluxes through the membrane. Thus these concentrations are given by $K^*_{p,i}(t^*)$ and $K^*_{d,i}(t^*)$ (the potassium concentrations in the proximal and distal paddles of the i^{th} microdomain, respectively) and $N^*_{p,i}(t^*)$ and $N^*_{d,i}(t^*)$ (the sodium concentrations in the proximal and distal paddles of the i^{th} microdomain, respectively). We have chosen not to explicitly include the chloride concentration, because it can be trivially determined from the potassium.

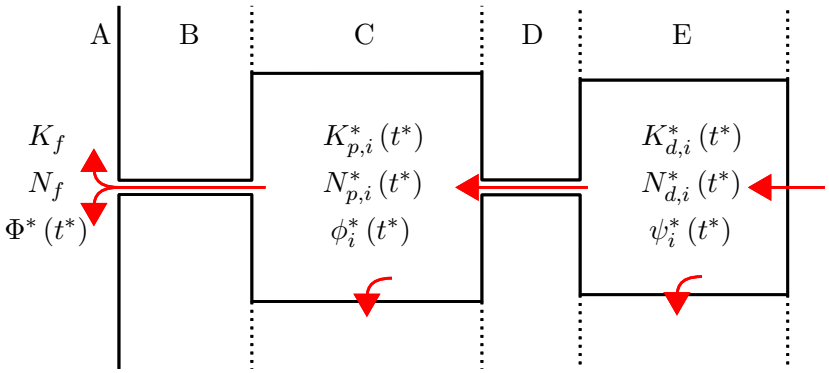

FIGURE 4.22: Ion concentrations and fluxes in the simple model of the microdomain. The fibre (A) is large enough that the ion concentrations are unaffected by the relatively small fluxes of ions from the microdomains, and hence are constant (K_f, N_f). The concentrations are constant throughout the proximal paddle ($K^*_{p,i}$ and $N^*_{p,i}$, C) and distal paddle ($K^*_{d,i}$ and $N^*_{d,i}$, E). Fluxes are driven through the stalks (B and D) by the concentration gradients between the paddles, and carried through the stalks and paddle membranes by the currents.

There are three significant fluxes through each of the stalks, a potassium and a sodium flux driven by the concentration gradient and a potassium flux carried by the current through the stalk. In appendix B we determine that the fluxes driven by the concentration gradients in the stalks are proportional to the concentration change across them, and that the current is carried by equal and opposite movements of potassium and chloride ions. The diffusive resistance of the stalks is determined by the ratio of their cross-sectional area to their length (longer, thinner stalks have a higher diffusive

resistance than shorter, fatter ones), which also determines their electrical resistance. Thus the estimates of the electrical resistances of the stalks obtained in section 4.2.4 can also be used to estimate their diffusive resistance.

In addition to the fluxes through the stalk, the model also accounts for the ion fluxes carried by leak currents through the paddle membranes. This model is derived in full detail in appendix B, and stated as follows for the potassium and sodium concentrations in the i^{th} proximal paddle

$$\begin{aligned} V_p \frac{dK^*_{p,i}}{dt^*} &= \frac{RT}{\Pi_0 F^2 \Omega^s_p}\left(K_f - K^*_{p,i}\right) + \frac{RT}{\Pi_0 F^2 \Omega^s_d}\left(K^*_{d,i} - K^*_{p,i}\right) - \frac{A_p g_p}{F}\phi^*_i \\ &\quad + \frac{1}{2F}\frac{K_f}{K_f + N_f}\left(\frac{\Phi^*(x_i) - \phi^*_i}{\Omega^s_p} + \frac{\psi^*_i - \phi^*_i}{\Omega^s_d}\right) \end{aligned} \tag{4.67}$$

$$\begin{aligned} V_p \frac{dN^*_{p,i}}{dt^*} &= \frac{RT}{\Pi_0 F^2 \Omega^s_p}\left(N_f - N^*_{p,i}\right) + \frac{RT}{\Pi_0 F^2 \Omega^s_d}\left(N^*_{d,i} - N^*_{p,i}\right) \\ &\quad + \frac{1}{2F}\frac{N_f}{K_f + N_f}\left(\frac{\Phi^*(x_i) - \phi^*_i}{\Omega^s_p} + \frac{\psi^*_i - \phi^*_i}{\Omega^s_d}\right) \end{aligned} \tag{4.68}$$

where V_p is the volume of the proximal paddle, K_f and N_f are the (constant) potassium and sodium concentrations in the fibre, and $K^*_{p,i}$ and $N^*_{p,i}$ are the potassium and sodium concentrations in the proximal paddle of the i^{th} microdomain, and $K^*_{d,i}$ and $N^*_{d,i}$ are the potassium and sodium concentrations in the distal paddle of the i^{th} microdomain. R is the ideal gas constant ($R = 8.31\,\text{J}\cdot\text{mol}^{-1}\cdot\text{K}^{-1}$), T is the temperature ($T = 310\,\text{K}$), Π_0 is the resting concentration of positive (potassium and sodium) ions ($\Pi_0 = 145\,\text{mol}\cdot\text{m}^{-3}$) and F is the Faraday constant ($F = 9.65\times10^4\,\text{C}\cdot\text{mol}^{-1}$). The terms in equation (4.67) represent, respectively, the concentration-gradient driven potassium flux between the fibre and the proximal paddle, the concentration-gradient driven potassium flux between the proximal and distal paddles, the potassium flux carried by the leak current through the proximal paddle membrane, the potassium flux carried by the current between the proximal paddle and the fibre and the potassium flux carried by the current between the proximal and distal paddles. The factor of one half in the terms representing the flux carried by the currents is derived from the fact that the transference number of the electrolyte is approximately one half, and thus current is carried by equal and opposite flows of positive and negative ions (i.e. half of the current is carried by sodium and potassium ions moving in one direction, and the other half by chloride ions moving

in the opposite direction). The factor of the ratio of the potassium concentration to the total concentration of positive ions (i.e. $\frac{K_f}{K_f + N_f}$) simply reflects the fact that potassium and sodium ions constitute the current flux in the same proportions they are present in in the electrolyte — strictly speaking this proportion will change as the ion concentrations fluctuate in the microdomains, but we have found in practice (much like for the resistances of the stalks as described above) that the actual variations are small enough that the resting concentration proportions can be used. The terms in equation (4.68) represent, respectively, the concentration-gradient driven sodium fluxes between the fibre and the proximal paddle, and the proximal paddle and the distal paddle, and the sodium fluxes driven by the current between the fibre and the proximal paddle and the proximal and distal paddles (the factor of on half is determined by the transference number, as noted for the potassium fluxes, and the remaining factor represents the ratio of sodium ions to positive ions present in the electrolyte).

The model of the potassium and sodium concentrations in the distal paddle is as follows

$$V_d \frac{dK^*_{d,i}}{dt^*} = \frac{RT}{\Pi_0 F^2 \Omega^s_d} \left(K^*_{p,i} - K^*_{d,i}\right) - \frac{A_d g_d}{F} \psi^*_i + \frac{1}{2F} \frac{K_f}{K_f + N_f} \frac{\phi^*_i - \psi^*_i}{\Omega^s_d} + \mathcal{F}^*_{\mathrm{K},i}\left(t^*\right) \quad (4.69)$$

$$V_d \frac{dN^*_{d,i}}{dt^*} = \frac{RT}{\Pi_0 F^2 \Omega^s_d} \left(N^*_{p,i} - N^*_{d,i}\right) + \frac{1}{2F} \frac{K_f}{K_f + N_f} \frac{\phi^*_i - \psi^*_i}{\Omega^s_d} + \mathcal{F}^*_{\mathrm{Na},i}\left(t^*\right) \quad (4.70)$$

where V_d is the volume of the distal paddle. The first term in each of these equations again represents the concentration-gradient driven flux, the second term in equation (4.69) the potassium flux carried by the leak current through the distal paddle membrane and the third term in equation (4.69) and the second in equation (4.70) represent the current between the proximal and distal paddles, divided into potassium and sodium components. The final terms in each equation ($\mathcal{F}^*_{\mathrm{K},i}\left(t^*\right)$ and $\mathcal{F}^*_{\mathrm{Na},i}\left(t^*\right)$) represent the ion fluxes carried into the distal paddle by the ion channels in the distal membrane responding to synaptic activity. Thus the ion channel current into the distal paddle, $I^*_{c,i}$, introduce in equation (4.48) and detailed in section 4.3.2, can be thought of as being driven by the sum of the fluxes of potassium and sodium ions, as follows

$$I^*_{c,i} = F \times \left(\mathcal{F}^*_{\mathrm{K},i}\left(t^*\right) + \mathcal{F}^*_{\mathrm{Na},i}\left(t^*\right)\right) \quad (4.71)$$

where F is the Faraday constant.

4.5 Nondimensionalisation of the complete model

We non-dimensionalise equations (4.59) to (4.70) as follows:

$$\Phi^* = F\tilde{\mathcal{F}}\Omega_d^s\Phi, \qquad \phi_i^* = F\tilde{\mathcal{F}}\Omega_d^s\phi_i, \qquad \psi_i^* = F\tilde{\mathcal{F}}\Omega_d^s\psi_i, \tag{4.72}$$

$$t^* = CA_d\Omega_d^s t, \qquad x^* = Lx, \tag{4.73}$$

$$K_{\mathrm{x},i}^* = \frac{CA_d\tilde{\mathcal{F}}\Omega_d^s}{V_d}K_{\mathrm{x},i}, \qquad N_{\mathrm{x},i}^* = \frac{CA_d\tilde{\mathcal{F}}\Omega_d^s}{V_d}N_{\mathrm{x},i}, \qquad \mathcal{F}_{\mathrm{x}}^* = \tilde{\mathcal{F}}\mathcal{F}_{\mathrm{x}} \tag{4.74}$$

This leads to the following dimensionless closed system for the electric potentials

$$\alpha\frac{\partial\Phi}{\partial t} = \beta\frac{\partial^2\Phi}{\partial x^2} - \bar{g}_f\Phi - \bar{\Omega}\sum_i \delta\left(x-\lambda_i\right)\left(\Phi-\phi_i\right), \tag{4.75}$$

$$\bar{A}\frac{d\phi_i}{dt} = \bar{\Omega}\left(\Phi\left(\lambda_i\right)-\phi_i\right) + \left(\psi_i-\phi_i\right) - \bar{g}_p\phi_i, \tag{4.76}$$

$$\frac{d\psi_i}{dt} = \left(\phi_i-\psi_i\right) - \bar{g}_d\psi_i + \mathcal{F}_{\mathrm{K},i}\left(t\right) + \mathcal{F}_{\mathrm{Na},i}\left(t\right), \tag{4.77}$$

with boundary and initial conditions

$$\left.\frac{\partial\Phi}{\partial x}\right|_{x=0} = \bar{g}_s\Phi\left(0,t\right), \qquad \left.\frac{\partial\Phi}{\partial x}\right|_{x=1} = -\bar{g}_e\Phi\left(1,t\right), \tag{4.78}$$

$$\Phi\left(x,0\right) = f_1\left(x\right), \qquad \phi_i\left(0\right) = f_2\left(x\right), \qquad \psi_i\left(0\right) = f_3\left(x\right). \tag{4.79}$$

in which the dimensionless parameters are given by

$$\alpha = \frac{2\pi LR_f}{A_d}, \qquad \beta = \frac{\sigma\pi R_f^2\Omega_d^s}{L}, \qquad \bar{g}_f = 2\pi LR_f g_f\Omega_d^s, \qquad \lambda_i = \frac{x_i}{L} \tag{4.80}$$

$$\bar{A} = \frac{A_p}{A_d}, \qquad \bar{\Omega} = \frac{\Omega_d^s}{\Omega_p^s}, \qquad \bar{g}_p = A_p g_p\Omega_d^s, \qquad \bar{g}_d = A_d g_d\Omega_d^s, \tag{4.81}$$

where

$$\bar{g}_s = \frac{A_s CLg_s}{\sigma\pi R_f^2}, \qquad \bar{g}_e = \frac{A_e Lg_e}{\sigma\pi R_f^2}, \tag{4.82}$$

The dimensionless model for the ion concentrations, which couples to that for the potentials, is given by

$$\bar{V}\frac{dK_{p,i}}{dt} = \gamma\bar{\Omega}\left(\bar{K} - K_{p,i}\right) + \gamma\left(K_{d,i} - K_{p,i}\right) - \bar{g}_p\phi_i + \frac{1}{2}\bar{\Omega}\left(\Phi\left(\lambda_i\right) - \phi_i\right) + \frac{1}{2}\left(\psi_i - \phi_i\right), \tag{4.83}$$

$$\frac{dK_{d,i}}{dt} = \gamma\left(K_{p,i} - K_{d,i}\right) - \bar{g}_d\psi_i + \mathcal{F}_{\mathrm{K},i} + \frac{1}{2}\left(\phi_i - \psi_i\right), \tag{4.84}$$

$$\bar{V}\frac{dN_{p,i}}{dt} = \gamma\bar{\Omega}\left(\bar{N} - N_{p,i}\right) + \gamma\left(N_{d,i} - N_{p,i}\right), \tag{4.85}$$

$$\frac{dN_{d,i}}{dt} = \gamma\left(N_{p,i} - N_{d,i}\right) + \mathcal{F}_{\mathrm{Na},i}, \tag{4.86}$$

and the initial concentrations are given by

$$K_{p,i}\left(0\right) = \bar{K}, \qquad K_{d,i}\left(0\right) = \bar{K}, \qquad N_{p,i}\left(0\right) = \bar{N}, \qquad N_{d,i}\left(0\right) = \bar{N}. \tag{4.87}$$

where the dimensionless parameters are given by

$$\gamma = \frac{A_d RT}{F^2\Pi_0 V_d}, \qquad \bar{V} = \frac{V_p}{V_d}, \tag{4.88}$$

$$\bar{K} = \frac{V_d}{A_d C\tilde{\mathcal{F}}\Omega_d^s}K_f, \qquad \bar{N} = \frac{V_d}{A_d C\tilde{\mathcal{F}}\Omega_d^s}N_f, \tag{4.89}$$

Details of the numerical solution of this problem are given in Appendix C.

4.6 Results of simulations

4.6.1 Comparison of the model to experimental data

To compare the model of the cell's electrical behaviour (equations 4.75 to 4.77) to the experimental data, we first need to account for the length constant of the fibre, which will mean that the potential drop is not equal across each microdomain. As the equivalent circuit model is linear in V, the potential drop across the microdomain, the current through a collection of microdomains at varying potential drops is equivalent to the current through the same number of microdomains all at the same, average potential drop. Thus to correctly determine the parameters of the cell with the equivalent circuit

model we first need to determine the average potential drop across the microdomain from the fibre length constant, and then use this as the potential drop in the equivalent circuit model. Using these parameters, we then simulate input currents at varying distances from the soma, and match the length constant of the cell to the data in figure 4.19 by varying the radius of the fibre.

The results of this simulation are shown in figures 4.23 and 4.25, where we see the fit to the length constant is excellent, but the fit to the voltage clamp data, while good, is not as good as before. This is perhaps to be expected, as the fibre membrane adds an (albeit small) capacitive effect which is not accounted for by the equivalent circuit model.

We are confident that the model makes very good qualitative (and good quantitative) predictions of the behaviour of the cell, and that the two-paddle representation of the microdomain is sufficient to model the response of the cell to stimulation, suggesting that the simplifications we have made are not eliminating any significant aspects of the cell's behaviour. Similarly, the cable equation representation of the fibre does not introduce any significant behaviour not seen in the experimental data.

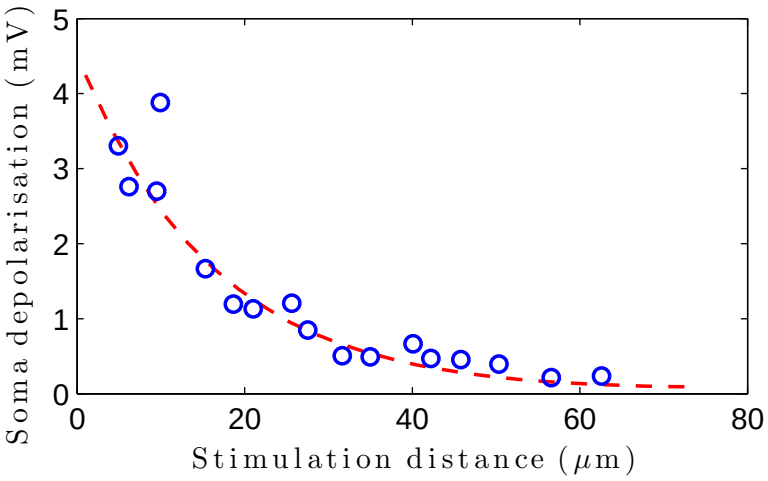

FIGURE 4.23: Comparison of the length constant determined by experiment (blue circles) to that predicted by the model (red , dashed curve). Parameters from table 4.3

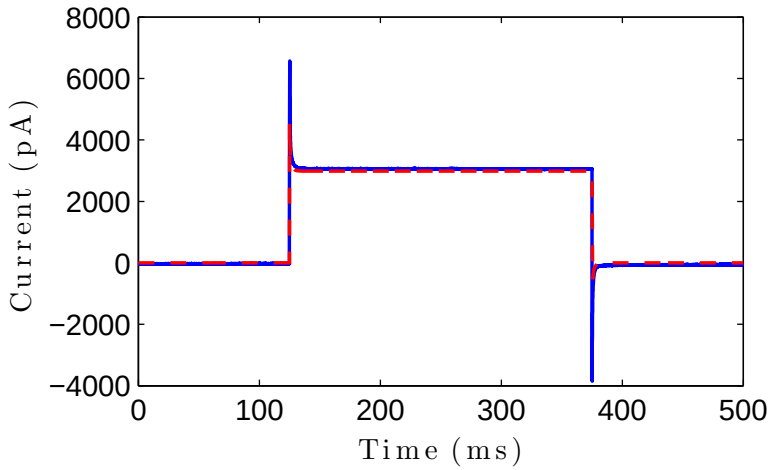

FIGURE 4.24: Comparison of model to voltage clamp data using same parameters as used for length constant in figure 4.23. Parameters from table 4.3

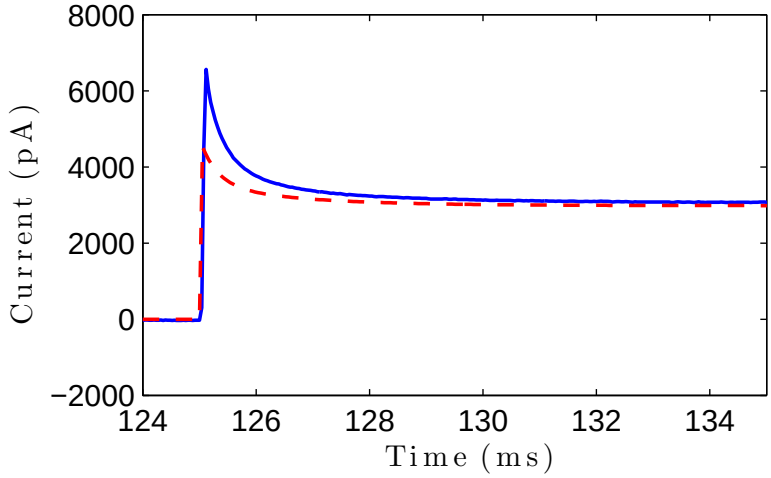

FIGURE 4.25: Comparison of model to voltage clamp data using same parameters as used for length constant in figure 4.23, over a shorter time scale. Parameters from table 4.3

4.6.2 Microdomain depolarisations — comparisons with existing model

We can also compare our model — and our choice of parameters — with the equivalent model used in [30], as shown in figures 4.26 to 4.29. Figure 4.26 shows the time course of the depolarisations in the different paddles of the microdomain predicted by Grosche. Our representation is much simpler than that in Grosche, so there is not a one-to-one correspondence between the regions of the microdomain, but we believe the region labelled "synapse 1" in their paper corresponds approximately to our distal paddle, that labelled "stalk" to our proximal paddle and that labelled "stem process" to our fibre.

TABLE 4.3: Parameters to produce figures 4.23 to 4.25

Parameter	Value	Unit
L	75×10^{-6}	m
R_f	0.5×10^{-6}	m
C	1×10^{-2}	$\mathrm{F} \cdot \mathrm{m}^{-2}$
σ	0.8	$\mathrm{S} \cdot \mathrm{m}$
A_s	1×10^{-11}	m^2
A_e	1×10^{-11}	m^2
V_d	5×10^{-18}	m^3
V_p	10×10^{-18}	m^3
K_f	140	$\mathrm{mol} \cdot \mathrm{m}^{-3}$
N_f	5	$\mathrm{mol} \cdot \mathrm{m}^{-3}$
R	8.31	$\mathrm{J} \cdot \mathrm{mol}^{-1} \cdot \mathrm{K}^{-1}$
T	310	K
Π_0	$K_f + N_f = 145$	$\mathrm{mol} \cdot \mathrm{m}^{-3}$
F	9.65×10^4	$\mathrm{C} \cdot \mathrm{mol}^{-1}$
Ω_p^s	1.0×10^9	Ω
Ω_d^s	1.4×10^9	Ω
A_p	52.5×10^{-12}	m^2
A_d	186×10^{-12}	m^2
g_f	0	$\mathrm{S} \cdot \mathrm{m}^2$
g_p	4.6	$\mathrm{S} \cdot \mathrm{m}^2$
g_d	4.6	$\mathrm{S} \cdot \mathrm{m}^2$
g_s	0	$\mathrm{S} \cdot \mathrm{m}^2$
g_e	0	$\mathrm{S} \cdot \mathrm{m}^2$

As we can see, with the parameters estimated from the voltage-clamp on cell one (figure 4.27), the response of the microdomains is much slower in our model than in Grosche. The speed of the response in each paddle of the microdomain is dictated by the capacitance, and as the areas of cell one (and therefore the capacitances) are larger than the estimates found in Grosche, it is perhaps understandable that our model responds more slowly. However, using the parameters from cell two, which are much closer to those in Grosche, the response of the cell is still significantly slower (figure 4.28). In fact, in order to see a response commensurate with that seen in figure 4.26, we must reduce the

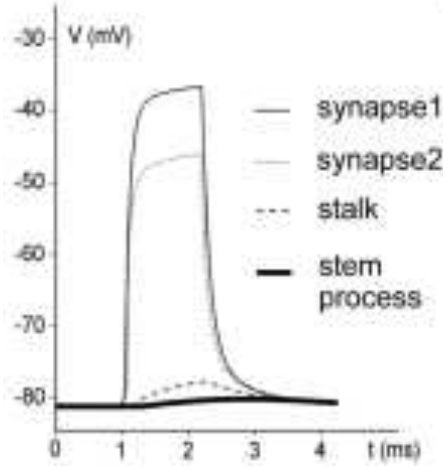

FIGURE 4.26: Time course of microdomain depolarisations, as predicted by model in [30]. Reproduced, with permission, from [30].

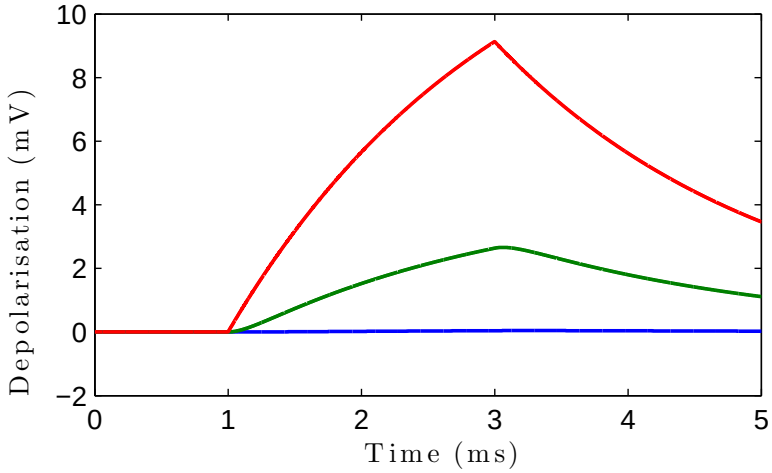

FIGURE 4.27: Time course of depolarisations in distal paddle (——), proximal paddle (——) and fibre (——), using parameters determined by voltage clamp on cell one (tables 4.4 and 4.5).

areas of the microdomains in our model by an order of magnitude (figure 4.29 shows the response when $A_p = A_d = 10\,\mu\text{m}^2$). This disparity is probably too big to be explained by random variations in the sizes of parameters — the estimate of the capacitive surface area of the paddles found by matching to [30] lies significantly outside the range of our predictions.

It is not clear the exact form that the model in [30] takes, but we suggest it represents one of the cases in figure 4.30 or 4.31, in which the current is being injected into a paddle with a very small surface area. The case in figure 4.30, with two paddles where the distal paddle is very small, is not consistent with the voltage clamp data, but it is possible that

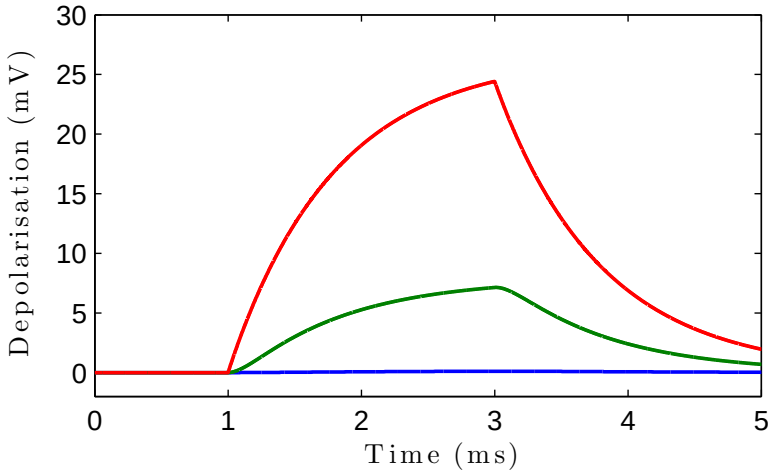

FIGURE 4.28: Time course of depolarisations in distal paddle (——), proximal paddle (——) and fibre (——), using parameters determined by voltage clamp on cell two (tables 4.4 and 4.6).

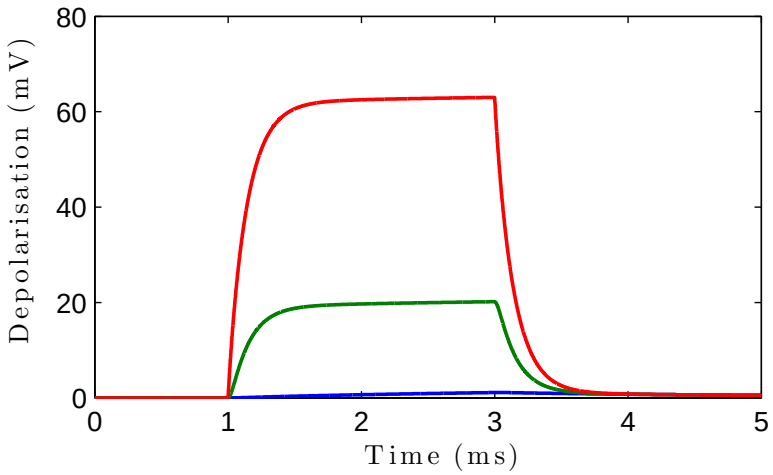

FIGURE 4.29: Time course of depolarisations in distal paddle (——), proximal paddle (——) and fibre (——), using parameters chosen to match to figure 4.26 (tables 4.4 and 4.7).

the microdomains contain more than two paddles, as in figure 4.31, but the contribution of the third paddle to the voltage clamp current is too small to be detected.

From the amplitude of the depolarisations in the different paddles, we can also see that the balance of resistances is slightly different in our model. In [30], almost all of the potential drop (and thus the majority of the resistance) in the microdomain occurs between the distal and proximal paddles, whereas our estimates suggest that the drop is more evenly distributed between the fibre and the proximal paddle and the proximal and distal paddles. This discrepancy may be explained by random variations in

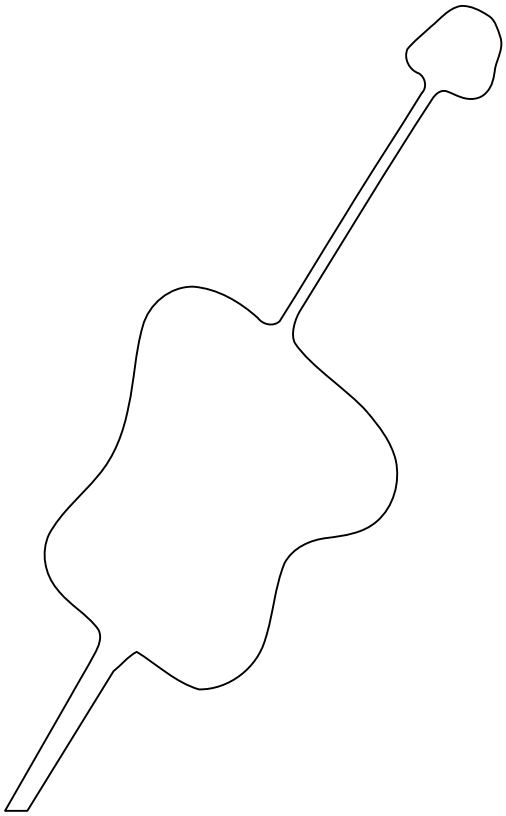

FIGURE 4.30: A two paddle microdomain with a small distal surface area and a large distal resistance.

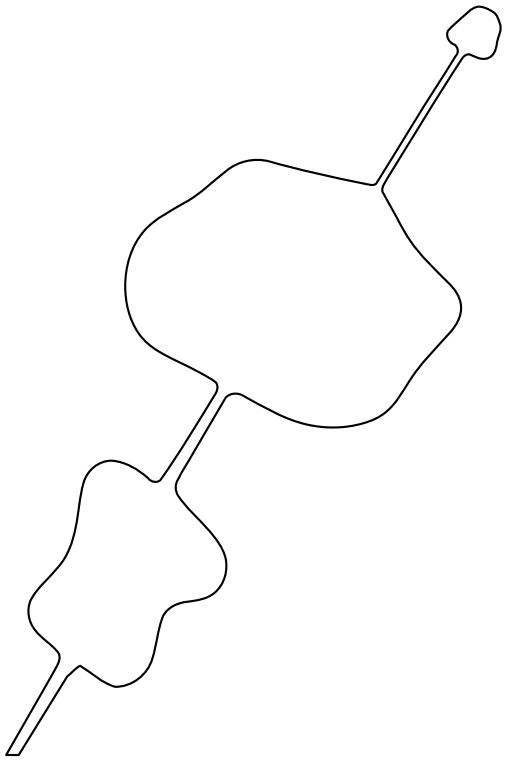

FIGURE 4.31: A three paddle microdomain, with the additional paddle having a small surface area, connected by a large resistance.

microdomain geometry, but we emphasis that our estimates are systematically derived from electrophysiological data.

4.6.3 Ion Movements

Another useful aspect of our model is that it allows us to predict the flux of potassium ions through the membrane of the cell. In particular, we can quantify how many and where ions flow into or out of the cell, allowing us to evaluate how effective the cell is at siphoning ions away from the synapses in the microdomains. To produce 4.32 and 4.33 we simulate injecting current into a microdomain in the centre of the fibre and record the fluxes out of the other regions of the cell, for sufficiently long that the cell returns to resting potential. This allows us to report the proportion of ions which are siphoned effectively (those that leave through the end-foot membrane) and the proportion which leak back into the surrounding extracellular space.

TABLE 4.4: Parameters to produce figures 4.27 to 4.29 and 4.32 to 4.38

Parameter	Value	Unit
L	200×10^{-6}	m
R_f	1.5×10^{-6}	m
C	1×10^{-2}	$\mathrm{F} \cdot \mathrm{m}^{-2}$
σ	0.8	$\mathrm{S} \cdot \mathrm{m}$
A_s	1×10^{-11}	m^2
A_e	1×10^{-11}	m^2
V_d	5×10^{-18}	m^3
V_p	10×10^{-18}	m^3
K_f	140	$\mathrm{mol} \cdot \mathrm{m}^{-3}$
N_f	5	$\mathrm{mol} \cdot \mathrm{m}^{-3}$
R	8.31	$\mathrm{J} \cdot \mathrm{mol}^{-1} \cdot \mathrm{K}^{-1}$
T	310	K
Π_0	$K_f + N_f = 145$	$\mathrm{mol} \cdot \mathrm{m}^{-3}$
F	9.65×10^4	$\mathrm{C} \cdot \mathrm{mol}^{-1}$

TABLE 4.5: Parameters to produce figure 4.27

Parameter	Value	Unit
Ω_p^s	0.9×10^9	Ω
Ω_d^s	2.0×10^9	Ω
A_p	45.5×10^{-12}	m^2
A_d	697×10^{-12}	m^2
g_f	1.7	$\mathrm{S} \cdot \mathrm{m}^2$
g_p	1.7	$\mathrm{S} \cdot \mathrm{m}^2$
g_d	1.7	$\mathrm{S} \cdot \mathrm{m}^2$
g_s	1.7	$\mathrm{S} \cdot \mathrm{m}^2$
g_e	1.7	$\mathrm{S} \cdot \mathrm{m}^2$

TABLE 4.6: Parameters to produce figures 4.28 and 4.32 to 4.38

Parameter	Value	Unit
Ω_p^s	0.9×10^9	Ω
Ω_d^s	1.9×10^9	Ω
A_p	42.9×10^{-12}	m^2
A_d	145×10^{-12}	m^2
g_f	3.6	$\mathrm{S} \cdot \mathrm{m}^2$
g_p	3.6	$\mathrm{S} \cdot \mathrm{m}^2$
g_d	3.6	$\mathrm{S} \cdot \mathrm{m}^2$
g_s	3.6	$\mathrm{S} \cdot \mathrm{m}^2$
g_e	3.6	$\mathrm{S} \cdot \mathrm{m}^2$

TABLE 4.7: Parameters to produce figure 4.29

Parameter	Value	Unit
Ω_p^s	0.9×10^9	Ω
Ω_d^s	2.0×10^9	Ω
A_p	10×10^{-12}	m^2
A_d	10×10^{-12}	m^2
g_f	1.7	$\mathrm{S} \cdot \mathrm{m}^2$
g_p	1.7	$\mathrm{S} \cdot \mathrm{m}^2$
g_d	1.7	$\mathrm{S} \cdot \mathrm{m}^2$
g_s	1.7	$\mathrm{S} \cdot \mathrm{m}^2$
g_e	1.7	$\mathrm{S} \cdot \mathrm{m}^2$

We can see qualitatively how the end-foot conductance affects the behaviour of the cell, although our exact representation of inward-rectifying potassium channels may not be very realistic.

Measurements from the literature suggest that the conductance per unit area of the end-foot can be ten to sixty times higher than that of the fibre membrane [70]. This estimate is used in figure 4.32, where the end-foot conductance per unit area is varied over this range, and the model shows that only a very small proportion of ions leave the cell through the end-foot membrane.

However, it may be the surface area of the end-foot is larger than we have estimated — figure 3 in [106], for example, shows the fibre flaring out significantly to form the end

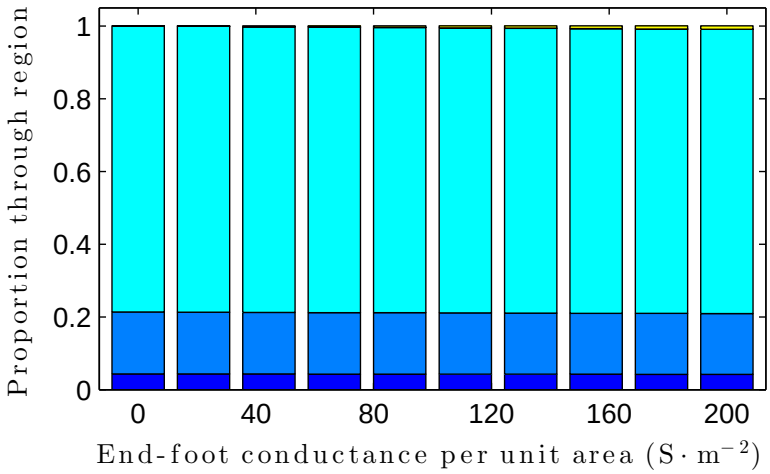

FIGURE 4.32: Proportion of ions flowing out of the cell by region, as a function of end-foot conductance per unit area: ( ) proportion out of fibre; ( ) proportion out of proximal paddle; ( ) proportion out of distal paddle; ( ) proportion out of soma; ( ) proportion out of end-foot. Parameters from tables 4.4 and 4.6 except end-foot conductance per unit area, which is varied.

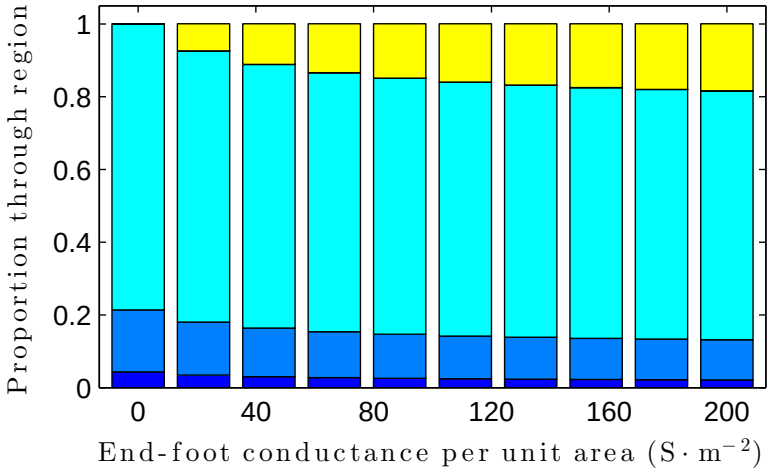

FIGURE 4.33: Proportion of ions flowing out of the cell by region, as a function of end-foot conductance per unit area: ( ) proportion out of fibre; ( ) proportion out of proximal paddle; ( ) proportion out of distal paddle; ( ) proportion out of soma; ( ) proportion out of end-foot. Parameters from tables 4.4 and 4.6 except end-foot conductance per unit area (g_e), which is varied and end-foot surface area ($A_e = 1 \times 10^{-9}\, m^{-2}$), which is increased.

foot. In this case, the total conductance of the end-foot membrane is doubly increased, by the effects of higher conductance per unit area and increased total surface area. Figure 4.33 shows the equivalent simulations to figure 4.32 but with end-foot surface area increased one hundred fold. In this case we start to see a significant proportion of ions flowing out of the end-foot, although the majority of ions still flow directly out of the microdomain.

4.6.4 Ion destinations

Figure 4.34 shows the currents out of the cell over a period of 300 ms (long enough for the current flows to have returned to zero) after a stimulation current was applied to a microdomain. The simulation uses the same parameters as those in the right-hand bar of figure 4.33 (i.e. from tables 4.4 and 4.6, but with end-foot conductance per unit area $g_e = 200\,\mathrm{S}\cdot\mathrm{m}^{-2}$ and surface area $A_e = 1\times10^{-9}\,\mathrm{m}^{-2}$).

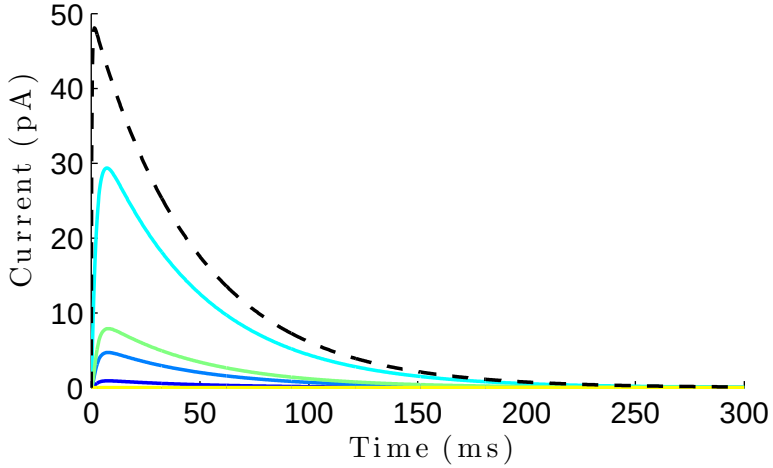

FIGURE 4.34: Current out of the cell by region: (——) proportion out of proximal paddle; (——) proportion out of distal paddle; (——) proportion out of fibre; (——) proportion out of soma; (——) proportion out of end-foot. Parameters equivalent to far right bar in figure 4.33 (i.e. from tables 4.4 and 4.6, but with end-foot conductance per unit area $g_e = 200\,\mathrm{S}\cdot\mathrm{m}^{-2}$ and surface area $A_e = 1\times10^{-9}\,\mathrm{m}^{-2}$). Dashed line shows stimulation current applied to microdomain.

Figures 4.35 and 4.36 show the ion fluxes into the microdomain on the left axis and the change in the total number of ions in the cell on the right. The fluxes are separated by where they enter the microdomain, either through the passive ion channels in the proximal and distal membrane, from the fibre driven by potential or concentration

gradients or introduced by the stimulation current through the active ion channels. We have chosen our input current to be carried by equal numbers of potassium and sodium ions to allows us to qualitatively judge how each species of ion behaves. The actual ionic composition of the current will vary depending on what kinds of ion channels are activated in the microdomain membrane, but the insights our model gives us are valid regardless of the exact details of the stimulation current.

Figure 4.35 is on the 300 ms scale of figure 4.34, over which we see that the fluxes are primarily driven by the depolarisation in the microdomain, which causes large fluxes out through the leak conductance in the distal paddle and smaller fluxes through the leak conductance in the proximal paddle and into the fibre. The flux driven into the fibre by concentration gradients is not significant on this scale. Figure 4.36 shows the behaviour of the simulation over a longer time-scale, on which the flux driven by the concentration gradient becomes significant. We see that the fast changes in potassium concentration driven by the large, membrane potential driven fluxes are counteracted by the smaller concentration gradient driven flux over a much longer time scale. The actual concentration of potassium ions changes only by a small amount, from an initial value of $140\,\mathrm{mol}\cdot\mathrm{m}^{-3}$ to a minimum of around $139\,\mathrm{mol}\cdot\mathrm{m}^{-3}$ in the stimulated microdomain, with the concentrations in other microdomains changing by less than $10^{-3}\,\mathrm{mol}\cdot\mathrm{m}^{-3}$.

Figures 4.37 and 4.38 show the equivalent results of the simulation for sodium ions. Note that the leak conductance out of the microdomains is thought to be carried through potassium channels, and the sodium concentration is small enough that potential driven fluxes are negligible, such that active ion channel currents and the concentration gradient driven flux to the fibre are the only significant fluxes here. As with the potassium concentration, the sodium concentration in the microdomains is changing only by small amounts, from an initial value of $5\,\mathrm{mol}\cdot\mathrm{m}^{-3}$ to a maximum of around $6\,\mathrm{mol}\cdot\mathrm{m}^{-3}$ in the stimulated microdomain.

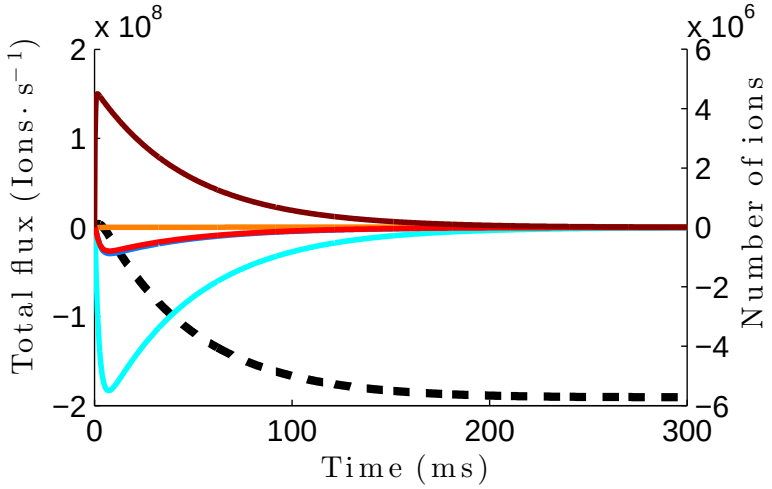

FIGURE 4.35: Potassium ions into microdomain by region: (——) proportion in through proximal paddle; (——) proportion in through distal paddle; (——) proportion in from fibre (concentration gradient); (——) proportion in from fibre (potential gradient); (——) proportion in through ion channels. Dashed, black curve shows accumulation of ions within microdomain.

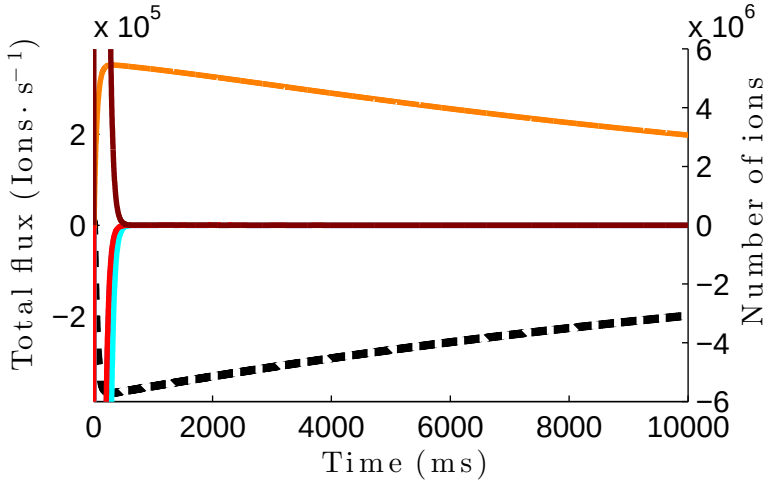

FIGURE 4.36: Potassium ions into microdomain by region: (——) proportion in through proximal paddle; (——) proportion in through distal paddle; (——) proportion in from fibre (concentration gradient); (——) proportion in from fibre (potential gradient); (——) proportion in through ion channels. Dashed, black curve shows accumulation of ions within microdomain.

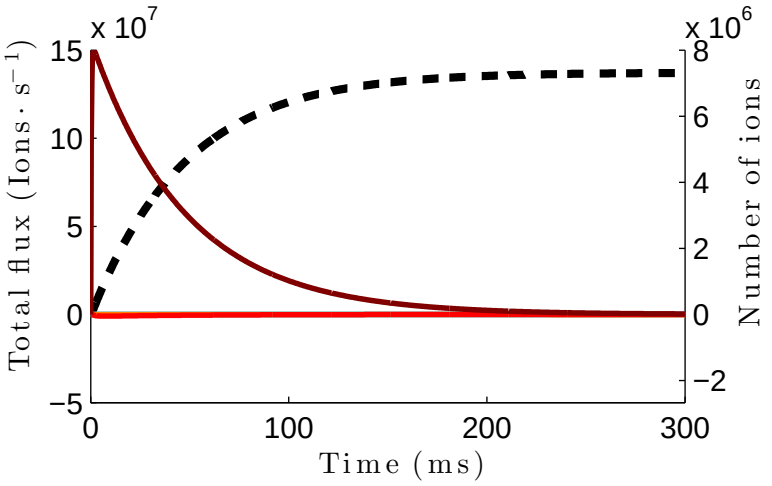

FIGURE 4.37: Sodium ions into microdomain by region: (——) proportion in through proximal paddle; (——) proportion in through distal paddle; (——) proportion in from fibre (concentration gradient); (——) proportion in from fibre (potential gradient); (——) proportion in through ion channels. Dashed, black curve shows accumulation of ions within microdomain.

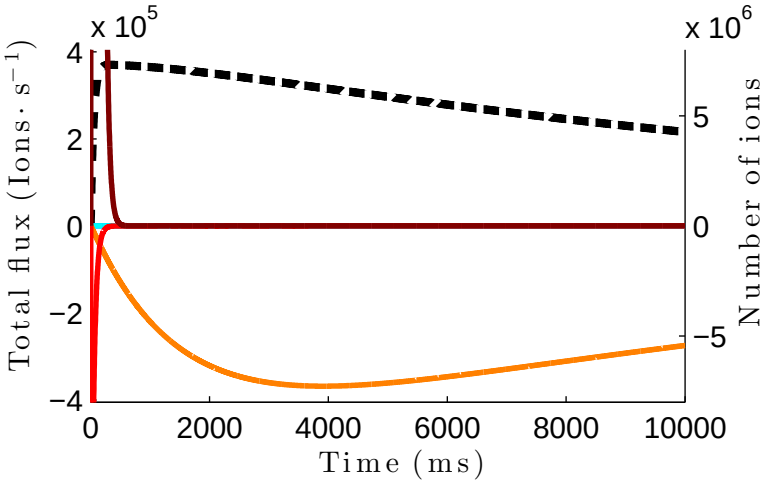

FIGURE 4.38: Sodium ions into microdomain by region: (——) proportion in through proximal paddle; (——) proportion in through distal paddle; (——) proportion in from fibre (concentration gradient); (——) proportion in from fibre (potential gradient); (——) proportion in through ion channels. Dashed, black curve shows accumulation of ions within microdomain.

4.7 Discussion

Our model is a simple representation of a Bergmann glial cell, which makes good predictions of its electrical behaviour. The key structural features of the microdomains have been determined from analysis of voltage-clamp data, with the resulting model of the microdomain being simple enough to easily use in a cell scale model. This model can accurately predict the length constant of the fibre of the cell while still reproducing the key qualitative features of the voltage-clamp data. Each stage of the modelling process has been informed by experimental data and used to inform the design of further experiments.

Using the insights into the structure of the cell gained from this analysis, we have also modelled the behaviour of the ion concentrations in the Bergmann glial cell, which allows us to assess how effectively the cell can perform certain functions involving moving ions around. The data from the voltage clamp experiments tells us about the electrical resistances in different regions of the cell, but importantly we can infer resistance to the flow of ions from the electrical resistance, which in turn allows us to infer the relative strengths of ion transport pathways.

Figure 4.33 shows that over a wide range of physiological parameter estimates, the majority of the potassium ions which enter the distal paddle leak straight back into the extracellular space surrounding it, albeit after a short time delay. This means that uptake of potassium ions in the microdomains is unlikely to be useful in terms of keeping potassium concentrations in the extracellular space low, because the very high resistances of the stalks compared to the resistance of the paddle membranes prevents significant ion fluxes into the fibre (and thus to the end-foot), but it may be that sequestering the potassium ions in the microdomain even briefly is useful to some extent.

The cell's ability to move sodium ions around is also limited by the slow rate at which the concentration gradients between the paddles can drive fluxes. This rate is quantified by the parameter γ appearing in equations (4.83) to (4.83), which is the ratio of the time scales on which the potentials charge and discharge the capacitance of the microdomain membrane and the concentrations diffuse between paddles. Our parameter estimates

give $\gamma = O\left(10^{-4}\right)$, or that the concentration gradients act around ten-thousand times more slowly than the membrane charges and discharges. Thus sodium ions accumulate in the microdomain and can only be moved out on a time scale of seconds or tens of seconds, which is far too long to have a significant effect on the behaviour of the glutamate transporter, unless the synapse is activated at an extremely low frequency. We conclude, therefore, that it seems unlikely that the microdomain is removing sodium ions to keep the glutamate transporters working effectively, as the geometry of the cell makes this behaviour too slow. It may again be useful however, just to remove the sodium ions from the extracellular space, and the fact that the glial cell can only redistribute them over a longer time scale is less important.

Some aspects of this work will be affected by the fact that we have not used accurate representations of the currents through the microdomain membranes. These currents are likely to contain components from several different types of ion channel and transporters, and the precise dynamics of these proteins will obviously influence the responses of the cell. Certain elements of our model's behaviour, therefore, need to be considered only as the response of the cell with the specific membrane currents we have modelled — the absolute value of the changes in ion concentrations, for example, will depend on the composition, size and duration of the input currents evoked by activity in the synapses, which is not easily measured. However, insights such as those above, related to the time scales over which ion movements occur, are founded primarily on the physical structure of the cell, and thus remain valid for any type of ion channel current.

Chapter 5

Conclusions

This thesis has presented mathematical models of three very different types of cell found in the nervous system. In each case the model is underpinned by the same basic electrochemistry, but the structure of the cell contributes to its function in a very different way.

In chapter 2 we examined the propagation of action potentials in very large unmyelinated axons and find that the cable equation approximation to the general model of the electrochemical behaviour in the axon relies on a small dimensionless parameter determined by the axon radius and the relative conductivities of the intracellular and extracellular electrolytes. We derive a numerical method to solve the general model, allowing us to evaluate the accuracy of the cable equation approximation, and find that it is a good model of the propagation speed and travelling wave profile of the action potential for physiological axon sizes when the intracellular and extracellular conductivities are equal (as in the *in vitro* case of the Hodgkin-Huxley experiment). When the extracellular conductivity is small, as is the case *in vivo*, in the confines of a nerve bundle, we find that for large, but physiologically feasible axons, the cable equation significantly overestimates the speed at which an action potential will propagate.

In chapter 3 we explored action potential propagation in myelinated axons, whose geometry is more complex than that of a uniform, unmyelinated axon. Asymptotic analysis,

exploiting the large difference between the width of a node of Ranvier and the internodal separation, yields insights into the behaviour of the transmembrane potential at the nodes of Ranvier which can be used to simplify existing models of myelinated axons. Further analysis yields a cell scale model of the myelinated axon which accounts for all of its structural features, and we demonstrate that two existing models are special cases of this model in appropriate limits. This allows us to gauge the validity of the existing models, and find that, for certain physiological parameter choices, neither accurately predicts the propagation speed or travelling wave profile of an action potential. We then apply our model to the problem of demyelination, where its form allows qualitative insights into how demyelination blocks action potential propagation.

Finally, in chapter 4 we present a model of the Bergmann glial cell, a cell which is very different again from the myelinated or unmyelinated neuron. We develop a simple equivalent circuit model of the microdomain — determining the basic structure from electron microscopy — which accurately predicts the response of the microdomain under voltage clamp conditions. Motivated by further experimental data, we couple a representation of the fibre of the Bergmann glial cell to our model of the microdomain, and demonstrate good cell scale predictions of the cell's electrical behaviour. We then explore the ion fluxes induced in the microdomains by the application of current, constructing a model of the concentration of two species of ions in the two paddles of the microdomain. This allows us to make qualitative predictions regarding the ability of the cell to redistribute ions taken up by the microdomains.

While this work has focussed on the differences in cell scale function created by the variation in geometry between the cells, there are certain unifying concepts connected the different models. Giant axons, discussed in chapter 2, and myelinated axons, discussed in chapter 3, are two adaptations which serve the same purpose, to increase the speed at which electrical signals propagate through the neuron. The adaptation of the giant axon is very simple, whereas the myelination of an axon requires the interaction and coordination of many attendant Schwann cells, but our work shows that (in certain cases) myelinated axons and giant axons in fact propagate signals in qualitatively identical ways, and both can be modelled by the cable equation.

The suitability of the cable equation to model the propagation of action potentials leads to a key theme of this thesis, in which we find it is hard to determine, *a priori*, how much physical and anatomical detail it is necessary to include in a model of any given cell. Chapter 2 demonstrates that, while the cable equation is a good model of the behaviour of unmyelinated axons under experimental conditions, the assumptions it makes about the properties of the extracellular space mean that it does not necessarily make correct predictions of the behaviour of cells *in vivo*. Chapter 3 shows that two simplified models of the myelinated axon found in the literature are special cases of the more general model we present. Both simplifications are appropriate only in certain limits, and physiological cases exist where neither makes predictions that agree well with those of the general model. The model presented in chapter 3 also demonstrates, however, that certain structural properties of the myelinated axon, such as the organisation of ion channels in and around the node of Ranvier, have no qualitative influence on its behaviour (at least from a theoretical perspective, we note that there may be physical limitations on the axon which necessitate this organisation). Asymptotic analysis of the equations describing the underlying electrochemical behaviour allow us to identify which features of the cell are significant and which are not, and thus propose a means for simplifying existing models of myelinated axons. Similarly, our analysis of experimental data obtained from Bergmann glial cells allows us to determine the significant anatomical features of the cell and extract quantitative information about these features. This in turn allows us to present a relatively simple, cell scale model which nonetheless makes good predictions of the cell's electrical behaviour.

Finally, we note that the work presented in chapter 4 can be extended in the future by considering additional physiological details. The inclusion of representations of the inwardly rectifying potassium channel and glutamate transporter in the microdomains, verified by experimental data, for example, would allow for quantitative predictions of the Bergmann glial cell's ability to clear the extracellular space and redistribute ions, when coupled to a model of the extracellular ion concentrations.

Appendix A

Bergmann glial cell parameters determined by equivalent circuit

TABLE A.1: Parameter estimates determined by the data from cell one

Fitted V_S (mV)	A_p $(\times 10^{-12}\,\mathrm{m}^2)$	A_d $(\times 10^{-12}\,\mathrm{m}^2)$	Ω_p^s $(\times 10^9\,\Omega)$	Ω_d^s $(\times 10^9\,\Omega)$	g^m $(\mathrm{S}\cdot\mathrm{m}^{-2})$
-60	45.5	707	0.92	2.24	1.565
-40	42.2	291	0.92	2.27	3.171
-20	41.2	179	0.81	2.33	4.089
20	42.9	618	0.90	2.02	2.020
40	44.7	965	0.96	1.84	1.245
60	44.8	944	0.85	1.92	0.998
80	45.2	946	0.88	1.83	0.851
100	45.1	825	0.91	1.82	0.902
120	45.9	735	0.96	1.81	1.055
140	57.0	762	1.09	1.83	1.187
Mean	45.5	697	0.92	1.99	1.710
Std. Dev	4.33	270.1	0.077	0.211	1.0920
%age	10	39	8	11	64

TABLE A.2: Parameter estimates determined by the data from cell two

Fitted V_S (mV)	A_p $(\times 10^{-12}\,\mathrm{m}^2)$	A_d $(\times 10^{-12}\,\mathrm{m}^2)$	Ω_p^s $(\times 10^9\,\Omega)$	Ω_d^s $(\times 10^9\,\Omega)$	g^m $(\mathrm{S}\cdot\mathrm{m}^{-2})$
-60	44.8	167	0.90	2.14	3.395
-40	38.6	99	0.85	1.87	4.496
-20	32.5	68	0.81	1.55	5.557
20	46.1	219	0.91	2.04	2.818
40	43.8	194	0.91	1.92	2.842
60	43.6	195	0.94	1.89	2.779
80	47.1	189	0.91	1.97	2.704
100	43.6	139	0.90	1.92	3.221
120	39.5	100	0.87	1.78	4.041
140	49.9	81	1.08	2.05	4.673
Mean	42.9	145	0.91	1.91	3.650
Std. Dev	4.96	54.7	0.071	0.163	0.9886
%age	12	38	8	9	27

TABLE A.3: Parameter estimates determined by the data from cell three

Fitted V_S (mV)	A_p $(\times 10^{-12}\,\mathrm{m}^2)$	A_d $(\times 10^{-12}\,\mathrm{m}^2)$	Ω_p^s $(\times 10^9\,\Omega)$	Ω_d^s $(\times 10^9\,\Omega)$	g^m $(\mathrm{S}\cdot\mathrm{m}^{-2})$
-60	54.0	265	1.15	2.99	3.167
-40	45.8	62	1.10	2.53	5.181
-20	45.8	86	1.12	2.41	4.577
20	50.4	146	1.14	2.59	3.265
40	51.4	172	1.15	2.55	3.014
60	51.1	190	1.16	2.46	2.815
80	51.5	197	1.19	2.46	2.716
100	54.4	182	1.15	2.73	2.818
120	49.2	90	1.13	2.57	3.836
140	43.4	52	1.10	2.07	4.882
Mean	49.7	144	1.14	2.53	3.630
Std. Dev	3.65	69.3	0.028	0.234	0.9307
%age	7	48	2	9	26

TABLE A.4: Parameter estimates determined by the data from cell four

Fitted V_S (mV)	A_p $(\times 10^{-12}\,\mathrm{m}^2)$	A_d $(\times 10^{-12}\,\mathrm{m}^2)$	Ω_p^s $(\times 10^9\,\Omega)$	Ω_d^s $(\times 10^9\,\Omega)$	g^m $(\mathrm{S}\cdot\mathrm{m}^{-2})$
-60	70.7	504	1.45	3.22	1.397
-40	67.1	153	1.43	3.50	2.473
-20	61.6	82	1.43	2.94	2.945
20	66.0	138	1.42	2.83	2.000
40	63.2	129	1.43	2.63	1.953
60	64.9	127	1.46	2.68	1.892
80	67.4	137	1.42	2.94	1.737
100	64.6	107	1.41	2.81	1.987
120	67.0	92	1.42	3.15	2.257
140	54.5	48	1.37	1.86	3.278
Mean	64.7	152	1.42	2.86	2.190
Std. Dev	4.38	127.8	0.025	0.439	0.5672
%age	7	84	2	15	26

TABLE A.5: Parameter estimates determined by the data from cell five

Fitted V_S (mV)	A_p $(\times 10^{-12}\,\mathrm{m}^2)$	A_d $(\times 10^{-12}\,\mathrm{m}^2)$	Ω_p^s $(\times 10^9\,\Omega)$	Ω_d^s $(\times 10^9\,\Omega)$	g^m $(\mathrm{S}\cdot\mathrm{m}^{-2})$
-60	48.9	132	1.18	1.98	3.647
-40	43.8	119	1.13	1.81	3.990
-20	46.6	166	1.17	1.92	3.575
20	52.9	257	1.21	1.97	2.612
40	51.1	294	1.20	1.91	2.301
60	51.2	327	1.21	1.86	2.072
80	50.9	331	1.23	1.81	2.003
100	54.5	281	1.22	1.88	2.237
120	49.3	198	1.19	1.84	2.848
140	40.5	101	1.12	1.61	4.424
Mean	49.0	221	1.19	1.86	2.970
Std. Dev	4.25	88.1	0.036	0.104	0.8724
%age	9	40	3	6	29
%age	9	40	3	6	28

Appendix B

Ion concentrations in Bergmann glia

B.1 Ion fluxes in the fibre

Firstly, we consider the problem of ion fluxes in the fibre — the volume of the fibre is significantly ($O(100)$ times) bigger than that of the microdomains, and so we approach the behaviour of the microdomains differently (in section B.2).

In the bulk of the cell (the regions outside the Debye layers, far from the cell membrane) the electrolyte is 'charge-neutral', which means that the concentration of positive charge in the electrolyte (contributed by K^+ and much smaller amounts of Na^+) is almost exactly balanced by the concentration of negative charge (contributed by Cl^+). The mobility of potassium ions in the electrolyte is approximately equal to that of chloride ions, and so currents in the electrolyte are carried by approximately equal fluxes of potassium and chloride ions being driven in opposite directions by the electric field.

Current through the cell membrane, however, is controlled by ion channels and other proteins, and therefore will not necessarily be carried by equal flows of positive and negative ions. Thus we wish to determine how the current through the membrane, which may be carried by a single ion species, is converted to current in the bulk electrolyte, carried by equal numbers of positive and negative ions. This change in the composition

of the current occurs between the bulk electrolyte and the Debye layer, in what we call the intermediate region.

As the volume of the fibre is reasonably big, we do not expect fluxes from the microdomains to have a significant impact on the ion concentrations in the fibre. However, the ion channels in the fibre membrane are specific to potassium ions, and so all outward current is carried by potassium ions, while in the bulk electrolyte, half of the current is carried by positive charges (potassium ions) moving in one direction and half by negative charges (chloride ions) moving in the other. These currents are matched across the intermediate region, and we can see that ions must accumulate in the intermediate layer as the composition of the current changes. We study the problem in the intermediate region in order to ascertain whether this accumulation of ions will have significant effects on the behaviour of the fibre.

The ion concentrations in the electrolyte are described by the Poisson-Nernst-Planck equations (see, for example, [72]). These comprise equations for the conservation of ions and descriptions of the fluxes induced by concentration and potential gradients. They take the form

$$\frac{\partial K^*}{\partial t^*} + \nabla^* \cdot \boldsymbol{F}_k{}^* = 0, \qquad \boldsymbol{F}_k{}^* = -D_k \left(\nabla^* K^* + \frac{F}{RT} K^* \nabla^* u^* \right), \tag{B.1}$$

$$\frac{\partial C^*}{\partial t^*} + \nabla^* \cdot \boldsymbol{F}_c{}^* = 0, \qquad \boldsymbol{F}_c{}^* = -D_c \left(\nabla^* C^* - \frac{F}{RT} C^* \nabla^* u^* \right), \tag{B.2}$$

$$\nabla^{*2} u^* = \frac{F}{\epsilon} \left(C^* - K^* \right) \tag{B.3}$$

where K^* and C^*, $\boldsymbol{F}_k{}^*$ and $\boldsymbol{F}_c{}^*$, and D_k and D_c are, respectively, the concentrations, fluxes and diffusion coefficients of potassium and chloride ions, and u^* is the electric potential. $\frac{RT}{F} \approx 25\,\mathrm{mV}$ is the thermal voltage, calculated from the Faraday constant, F, the gas constant R and the temperature, T.

The boundary conditions to the problem are, in general, determined from the flux through the ion channels

$$\boldsymbol{F}_k{}^*|_{x^*=0} \cdot \boldsymbol{e}_x = f_k{}^*, \qquad \boldsymbol{F}_c{}^*|_{x^*=0} \cdot \boldsymbol{e}_x = f_c{}^*, \tag{B.4}$$

where $x^* = 0$ is the position of the cell membrane. In the more specific case we are interested in (where only leak currents are present), ${f_c}^* = 0$ and all the current through the channels is carried by potassium ions.

B.1.1 Non-dimensionalisation

We non-dimensionalise the problem as follows

$$t^* = \tau t, \qquad K^* = \Pi_0 K, \qquad C^* = \Pi_0 C, \tag{B.5}$$

$$u^* = \frac{RT}{F} u, \qquad {f_k}^* = \tilde{F} f_k, \qquad {f_c}^* = \tilde{F} f_c, \tag{B.6}$$

$$x^* = Lx, \qquad {\boldsymbol{F}_k}^* = \tilde{F} \boldsymbol{F}_k, \qquad {\boldsymbol{F}_c}^* = \tilde{F} \boldsymbol{F}_c \tag{B.7}$$

where Π_0 is the total concentration of positive ions in the bulk ($\approx 140\,\mathrm{mol} \cdot \mathrm{m}^{-3}$), $\tilde{F}$ is a typical flux of ions through the cell membrane, τ is the typical time-scale of the problem, and L the length-scale. This yields the following dimensionless problem:

$$\frac{\partial K}{\partial t} + \delta \nabla \cdot \boldsymbol{F}_k = 0, \qquad \boldsymbol{F}_k = -\bar{D}_k \left(\nabla K + K \nabla u \right), \tag{B.8}$$

$$\frac{\partial C}{\partial t} + \delta \nabla \cdot \boldsymbol{F}_c = 0, \qquad \boldsymbol{F}_c = -\bar{D}_c \left(\nabla C - C \nabla u \right), \tag{B.9}$$

$$\nabla^2 u = \frac{1}{\delta^2} \left(C - K \right), \tag{B.10}$$

$$\boldsymbol{F}_k|_{x=0} \cdot \boldsymbol{e}_x = f_k, \qquad \boldsymbol{F}_c|_{x=0} \cdot \boldsymbol{e}_x = f_c, \tag{B.11}$$

where

$$L = \frac{D \Pi_0}{\tilde{F}}, \qquad \lambda_D = \sqrt{\frac{\epsilon RT}{F^2 \Pi_0}}, \qquad \tau = \frac{\Pi_0}{\tilde{F}} \lambda_D \tag{B.12}$$

and we have defined the dimensionless constants

$$\delta = \frac{\lambda_D}{L}, \qquad \bar{D}_k = \frac{D_k}{D}, \qquad \bar{D}_c = \frac{D_c}{D} \tag{B.13}$$

The scale L is the scale where electric field contributions to ion fluxes balance transmembrane ion fluxes, and λ_D is the Debye length. Using the parameters in table B.1, the

Debye length is between 3×10^{-10} m and 1×10^{-9} m, and the length-scale L is between 1.4×10^{-3} m and 4.2×10^{-3} m. Thus the dimensionless parameter $\delta = \dfrac{\lambda_D}{L}$ is small (between 6.9×10^{-8} and 8.3×10^{-7}) and $\bar{D}_k$ and $\bar{D}_c$ are order 1.

The problem we are interested is that in the intermediate region. The problems in the bulk electrolyte and the Debye layer are solved in [88] and where necessary we will use these solutions to impose boundary conditions on the problem in the intermediate region.

TABLE B.1: Parameters for the analysis of the electrochemical problem

Parameter	Value	Unit
T	310	K
Π_0	140	$\text{mol} \cdot \text{m}^{-3}$
D	2×10^{-9} [35]	m^2s^{-1}
ϵ	4.4×10^{-11} to 7.1×10^{-10}	$\text{C} \cdot \text{V}^{-1} \cdot \text{m}^{-1}$
R	8.31	$\text{J} \cdot \text{mol}^{-1} \cdot \text{K}^{-1}$
F	9.65×10^4	$\text{mol} \cdot \text{m}^{-2}$
$\tilde{F}$	6.7×10^{-5} to 2×10^{-4}	$\text{mol} \cdot \text{m}^{-2} \cdot \text{s}^{-1}$

B.1.2 Problem in the intermediate layer

The problem on the intermediate length scale is, on writing

$$\boldsymbol{F}_k = F_{kx}\boldsymbol{e}_x + F_{ky}\boldsymbol{e}_y + F_{kz}\boldsymbol{e}_z, \tag{B.14}$$

$$\boldsymbol{F}_c = F_{cx}\boldsymbol{e}_x + F_{cy}\boldsymbol{e}_y + F_{cz}\boldsymbol{e}_z \tag{B.15}$$

and rescaling to the intermediate length scale $x = \delta^{\frac{1}{2}} w$, given by

$$\frac{1}{\delta}\frac{\partial K}{\partial t} + \frac{1}{\delta^{\frac{1}{2}}}\frac{\partial F_{kx}}{\partial w} + \frac{\partial F_{ky}}{\partial y} + \frac{\partial F_{kz}}{\partial z} = 0, \qquad F_{kx} = -\frac{\bar{D}_k}{\delta^{\frac{1}{2}}}\left(\frac{\partial K}{\partial w} + K\frac{\partial u}{\partial w}\right), \tag{B.16}$$

$$\frac{1}{\delta}\frac{\partial C}{\partial t} + \frac{1}{\delta^{\frac{1}{2}}}\frac{\partial F_{cx}}{\partial w} + \frac{\partial F_{cy}}{\partial y} + \frac{\partial F_{cz}}{\partial z} = 0, \qquad F_{cx} = -\frac{\bar{D}_c}{\delta^{\frac{1}{2}}}\left(\frac{\partial C}{\partial w} - C\frac{\partial u}{\partial w}\right), \tag{B.17}$$

$$\delta\frac{\partial^2 u}{\partial w^2} + \delta^2\left(\frac{\partial^2 u}{\partial y^2} + \frac{\partial^2 u}{\partial z^2}\right) = C - K \tag{B.18}$$

We replace K, C and u with the asymptotic expansions in powers of $\delta^{\frac{1}{2}}$ below

$$K = K_0^{(\mathrm{I})} + \delta^{\frac{1}{2}} K_1^{(\mathrm{I})} + \cdots, \tag{B.19}$$

$$C = C_0^{(\mathrm{I})} + \delta^{\frac{1}{2}} C_1^{(\mathrm{I})} + \cdots, \tag{B.20}$$

$$u = u_0^{(\mathrm{I})} + \delta^{\frac{1}{2}} u_1^{(\mathrm{I})} + \cdots \tag{B.21}$$

and find the leading order behaviour is

$$K_0^{(\mathrm{I})} = \bar{K}^{(\mathrm{I})}, \tag{B.22}$$

$$C_0^{(\mathrm{I})} = \bar{K}^{(\mathrm{I})}, \tag{B.23}$$

$$u_0^{(\mathrm{I})} = u_0^{(\mathrm{I})}(y, z, t) \tag{B.24}$$

The first-order problem is

$$\frac{\partial K_1^{(\mathrm{I})}}{\partial t} + \frac{\partial F_{kx,0}^{(\mathrm{I})}}{\partial w} = 0, \tag{B.25}$$

$$\frac{\partial C_1^{(\mathrm{I})}}{\partial t} + \frac{\partial F_{cx,0}^{(\mathrm{I})}}{\partial w} = 0, \tag{B.26}$$

$$C_1^{(\mathrm{I})} = K_1^{(\mathrm{I})} \tag{B.27}$$

Subtracting equation (B.26) from (B.25), using (B.27) to cancel the time-derivative, and integrating with respect to w tells us that

$$F_{kx,0}^{(\mathrm{I})} - F_{cx,0}^{(\mathrm{I})} = j(y, z, t) \tag{B.28}$$

Here j, the dimensionless current through the intermediate layer is seen to be independent of the distance, w, from the membrane.

The leading order fluxes are given by

$$F_{kx,0}^{(\mathrm{I})} = -\bar{D}_k \left(\frac{\partial K_1^{(\mathrm{I})}}{\partial w} + \bar{K}^{(\mathrm{I})} \frac{\partial u_1^{(\mathrm{I})}}{\partial w} \right), \tag{B.29}$$

$$F_{cx,0}^{(\mathrm{I})} = -\bar{D}_c \left(\frac{\partial K_1^{(\mathrm{I})}}{\partial w} - \bar{K}^{(\mathrm{I})} \frac{\partial u_1^{(\mathrm{I})}}{\partial w} \right), \tag{B.30}$$

such that, when we substitute these into equations (B.25) and (B.26), we obtain

$$\frac{\partial K_1^{(\mathrm{I})}}{\partial t} - \bar{D}_k \frac{\partial^2 K_1^{(\mathrm{I})}}{\partial w^2} - \bar{D}_k \bar{K}^{(\mathrm{I})} \frac{\partial^2 u_1^{(\mathrm{I})}}{\partial w^2} = 0, \tag{B.31}$$

$$\frac{\partial K_1^{(\mathrm{I})}}{\partial t} - \bar{D}_c \frac{\partial^2 K_1^{(\mathrm{I})}}{\partial w^2} + \bar{D}_c \bar{K}^{(\mathrm{I})} \frac{\partial^2 u_1^{(\mathrm{I})}}{\partial w^2} = 0, \tag{B.32}$$

We can eliminate derivatives of $u_1^{(\mathrm{I})}$ by taking $(\bar{D}_c(\text{B.31}) + \bar{D}_k(\text{B.32}))$, as follows

$$\frac{\partial K_1^{(\mathrm{I})}}{\partial t} = \frac{2\bar{D}_c \bar{D}_k}{\bar{D}_c + \bar{D}_k} \frac{\partial^2 K_1^{(\mathrm{I})}}{\partial w^2}, \tag{B.33}$$

Using the definitions of the leading order fluxes (equations (B.29) and (B.30)), equation (B.28) can be rewritten as follows

$$-\left(\bar{D}_c + \bar{D}_k\right) \bar{K}^{(\mathrm{I})} \frac{\partial u_1^{(\mathrm{I})}}{\partial w} + \left(\bar{D}_c - \bar{D}_k\right) \frac{\partial K_1^{(\mathrm{I})}}{\partial w} = j\left(y, z, t\right) \tag{B.34}$$

The boundary conditions on the problem on the intermediate length scale come from matching to the Debye layer as $w \to 0$ and the outer as $w \to \infty$.

B.1.3 Problem in the outer

In the outer region, we replace K, C and u with the asymptotic expansion in powers of $\delta^{\frac{1}{2}}$ below

$$K = K_0^{(\mathrm{O})} + \delta K_1^{(\mathrm{O})} + \cdots, \tag{B.35}$$

$$C = C_0^{(\mathrm{O})} + \delta C_1^{(\mathrm{O})} + \cdots, \tag{B.36}$$

$$u = u_0^{(\mathrm{O})} + \delta u_1^{(\mathrm{O})} + \cdots \tag{B.37}$$

On substituting this expansion into equations (B.8) to (B.11) we find that the ion concentrations are independent of time (to leading order), thus we find

$$K_0^{(\mathrm{O})} = C_0^{(\mathrm{O})} = \bar{K}^{(\mathrm{O})}\left(\boldsymbol{x}\right) \tag{B.38}$$

The leading order fluxes are given by substituting the expansions in equations (B.35) to (B.37) in equations (B.8) to (B.11) and are

$$\boldsymbol{F}_{k,0}^{(\mathrm{O})} = -\bar{D}_k \left(\nabla \bar{K}^{(\mathrm{O})} + \bar{K}^{(\mathrm{O})} \nabla u_0^{(\mathrm{O})} \right), \tag{B.39}$$

$$\boldsymbol{F}_{c,0}^{(\mathrm{O})} = -\bar{D}_c \left(\nabla \bar{K}^{(\mathrm{O})} - \bar{K}^{(\mathrm{O})} \nabla u_0^{(\mathrm{O})} \right), \tag{B.40}$$

Thus the leading order current is given by:

$$\boldsymbol{j}_0^{(\mathrm{O})} = \boldsymbol{F}_{k,0}^{(\mathrm{O})} - \boldsymbol{F}_{c,0}^{(\mathrm{O})} = \left(\bar{D}_c - \bar{D}_k \right) \nabla \bar{K}^{(\mathrm{O})} - \left(\bar{D}_k + \bar{D}_c \right) \bar{K}^{(\mathrm{O})} \nabla u_0^{(\mathrm{O})} \tag{B.41}$$

Matching the intermediate solution as $w \to \infty$ to the outer as $x \to 0^+$ leads to the following conditions

$$\lim_{x \to 0^+} F_{kx,0}^{(\mathrm{O})} = \lim_{w \to \infty} F_{kx,0}^{(\mathrm{I})}, \tag{B.42}$$

$$\lim_{x \to 0^+} F_{cx,0}^{(\mathrm{O})} = \lim_{w \to \infty} F_{cx,0}^{(\mathrm{I})} \tag{B.43}$$

which stipulate that the leading order fluxes normal to the cell membrane must be continuous between the outer and intermediate regions. Substituting in the definitions of the flux in the outer (from equations (B.39) and (B.40)) and in the intermediate layer (from equations (B.29) and (B.30)) yields

$$\lim_{w \to \infty} \frac{\partial K_1^{(\mathrm{I})}}{\partial w} = \left. \frac{\partial \bar{K}^{(\mathrm{O})}}{\partial x} \right|_{x=0}, \tag{B.44}$$

$$\lim_{w \to \infty} \bar{K}^{(\mathrm{I})} \frac{\partial u_1^{(\mathrm{I})}}{\partial w} = \bar{K}^{(\mathrm{O})}(0) \left. \frac{\partial u_0^{(\mathrm{O})}}{\partial x} \right|_{x=0}. \tag{B.45}$$

B.1.4 Problem in the Debye layer

The matching conditions between the intermediate region and Debye layer come from again stipulating that the leading order fluxes normal to the membrane are continuous

$$\lim_{\xi\to\infty} F^{(\mathrm{D})}_{kx,0} = \lim_{w\to 0^+} F^{(\mathrm{I})}_{kx,0}, \tag{B.46}$$

$$\lim_{\xi\to\infty} F^{(\mathrm{D})}_{cx,0} = \lim_{w\to 0^+} F^{(\mathrm{I})}_{cx,0} \tag{B.47}$$

Analysis of the problem in the Debye layer determines that the flux density out of the Debye layer into the intermediate layer is equal to the flux density into the Debye layer through the cell membrane [88]

$$F^{(\mathrm{I})}_{kx,0}\Big|_{w=0^+} = f_k, \tag{B.48}$$

$$F^{(\mathrm{I})}_{cx,0}\Big|_{w=0^+} = f_c, \tag{B.49}$$

Substituting the definitions of the leading order fluxes in the intermediate layer (equations (B.29) and (B.30)) into the above yields the following boundary conditions on the intermediate problem

$$\left.\frac{\partial K^{(\mathrm{I})}_1}{\partial w}\right|_{w=0^+} = -\frac{1}{2}\left(\frac{1}{\bar{D}_k}f_k + \frac{1}{\bar{D}_c}f_c\right), \tag{B.50}$$

$$\left.\frac{\partial u^{(\mathrm{I})}_1}{\partial w}\right|_{w=0^+} = -\frac{1}{2\bar{K}^{(\mathrm{I})}}\left(\frac{1}{\bar{D}_k}f_k - \frac{1}{\bar{D}_c}f_c\right), \tag{B.51}$$

B.1.5 Analysis of the problem in the intermediate region

The problem in the intermediate layer, from equations (B.33) and (B.34), with boundary conditions from equations (B.44) and (B.45), and (B.50) and (B.51), is now stated in

its entirety as follows

$$\frac{\partial K_1^{(\mathrm{I})}}{\partial t} = \frac{2\bar{D}_c\bar{D}_k}{\bar{D}_c+\bar{D}_k}\frac{\partial^2 K_1^{(\mathrm{I})}}{\partial w^2}, \tag{B.52}$$

$$j\left(y,z,t\right) = -\left(\bar{D}_c+\bar{D}_k\right)\bar{K}^{(\mathrm{I})}\frac{\partial u_1^{(\mathrm{I})}}{\partial w} + \left(\bar{D}_c-\bar{D}_k\right)\frac{\partial K_1^{(\mathrm{I})}}{\partial w} \tag{B.53}$$

$$\left.\frac{\partial K_1^{(\mathrm{I})}}{\partial w}\right|_{w=0^+} = -\frac{\bar{D}_c f_k + \bar{D}_k f_c}{2\bar{D}_c\bar{D}_k}, \tag{B.54}$$

$$\lim_{w\to\infty}\frac{\partial K_1^{(\mathrm{I})}}{\partial w} = \left.\frac{\partial \bar{K}}{\partial x}\right|_{x=0}, \tag{B.55}$$

$$\left.\frac{\partial u_1^{(\mathrm{I})}}{\partial w}\right|_{w=0^+} = -\frac{\bar{D}_c f_k - \bar{D}_k f_c}{2\bar{K}^{(\mathrm{I})}\bar{D}_c\bar{D}_k}, \tag{B.56}$$

$$\lim_{w\to\infty}\bar{K}^{(\mathrm{I})}\frac{\partial u_1^{(\mathrm{I})}}{\partial w} = \bar{K}^{(\mathrm{O})}\left(0\right)\left.\frac{\partial u_0^{(\mathrm{O})}}{\partial x}\right|_{x=0}, \tag{B.57}$$

Equation (B.53) can be used to match the leading order current through the membrane to the leading order current into the outer, by noting

$$\left(-\left(\bar{D}_c+\bar{D}_k\right)\bar{K}^{(\mathrm{I})}\frac{\partial u_1^{(\mathrm{I})}}{\partial w} + \left(\bar{D}_c-\bar{D}_k\right)\frac{\partial K_1^{(\mathrm{I})}}{\partial w}\right)\Bigg|_{w=\infty} = \left(-\left(\bar{D}_c+\bar{D}_k\right)\bar{K}^{(\mathrm{I})}\frac{\partial u_1^{(\mathrm{I})}}{\partial w} + \left(\bar{D}_c-\bar{D}_k\right)\frac{\partial K_1^{(\mathrm{I})}}{\partial w}\right)\Bigg|_{w=0^+}. \tag{B.58}$$

Substituting in the boundary conditions from equations (B.54) to (B.56) yields

$$\left(-\left(\bar{D}_c+\bar{D}_k\right)\bar{K}^{(\mathrm{O})}\frac{\partial u_0^{(\mathrm{O})}}{\partial x} + \left(\bar{D}_c-\bar{D}_k\right)\frac{\partial \bar{K}^{(\mathrm{O})}}{\partial x}\right)\Bigg|_{x=0^+} = f_k - f_c \tag{B.59}$$

The remaining problem for the ion concentration in the intermediate layer is stated as follows (equations (B.33), with boundary conditions from equations (B.44) and (B.50))

$$\frac{\partial K_1^{(\mathrm{I})}}{\partial t} = \frac{2\bar{D}_c\bar{D}_k}{\bar{D}_c+\bar{D}_k}\frac{\partial^2 K_1^{(\mathrm{I})}}{\partial w^2}, \tag{B.60}$$

$$\left.\frac{\partial K_1^{(\mathrm{I})}}{\partial w}\right|_{w=0^+} = -\frac{\bar{D}_c f_k + \bar{D}_k f_c}{2\bar{D}_c\bar{D}_k}, \tag{B.61}$$

$$\lim_{w\to\infty}\frac{\partial K_1^{(\mathrm{I})}}{\partial w} = \left.\frac{\partial \bar{K}}{\partial x}\right|_{x=0}, \tag{B.62}$$

We are in interested in the case where the membrane flux is comprised entirely of potassium ions (to model membrane containing only potassium specific ion channels), such that $f_c = 0$

$$\frac{\partial K_1^{(\mathrm{I})}}{\partial t} = \frac{2\bar{D}_c\bar{D}_k}{\bar{D}_c + \bar{D}_k}\frac{\partial^2 K_1^{(\mathrm{I})}}{\partial w^2} \tag{B.63}$$

$$\left.\frac{\partial K_1^{(\mathrm{I})}}{\partial w}\right|_{w=0^+} = -\frac{f_k}{2\bar{D}_k} \tag{B.64}$$

$$\lim_{w\to\infty}\frac{\partial K_1^{(\mathrm{I})}}{\partial w} = \left.\frac{\partial \bar{K}}{\partial x}\right|_{x=0} \tag{B.65}$$

The key qualitative insight we require from this analysis is regarding the depletion or accumulation of ions in the intermediate region. In fact, we can determine the scale of the ion depletion without solving the above system. Firstly we note that, if the intermediate region is not to grow indefinitely, we require

$$\frac{1}{2\bar{D}_k}\int_0^{t_1} f_k\left(t\right)\,dt = \int_0^{t_1}\left.\frac{\partial \bar{K}}{\partial x}\right|_{x=0} dt, \tag{B.66}$$

$$\Rightarrow \left.\frac{\partial \bar{K}}{\partial x}\right|_{x=0} = \frac{1}{2\bar{D}_k t_1}\int_0^{t_1} f_k\left(t\right)\,dt \tag{B.67}$$

over some time interval t_1 which is long compared to the characteristic time scale of f_k. We estimate that f_k will be an oscillatory function, switching on and off as synapses fire near the microdomains (at between 40 to 200 Hz), with a maximum amplitude of around $10^{-6}\,\mathrm{mol}\cdot\mathrm{m}^{-2}\cdot\mathrm{s}^{-1}$ and a characteristic time scale of between 5×10^{-3} and $2.5\times10^{-2}\,\mathrm{s}$, such that the (dimensional) flux out of the outer region must be

$$F_{kx,0}^{*\,(\mathrm{O})} = -D_k\frac{\partial \bar{K}^*}{\partial x^*} \approx 10^{-6}\,\mathrm{mol}\cdot\mathrm{m}^{-2}\cdot\mathrm{s}^{-1} \tag{B.68}$$

This allows us to estimate the length scale over which $\bar{K}^*\left(x^*\right)$ will vary as follows

$$D_k\frac{\tilde{K}}{\lambda} \approx 10^{-6}, \tag{B.69}$$

$$\Rightarrow \lambda \approx \frac{D_k\tilde{K}}{10^{-6}} \tag{B.70}$$

$$\approx 0.1\,\mathrm{m} \tag{B.71}$$

which is much larger than the length of the cell fibre (around 10^{-4} m). There are proteins in the cell membrane (particularly Na^+/K^+-ATPase, the sodium-potassium pump) which will contribute small inward fluxes of potassium ions, which we have thus far ignored in this analysis. As the length scale of the $\bar{K}$ variations is so long, it is safe to assume that the effects of the potassium flux out of the membrane can be countered by a relatively small gradient in the concentration in the bulk of the electrolyte in the cell, and this small gradient can easily be maintained by small fluxes contributed by proteins distributed throughout the entire fibre membrane.

Thus we conclude that our assumption that the concentration is constant throughout the fibre is reasonable, and will not be invalidated by the ion fluxes leaving the cell as it functions. Most significantly, this means that the conductivity of the electrolyte will be constant throughout the fibre and microdomains.

B.2 Ion fluxes between the proximal and distal paddles, and between the proximal paddle and the fibre

What we take from the behaviour of the intermediate layers is that the concentrations in most of the cell are almost uniform, with major concentration changes only occurring in the very narrow Debye layers and possible across the very narrow stalks connecting the fibre and paddles. The microdomains have very small volumes compared to that of the fibre, and so we expect the ion fluxes through their membranes to have a more significant effect on the concentrations within them.

The ion fluxes in the microdomains are again described by the Poisson-Nernst-Planck equations, except we add an equation describing the sodium concentration, as this is

relevant to the behaviour of the glutamate transmitters in the microdomain membrane.

$$\frac{\partial K^*}{\partial t^*} + \nabla^* \cdot \boldsymbol{F}_k{}^* = 0, \qquad \boldsymbol{F}_k{}^* = -D_k \left(\nabla^* K^* + \frac{F}{RT} K^* \nabla^* u^* \right), \tag{B.72}$$

$$\frac{\partial N^*}{\partial t^*} + \nabla^* \cdot \boldsymbol{F}_n{}^* = 0, \qquad \boldsymbol{F}_n{}^* = -D_n \left(\nabla^* N^* + \frac{F}{RT} N^* \nabla^* u^* \right), \tag{B.73}$$

$$\frac{\partial C^*}{\partial t^*} + \nabla^* \cdot \boldsymbol{F}_c{}^* = 0, \qquad \boldsymbol{F}_c{}^* = -D_c \left(\nabla^* C^* - \frac{F}{RT} C^* \nabla^* u^* \right), \tag{B.74}$$

$$\nabla^{*2} u^* = \frac{F}{\epsilon} \left(C^* - K^* - N^* \right) \tag{B.75}$$

However, the sodium concentration is small compared to that of the potassium and chloride ions (i.e. $N^* \ll K^*$) [51, 97], and so equation (B.73) decouples from the problem as follows

$$\frac{\partial K^*}{\partial t^*} + \nabla^* \cdot \boldsymbol{F}_k{}^* = 0, \qquad \boldsymbol{F}_k{}^* = -D_k \left(\nabla^* K^* + \frac{F}{RT} K^* \nabla^* u^* \right), \tag{B.76}$$

$$\frac{\partial C^*}{\partial t^*} + \nabla^* \cdot \boldsymbol{F}_c{}^* = 0, \qquad \boldsymbol{F}_c{}^* = -D_c \left(\nabla^* C^* - \frac{F}{RT} C^* \nabla^* u^* \right), \tag{B.77}$$

$$\nabla^{*2} u^* = \frac{F}{\epsilon} \left(C^* - K^* \right) \tag{B.78}$$

$$\frac{\partial N^*}{\partial t^*} + \nabla^* \cdot \boldsymbol{F}_n{}^* = 0, \qquad \boldsymbol{F}_n{}^* = -D_n \left(\nabla^* N^* + \frac{F}{RT} N^* \nabla^* u^* \right), \tag{B.79}$$

Thus the electric field is now generated only by the concentrations of potassium and chloride ions, and the sodium ions passively advect and diffuse in this field.

The current density generated by the fluxes and the total ionic flux are given by

$$\frac{\boldsymbol{j}^*}{F} = \boldsymbol{F}_k^* - \boldsymbol{F}_c^*, \tag{B.80}$$

$$\boldsymbol{\mathcal{F}}^* = \boldsymbol{F}_k^* + \boldsymbol{F}_c^*, \tag{B.81}$$

where we have neglected the contribution from the sodium ions to the current and flux densities, because it is small compared to the contributions from the potassium and chloride ions. Substituting equations (B.76b), (B.77b) and (B.79b) into the above yields

$$\frac{\boldsymbol{j}^*}{F} = -D_k \nabla^* K^* + D_c \nabla^* C^* - \left(D_k K^* + D_c C^* \right) \frac{F}{RT} \nabla^* u^*, \tag{B.82}$$

$$\boldsymbol{\mathcal{F}}^* = -D_k \nabla^* K^* - D_c \nabla^* C^* - \left(D_k K^* - D_c C^* \right) \frac{F}{RT} \nabla^* u^*, \tag{B.83}$$

Charge neutrality, as in the intermediate region problem, tells us that the positive charge is balanced by the negative at leading order, thus $C^* = K^*$. The diffusivities of the three ions are also approximately equal (so $D_k = D_n = D_c = D$ is a reasonable approximation), and therefore

$$\frac{\boldsymbol{j}^*}{F} = -2\frac{F}{RT}DK^*\nabla^* u^*, \tag{B.84}$$

$$\boldsymbol{\mathcal{F}}^* = -2D\nabla^* K^*, \tag{B.85}$$

The time-scale for diffusion is given by

$$\tau = \frac{\lambda^2}{2D} \tag{B.86}$$

Choosing the length scale, λ, to be on the order of $1\,\mu$m, which is the characteristic length of the microdomains, yields a value of τ on the order of $10^{-4}\,$s. The frequency of inputs to the cell can be estimated from the rate of activity of the cells forming the synapses the Bergmann glial cell ensheathes, which is around 40 Hz. Thus the diffusion time scale is sufficiently smaller than the time scale of inputs to the cell ($O(\varepsilon)$, for some small ε), and we can write

$$\varepsilon\frac{\partial K^*}{\partial t^*} + \nabla^* \cdot \boldsymbol{\mathcal{F}}^* = 0 \tag{B.87}$$

The first result of this is that, assuming the membrane flux into a single paddle of the microdomain is uniformly distributed, the concentration within the paddle will be a function of time only — that is, the concentration equilibrates quickly over the entire paddle.

Secondly, in the approximately one-dimensional stalks which connect the paddles (the stalks are much longer than they are wide), the expression for the flux can, at leading order, be simplifed as follows

$$\boldsymbol{\mathcal{F}}^* = (\mathcal{F}^*, 0, 0)\,, \tag{B.88}$$

$$\frac{\partial \mathcal{F}^*}{\partial x^*} = 0, \tag{B.89}$$

$$\Rightarrow \mathcal{F}^* = \mathcal{F}^*(t^*) \tag{B.90}$$

Thus, at leading order, the flux of ions is entirely directed longitudinally through the stalk, and is independent of distance along the stalk — as we would expect if there is to be no build-up of concentration within the stalk.

Conservation of current also tells us that

$$\nabla^* \cdot \boldsymbol{j}^* = 0 \tag{B.91}$$

which allows us to simplify the expression for the current flow through the (one-dimensional) stalk, as follows

$$\boldsymbol{j}^* = (j^*, 0, 0)\,, \tag{B.92}$$

$$\frac{\partial j^*}{\partial x^*} = 0, \tag{B.93}$$

$$\Rightarrow j^* = j^*(t^*) \tag{B.94}$$

or that the current density is also, at leading order, directed longitudinally through the stalk and independent of distance along the stalk — as we would expect if there is to be no build-up of charge within the stalk.

These simplifications lead to the picture of ion fluxes in the microdomains summarised in figure B.1. Each stalk can be thought of as connecting two reservoirs of ions (with concentrations that vary with time) at given potentials (which also vary with time). We now determine the current density and potassium flux through the stalk (and note that the sodium flux is determined identically to the potassium).

In order to determine the concentration in the stalk, we substitute equation (B.90) into equation (B.85) and rewrite as follows

$$\frac{\partial K^*}{\partial x^*} = -\frac{\mathcal{F}^*(t^*)}{2D}. \tag{B.95}$$

By integrating with respect to x^*, we obtain the following expression for the concentration in the stalk

$$K^*(x^*, t^*) = -\frac{\mathcal{F}^*(t^*)}{2D}x^* + c_1(t^*) \tag{B.96}$$

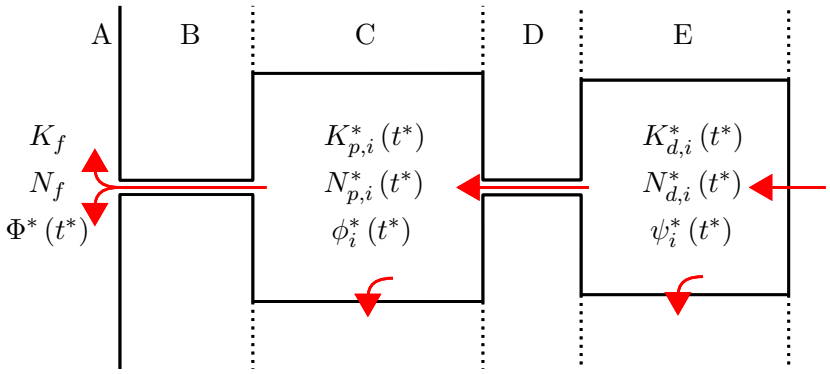

FIGURE B.1: Ion concentrations and fluxes in the microdomain. The fibre (A) is large enough that the ion concentrations are unaffected by the relatively small fluxes of ions from the microdomains, and hence are constant (K_f and N_f denote the potassium and sodium concentrations, respectively). The concentrations equilibrate quickly in the proximal paddle (C) and distal paddle (E), such that they are independent of distance from the fibre, and thus functions of time only ($K^*_{p,i}$ and $N^*_{p,i}$ denote the potassium and sodium concentrations in the proximal paddle, $K^*_{d,i}$ and $N^*_{d,i}$ in the distal).

The constant of integration c_1 is determined by the concentration in the stalk at $x^* = 0$, which we call $K^*_l(t^*)$, thus $c_1 = K^*_l(t^*)$ (identical analysis holds for the proximal stalk, where $K^*_l(t^*) = K_f$, and the distal stalk, where $K^*_l(t^*) = K^*_{p,i}(t^*)$). Matching the concentration at the far end of the stalk ($x = L_s$, where L_s is the length of the stalk) with the concentration in the reservoir $K^*_r(t^*)$ (where $K^*_r(t^*) = K^*_{p,i}(t^*)$ in the proximal stalk and $K^*_r(t^*) = K^*_{d,i}(t^*)$ in the distal) yields the following expression for the flux through the stalk

$$\mathcal{F}^*(t^*) = -\frac{2D}{L_s}\left(K^*_r(t^*) - K^*_l(t^*)\right). \tag{B.97}$$

The potential in the stalk can be determined by substituting equation (B.94) into equation (B.85) and rewriting as follows

$$\frac{\partial u^*}{\partial x^*} = -\frac{RT}{2DF^2} j^*(t) \frac{1}{K^*(x^*, t^*)}, \tag{B.98}$$

Again, by integrating with respect to x^* we obtain the following expression for the potential in the stalk

$$u(x^*, t^*) = -\frac{RT}{F^2}\frac{j^*(t^*)}{\mathcal{F}(t^*)}\left(\log\left(K^*(x^*, t^*)\right) - \log\left(K^*_l(t^*)\right)\right) + c_2 \tag{B.99}$$

The constant of integration is fixed by imposing $u^*(0,t^*) = u_l^*(t^*)$ (where $u_l^*(t^*) = \Phi^*(t^*)$ in the proximal stalk and $u_l^*(t^*) = \phi_i^*(t^*)$ in the distal), to yield

$$u(x^*,t^*) = -\frac{RT}{F^2}\frac{j^*(t^*)}{\mathcal{F}(t^*)}\left(\log\left(K^*(x^*,t^*)\right) - \log\left(K_l(t^*)\right)\right) + u_l^*(t^*) \tag{B.100}$$

Matching the potential at the far end of the stalk ($x = L_s$) with the potential in the reservoir $u_r^*(t^*)$ (where $u_r^*(t^*) = \phi_i^*(t^*)$ in the proximal stalk and $u_r^*(t^*) = \psi_i^*(t^*)$ in the distal) yields the following expression for the current density through the stalk

$$j^* = 2D\frac{F^2}{RT}\frac{\left(K_r^*(t^*) - K_l^*(t^*)\right)}{L_s\log\left(\frac{K_r^*(t^*)}{K_l^*(t^*)}\right)}\left(u_r^*(t^*) - u_l^*(t^*)\right), \tag{B.101}$$

The total current and ion flow through the stalk are therefore given by integrating the current density and flux over the cross-sectional area of the stalk. Both quantities are constant over this area, however, so the integration is simply equivalent to multiplying by the cross-sectional area, X_s, as follows:

$$I_s^* = 2D\frac{F^2}{RT}\frac{X_s}{L_s}\frac{\left(K_r^*(t^*) - K_l^*(t^*)\right)}{\log\left(\frac{K_r^*(t^*)}{K_l^*(t^*)}\right)}\left(u_r^*(t^*) - u_l^*(t^*)\right), \tag{B.102}$$

$$F_{tot}^* = -2D\frac{X_s}{L_s}\left(K_r^*(t^*) - K_l^*(t^*)\right) \tag{B.103}$$

In the case with no concentration gradients ($K_l^*(t^*) = K_r^*(t^*)$), it is interesting to consider the resistance of the stalk predicted by this analysis, and compare it to our previous estimates, both from fitting to the voltage clamp data and from estimates of the axoplasmic conductivity and stalk size given in the literature. Firstly, we note the following limit

$$\lim_{(K_l,K_r)\to\Pi_0}\left(\frac{K_r - K_l}{\ln\left(\frac{K_r}{K_l}\right)}\right) = \Pi_0, \tag{B.104}$$

such that the conductivity of the axoplasm in the stalk, given by

$$\sigma_{\text{axoplasm}} = 2D\frac{F^2}{RT}\frac{K_r^*(t^*) - K_l^*(t^*)}{\ln\left(\frac{K_r^*(t^*)}{K_l^*(t^*)}\right)} \tag{B.105}$$

can be reduced to

$$\sigma_{\text{axoplasm}} = 2D\Pi_0 \frac{F^2}{RT} \approx 2\,\text{S}\cdot\text{m}^{-1} \tag{B.106}$$

using the figures in table B.1, which compares well to the $\approx 0.8\,\text{S}\cdot\text{m}^{-1}$ quoted in the literature. The total resistance of the stalk is

$$\frac{1}{2D\Pi_0}\frac{L_s}{X_s}\frac{RT}{F^2} \approx 2\times 10^6\,\Omega \tag{B.107}$$

which is significantly smaller than that found by the data analysis. However, we expect this idealised version to underestimate the resistance of the stalk, as there are likely to be other considerations involved *in vivo* (for example, constrictions in the stalk reducing its effective cross-sectional area, larger molecules inside the axoplasm increasing the tortuosity of the paths ions must take through the stalk or organelles such as mitochondria partially blocking the stalk), as well as natural variations in the sizes and shapes of the stalks.

Given that the resistances of the stalks can be determined from experimental data by the equivalent circuit analysis, it is more useful to use this data to fix the value of $\frac{X_s}{L_s}$, as follows

$$\frac{X_s}{L_s} = \frac{RT}{2D\Pi_0 F^2 \Omega^s} \tag{B.108}$$

and then use this value to determine the diffusive resistance of the stalk and thus the ion flux in equation (B.103).

$$F^*_{tot} = -\frac{RT}{\Pi_0 F^2 \Omega^s}\left(K^*_r - K^*_l\right) \tag{B.109}$$

B.2.1 Determining the ion concentrations in each region of the microdomain

We have now determined that the ion concentrations are independent of position within a single paddle (equation (B.87)), and we know the currents (equation (B.102)) and fluxes (equation (B.109)) through the stalks that connect them. Thus we can write

down equations governing the concentrations of sodium and potassium ions in the microdomains, and these equations take the following form for the potassium and sodium concentrations in the proximal paddle

$$\begin{aligned} V_p \frac{dK^*_{p,i}}{dt^*} &= \frac{RT}{\Pi_0 F^2 \Omega^s_p}\left(K_f - K^*_{p,i}\right) + \frac{RT}{\Pi_0 F^2 \Omega^s_d}\left(K^*_{d,i} - K^*_{p,i}\right) - \frac{A_p g_p}{F}\phi^*_i \\ &\quad + \frac{1}{2F}\frac{K_f}{K_f + N_f}\left(\frac{\Phi^*(x_i) - \phi^*_i}{\Omega^s_p} + \frac{\psi^*_i - \phi^*_i}{\Omega^s_d}\right) \end{aligned} \tag{B.110}$$

$$\begin{aligned} V_p \frac{dN^*_{p,i}}{dt^*} &= \frac{RT}{\Pi_0 F^2 \Omega^s_p}\left(N_f - N^*_{p,i}\right) + \frac{RT}{\Pi_0 F^2 \Omega^s_d}\left(N^*_{d,i} - N^*_{p,i}\right) \\ &\quad + \frac{1}{2F}\frac{N_f}{K_f + N_f}\left(\frac{\Phi^*(x_i) - \phi^*_i}{\Omega^s_p} + \frac{\psi^*_i - \phi^*_i}{\Omega^s_d}\right) \end{aligned} \tag{B.111}$$

where V_p is the volume of the proximal paddle, K_f and N_f are the (constant) potassium and sodium concentrations in the fibre, and $K^*_{p,i}$ and $N^*_{p,i}$ are the potassium and sodium concentrations in the proximal paddle of the i^{th} microdomain, and $K^*_{d,i}$ and $N^*_{d,i}$ are the potassium and sodium concentrations in the distal paddle of the i^{th} microdomain. R is the ideal gas constant ($R = 8.31\,\text{J}\cdot\text{mol}^{-1}\cdot\text{K}^{-1}$), T is the temperature ($T = 310\,\text{K}$), Π_0 is the resting concentration of positive (potassium and sodium) ions ($\Pi_0 = 145\,\text{mol}\cdot\text{m}^{-3}$) and F is the Faraday constant ($F = 9.65\times10^4\,\text{C}\cdot\text{mol}^{-1}$). The terms in equation (B.110) represent, respectively, the concentration-gradient driven potassium flux between the fibre and the proximal paddle, the concentration-gradient driven potassium flux between the proximal and distal paddles, the potassium flux carried by the leak current through the proximal paddle membrane, the potassium flux carried by the current between the proximal paddle and the fibre and the potassium flux carried by the current between the proximal and distal paddles. The factor of one half in the terms representing the flux carried by the currents is derived from the fact that the transference number of the electrolyte is approximately one half, and thus current is carried by equal and opposite flows of positive and negative ions (i.e. half of the current is carried by sodium and potassium ions moving in one direction, and the other half by chloride ions moving in the opposite direction). The factor of the ratio of the potassium concentration to the total concentration of positive ions (i.e. $\dfrac{K_f}{K_f + N_f}$) simply reflects the fact that potassium and sodium ions constitute the current flux in the same proportions they are present in in the electrolyte — strictly speaking this proportion will change as the ion

concentrations fluctuate in the microdomains, but we have found in practice (much like for the resistances of the stalks as described above) that the actual variations are small enough that the resting concentration proportions can be used. The terms in equation (B.111) represent, respectively, the concentration-gradient driven sodium fluxes between the fibre and the proximal paddle, and the proximal paddle and the distal paddle, and the sodium fluxes driven by the current between the fibre and the proximal paddle and the proximal and distal paddles (the factor of on half is determined by the transference number, as noted for the potassium fluxes, and the remaining factor represents the ratio of sodium ions to positive ions present in the electrolyte).

The model of the potassium and sodium concentrations in the distal paddle is as follows

$$V_d \frac{dK^*_{d,i}}{dt^*} = \frac{RT}{\Pi_0 F^2 \Omega^s_d}\left(K^*_{p,i} - K^*_{d,i}\right) - \frac{A_d g_d}{F}\psi^*_i + \frac{1}{2F}\frac{K_f}{K_f + N_f}\frac{\phi^*_i - \psi^*_i}{\Omega^s_d} + \mathcal{F}^*_{\mathrm{K},i}\left(t^*\right) \tag{B.112}$$

$$V_d \frac{dN^*_{d,i}}{dt^*} = \frac{RT}{\Pi_0 F^2 \Omega^s_d}\left(N^*_{p,i} - N^*_{d,i}\right) + \frac{1}{2F}\frac{K_f}{K_f + N_f}\frac{\phi^*_i - \psi^*_i}{\Omega^s_d} + \mathcal{F}^*_{\mathrm{Na},i}\left(t^*\right) \tag{B.113}$$

where V_d is the volume of the distal paddle. The first term in each of these equations again represents the concentration-gradient driven flux, the second term in equation (B.112) the potassium flux carried by the leak current through the distal paddle membrane and the third term in equation (B.112) and the second in equation (B.113) represent the current between the proximal and distal paddles, divided into potassium and sodium components. The final terms in each equation ($\mathcal{F}^*_{\mathrm{K},i}\left(t^*\right)$ and $\mathcal{F}^*_{\mathrm{Na},i}\left(t^*\right)$) represent the ion fluxes carried into the distal paddle by the ion channels in the distal membrane responding to synaptic activity.

Appendix C

Numerical solution of the model of the Bergmann glia

Here we discuss the numerical solution of equations (4.75) to (4.77), and (4.83) to (4.86), the model of the transmembrane potentials and ionic concentrations in the Bergmann glial cell. Equations (4.76) and (4.77), and (4.83) to (4.86) are linear, ordinary differential equations, and are solved using the `ode15s` routines from MATLAB. Equation (4.75), however, is more complicated in that the delta function must be accounted for.

Briefly, we multiply the equation by a test function $w_k(x)$ and integrate with respect to x to yield

$$\alpha \int_0^1 w_k(x) \frac{\partial \Phi}{\partial t}\, dx = \beta \int_0^1 w_k(x) \frac{\partial^2 \Phi}{\partial x^2}\, dx - \bar{g}_f \int_0^1 w_k(x)\, \Phi\, dx - \sum_i \int_0^1 w_k(x)\, \delta(x - \lambda_i) \left(\Phi(\lambda_i) - \phi_i\right)\, dx \quad \text{(C.1)}$$

We then perform integration by parts on the first term on the right-hand-side of the equation above, and perform the integration on the final term on the right-hand side to

eliminate the delta function, to obtain the following weak formulation of the problem

$$\alpha \int_0^1 w_k(x) \frac{\partial \Phi}{\partial t}\, dx = \beta \left(w_k(1) \left.\frac{\partial \Phi}{\partial x}\right|_{x=1} - w_k(0) \left.\frac{\partial \Phi}{\partial x}\right|_{x=0} - \int_0^1 \frac{\partial}{\partial x}\left(w_k(x)\right) \frac{\partial \Phi}{\partial x}\, dx \right) - \bar{g}_f \int_0^1 w_k(x)\, \Phi\, dx - \sum_i w_k(\lambda_i) \left(\Phi(\lambda_i) - \phi_i\right) \quad \text{(C.2)}$$

We approach this by writing Φ as the sum over a set of basis functions

$$\Phi(x,t) = \sum_j \Phi_j(t)\, w_j(x) \quad \text{(C.3)}$$

From the weak formulation of the problem, we only require our basis functions to be once-differentiable, and so we choose the following, piecewise-linear, set of basis functions

$$w_k(x) = \begin{cases} \dfrac{x - (k-1)\Delta x}{\Delta x} & (k-1)\Delta x \le x \le k\Delta x \\ \dfrac{(k+1)\Delta x - x}{\Delta x} & k\Delta x \le x \le (k+1)\Delta x \\ 0 & x < (k-1)\Delta x \text{ or } x > (k+1)\Delta x \end{cases} \quad \text{(C.4)}$$

such that we have replaced Φ with a linear interpolation on the points $k\Delta x$, for $k = 0, \ldots, N$ (where $N\Delta x = 1$).

We can now perform the integration in equation (C.2). Proceeding term by term we find, for $k = 1, \ldots, N-1$

$$\int_0^1 w_k(x) \frac{\partial \Phi}{\partial t}\, dx = \int_0^1 w_k(x) \sum_j \dot{\Phi}_j(t)\, w_j(x)\, dx, \quad \text{(C.5)}$$

$$= \sum_j \dot{\Phi}_j \int_0^1 w_j(x) w_k(x)\, dx, \quad \text{(C.6)}$$

$$= \frac{\Delta x}{6}\left(\dot{\Phi}_{k-1} + 4\dot{\Phi}_k + \dot{\Phi}_{k+1}\right) \quad \text{(C.7)}$$

For $k = 0$

$$\int_0^1 w_0(x) \frac{\partial \Phi}{\partial t}\, dx = \frac{\Delta x}{6}\left(2\dot{\Phi}_0 + \dot{\Phi}_1\right) \quad \text{(C.8)}$$

For $k = N$

$$\int_0^1 w_N(x) \frac{\partial \Phi}{\partial t}\, dx = \frac{\Delta x}{6}\left(\dot{\Phi}_{N-1} + 2\dot{\Phi}_N\right) \quad \text{(C.9)}$$

The first integral on the right-hand side yields, for $k = 1, \ldots, N-1$

$$\int_0^1 \frac{\partial}{\partial x}\left(w_k\left(x\right)\right)\frac{\partial \Phi}{\partial x}\,dx = \int_0^1 \frac{\partial}{\partial x}\left(w_k\left(x\right)\right)\sum_{j=0}^{N}\Phi_j\frac{\partial}{\partial x}\left(w_j\left(x\right)\right)\,dx \tag{C.10}$$

$$= \sum_{j=0}^{N}\Phi_j\int_0^1 \frac{\partial}{\partial x}\left(w_k\left(x\right)\right)\frac{\partial}{\partial x}\left(w_j\left(x\right)\right)\,dx \tag{C.11}$$

$$= \frac{1}{\Delta x}\left(-\Phi_{k-1} + 2\Phi_k - \Phi_{k+1}\right) \tag{C.12}$$

For $k = 0$

$$\int_0^1 \frac{\partial}{\partial x}\left(w_0\left(x\right)\right)\frac{\partial \Phi}{\partial x}\,dx = \int_0^1 \frac{\partial}{\partial x}\left(w_0\left(x\right)\right)\sum_{j=0}^{N}\Phi_j\frac{\partial}{\partial x}\left(w_j\left(x\right)\right)\,dx \tag{C.13}$$

$$= \sum_{j=0}^{N}\Phi_j\int_0^1 \frac{\partial}{\partial x}\left(w_0\left(x\right)\right)\frac{\partial}{\partial x}\left(w_j\left(x\right)\right)\,dx \tag{C.14}$$

$$= \frac{1}{\Delta x}\left(\Phi_0 - \Phi_1\right) \tag{C.15}$$

Similarly, for $k = N$

$$\int_0^1 \frac{\partial}{\partial x}\left(w_N\left(x\right)\right)\frac{\partial \Phi}{\partial x}\,dx = \int_0^1 \frac{\partial}{\partial x}\left(w_N\left(x\right)\right)\sum_{j=0}^{N}\Phi_j\frac{\partial}{\partial x}\left(w_j\left(x\right)\right)\,dx \tag{C.16}$$

$$= \sum_{j=0}^{N}\Phi_j\int_0^1 \frac{\partial}{\partial x}\left(w_N\left(x\right)\right)\frac{\partial}{\partial x}\left(w_j\left(x\right)\right)\,dx \tag{C.17}$$

$$= \frac{1}{\Delta x}\left(-\Phi_{N-1} + \Phi_N\right) \tag{C.18}$$

The integration of the second term on the right-hand side is the same as that of the time derivative (equations (C.5) to (C.5)). For $k = 1 \ldots, N-1$

$$\int_0^1 w_k\left(x\right)\Phi\,dx = \frac{\Delta x}{6}\left(\Phi_{k-1} + 4\Phi_k + \Phi_{k+1}\right) \tag{C.19}$$

For $k = 0$

$$\int_0^1 w_0\left(x\right)\Phi\,dx = \frac{\Delta x}{6}\left(2\Phi_0 + \Phi_1\right) \tag{C.20}$$

For $k = N$

$$\int_0^1 w_N\left(x\right)\Phi\,dx = \frac{\Delta x}{6}\left(\Phi_{N-1} + 2\Phi_N\right) \tag{C.21}$$

We can now rewrite the weak formulation (equation (C.2)), for $k = 1, \ldots, N-1$

$$\begin{aligned}\alpha\frac{\Delta x}{6}\left(\dot{\Phi}_{k-1} + 4\dot{\Phi}_k + \dot{\Phi}_{k+1}\right) = \beta\frac{1}{\Delta x}\left(\Phi_{k-1} - 2\Phi_k + \Phi_{k+1}\right) \\ - \bar{g}_f\frac{\Delta x}{6}\left(\Phi_{k-1} + 4\Phi_k + \Phi_{k+1}\right) \\ - \sum_i w_k\left(\lambda_i\right)\left(\Phi\left(\lambda_i\right) - \phi_i\right)\end{aligned} \tag{C.22}$$

For $k = 0$

$$\begin{aligned}\alpha\frac{\Delta x}{6}\left(2\dot{\Phi}_0 + \dot{\Phi}_1\right) = -\beta\left(\left.\frac{\partial\Phi}{\partial x}\right|_{x=0} + \frac{1}{\Delta x}\left(\Phi_0 - \Phi_1\right)\right) \\ - \bar{g}_f\frac{\Delta x}{6}\left(2\Phi_0 + \Phi_1\right) - \sum_i w_0\left(\lambda_i\right)\left(\Phi\left(\lambda_i\right) - \phi_i\right)\end{aligned} \tag{C.23}$$

For $k = N$

$$\begin{aligned}\alpha\frac{\Delta x}{6}\left(\dot{\Phi}_{N-1} + 2\dot{\Phi}_N\right) = \beta\left(\left.\frac{\partial\Phi}{\partial x}\right|_{x=1} + \frac{1}{\Delta x}\left(\Phi_{N-1} - \Phi_N\right)\right) \\ - \bar{g}_f\frac{\Delta x}{6}\left(\Phi_{N-1} + 2\Phi_N\right) - \sum_i w_N\left(\lambda_i\right)\left(\Phi\left(\lambda_i\right) - \phi_i\right)\end{aligned} \tag{C.24}$$

Equations (C.22) to (C.24) can now be written in matrix form as follows

$$\alpha\mathbf{A}\dot{\mathbf{\Phi}} = \beta\mathbf{B}\mathbf{\Phi} - \bar{g}_f\mathbf{C}\mathbf{\Phi} - \boldsymbol{V} \tag{C.25}$$

where

$$\mathbf{\Phi} = \begin{bmatrix} \Phi_0 \\ \Phi_1 \\ \vdots \\ \Phi_{N-1} \\ \Phi_N \end{bmatrix} \tag{C.26}$$

and

$$\mathbf{A} = \begin{bmatrix} \frac{\Delta x}{3} & \frac{\Delta x}{6} & 0 & \cdots & 0 \\ \frac{\Delta x}{6} & \frac{2\Delta x}{3} & \frac{\Delta x}{6} & \cdots & 0 \\ \vdots & \ddots & \ddots & \ddots & \vdots \\ 0 & \cdots & \frac{\Delta x}{6} & \frac{2\Delta x}{3} & \frac{\Delta x}{6} \\ 0 & \cdots & 0 & \frac{\Delta x}{6} & \frac{\Delta x}{3} \end{bmatrix} \tag{C.27}$$

$$\mathbf{B} = \begin{bmatrix} -\frac{1}{\Delta x} & \frac{1}{\Delta x} & 0 & \cdots & 0 \\ \frac{1}{\Delta x} & -\frac{2}{\Delta x} & \frac{1}{\Delta x} & \cdots & 0 \\ \vdots & \ddots & \ddots & \ddots & \vdots \\ 0 & \cdots & \frac{1}{\Delta x} & -\frac{2}{\Delta x} & \frac{1}{\Delta x} \\ 0 & \cdots & 0 & \frac{1}{\Delta x} & -\frac{1}{\Delta x} \end{bmatrix} \tag{C.28}$$

$$\mathbf{C} = \mathbf{A} \tag{C.29}$$

$$\boldsymbol{V} = \sum_i \begin{bmatrix} \left(\sum_j \Phi_j w_j\left(\lambda_i\right) - \phi_i\right) w_0\left(\lambda_i\right) - \beta \left.\frac{\partial \Phi}{\partial x}\right|_{x=0} \\ \left(\sum_j \Phi_j w_j\left(\lambda_i\right) - \phi_i\right) w_1\left(\lambda_i\right) \\ \vdots \\ \left(\sum_j \Phi_j w_j\left(\lambda_i\right) - \phi_i\right) w_{N-1}\left(\lambda_i\right) \\ \left(\sum_j \Phi_j w_j\left(\lambda_i\right) - \phi_i\right) w_N\left(\lambda_i\right) + \beta \left.\frac{\partial \Phi}{\partial x}\right|_{x=1} \end{bmatrix} \tag{C.30}$$

Equation (C.25) now defines a linear system of ODEs, which can also be solved using `ode15s` in MATLAB.

Bibliography

[1] R. K. Adair. Optimum ion channel properties in the squid giant axon. *Phys Rev E*, 69(4):042902, 2004.

[2] K. W. Altman and R. Plonsey. Point source nerve bundle stimulation: Effects of fiber diameter and depth on simulated excitation. *IEEE Trans Biomed Eng*, 37(7):688–698, 1990.

[3] C. M. Anderson and M. Nedergaard. Astrocyte-mediated control of cerebral microcirculation. *Trends Neurosci*, 26(7):340–344, 2003.

[4] A. Araque, V. Parpura, R. P. Sanzgiri, and P. G. Haydon. Tripartite synapses: glia, the unacknowledged partner. *Trends Neurosci*, 22(5):208–215, 1999.

[5] E. R. Arbuthnott, I. A. Boyd, and K. U. Kalu. Ultrastructural dimensions of myelinated peripheral nerve fibres in the cat and their relation to conduction velocity. *J Physiol*, 308:125–157, 1980.

[6] C. M. Armstrong and F. Benzanilla. Inactivation of the sodium channel: II. gating current experiments. *J Gen Physiol*, 70:567–590, 1977.

[7] P. J. Basser. Cable equation for a myelinated axon derived from its microstructure. *Med Biol Eng Comput*, 31:S87–S92, 1993.

[8] B. P. Bean. Sodium channel inactivation in the crayfish giant axon. *Biophys J*, 35:595–614, 1981.

[9] R. S. Bear, F. O. Schmitt, and J. Z. Young. The sheath components of the giant nerve fibres of the squid. *P Roy Soc Lond B Bio*, 123(833):496–504, 1937.

[10] R. Beck. Muscle fiber conduction velocity. In *Wiley Encyclopedia of Biomedical Engineering*. Wiley, 2006.

[11] F. Benzanilla and C. M. Armstrong. Inactivation of the sodium channel: I. sodium current experiments. *J Gen Physiol*, 70:549–566, 1977.

[12] D. E. Bergles, J. A. Dzubay, and C. E. Jahr. Glutamate transporter currents in bergmann glial cells follow the time course of extrasynaptic gluatamate. *Proc Natl Acad Sci USA*, 94:14821–14825, 1997.

[13] H. Bostock and T. A. Sears. The internodal axon membrane: Electrical excitability and continuous conduction in segmental demyelination. *J Physiol*, 280:273–301, 1978.

[14] M. H. Brill, S. G. Waxman, J. W. Moore, and R. W. Joyner. Conduction velocity and spike configuration in myelinated fibres: computed dependence on internode distance. *J Neurol Neurosurg Psychiatry*, 40:769–774, 1977.

[15] D. Bucher and J. Goallaird. Beyond faithful conduction: Short-term dynamics, neuromodulation, and long-term regulation of spike propagation in the axon. *Prog Neurobiol*, 94:307–346, 2011.

[16] J. H. Caldwell, K. L. Schaller, R. S. Lasher, E. Peles, and S. R. Levinson. Sodium channel $Na_v1.6$ is localized at nodes of ranvier, dendrites, and synapses. *PNAS*, 97(10):5616–5620, 2000.

[17] D. C. Camerino, D. Tricarico, and J-F. Desaphy. Ion channel pharmacology. *Neurotherapeutics*, 4:184–198, 2007.

[18] K. C. Chen and C. Nicholson. Spatial buffering of potassium ions in brain extracellular space. *Biophys J*, 78:2776–2797, 2000.

[19] B. A. Clark and B. Barbour. Currents evoked in Bergmann glial cells by parallel fibre stimulation in rat cerebellar slices. *J. Physiol.*, 502(2):335–350, 1997.

[20] M. J. Craner, A. C. Lo, J. A. Black, and S. G. Waxman. Abnormal sodium channel distribution in optic nerve axons in a model of inflammatory demyelination. *Brain*, 126:1552–1561, 2003.

[21] C. de Solages, G. Szapiro, N. Brunel, V. Hakim, P. Isope, P. Buisseret, C. Rousseau, B. Barbour, and C. Lena. High-frequency organisation and synchrony of activity in the Purkinje cell layer of the cerebellum. *Neuron*, 58:775–788, 2008.

[22] A. A. Faisal and S.B. Laughlin. Stochastic simulations on the reliability of action potential propagation in thin axons. *PLoS Comput Biol*, 3(5):783–795, May 2007.

[23] P. A. Felts, T. A. Baker, and K. J. Smith. Conduction in segmentally demyelinated mammalian central axons. *J Neurosci*, 17(19):7267–7277, 1997.

[24] J. H. M. Frijns, J. Mooij, and J. H. ten Kate. A quantitative approach to modelling mammalian myelinated nerve fibers for electrical prosthesis design. *IEEE Trans Bio-Med Eng*, 41(6):556–566, 1994.

[25] S. George, K. L. Dobson, S. Coombes, G. Richardson, and T. C. Bellamy. Computationally efficient modelling of cerebellar Bergmann glia. *Manuscript in preparation*, 2014.

[26] S. George, J. M. Foster, and G. Richardson. Modelling in vivo action potential propagation along a giant axon. *J Math Biol*, pages 1–27, 2014.

[27] W. Gerstner and W. M. Kistler. *Spiking Neuron Models: Single Neurons, Populations, Plasticity*. Cambridge University Press, August 2002.

[28] C. Ghez and S. Fahn. *Principles of Neural Science*, chapter "The cerebellum", pages 502–522. Elsevier, 2nd edition, 1985.

[29] D. E. Goldman. Potential, impedance and rectification in membranes. *J Gen Physiol*, 27(1):37–60, 1943.

[30] J. Grosche, H. Kettenmann, and A. Reichenbach. Bergmann glial cells form distinct morphological structures to interact with cerebellar neurons. *J Neurosci Res*, 68:138–149, 2002.

[31] J. Grosche, V. Matyash, T. Möller, A. Verkhratsky, A. Reichenbach, and H. Kettenmann. Microdomains for neuron-glia interaction: parallel fiber signaling to Bergmann glial cells. *Nat Neurosci*, 2(2):139–143, 1999.

[32] M. M. Halassa, T. Fellin, and P. G. Haydon. The tripartite synapse: roles for gliotransmission in health and disease. *Trends Mol Med*, 13(2):54–63, 2007.

[33] W. L. Hardy. Propagation speed in myelinated nerve i. experimental dependence on external Na^+ and on temperature. *Biophys J*, 13:1054–1070, 1973.

[34] W. L. Hardy. Propagation speed in myelinated nerve ii. theoretical dependence on external Na^+ and on temperature. *Biophys J*, 13:1071–1089, 1973.

[35] H. S. Harned and R. L. Nutall. The diffusion coefficient of potassium chloride in dilute aqueous solution. *J. Am. Chem. Soc.*, 69(4):736–740, 1947.

[36] D. K. Hartline and D. R. Colman. Rapid conduction and the evolution of giant axons and myelinated fibers. *Curr Biol*, 17:R29–R35, 2007.

[37] J. E. Heuser and C. F. Doggenweiler. The fine structural organization of nerve fibers, sheaths and glial cells in the prawn, *palaemonetes vulgaris*. *J Cell Biol*, 30:381–403, 1966.

[38] B. Hille. *Ionic Channels of Excitable Membranes*. Sinauer Associates, 3 edition, 2001.

[39] A. L. Hodgkin. A note on conduction velocity. *J Physiol*, 125(221–224), 1954.

[40] A. L. Hodgkin and A. F. Huxley. The components of membrane conductance in the giant axon of *loligo*. *J Physiol*, 116:473–496, 1952.

[41] A. L. Hodgkin and A. F. Huxley. Currents carried by sodium and potassium ions through the membrane of the giant axon of *loligo*. *J Physiol*, 116:449–472, 1952.

[42] A. L. Hodgkin and A. F. Huxley. The dual effect of membrane potential on sodium conductance in the giant axon of *loligo*. *J Physiol*, 116:497–506, 1952.

[43] A. L. Hodgkin and A. F. Huxley. Propagation of electrical signals along giant nerve fibres. *P Roy Soc Lond B Bio*, 140(899):177–183, 1952.

[44] A. L. Hodgkin and A. F. Huxley. A quantitative description of membrane current and its application to conduction and excitation in nerve. *J Physiol*, 117:500–544, 1952.

[45] A. L. Hodgkin, A. F. Huxley, and B Katz. Measurement of current-voltage relations in the membrane of the giant axon of *loligo*. *J Physiol*, 116:424–448, 1952.

[46] G. M. Hughes and L. Tauc. An electrophysiological study of the anatomical relations of two giant nerve cells in *aplysia depilans*. *J Exp Biol*, 40:469–486, 1963.

[47] M. Iino, K. Goto, W. Kakegawa, H. Okado, M. Sudo, S. Ishiuchi, A. Miwa, Y. Takayasu, I. Saito, K. Tsuzuki, and S. Ozawa. Glia-synapse interaction through Ca^{2+}-permeable AMPA receptors in Bergmann glia. *Science*, 292(5518):926–929, 2001.

[48] C. J. Karwoski, H-K. Lu, and E. A. Newman. Spatial buffering of light-evoked potassium increases by retinal Müller (glial) cells. *Science*, 244(4904):578–580, 1989.

[49] B. Katz and R. Miledi. The characteristics of 'end-plate noise' produced by different depolarizing drugs. *J Physiol*, 230:707–717, 1973.

[50] H. Kettenmann and B. R. Ranson. Electrical coupling between astrocytes and between oligodendrocytes studied in mammalian cell cultures. *Glia*, 1(1):64–73, 1988.

[51] S. Kirischuk, H. Kettenmann, and A. Verkhratsky. Membrane currents and cytoplasmic sodium transients generated by glutamate transport in Bergmann glial cells. *Eur. J. Physiol.*, 454:245–252, 2007.

[52] A. Konnerth, I. Llano, and C. M. Armstrong. Synaptic currents in cerebellar Purkinje cells. *Proc Natl Acad Sci USA*, 87:2662–2665, 1990.

[53] K. A. Lindsay, J. R. Rosenberg, and G. Tucker. From Maxwell's equation to the cable equation and beyond. *Prog Biophys Mol Bio*, 85:71–116, 2004.

[54] J. J. Lippman, T. Lordkipanidze, M. E. Buell, S.O. Yoon, and A. Dunaevsky. Morphogenesis and regulation of Bergmann glial processes during Purkinje cell dendritic spine ensheathment and synaptogenesis. *GLIA*, 56:1463–1477, 2008.

[55] I. Llano, C. K. Webb, and F. Bezanilla. Potassium conductance of the squid giant axon: Single channel studies. *J Gen Physiol*, 22:179–196, 1988.

[56] L. Mayo, F. J. Quintana, and H. L. Weiner. The innate immune system in demyelinating disease. *Immunol Rev*, 248(1):170–187, 2012.

[57] D. R. McNeal. Analysis of a model for excitation of myelinated nerve. *IEEE Trans Bio-Med Eng*, 23(4):329–337, 1976.

[58] D. M. Menichella, M. Majdan, R. Awatramani, D. A. Goodenough, E. Sirkowski, S. S. Scherer, and D. L. Paul. Genetic and physiological evidence that oligodendrocyte gap junctions contribute to spatial buffering of potassium released during neuronal activity. *J Neurosci*, 26(43):10984–10991, 2006.

[59] M. R. Metea, P. Kofuji, and E. A. Newman. Neurovascular coupling is not mediated by potassium siphoning from glial cells. *J Neurosci*, 27(10):2468–2471, 2007.

[60] S. J. Middleton, C. Racca, M. O. Cunningham, R. D. Traub, H. Monyer, T. Knöpfel adn I. S. Schofield, A. Jenkins, and M. A. Whittington. High-frequency network oscillations in cerebellar cortex. *Neuron*, 58:763–774, 2008.

[61] M. Montal and P. Mueller. Formation of bimolecular membranes from lipid monolayers and a study of their electrical properties. *Proc Nat Acad Sci USA*, 69(12):3561–3566, 1972.

[62] J. W. Moore and K. S. Cole. Resting and action potentials of the squid giant axon *in vivo*. *J Gen Physiol*, 43:961–970, 1960.

[63] J. W. Moore, R. W. Joyner, M. H. Brill, S. D. Waxman, and M. Najar-Joa. Simulations of conduction in uniform myelinated fibers. *Biophys J*, 21:147–160, 1978.

[64] T. Müller, J. M. Fritschy, J. Grosche, G.D. Pratt, H. Möhler, and H. Kettenmann. Developmental regulation of voltage-gated K^+ channel and GABA receptor expression in Bergmann glial cells. *J. Neurosci.*, 14(5):2503–2514, 1994.

[65] S. Nadkarni and P. Jung. Modeling synaptic transmission of the tripartite synapse. *Phys Biol*, 4:1–9, 2007.

[66] E. Neher and B. Sakmann. Single-channel currents recorded from membrane of denervated frog muscle fibres. *Nature*, 260:799–802, 1976.

[67] E. Neher, B. Sakmann, and J. H. Steinbach. The extracellular patch clamp: A method for resolving currents through individual open channels in biological membranes. *Pflug Arch Eur J Phy*, 375(2):219–228, 1978.

[68] J. C. Neu and W. Krassowska. Homogenization of syncytial tissues. *Crit Rev Biomed Eng*, 21:137–199, 1993.

[69] C. Neusch, J. H. Weishaupt, and M. Bähr. Kir channels in the CNS: emerging new roles and implications for neurological diseases. *Cell Tissue Res*, 311:131–138, 2003.

[70] E. A. Newman. High potassium conductance in astrocyte endfeet. *Science*, 233(4762):453–454, 1986.

[71] E. A. Newman, D. A. Frambach, and L. L. Odette. Control of extracellular potassium levels by retinal glial cell K^+ siphoning. *Science*, 225(4667):1174–1175, 1984.

[72] J. Newman and K. E. Thomas-Alyea. *Electrochemical Systems*. Wiley-Interscience, 3^{rd} edition, 2004.

[73] A. Nygren and J. A. Halter. A general approach to modeling conduction and concentration dynamics in excitable cells of concentric cylindrical geometry. *J Theor Biol*, 199:329–358, 1999.

[74] R. K. Orkand, J. G. Nicholls, and S. W. Kuffler. Effect of nerve impulses on the membrane potential of glial cells in the central nervous system of amphibia. *J Neurophysiol*, 29(4):788–806, 1966.

[75] T. S. Otis and W. F. Gilly. Jet-propelled escape in the squid *loligo opalescens*: concerted control by giant and non-giant motor axon pathways. *P Natl Acad Sci USA*, 87(8):2911–2915, 1990.

[76] G. Perea, M. Navarrete, and A. Araque. Tripartite synapses: astrocytes process and control synaptic information. *Trends Neurosci*, 32(8):421–431, 2009.

[77] E. Pérez-Torrero, P. Durán, L. Granados, G. Gutiérrez-Ospina, L. Cintra, and S. Díaz-Cintra. Effects of acute prenatal ethanol exposure on Bergmann glial cells early postnatal development. *Brain Res*, 746:305–308, 1997.

[78] J. W. Perram and P. J. Stiles. A dynamical system for action potentials in the giant axon of the squid. *J Phys Chem-US*, 114:20350–20361, 2010.

[79] S. Poliak and E. Peles. The local differentiation of myelinated axons at nodes of ranvier. *Nat Rev Neurosci*, 4:968–980, 2003.

[80] T. Preuss and W. F. Gilly. Role of prey-capture experience in the development of the escape response in the squid *loligo opalescens*: A physiological correlate in an identified neuron. *J Exp Biol*, 203:559–565, 2000.

[81] D. Purves, G. J. Augustine, D. Fitzpatrick, W. C. Hall, A. LaMantia, and L. E. White, editors. *Neuroscience*. Sinauer Associates, 5 edition, 2011.

[82] P. Rakic and R. L. Sidman. Weaver mutant mouse cerebellum: defective neuronal migration secondary to abnormality of Bergmann glia. *Proc Nat Acad Sci USA*, 70(1):240–244, 1973.

[83] C. B. Ransom and H. Sontheimer. Biophysical and pharmacological characterization of inwardly rectifying K^+ currents in rat spinal cord astrocytes. *J Neurophysiol*, 73(1):333–346, 1995.

[84] M. N. Rasband and J. S. Trimmer. Developmental clustering of ion channels at and near the node of ranvier. *Dev Biol*, 236:5–16, 2001.

[85] F. Rattay. Analysis of models for external stimulation of axons. *IEEE Trans Biomed Eng*, 33(10):974–977, 1986.

[86] A. Reichenbach, A. Siegel, M. Rickmann, J. R. Wolff, D. Noone, and S. R. Robinson. Distribution of Bergmann glial somata and processes: implications for function. *J. Hirnforsch.*, 36(4):509–517, 1995.

[87] A. G. Richardson, C. C. McIntyre, and W. M. Grill. Modelling the effects of electric fields on nerve fibres: influence of the myelin sheath. *Med Biol Eng Comput*, 38:438–446, 2000.

[88] G. Richardson. A multiscale approach to modelling electrochemical processes occurring across the cell membrane with application to transmission of action potentials. *Math Med Biol*, 26(3):201–224, 2009.

[89] G. Richardson and S. J. Chapman. Derivation of the bidomain equations for a beating heart with a general microstructure. *SIAM J Appl Math*, 71(3):657–675, 2011.

[90] J. M. Ritchie and R. B. Rogart. Density of sodium channels in mammalian myelinated nerve fibers and nature of the axonal membrane under the myelin sheath. *Proc Natl Acad Sci USA*, 74(1):211–215, 1977.

[91] J. D. Rothstein, L. Martin, A. I. Levey, M. Dykes-Hoberg, L. Jin, D. Wu, N. Nash, and R. W. Kunci. Localization of neuronal and glial glutamate transporters. *Neuron*, 13(3):713–725, 1994.

[92] M. Rydmark. Nodal axon diameter correlates linearly with internodal axon diameter in spinal roots of the cat. *Neuroscience Letters*, 24(3):247–250, 1981.

[93] M. Rydmark and C. H. Berthold. Electron microscopic serial section analysis of nodes of ranvier in lumbar spinal roots of the cat: a morphometric study of nodal compartments in fibres of different sizes. *J Neurocytol*, 12:537–565, 1983.

[94] D. Sadava, H. C. Heller, G. H. Orians, W. K. Purves, and D. Hillis. *Life: The Science of Biology*, volume II. Sinauer Associates, Inc and W. H. Freeman & Co., eighth edition, 2007.

[95] T. Sano, N. Takayama, and T. Shimamoto. Directional difference of conduction velocity in the cardiac ventricular syncytium studied by microelectrodes. *Circ Res*, 7:262–267, 1959.

[96] W. Schwartz, B. Neumcke, and R. Stämpfli. Lonitudinal resistance of axoplasm in myelinated nerve fibers of the frog. *Pflug Arch Eur J Phy*, 379(Suppl. R41), 1979.

[97] Y. Shao and K.D. McCarthy. Responses of Bergmann glia and granule neurons in situ to N-Methyl-D-Aspartate, norepinephrine and high potassium. *J. Neurochem.*, 68(6):2405–2411, 1997.

[98] C. Solsona, B. Innocenti, and J. M. Fernández. Regulation of exocytotic fusion by cell inflation. *Biophys J*, 74:1061–1073, 1998.

[99] R. Stämpfli. Bau und funktion isolierter markhaltiger nervenfasern. *Ergeb Physiol*, 47:70, 1952.

[100] B. Steinberg, Y. Wang, H. Huang, and R. M. Miura. Spatial buffering mechanism: mathematical model and computer simulations. *Math Biosci Eng*, 1(1):1–28, 2005.

[101] T. Storck, S. Schulte, K. Hofmann, and W. Stoffel. Structure, expression and functional analysis of a Na^+-dependent glutamate/aspartate transporter from rat brain. *Proc Natl Acad Sci USA*, 89:10955–10959, 1992.

[102] A. F. Strassberg and L. J. DeFelice. Limitations of the Hodgkin-Huxley formalism: Effects of single channel kinetics on transmembrane voltage dynamics. *Neural Comput*, 5:843–855, 1993.

[103] M. Tanaka, K. Yamaguchi, T. Tatsukawa, M. Theis, K. Willicke, and S. Itohara. Connexin43 and Bergmann glial gap junctions in cerebellar function. *Front Neurosci*, 2(2):225–233, 2008.

[104] W. T. Thach. On the specific role of the cerebellum in motor learning and cognition: Clues from PET activation and lesion studies in man. *Behav Brain Sci*, 19(3):411–433, 1996.

[105] W. Thompson. On the theory of the electric telegraph. *Proc R Soc*, 1855.

[106] A. van Harreveld, J. Crowell, and S. K. Malhotra. A study of extracellular space in central nervous tissue by freeze-substitution. *J Cell Biol*, 25(1):117–137, 1965.

[107] C. A. Vandenberg and F. Benzanilla. A sodium channel gating model based on single channel, macroscopic ionic, and gating currents in the squid axon. *Biophys J*, 60(6):1511–1533, 1991.

[108] A. Wallraff, R. Köhling, W. Heinemann, M. Theis, K. Willicke, and C. Steinhäuser. The impact of astrocytic gap junctional coupling on potassium buffering in the hippocampus. *J Neurosci*, 26(20):5438–5447, 2006.

[109] W. Walz. Role of astrocytes in the clearance of excess extracellular potassium. *Neurochem Int*, 36:291–300, 2000.

[110] D. D. Wang and A. Bordey. The astrocyte odyssey. *Prog Neurobiol*, 86:342–367, 2008.

[111] E. N. Warman, W. M. Grill, and D. Durand. Modeling the effects of electric fields on nerve fibers: Determination of excitation thresholds. *IEEE Trans Bio-Med Eng*, 39(12):1244–1254, 1992.

[112] A. Witthoft, J. Filosa, and G. E. Karniadakis. Potassium buffering in the neurovascular unit: models and sensitivity analysis. *Biophys J*, 105:2046–2054, 2013.

[113] K. Yamada and M. Watanabe. Cytodifferentiation of Bergmann glia and its relationship with purkinje cells. *Anat Sci Int*, 77:94–108, 2002.

[114] L. Zhou and S. Y. Chiu. Computer model for action potential propagation through branch point in myelinated nerves. *J Neurophysiol*, 85:197–210, 2001.

[115] M. Zochowski, M. Wachowiak, C. X. Falk, L. B. Cohen, Y. W. Lam, S. Antic, and D. Zeceviv. Imaging membrane potential with voltage sensitive dyes. *Biol Bull*, 198:1–21, 2000.

[116] B. Zuber, I. Nikinenko, P. Klauser, D. Muller, and J. Dubochet. The mammalian central nervous synaptic cleft contains a high density of periodically organized complexes. *PNAS*, 102(52):19192–19197, 2005.